Departamento de Lenguajes y Ciencias de la Computación

Ph. D. Thesis

Numerical simulation of the molecular orientation and degree of crystallization of semi–crystalline fibres

Autor:
Francisco José Blanco Rodríguez

Director:
Dr. Juan Ignacio Ramos Sobrados

2012

UNIVERSIDAD DE MÁLAGA

SPICUM
servicio de publicaciones

AUTOR: Francisco José Blanco Rodríguez

EDITA: Servicio de Publicaciones de la Universidad de Málaga

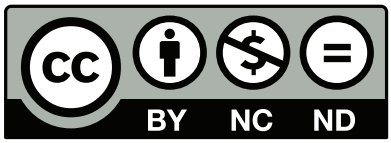

El Dr. Juan Ignacio Ramos Sobrados, Catedrático de Universidad en el Departamento de Lenguajes y Ciencias de la Computación de la Universidad de Málaga

Certifica

Que D. Francisco José Blanco Rodríguez, Ingeniero Industrial, ha realizado bajo su dirección la tesis doctoral titulada Numerical simulation of the molecular orientation and degree of crystallization of semi–crystalline fibres, que se recoge en la presente memoria, cumpliendo todos los requisitos legales para optar al grado Europeo de DOCTOR, por lo que autoriza su lectura y defensa pública.

Y para que así conste y tenga los efectos oportunos, firmo el presente certificado en

Málaga, a 20 de diciembre de 2011

Dr. Juan Ignacio Ramos Sobrados

If you live each day as if it was your last,
someday you'll most certainly be right.

— Unknown

Dedicated to the memory of my beloved father.
Juan Antonio Blanco Mejías (1956 – 2004)

Dedicado a la memoria de mi querido padre.
Juan Antonio Blanco Mejías (1956 – 2004)

Tesis doctoral

Numerical simulation of the molecular orientation and degree of crystallization of semi–crystalline fibres

Autor: Francisco José Blanco Rodríguez

Director: Dr. Juan I. Ramos

Tribunal Calificador

Firma

Presidente:	D. Manuel Laso Carbajo
Vocal:	D. Vicente Hernández García
Vocal:	D. Ignacio Gónzalez Loscertales
Vocal:	D. Alberto de Lózar Muñoz
Secretario:	D. Francisco Román Villatoro Machuca
Suplente:	D. Carlos Manuel del Pino Peñas
Suplente:	D. Enrique SanMiguel Rojas

Calificación

Málaga, 23 de marzo de 2012

Este trabajo de investigación ha sido financiado por el Ministerio de Educación y Ciencia del Gobierno de España mediante el programa de Formación de Profesorado Universitario (FPU) con referencia de beca AP2006-02204.

This research work has been funded by the Spanish Ministerio de Educación y Ciencia under the program of Formación de Profesorado Universitario (FPU) with grant No. AP2006-02204.

An Abstract of

Numerical simulation of the molecular orientation and degree of crystallization of semi–crystalline fibres

Francisco José Blanco Rodríguez

Submitted as partial fulfilment of the requirements for
the Doctor of Philosophy Degree in Engineering (*Doctor Europeus*)

Universidad de Málaga

March 2012

A two–dimensional model of the non–isothermal melt spinning of compound and hollow compound semi–crystalline fibres which accounts for molecular orientation and crystallization is presented in this work. The model is based on the leading–order equations for the fibre's geometry and axial velocity component for slender fibres at low Reynolds and Biot numbers, and two–dimensional equations for the temperature, orientation and crystallization. Furthermore, the model employs a Newtonian rheology, includes the effects of both temperature and flow–induced crystallization, and accounts for the effects of the molecular orientation on both the stress tensor and the crystallization through a Doi–Edwards formulation and the Avrami–Kolmogorov kinetics, respectively. Molecular orientation is modelled by means of a tensor whose evolution depends mainly on the strain rate tensor, while the crystallization depends on the molecular orientation and the temperature field; the equations for the crystallization and molecular orientation are strongly coupled to those of mass, linear momentum and energy conservation.

The model presented here has been used to study the steady melt spinning of both compound and hollow compound fibres numerically by means of finite difference equations in the computational domain which results from mapping the curvilinear geometry of the compound fibre onto two rectangles. Numerical experiments have been performed at moderate draw ratios in a physical domain that, in the axial location, is bounded by the maximum swell location and the take–up cross–section. The numerical results indicate that, even at low Biot numbers, the temperature may not be uniform across the compound fibre because of heat losses. For the cases reported here, the temperature non–uniformities are mainly a function of the Biot number, the thermal conductivity and the pre–exponential factor and activation energy of the dynamic viscosity law for the cladding. The results also show that the cross–sectional averaged temperature predicted by the two–dimensional model exhibits the same qualitative trends as those of an asymptotic one–dimensional model which does not account for axial conduction and which is only valid for slender fibres at low Reynolds and Biot numbers.

For hollow compound semi–crystalline fibres, it is shown that almost complete molecular orientation is achieved close to the maximum swell region due to the large contraction of the fibre there, whereas, for the conditions considered here, the ultimate degree of crystallization is not achieved at the take–up point. It is also shown that there are non–uniformities in the temperature and crystallinity profiles at the take–up point; these non–uniformities may have a great effect on the fibre's properties. Some areas for future work are also indicated.

ACKNOWLEDGMENTS

First and foremost, I would like to thank my advisor, Dr. Juan I. Ramos, for giving me this great opportunity to carry through this research. His encouragement, patience, and advice made this research and the completion of this dissertation possible. I also want to thank Dr. Francisco R. Villatoro for providing useful suggestions. I would also like to appreciate my dissertation committee for their advice and comments.

I want to specially thank Dr. Luis Parras, Dr. Patricio Bohórquez and Sebastián Martín, who helped me a lot with programming matters. I got many suggestions and learnt very much from them. Additionally, I would also like to thank Dr. Carlos del Pino for his help with the application for the stay at the University of Manchester (United Kingdom) and offering me to collaborate in several research topics.

I would also like to thank Prof. Matthias Heil of School of Mathematics at the University of Manchester (United Kingdom) for providing me with the opportunity to participate in a great project such `oomph-lib` and Dr. Martien Hulsen of the Mechanical Engineering Department at Eindhoven University of Technology (The Netherlands) for teaching me the electrospinning technique and allow to me the development of the solver for computing the numerical solution of electrospinning of viscoelastic fluids with `tfem`.

I gratefully acknowledge the Spanish Government through the Ministerio de Educación y Ciencia and the Universidad de Málaga for providing financial support to this research.

I would also like to thank María Obregón, Miguel Ángel Pérez, Jorge Hurel, Alberto Calaf and all friends at the Universidad de Málaga for the good times that we share during my four–year Ph. D. studies.

I am indebted to my parents, uncles and aunts for offering me their kind words of encouragement and support during all my life and allow me to do at every moment what I wanted to.

Finally, I want to thank a lot my girlfriend, Inmaculada Haro, for her support, comprehension and love in these four long years during which we have had no opportunity to be together. Inma, I am heartedly in love with you.

CONTENTS

LIST OF FIGURES

LIST OF TABLES

ACRONYMS

FIC Flow–induced crystallization

PBAT Poly(butylene adipate–co–terephthalate)

PBT Poly(butylene terephthalate)

PE Polyethylene

PET Polyethylene terephalate

PMMA Polymethyl methacrylate

POF Polymer Optical Fibre

PP Polypropylene

PTT Phan–Thien/Tanner

TFA Thin Filament Analysis

TFE Thin Filament Equations

TLCP Thermotropic Liquid–Crystalline Polymer

UCM Upper Convective Maxwell

Part I

PRELIMINARIES

1

INTRODUCTION AND BACKGROUND. MOTIVATION

Contents

1.1 INTRODUCTION

1.1.1 *The melt spinning fibre formation process*

Melt spinning, whose study is the main objective of this work, is the production of continuous solid filaments from polymeric melts and involves the extrusion and drawing of a liquid. The fibre formation process includes change in the shape, structure and properties of the thermoplastic polymer. A diagram of a typical process is illustrated in Figure 1.1 (a). The polymer pellets or granules are fed into an extruder where, through heating, their melting temperature is exceeded. The polymeric melt is then transported, under pressure, to the spinneret. Hygroscopic polymers require vacuum drying prior to processing in order to ensure a low water content. The extrusion temperature T_0 is roughly $30 - 50\,K$ above the melting temperature T_m of the polymer, i.e. $T_0 = 550 - 570\,K$ for Polyethylene terephalate (PET). A constant mass flow rate of the melt is achieved by a metering pump (the spinning pump) which can be positioned inside the spinning head. Within the spinneret, the melt flow is channelled into a number of individual capillary holes, each is responsible for the formation of a single filament. After the melt flow passes through these spinneret orifices into the air, the single filaments are drawn and cooled until they solidify in the draw zone. The final fibre velocity is fixed by the godet which consists of one or more

wheels rotating at a constant rate. The solid fibre moves at the same linear velocity as the wheels due to contact frictional forces. Like a sewing thread, the fibre is finally wound on a spool for storage. The take–up speed is much higher than the average extrusion velocity at the spinneret exit. The ratio between the spinning velocity u_L (take–up speed at any distance L) and the (average) extrusion speed u_0 at the spinneret exit defines the draw ratio D_r:

$$D_r = \frac{u_L}{u_0}. \tag{1.1}$$

Some authors define the draw ratio as the ratio between the radius at the die–exit and that at the take–up point.

The properties of fibres manufactured by melt spinning processes depend on the processing conditions to which the polymer is subject during their manufacture.

Compound (hollow) fibre spinning differs from solid fibre spinning in that two fluids are co–extruded and co–drawn. The inner or core fluid is often a fluid but may be an inert gas; in this case, hollow fibres are obtained. In hollow compound fibres, the outer or external material may protect the inner one, serve as a waveguide in signal transmission, etc. and the principle guiding their manufacture is that the combination of two or more different materials with different properties may result in composite fibres with highly desirable properties. Depending on the extrusion conditions and the rheology of the inner and outer materials, the hollow compound fibre may swell after exiting the nozzle.

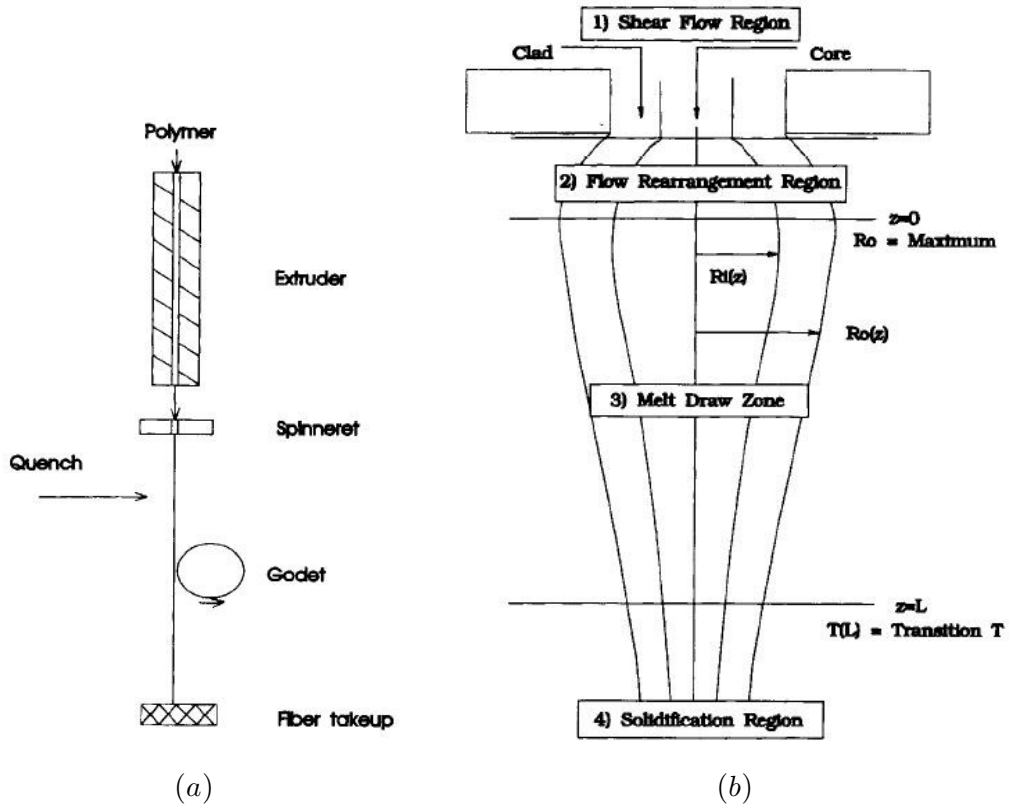

(a) (b)

Figure 1.1: *Schematic figure* (a) *and drawing zones* (b) *of the melt spinning process. This figure has been taken from [91].*

Melt spinning processes are commonly divided into four regions for analysis: (1) the *shear flow region* which exists within the spinneret; (2) the *flow rearrangement region* in which the shear flow becomes an elongational flow; (3) the *melt draw zone* where the fibre is drawn down to the desired size and put in contact with a quench fluid to facilitate heat transfer; and (4) the *solidification region* where as the fluid cools, it becomes a solid. Each of these regions is identified in Figure 1.1 (*b*). It must be noted, that at high drawing speeds, a *neck–in* region has also observed.

The most commonly specified operating variables are the spinneret diameter and temperature, quench fluid temperature and velocity, extrusion mass flow rate and rotation rate of the godet wheels. Proper specification of the operating variables permits production of a given fibre size at a given rate.

A rigorous analysis of this process would require solving the conservation of mass, energy and momentum equations in complex three–dimensional domains. To avoid lengthy and expensive numerical solutions, a number of simplifying approximations have been introduced in the literature which provide the basis for the Thin Filament Analysis (TFA) or Thin Filament Equations (TFE) model.

Explicit treatment of regions 1 and 2 is avoided in this study by assuming the shear flow within the spinneret rearranges to an elongational flow over a distance much shorter than the total draw zone length. Finite element calculations have shown this to be an accurate approximation for both solid and hollow fibre spinning and indicate that flow rearrangement typically occurs over a distance equal to two or three spinneret diameters [79]. In addition, we shall concern ourselves here with moderate drawing speeds so that the neck–in phenomenon does not arise.

Although the exact origin of the draw zone is undefined, the ambiguity is much smaller than the draw zone length. The initial fibre diameter is usually set equal to the spinneret diameter or the maximum die swell radius if die swell is significant. However, direct experimental measurement or an appropriate correlation for die swell is required [49].

The analysis of region 4 is usually avoided by assuming an instantaneous, iso–enthalpic transition to an undeformable solid at an appropriate transition temperature (e.g. melt or glass transition). The significance of this assumption is not well defined in the existing literature. For materials that possess significant crystallinity, especially at high speeds (velocities greater than 1000 m/min), the validity is questionable because the glass transition may be a strong function of crystallinity and crystal orientation [49].

For glassy materials at lower speeds, the use of the glass transition temperature appears to give reasonable results. Small variations in the glass transition temperature do not significantly change the final fluid stress level nor the final fibre diameter [49, 50]. This is not unexpected since both of these important spinline variables asymptotically approach their final values; shifting the exact transition point has little effect within the plateau region.

The above assumptions reduce the problem to an analysis of region 3 only. The fact that the fibre diameter is typically much smaller than the overall draw zone length allows one to simplify the analysis further. The mechanics of this simplification have taken various forms in the literature but all yield the same result: the TFE model.

1.1.2 *Manufacture and applications features*

Most of the man–made fibres used in the textile industry are manufactured by means of fibre spinning processes. Fibre spinning processes are also used in the manufacture of reinforced fibres and optical fibres.

While textile fibre studies, in general, strive to avoid fibre rupture and gross distortion of the thread line, the drawing of optical fibres takes filament continuity for granted, and the application of optical fibres requires that the main issue in their manufacture be the sensitivity to perturbations in the diameter. It must be noted that, when continuous drawing of textile fibres is impossible, much emphasis is placed on the prediction and control of the thread length, i.e., the filament length attainable between spontaneous ruptures.

About thirty years ago, a new optical fibre, i.e., the Polymer Optical Fibre (POF), emerged, but did not find many optical applications due to its high attenuation, until about fifteen years ago when graded–index optical fibres and low–attenuation perfluorinated fibres were developed [155]. POFs are now available as high–capacity transmission media thanks to their transparency and bandwidth; they are currently replacing copper fibres in short–haul communications links due to their transmission capacity, immunity to interference and small weight. In addition, POFs serve as a complement to glass fibres in short–haul communications links because they are easy to handle, flexible, and economical, although they are not used for very long distances because of their relatively high attenuation.

POFs used for optical communications are highly flexible wave guides composed of nearly transparent dielectric materials. The cross–section of these fibres is circular and, generally, consists of three layers. The inner layer is called the core, the middle one is the cladding, and the outer layer is the jacket or protective cover. Within the core, the refractive index profile may be uniform (step–index fibres) or graded (graded–index fibres), whereas the cladding is typically uniform.

Figure 1.2: *Schematic of a plastic optical fibre [140].*

Optical fibres can be classified in two main groups from the point of view of wave propagation: *single–mode fibres* which have a relative small core, and *multimode fibres*, whose core is large enough so that propagation may be analysed by means of geometric ray–tracing models. Single–mode POFs exhibit a much larger attenuation than single–mode glass fibres and lack the main advantages of conventional POFs, i.e., ease to handle and low cost connectors. As a consequence, research on these fibres has not been very active, although single–mode POFs can be easily coupled to planar wave guides and serve as components for some devices such as sensors, and their core may be doped with a dye to control absorption and non–linear wave propagation.

Two steps are usually followed in the manufacture of POFs. First, a solid cylindrical rod, called preform, which is approximately $0.5 - 1\,m$ long and several centimetres in diameter, is made; the structure of this preform determines the core and cladding refractive index profiles. The second step consists in the heating and extrusion of the preform, which yields a POF length in a range between half a kilometre and several kilometres. Step–index POFs are manufactured by means of a melt spinning process in which fibres are obtained by either continuous or batch extrusion. In the continuous extrusion process, a monomer, an initiator and a chain transfer agent are continuously fed into the reactor and the fibre is continuously drawn from the die. This is an efficient process due to its high production rate.

In order to obtain a particular refractive index profile in the core along the radial direction, a preform with the desired profile can be employed; whenever more complex refractive index profiles are required such as graded–index ones, a technique based on drawing a preform by melting its tip with the aid of an oven is used. The preform is, in this case, a cylinder of a polymer whose refractive index distribution in the radial direction can be made to coincide with that desired for the POFs core.

Currently, there are two main techniques to produce graded–index POFs: *gel polymerization* and *diffusion*. The gel polymerization technique requires the manufacture of a hollow cylinder made of a polymer, e.g., Polymethyl methacrylate (PMMA), which will be the POFs cladding. The hollow cylinder is filled with a mixture of a monomer from which the polymer cylinder is made, a dopant with a higher refractive index than that of the polymer, an initiator, and a chain transfer. The filled cylinder is then heated for some time and, as a consequence of the heating, the cylinder softens due to the formation of a gel phase which accelerates the polymerization reactions, i.e., the polymer is formed from the gel phase on the inner wall of the cylinder; the reaction is completed when the initially hollow cylinder becomes a solid one. The reason for the use of dopants with a higher refractive index than that of the polymer is that light should be confined in the structure, and the mechanism for the correct distribution of the refractive index consists in the selective diffusion of the monomer and dopant materials in the gel–polymer phases created in the inner wall of the hollow cylinder. Moreover, since the molecular volume of dopants is higher than that of the monomer, the monomer diffuses faster than the dopant in the gel phase. For this reason, dopant molecules are concentrated in the central region of the cylinder, so that the refractive index is higher in this region.

Once the preform has been obtained, it is held up by a support in the fibre extrusion tower, where the lower end of the preform is heated with the aid of a furnace, so that it acquires the necessary low viscosity to be extruded downward. The extrusion velocity and the speed at which the mandrel rotates are adjusted by a controlled mechanism, so that the fibre reaches the desired constant diameter.

During the extrusion process, the geometrical relationship between the core and the cladding is kept constant, even though there is a drastic reduction from the diameter of the preform to the final diameter of the extruded fibre. Finally, a coating is applied to the fibre in order to protect it against microcurvatures or microbends, improve its mechanical resistance, and ease its handling. When the coating has hardened by the effect of heat or ultraviolet radiation, the optical fibre's resistance to traction is continuously tested by forcing the coated POF to pass through a series of pulleys that exert mechanical tension on it. In this manner, the optical fibre must resist a minimum load before it is wound onto a cylindrical drum.

Other processes that usually use polymeric membranes (see Fig. 1.3 (a)) in either hollow fibre or flat sheet forms, are membrane separation processes. These processes are employed in

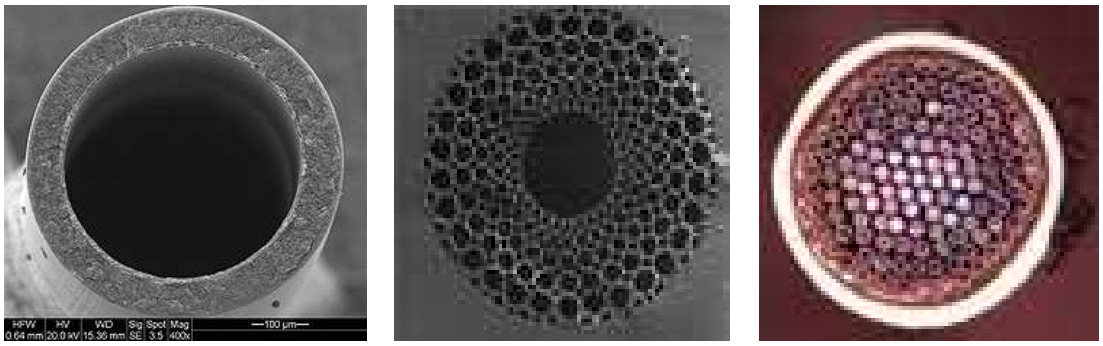

(a) (b) (c)

Figure 1.3: *Some applications of the hollow compound semi–crystalline fibres.* (*a*) *Filtration process,* (*b*) *optics and* (*c*) *infrared imaging and sensing.*

a variety of industries ranging from water treatment to industrial gas separation [115]. Hollow fibre membranes are mass–produced by a variety of spinning processes. These include variations of the melt, dry and wet spinning processes.

The main reason why the spinning process is important to the development of gas separation applications is that overall process economics are dictated by the rate at which hollow fibres of uniform size and properties can be produced. Ideally, one could produce hollow fibres at arbitrarily fast line speeds. In practice, however, rates are limited by instabilities that arise in the process. Commonly encountered instabilities will be discuss below.

Hollow fibres are also broadly used because of their high surface–to–volume ratio and are preferred in ultrafiltration and dialysis [12]. They are also used in the textile industry as well as in optics, e.g., micro–structured optical fibres (Fig. 1.3 (*b*)), for infrared imaging and sensing (see Fig. 1.3 (*c*)), wave transmission, etc., in military and medical applications, etc. [114]. Hollow fibre bio–reactors have been in use for more than thirty years for the production of secreted proteins and antibodies from mammalian cells, while polymeric solid hollow fibres of Polypropylene (PP) have been used in heat exchangers for thermal desalination to replace the conventionally used metallic shell–and–tube heat exchangers which require huge capital investments, suffer from corrosion/erosion problems, create heavy metal pollution, and display a large footprint [135].

1.2 BACKGROUND

1.2.1 *Models for amorphous compound fibres*

Although there has been quite a lot research on the development of one–dimensional, mathematical models for the analysis of the drawn–down region of single–component filaments and jets under both isothermal and non–isothermal conditions at low Reynolds numbers [28, 29, 52, 111, 112, 126, 145, 148, 153], compound fibres such as those used in reinforced materials and optical fibres (which are manufactured in co–extrusion processes) have received very little attention despite the fact that the combination of two or more different materials with different properties may result in composite fibres which highly desirable properties [71, 72, 90, 101, 109, 117, 121]. For example, in the manufacture of optical fibres, the core is surrounded by a sheath of cladding material.

Ramos [117] developed an asymptotic model for isothermal, compound fibres consisting of Newtonian fluids, from the time–dependent axisymmetric form of the conservation equations and obtained some analytical solutions under steady–state conditions.

Park [109] used perturbations methods based on the slenderness ratio and the smallness of the Deborah number in his studies of steady, isothermal, two–phase or compound fibres consisting of a Newtonian core layer surrounded by a sheath of a non–Newtonian fluid with a Maxwell rheology. His studies result in a system of ordinary differential equations for the axial velocity component and radii of the two–phase fibre which is more manageable than the two–dimensional conservation equations of mass and linear momentum from which it was derived. Lee and Park [90] employed the one–dimensional equations developed by Schultz [126] to study the linear stability of the spinning of isothermal, bi–component fibres characterized by a Newtonian fluid for the core and an upper–convected Maxwell fluid for the cladding, and showed that the stability of the fibre can be maintained at higher draw ratios than those that result when the same fluid is employed for both the core and the cladding. Naboulsi and Bechtel [101] introduced a one–dimensional model of isothermal, Newtonian, bi–component fibre filaments by integrating the three–dimensional equations over the filament cross–section, and examined the influence of density, viscosity and surface tension ratios on the steady–state fluid dynamics of isothermal, compound jets at low Reynolds numbers. Ji and Yang [71] and Ji et al. [72] studied isothermal, bi–component fibres characterized by a Newtonian fluid for the core and a Phan–Thien/Tanner (PTT) fluid for the cladding.

As stated above, previous studies of the drawn–down region of bi–component or compound fibres at low Reynolds numbers [71, 72, 90, 101, 109, 117, 121] have only considered isothermal, steady–state flows or determined the linear stability of these flows; in addition, except for that of Ramos [121], none of these studies has considered the possible steady–state solutions of isothermal, steady, bi–component fibres, and determined the effects of the downstream boundary conditions, forcing and fluid dynamics parameters on the non–linear dynamics of isothermal, compound liquid fibres. Moreover, there does not seem to be any studies concerning the cooling as well as the non–linear response of non–isothermal, bi–component or compound fibres to perturbations in the fibre's geometry, axial velocity and temperature, perturbations in the operating conditions, etc., analogous to those performed by, for example, Geyling [52], for single–component, round fibres. It must be noted that compound fibres reduce to single–component ones whenever the core and cladding are made of exactly the same material, and, therefore, any model for compound fibres should reduce to a model for single–component, round fibres when the materials of the core and cladding are identical.

1.2.2 *Models for amorphous hollow fibres*

Although some one–dimensional models have been developed to study the melt spinning (and drawing) of single–component hollow fibres [40, 118, 142, 146, 147] based on Taylor's series expansions in the radial direction, asymptotic methods or integral formulations of the governing equations for slender fibres under isothermal and non–isothermal conditions, there have been few studies on the melt spinning of hollow compound fibres [119, 122] and these studies have been limited to very small Biot numbers for which an asymptotic analysis for slender fibres indicates that the temperature across the fibre is uniform at leading–order. For moderate or large Biot numbers, such a uniform temperature approximation is not expected to be valid, especially at the interfaces between the hollow compound fibre and its surrounding media and at

the interface between the inner and outer materials that make up the hollow compound fibre. These temperature uniformities, in turn, affect the velocity field through the dependence of the dynamic viscosity on the temperature, and the molecular orientation and crystallization of semi–crystalline polymer fibres through their dependence on the thermal field and the strain rate and stress tensors. As a consequence, temperature non–uniformities across a hollow, compound fibre may result in non–uniformities on the degrees of molecular orientation and crystallization which, in turn, affect the fibre's morphology and mechanical, chemical, optical, etc., properties.

1.2.3 *Instabilities of fibre spinning processes*

Stability is critical to any practical manufacturing process including commercial fibre spinning processes. Many factors affect the ability to produce fibres with uniform size and properties. The onset of spinning instabilities is one of the major factors that influence process productivity and quality control. Two major process instabilities have been observed during fibre spinning: *melt fracture* and *draw resonance*. Both instabilities yield fibres with non–uniform dimensions and an excellent summary of the related literature is provided by Petrie and Denn [113].

Melt fracture refers to extrudate distortion and typically appears as exaggerated surface roughness. When the extrusion rate increases beyond a critical value, the exit flow becomes unstable and an extrudate with a smooth surface cannot be produced. If the surface distortions are too severe, the filament can break.

The nature of the surface distortion depends on extrusion conditions and the material being extruded. As the extrusion rate increases, the extrudate surface can change from smooth to sharkskin, stick–slip, and then finally gross melt fracture [63, 75, 97, 133].

Typically, sharkskin is the first surface irregularity observed upon increasing the flow rate. This distortion is characterized by a fine–scale texture of relatively small amplitude and short wavelength [62, 98]. As the extrusion rate increases further, a stick–slip (or spurt–flow) surface distortion may appear that is characterized by alternating smooth and sharkskin regions [51, 92]. Finally, at higher extrusion rates, extreme distortions referred to as gross or wavy melt fracture may occur [26, 81]. For some systems, a second stable region may exist between the stick–slip and gross melt fracture regions. In this region, a smooth extrudate is obtained but at much higher extrusion rates than in the first stable region. This region is usually referred to as the super–extrusion or super–flow region.

The mechanism of melt fracture is complex and poorly understood. Researchers have proposed a multitude of mechanisms but have not reached consensus on the underlying physics [8, 58, 59, 61, 62, 106–108, 134, 141]. Most researchers agree that the instability starts inside the spinneret but have different opinions on where: some point inside the die, at the die entrance, at the die exit or some combination of these locations.

Researchers also believe that melt fracture is associated with the elastic deformation that arises from the difference between the normal stress of the extrudate and the applied shear stress [97]. Theoretical studies of melt fracture have ranged from simple linear stability analyses [97] to much more complicated models [55, 133].

Draw resonance is another type of instability observed in fibre spinning processes. It is characterized by periodic, long wave length variations in extrudate dimensions in contrast to the random, short wave length surface irregularity associated with melt fracture. Draw resonance in

fibre spinning processes was first reported by several researchers [23, 47, 99] in the early 1960's and later was found to depend only on the draw ratio [31] under isothermal conditions and for Newtonian fluids at low Reynolds numbers. Therefore, operating at low extrusion rates may avoid melt fracture but draw resonance can occur if the draw ratio is sufficiently large.

Unlike melt fracture, draw resonance can occur in Newtonian fluids. This suggests the instability has a viscous origin contrary to the elastic origin of melt fracture [19, 31]. Additionally, heat transfer is not a direct trigger because draw resonance is observed in isothermal or nearly isothermal spinning processes [19, 27, 31, 103, 144]. These observations initially led researchers to develop theoretical stability analyses of isothermal, Newtonian spinlines. The first analyses were based on linear perturbation theory applied to the TFE linearised about the steady–state. Pearson [110], Shah [131], Han [59], Kase [76] and co–workers treated the linearised system as an initial–value problem in which the system is perturbed from steady state with a periodic disturbance in the inlet boundary conditions. The response of the system, as a function of the disturbance frequency, was determined numerically by a two–step finite difference method. Gelder [48] and Fisher and Denn [39] used classical stability theory in their work. Infinitesimal fluctuations are introduced into the steady–state system while maintaining the boundary conditions at the ends of the draw zone. The solution of the resulting linearised, transient thin filament equations is an eigenvalue problem. For a given value of the draw ratio, the spinning process is stable if the real parts of the calculated eigenvalues are negative. Otherwise the spinning process is unstable. Both types of stability analysis predict the existence of a single critical draw ratio, $D_r^* \sim 20.22$, for isothermal spinning of Newtonian fluids. When the draw ratio exceeds D_r^*, steady spinning is not possible. Donnelly [31] provides the first experimental confirmation of this prediction. This is now a well–recognized result that serves as a benchmark for the evaluation of new models and numerical methods.

Linear perturbation theory can predict the stability of the spinline only to infinitesimal disturbances. It cannot predict in stability to finite disturbances. Furthermore, the transition from an initial infinitesimal disturbance to the observed macroscopic draw resonance behaviour cannot be demonstrated with a linear analysis: a non–linear stability analysis is required. Fisher and Denn [38, 39] extended their linear analysis to a non–linear analysis to evaluate stability for finite–amplitude disturbances. They demonstrate that isothermal spinning of Newtonian fluids is stable when the draw ratio is below D_r^* for both infinitesimal and finite disturbances. Hyun [67, 68], Kim [80], Jung [74], Lee [88, 89] and co–workers examined isothermal spinning stability using kinematic wave theory and found the same critical draw ratio. Ishihara and Kase [69, 70] and Cao [15, 16] obtained a numerical approximation to the solution of the transient, non–linear TFE to demonstrate the evolution of a disturbance into draw resonance. Their results are in excellent agreement with previous stability analyses.

Ramos [121] performed a linear stability analysis of the steady solution for isothermal compound fibres or jets and carried out time–dependent numerical simulations below and above the critical draw ratio predicted by linear stability theory in order to determine the dynamic response of compound fibres to time–dependent axial velocity variations at the die exit and/or take–up point. This stability analysis for what he refers to as the viscous regime, provides the same stability condition on the draw ratio as analogous analyses for planar film casting [120], single–component fibres [54, 110, 127, 149], single–component annular jets [118] and bi–component or compound, annular liquid jets [119], when there is no surface tension and pressure differences across the annular jet.

Near the critical draw ratio, bifurcation theory for isothermal, single–component, round fibres yields a stable supercritical Hopf bifurcation, the frequency of which decreases as the winder speed is increased near the critical one [128]. For draw ratios higher than the critical one, Schultz et al. [128] found that the oscillation amplitude compares favourably with experimental data for isothermal fibres; however, they found quantitative differences in the disturbance frequency. This discrepancy can be attributed to the rheology of the fibres used in the experiments, for it was observed that, with viscoelastic fluids, the frequency decreases with the amplitude.

Draw resonance for non–Newtonian fluids is a more complex problem. Unlike for Newtonian fluids, a single critical draw ratio does not exist. The critical draw ratio is highly dependent on the fluid rheology. For an inelastic non–Newtonian fluid with a power law viscosity, the critical draw ratio is directly proportional to the power law index. For shear thinning fluids (i.e., power law indices less than unity), the critical draw ratio is less than that predicted for Newtonian fluids and decreases as the power law index decreases.

For shear thickening fluids (i.e., power law indices greater than unity), the critical draw ratio is greater than that of Newtonian fluids and increases with increasing power law index [39, 59, 68, 131]. The predicted drop of critical draw ratio for a shear thinning fluid is in good agreement with experimental observations [59, 103, 144]. Fluid elasticity also has a significant effect on the stability of non–Newtonian fluids. Fisher [39], Hyun [68], Jung [74] and co–workers examined spinning stability using a simple Maxwell model, while Lee et al. [87–89] use the PTT model. All of the results indicate that elasticity has a stabilizing effect for extensional–thickening fluids: the critical draw ratio increases as the fluid relaxation time increases.

Any disturbance in the spinline eventually shows up as a fluctuation in the force applied to the filament at the take–up point. For Newtonian fluids, the take–up force responds immediately to the disturbance. However, a delay may occur for non–Newtonian fluids. This delay gives the system time to return to its original stable state from a perturbed state and thereby increase the critical draw ratio. Additionally, a second critical draw ratio exists for some non–Newtonian fluids. Spinning is unstable between the two critical values. This suggests that draw resonance is a dynamic phenomenon rather than an elastic one.

Temperature is another factor that affects draw resonance. Non–isothermal analyses [57, 129, 130] indicate that cooling stabilizes the spinning process for both Newtonian and non–Newtonian fluids. This increased stability is due to the strong dependence of viscosity on temperature. As the filament cools, viscosity increases dramatically along the spinline and the filament becomes less sensitive to any force fluctuations at the take–up device. Gupta et al. [57] predict critical draw ratios as high as 10^4 for non–isothermal spinning. This value is not as high as that found in stable commercial spinlines but does demonstrate the tremendous stabilization effects of cooling and fluid elasticity.

Fluid inertia, gravity and surface tension also affect spinline stability. Shah [130] and Chang [20] and co–workers theoretically studied these effects and found that inertia has a strong stabilizing effect and dominates the effects of gravity and surface tension. Experimental results reported by D'Andrea and Weinberger [25] qualitatively agree with the numerical predictions. Therefore, gravity and surface tension forces can be neglected when analyzing the stability problems of most practical spinning processes.

Solid fibre spinning has been the focus of all of the stability analyses discussed thus far. While similar analyses have been conducted for tubular film blowing processes [14, 53, 60, 82, 84, 96, 100, 151], the stability of hollow fibre spinning has not been addressed until recently [54, 91, 118, 119,

150]. These works demonstrate that isothermal hollow fibre spinning also is unstable when the draw ratio exceeds D_r^* for Newtonian fluids. While, no direct evidence of draw resonance has been reported in the literature, past work [2, 6] demonstrates an instability that is unique to hollow fibre spinning. Under certain operating conditions, the filament periodically forms "bubbles" along its length. These bubbles are short regions of much greater fibre diameter separated by regions of much smaller fibre diameter. Although the bubbling instability is superficially similar to draw resonance, the two phenomena appear to originate from different physics. In particular, the variation in fibre size is not sinusoidal as with draw resonance; the distance between "bubbles" is much greater than the length of a bubble. Additionally, the instability appears to occur at a critical bore–to–clad flow rate ratio instead of at a critical draw ratio.

1.3 POLYMER ORIENTATION AND CRYSTALLIZATION

As stated above, most plastic products are manufactured by heating the polymer to above its melting temperature and then cooling it in a mould as in injection moulding or deforming the melt while simultaneously cooling it to get the desired shape as in film blowing and melt spinning. The properties of the final product depend on the processing conditions to which the polymer is subject during its manufacture. Furthermore, depending on the molecular structure and processing conditions, the final product can be in either an amorphous or a semi–crystalline state. Polymers that are unable to crystallize on cooling below their glass transition temperature, form amorphous solids, and, if these solids are formed by deforming the polymer while cooling it through the glass transition temperature, they can exhibit strong anisotropy. As the deformed amorphous polymer melt cools below its glass transition temperature, its molecules lose their mobility and become frozen in this oriented configuration.

Polymers having a regular or ordered molecular structure form a semi–crystalline solid when kept at a temperature below the melting one for a sufficiently long time. Under quiescent conditions, the crystallization process can be very slow especially at temperatures just below the equilibrium melting temperature, and the resulting solid has a spherulitic morphology.

The rate of crystallization depends on the molecular orientation in the melt; when subject to deformations that align the polymer molecules, the rate of crystallization increases dramatically, and, when the temperature drops below the glass transition temperature, there is a cessation of molecular motion and the crystallization rate decreases and may stop. As the crystallinity increases, it retards the crystallization process and decreases the mobility of the polymer molecules in the amorphous phase.

Some polymers such as, for example, Polyethylene (PE), find applications at temperatures between their melting and glass transition temperatures. At these temperatures, the solid consists essentially of rigid crystals and a flexible amorphous phase and it is therefore solid and tough.

The properties of the final product depend on the final morphology of the amorphous and semi–crystalline phases; the morphology, in turn, depends on the thermal and deformation histories undergone by the material during processing. Moreover, many products such as fibres and films are subjected to large inelastic deformations after manufacture, and, during the course of these deformations, further crystallization may take place, and the morphology and properties of the product evolve with the deformation.

Liquid–crystalline solutions may phase separate even under isothermal conditions due to electrostatic and steric interactions that result from the rigidity of the polymer chain backbones

even at low polymer concentrations, and form anisotropic phases with a degree of molecular orientation even in the quiescent state as evidenced by their ability to exhibit birefringence under static conditions. During processing, e.g., isothermal spinning, these molecules are aligned by the flow, thus yielding products with highly anisotropic properties [116]. For example, ultrastrength textile fibres such as Vectran and Kevlar achieve their distinguished commercial properties (tensile modulus) as a result of the interaction between the anisotropic molecular–scale structure of the melt or solution, the macroscopic hydrodynamics of spinning flows and non–isothermal effects including radial heat transfer through the round fibre free surface, temperature dependence of material properties, crystallization, and phase change.

The phase change from the amorphous to the semi–crystalline stage is referred to as a *phase transition*. Early work on phase transitions considered that heat conduction was dominant and assumed that the temperature was the basic variable. Mean–phase field models were subsequently developed; these models introduce both the temperature and an order parameter, modify the energy equation to account for the order parameter, and introduce an additional equation the origin of which can be traced back to the Landau–Ginzburg theory of phase transitions. However, in most situations of practical interest, other mechanisms than conduction, e.g., convection in the liquid and deformation of the solid, take place and must be considered by introducing the kinematics of both the liquid and solid. Moreover, these mean–phase field models are unable to predict the mechanical properties of the newly formed solid, and, in many materials, after crystallization is initiated, the material goes through an intermediate set of states where it is mixture of a liquid and solid, i.e., a mush, before being completely transformed into a solid. Although there have been some studies on mushy zones, these studies have not addressed the issues of changes in symmetry associated with the phase change and the large deformations of the solid.

In the liquid phase, there are density fluctuations caused by thermal agitation [85, 86]. These fluctuations may eventually create small *clusters* or aggregates of polymer molecules having the same properties as the crystalline phase; the small crystals are continuously being created and destroyed by fluctuations because the formation of a crystal involves the creation of an interface between the liquid and the crystal and its consequent energy cost, i.e., the creation of crystals is a competitive process whereby there is a decrease of energy due to the fact that the chemical potential of the crystal phase is lower than that of the liquid and an increase of energy and an energy cost associated with the creation of interfaces. Moreover, surface effects are dominant in clusters of small size and, as a consequence, their growth is not energetically favourable, and small crystals tend to dissolve. There exists, however, a critical size beyond which volume effects dominate over surface ones, and the growth of the cluster is favoured by a global reduction of energy. The size that determines the stability of the clusters is called *critical size*, and the process of formation of crystals of size larger than or equal to the critical size is called *nucleation*. There are two basic types of nucleation: homogeneous nucleation which occurs in the bulk of a pure substance and heterogeneous nucleation which takes place in the presence of impurities, pre–existing crystals, boundaries, etc.

Nucleation is the first step in the crystallization process, for it determines the appearance of the first crystal nuclei which are the germ of the second stage of crystallization, i.e., growth. In this second stage, nuclei larger than the critical size tend to grow either through the addition of monomers or by acting as sites of heterogeneous nucleation, e.g., nucleation on the surface of a growing crystal.

Crystals grow freely until they begin to completely fill the whole space. Once they hit each other, their growth stops at the contact surface. This phenomenon, referred to as *impingement*, determines the final morphology of the processed polymer. In the final stage of crystallization, the impingement impedes the subsequent nucleation of the crystals and, therefore, amorphous matter remains trapped among clusters. Furthermore, the clusters themselves are not fully crystalline because they may contain some amorphous inclusions. This trapped material can eventually join the main crystal structure and, therefore, increase the degree of crystallization in a process referred to as secondary crystallization.

As stated previously, the first step in the kinetics of phase transitions is nucleation. This is an activated process where an energy barrier has to be overcome in order to form nuclei of a critical size, beyond which the new phase grows spontaneously. Models for the crystallization of polymers have been mainly based on the Avrami–Kolmogorov equation [3–5, 83] that is based on the theory of filling the space through the nucleation and growth of one phase into another. This equation was initially developed for isothermal, quiescent crystallization, although it has been extended to account for non–isothermal conditions [13, 17, 36, 37]. Experimental results for PE and PP show that there is a temperature drop before crystallization is initiated, after which there is plateau where vigorous crystallization takes place at an almost constant temperature, followed by a temperature drop to the ambient value after the cessation of crystallization.

When phase transitions occur in a flowing polymer melt, crystallization takes place under strain and non–isothermal conditions, and the morphology of the processed polymer depends on the temperature and deformation history. In fact, it has been observed that crystallization may be enhanced by shear, pressure and strain, and that shear may increase the nucleation density, whereas the crystallization rate decreases as the cooling rate is increased. Usually, a highly oriented crystalline morphology is obtained under isothermal and non–isothermal deformations, in contrast with the spherulite morphology observed under quiescent conditions. In spun fibres, for example, lamellae are found to be perpendicular to the fibre axis and enhanced crystallization is caused by chain extension arising from entanglement between molecules. Orientation in the melt usually accelerates the phase transition process, but the molecular orientation may be enhanced or relaxed depending on the deformation history and the relaxation time of the melt.

Flow–induced crystallization (FIC) in melts have been modelled in a number of different manners. A frequently used approach is based on the Avrami–Kolmogorov equation which is modified to account for enhanced crystallization due to the flow. In this approach, the effect of the flow is accounted for by the inclusion of an orientation factor which depends on the flow [153]. Another approach is based on an extension of the work of Flory [41] on the stress–induced crystallization of rubber. Such an extension assumes that the temporary network junctions play the same role as the chemical cross–links in the theory of rubber crystallization and is based on the decrease in entropy of the stretched molecules and the tendency of the polymer to crystallize. A third approach is based on the formulation of constitutive equations that involve the concept of multiple natural configurations and obtain evolution equations for the natural configuration and mass fraction of the crystalline material by maximizing a prescribed rate of dissipation [125]. This approach combines continuum mechanics and thermodynamics, assumes that effects are additive, and results in different models that depend on the forms used for the internal energy, entropy and dissipation rate.

1.3.1 *Review of previous melt spinning models which include orientation and/or crystallization*

Models that only account for the orientation–hydrodynamics interactions in fibre spinning processes and, therefore, neglect energy effects and phase changes have been developed by Forest and co–workers [43, 44] for liquid crystalline, round polymer fibres. These authors considered the evolution of the microstructure in isothermal flows by starting from the three–dimensional Doi–Edwards averaged kinetic equations before undertaking the study of the spinline crystallization under isothermal [42] and non–isothermal flow conditions [45]. It is commonly accepted that crystallization kinetics is triggered by a combination of orientation, stress and temperature [153].

It is well known that non–isothermal effects due to the rapid cooling by the surrounding quench air and the low thermal conductivity of fibres can result in non–uniform fibre microstructure and (mechanical, electrical, chemical, optical) properties. As a result, skin–core differentiation or molecular orientation and structure can be observed in many fibres. Although considerable efforts have been made to understand the dynamics of the melting spinning process and the relationship between spinning conditions and fibre structure, most previous studies on melting spinning processes are based primarily on one–dimensional models which include a single–phase two–component submodel to describe stress–induced crystallization along the spinning line [32, 34, 35, 95]. However, the results of these models do not provide any information about radial variations and on the implications of these variations on the fibre microstructure. Moreover, if one–dimensional models of the draw–down region of fibre spinning processes overestimate the heat transfer at the fibre's outer surface, they predict inaccurate temperature fields which, in turn, influence the average axial velocity, tensile stress, crystallinity, and free–surface shape due to the non–linear couplings between the mass, linear momentum and energy equations. Through the dependence of the crystallization kinetics on temperature and molecular orientation, a strong crystallinity profile is developed, and the radial variation of the molecular orientation and crystallinity has a strong influence on the fibre microstructure and properties, i.e., physical, mechanical, thermal, chemical, electrical and optical properties, such as tensile modulus and optical birefringence.

In order to account for the effects of crystallization on melt spinning processes, one must account for the rheological behaviour of the amorphous phase (the melt), the semi–crystalline phase, and the rate of crystallization. From the rheological point of view, it may be assumed that the two phases (amorphous and semi–crystalline) act in parallel and, therefore, the strain rate tensor is the same for both phases, while the total stress is simply the superposition of the individual stresses.

A simple model to account for the crystallization (if any) of spun filaments under non–isothermal conditions consists in approximating the *thermal* crystallization rate by a quasi–static Avrami–Kolmogorov equation, e.g.,

$$\frac{d}{dt}[-\ln(1-\mathcal{Y})]^{\frac{1}{n}} = K_{st}(T, \Delta p), \tag{1.2}$$

where n denotes the Avrami exponent (usually assumed to be an integer $1 \leq n \leq 4$), and K_{st} is the steady–state crystallization rate which depends on the temperature and spinning stress, Δp, which may be approximated by

$$K_{st}(T, \Delta p) = K_{st}(T, 0) \exp[C_3(\Delta p)^2], \tag{1.3}$$

where C_3 is a constant and $K_{st}(T, 0)$ is the crystallization rate of an isotropic crystallization [154]. This *thermal* crystallization rate can be added to the *athermal* one and to flow– and shear–induced crystallization rates in order to determine the whole rate.

The one–dimensional model of fibre spinning of round fibres developed by Doufas et al. [32, 34, 35, 95] includes the combined effects of flow–induced crystallization, viscoelasticity, filament cooling, air drag, inertia, surface tension, latent heat and gravity. It also includes both an amorphous phase (simulated as a modified Giesekus fluid) and a semi–crystalline phase (approximated as rigid rods that grow and orient in the flow field) and are coupled through the stress and linear momentum balance and the feedback of the crystallinity to the system of relaxation times, predicts neck–like deformation and associated strain softening, and shows that crystallization occurs mostly after the freeze point.

The microstructure model prior to the onset of crystallization used by Doufas et al. [32, 34, 35, 95] assumes that the polymer melt exiting the spinneret is coarse–grained as a concentration of n non–linear dumbbell molecules per unit volume. In a mean field approximation, each of the polymer melts is assumed to contain N_0 flexible statistical links of length l. The microstructure, i.e., orientation and stretching, of the melt is characterized by the conformational tensor $\mathbf{c} =< \mathbf{RR} >$ that represents the second moment of the end–to–end vector $\mathbf{R}$ of the polymer chains [9], and the bracket denotes averaging with respect to the distribution function of the melt phase. Moreover, the conformational tensor is assumed to be determined from a differential equation and allows to determine the extra stress tensor.

Doufas et al. [32, 34, 35, 95] also assumed that crystallization begins when the axial temperature in the filament reaches the equilibrium melting temperature, although experimental data suggest that crystallization in high–speed melt spinning occurs below that temperature. After the onset of crystallization, it is assumed that crystallization corresponds to the transfer of N statistical links from the amorphous (melt) phase to the semi–crystalline phase at an arbitrary position along the spin line under both undercooling and stress; this implies that stretching and crystallization may occur simultaneously, and the degree of transformation from the amorphous to the semi–crystalline phase is defined as $z = \frac{N}{N_0}$. In general, the semi–crystalline phase consists of amorphous and crystalline regions, and the absolute degree of crystallization is defined as the ratio of the mass of the pure crystalline material to the total mass of the system, i.e., $\mathcal{Y} = z\mathcal{Y}_\infty$, where $\mathcal{Y}_\infty$ is the degree of crystallization within the semi–crystalline phase, i.e., the ratio of the mass of pure crystalline material to the mass of the semi–crystalline phase.

Fully steady–state two–dimensional models that account for viscoelasticity, non–isothermal conditions, crystallization kinetics, and free–surface conditions have been developed by Joo et al. [73] and Sun et al. [136] who employed a non–isothermal, viscoelastic Giesekus constitutive model, the non–isothermal crystallization kinetics of Nakamura et al. [102] where the crystallization rate which is a function of both the temperature and molecular orientation, is evaluated according to the equation proposed by Ziabicki [153], the thermally–induced crystallization is approximated by a Gaussian function in Ziabicki's formulation, and the molecular orientation is

determined from a stress–optical law that introduces stress–induced crystallization. It must be noted that Joo et al. [73] assumed that the solvent viscosity can be expressed as the product of two terms; the first term corresponds to amorphous polymers and depends exponentially on the temperature through an Arrhenius equation, while the second one is an exponential function of the relativity crystallinity defined as the ratio of the crystallinity to the maximum obtainable crystallinity. Moreover, their crystallization kinetics is based on the assumption of iso–kinetic conditions, for which the ratio of the linear crystal growth rate to the volume of the crystal grain does not depend on time; they also neglected secondary crystallization and overlapping of growing grains, and used an extension of the isothermal Avrami–Kolmogorov equation to describe non–isothermal crystallization, where the crystallinity is governed by an advection equation.

1.4 NUMERICAL CONSIDERATIONS ON THE FIBRE SPINNING PROCESS

It is well–known that two special characteristics of fibre spinning and many other polymer manufacturing processes are the presence of free surfaces and die swell.

One generally thinks of a gas–liquid interface when talking about free surfaces. However, free surfaces (free boundaries) also include the interface between two immiscible liquid phases and the interface between a solid and a gas or liquid that might be moving due to evaporation, sublimation, or melting.

In compound fibre spinning, the outer fibre radius is a gas–liquid free surface while the inner one is a liquid–liquid interface due to the inmiscibility of the core and cladding. On the other hand, in hollow compound melt spinning, one has an additional gas–liquid interface.

When simulating the melt fibre spinning process, the unknown interface positions are additional variables that must be determined simultaneously with the velocity, pressure, temperature and molecular orientation and degree of crystallization in the filament.

When a liquid is pumped out from a capillary, the jet diameter may increase and becomes larger than the original capillary diameter. This well known phenomenon is referred to as *die swell* or *extrudate swell*. For two–dimensional axisymmetric problems, the die swell ratio S is defined as the ratio of the maximum fibre diameter in the transition region to the original capillary diameter. Even Newtonian fluids show die swell at low Reynolds number. The swell ratio for Newtonian fluids is ~ 1.13 or a 13% increase in diameter [1, 18, 24, 104, 139]. Much larger swell ratios can be observed for non–Newtonian fluids due to elastic and thermal effects. Die swell is discussed extensively in the literature [18, 24, 66, 104, 137–139].

As noted previously, most fibre spinning analyses focus on the draw zone region and neglect the transition region. By doing this, the difficulties associated with predicting die swell is avoided and the determination of the location of the inner and outer free surfaces becomes easier. To simulate die swell, one must use a solution domain that includes a sufficiently long portion of the shear flow region within the spinneret to allow specification of a fully developed shear flow boundary condition up–stream. Unfortunately, due to the complexities of the solution domain and governing conservation equations as well as the change of boundary conditions, one cannot solve the equations analytically and must use a numerical approximation instead.

1.5 OBJECTIVES OF THIS RESEARCH WORK

The main objective of this work is to develop a simplified two–dimensional model for the numerical study of the melt spinning of compound and hollow compound semi–crystalline polymeric fibres based on the leading–order equations for the fibre's geometry and axial and radial velocity components obtained from an asymptotic analysis of slender fibres at low Reynolds and Biot numbers, and two–dimensional equations for the temperature, molecular orientation and crystallization. The model employs a modified Newtonian rheology, accounts for the degrees of molecular orientation using an order parameter deduced from the Doi–Edwards equation for the orientation tensor [30] with a Maier–Saupe potential [93], and the thermal Avrami–Kolmogorov [5, 83] crystallization kinetics modified by taking into account the effects of the flow–induced crystallization. In addition, the model allows to determine the radial variations of these quantities as well as those of the temperature across the compound fibre which affect the mechanical, electrical, optical, etc. properties of the manufactured compound fibres. Of particular concern is the radial variations of temperature, molecular orientation and degree of crystallization that develop due to temperature gradients across the fibre in the production of axisymmetric compound and hollow compound optical fibres by melt spinning processes due to their importance in the properties of optical fibres.

1.6 STRUCTURE OF THE THESIS

The work has been arranged as follows. In the present chapter, an introduction to the melt spinning process and applications of the manufactured fibres using this technique have been presented. Moreover, a background and literature review of the models developed in the past for solving the melt spinning problem for both amorphous and semi–crystalline compound fibres have been provided. The instabilities and some numerical considerations of the fibre spinning process have been briefly described in the present chapter. In addition, the main objectives and the significance of this work have been also introduced in the present chapter.

In Chapter 2, a mathematical description of the two–dimensional model for semi–crystalline compound and hollow compound fibres is presented together with its assumptions and simplifications. Boundary conditions are carefully detailed in the Chapter 2. The non–dimensionalization stage is also carried out in the Chapter 2 together with the identification of the most important parameters that govern the problem.

The one–dimensional models of the melt spinning of both amorphous and semi–crystalline compound and hollow compound fibres are provided in Chapter 3. Some analytical solutions for simplified flows, which are useful for code validation purposes, are reported. Finally, the numerical method employed in this work for the one–dimensional model of semi–crystalline compound and hollow compound fibres is also described briefly in Chapter 3.

Chapter 4 deals with the formulation of a two–dimensional model of fibre formation in melt spinning processes. The numerical method which uses a mapping transformation of the physical domain in order to obtain the solution of the two–dimensional equations for temperature, molecular orientation and degree of crystallization is presented in this chapter.

Some sample results for the melt spinning of semi–crystalline compound fibres are presented in Chapter 5. Comparisons between the predictions of the one–dimensional and two–dimensional

models are also carried out in this chapter. Moreover, the final section of Chapter 5 summarizes the most important findings extracted from the results.

In Chapter 6, some sample results for the melt spinning of semi–crystalline hollow compound fibres are presented. The most relevant conclusions of these results are presented in the last section of this chapter.

Finally, Chapter 7 summarizes the final conclusions extracted from this research work and proposes some future research lines.

The symbols that appear throughout the text have been collected and defined in the Nomenclature.

Part II

MATHEMATICAL MODELS FOR THE MELT SPINNING OF SEMI–CRYSTALLINE FIBRES

2

MODEL OF FIBRE FORMATION IN MELT SPINNING PROCESSES

Contents

2.1 MODEL FORMULATION. GOVERNING EQUATIONS AND BOUNDARY CONDITIONS

Let us consider an axisymmetric, hollow compound liquid jet such as the one shown schematically in Figure 2.1 (a), consisting of two immiscible, incompressible (constant density) fluids. The inner (subscript 1) and outer (subscript 2) jets correspond to $R(t,x) \leq r \leq R_1(t,x)$ and $R_1(t,x) \leq r \leq R_2(t,x)$, respectively, and generate three interfacial surfaces which mathematically are given by

$$S : \quad S\ (r,x,t) = r - R\ (x,t) = 0, \tag{2.1}$$

$$S_1 : \quad S_1(r,x,t) = r - R_1(x,t) = 0, \tag{2.2}$$

$$S_2 : \quad S_2(r,x,t) = r - R_2(x,t) = 0. \tag{2.3}$$

As we stated in Chapter 1 and, in order to model the fluid dynamics, heat transfer, molecular orientation and crystallization processes that occur in the manufacture of semi–crystalline (hollow) compound fibres by melt spinning or preform processes, we only consider the fluid mechanical and thermal phenomena that occur beyond the maximum swell section which we take as $x = 0$, i.e., we only consider phenomena that occur beyond the maximum swell cross–section where the radii of the hollow compound fibre are decreasing functions of the axial distance. In this region, cooling due to forced convection and radiation with the surrounding media cause a radial temperature distribution across each section of the fibre which, in turn, results in a radial variation of the dynamic viscosity of the materials and thermally–induced crystallization.

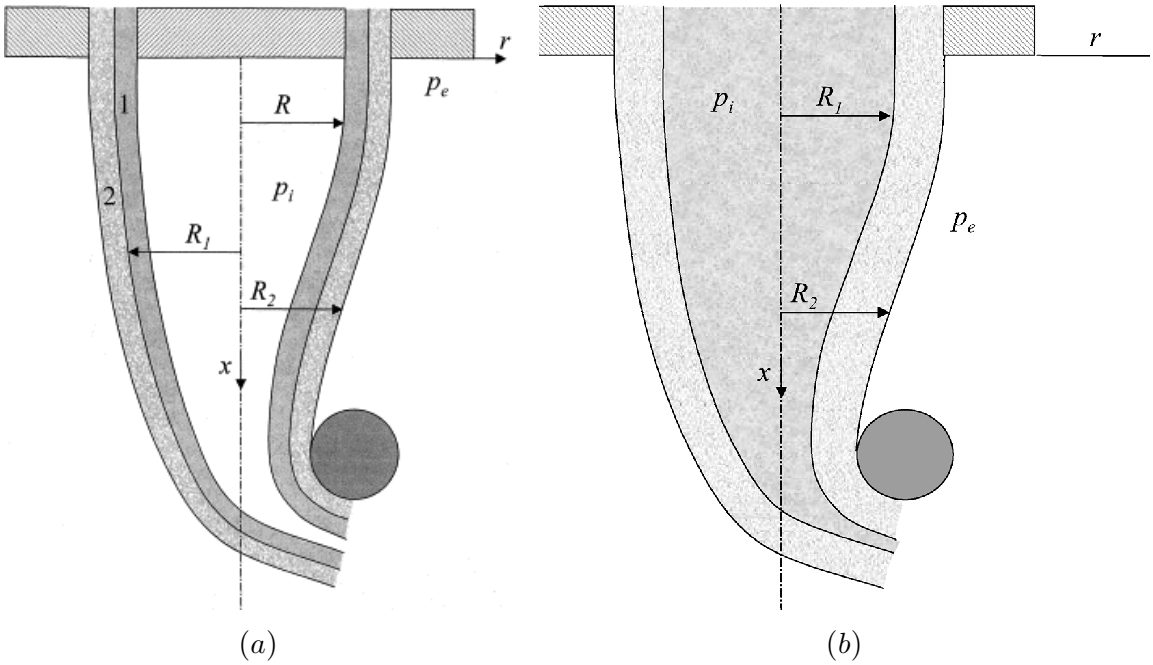

Figure 2.1: *Schematic of a hollow compound fibre* (a) *and a compound fibre* (b).

The fluid dynamics of bi–component fibres are governed by the following two–dimensional conservation equations of mass, linear momentum and energy, respectively,

$$\nabla \cdot \mathbf{v}_i = 0, \qquad i = 1,\, 2, \tag{2.4}$$

$$\rho_i \left(\frac{\partial \mathbf{v}_i}{\partial t} + \mathbf{v}_i \cdot \nabla \mathbf{v}_i \right) = -\nabla p_i + \nabla \cdot \boldsymbol{\tau}_i + \rho_i \cdot \mathbf{f}_i^m, \qquad i = 1,\, 2, \tag{2.5}$$

$$\rho_i \, C_i \, \left(\frac{\partial T_i}{\partial t} + \mathbf{v}_i \cdot \nabla T_i \right) = -\nabla \cdot \mathbf{q}_i + \boldsymbol{\tau}_i : \nabla \mathbf{v}_i, \qquad i = 1,\, 2, \tag{2.6}$$

where $\mathbf{v}$ is the velocity field vector and ρ_i and C_i are the density and specific heat per unit mass of the fluids, respectively. T_i and p_i are the absolute temperature and pressure, $\boldsymbol{\tau}_i$ denotes the stress tensor which depends on the rheology of the fluids, and $\mathbf{f}^m = \mathbf{g}$ is the volumetric force acting on the compound liquid jet due to gravity.

We adopt cylindrical coordinates (r, θ, x) with orthonormal basis $\boldsymbol{e_r}$, $\boldsymbol{e_\theta}$, $\boldsymbol{e_x}$ with the axial direction coincident with the direction of gravity, i.e., $\mathbf{g} = g\, \boldsymbol{e_x}$ where g is the constant gravitational acceleration. The velocity is given by

$$\mathbf{v} = v(r, x, t)\, \boldsymbol{e_r} + u(r, x, t)\, \boldsymbol{e_x}, \tag{2.7}$$

where we assume $\mathbf{v} \cdot \boldsymbol{e_\theta} = 0$. This torsionless assumption is made for simplicity and may be generalized to allow axisymmetric swirl in the flow.

The velocity gradient tensor for an axisymmetric flow is given in cylindrical coordinates by

$$\nabla \mathbf{v} = \begin{pmatrix} \frac{\partial v}{\partial r} & 0 & \frac{\partial v}{\partial x} \\ 0 & \frac{v}{r} & 0 \\ \frac{\partial u}{\partial r} & 0 & \frac{\partial u}{\partial x} \end{pmatrix}. \tag{2.8}$$

Moreover, we use the Fourier law for the heat flux $\mathbf{q}_i$

$$\mathbf{q}_i = -k_i \nabla T, \qquad i = 1, 2, \tag{2.9}$$

where k is the thermal conductivity and $\nabla \equiv \frac{\partial}{\partial r}\boldsymbol{e_r} + \frac{\partial}{\partial x}\boldsymbol{e_x}$. It must be noted that the term $\boldsymbol{\tau} : \nabla \mathbf{v}$ corresponds to viscous heating. We follow Ziabicki [153], which is the standard in the fibre literature, by neglecting the variation of internal energy due to latent heat effects and assuming that heat flux is due to conduction alone (cf. Eq. (2.9)). We make no claims as to the global thermodynamics consistency of these assumptions.

Equations (2.4)–(2.6) may be written as

- **Mass conservation equation**

$$\frac{1}{r}\frac{\partial}{\partial r}(r\, v_i) + \frac{\partial u_i}{\partial x} = 0, \qquad i = 1, 2, \tag{2.10}$$

- **Linear momentum equation – r axis**

$$\rho_i \mathcal{L}(v_i) = -\frac{\partial p_i}{\partial r} + \frac{1}{r}\frac{\partial}{\partial r}(r\, \boldsymbol{\tau}_{i\, rr}) + \frac{\partial}{\partial x}(\boldsymbol{\tau}_{i\, rx}) - \frac{\boldsymbol{\tau}_{i\, \theta\theta}}{r}, \qquad i = 1, 2, \tag{2.11}$$

- **Linear momentum equation – x axis**

$$\rho_i \mathcal{L}(u_i) = -\frac{\partial p_i}{\partial x} + \frac{1}{r}\frac{\partial}{\partial r}(r\, \boldsymbol{\tau}_{i\, rx}) + \frac{\partial}{\partial x}(\boldsymbol{\tau}_{i\, xx}) + \rho_i g, \qquad i = 1, 2, \tag{2.12}$$

- **Energy conservation equation**

$$\rho_i C_i \mathcal{L}(T_i) = k_i \left(\frac{\partial^2 T_i}{\partial x^2} + \frac{1}{r}\frac{\partial}{\partial r}\left(r \frac{\partial T_i}{\partial r} \right) \right) + \Phi_i, \qquad i = 1, 2, \tag{2.13}$$

where the material derivative operator, $\mathcal{L}$, applied to the field $\mathrm{Y}_i(r, x, t)$ is given by

$$\mathcal{L}(\mathrm{Y}_i) = \frac{\partial \mathrm{Y}_i}{\partial t} + u_i \frac{\partial \mathrm{Y}_i}{\partial x} + v_i \frac{\partial \mathrm{Y}_i}{\partial r}, \qquad i = 1, 2, \tag{2.14}$$

and the rate of heat dissipation, Φ, has the following expression,

$$\Phi_i = \boldsymbol{\tau}_{i\, rr}\frac{\partial v_i}{\partial r} + \boldsymbol{\tau}_{i\, rx}\left(\frac{\partial u_i}{\partial r} + \frac{\partial v_i}{\partial x} \right) + \boldsymbol{\tau}_{i\, \theta\theta}\left(\frac{v_i}{r} \right) + \boldsymbol{\tau}_{i\, xx}\frac{\partial u_i}{\partial x}, \qquad i = 1, 2. \tag{2.15}$$

In the model presented here, it is assumed that the specific heat and thermal conductivity are constant.

2.1.1 *Constitutive equations for stresses*

Isotropic Newtonian flows. Purely viscous behaviour. In Newtonian, incompressible and isotropic flows, the linear Newton[†] law links the viscous stress tensor with the strain rate tensor as

$$\boldsymbol{\tau}_N = 2\mu\,\boldsymbol{D} = \mu\left(\nabla\mathbf{v} + \nabla\mathbf{v}^T\right), \tag{2.16}$$

where $\boldsymbol{D}$ is the rate–of–strain tensor and ^{T} denotes transpose.

In this manner, the viscous stress tensor, $\boldsymbol{\tau}$, for each fluid may be written as

$$\boldsymbol{\tau} = 2\,\mu \begin{pmatrix} \frac{\partial v}{\partial r} & 0 & \frac{1}{2}\left(\frac{\partial v}{\partial x} + \frac{\partial u}{\partial r}\right) \\ 0 & \frac{v}{r} & 0 \\ \frac{1}{2}\left(\frac{\partial u}{\partial r} + \frac{\partial v}{\partial x}\right) & 0 & \frac{\partial u}{\partial x} \end{pmatrix}, \tag{2.17}$$

where the (Newtonian) dynamic viscosity depends on the temperature, T, following an Arrhenius relation as

$$\mu(T) = A\exp\left(-\frac{E}{R_g}\left(\frac{1}{T} - \frac{1}{T_0}\right)\right), \tag{2.18}$$

where A, E, R_g and T_0 denote the pre–exponential factor, activation energy, universal gas constant and an experimental temperature above the melting point, respectively.

The linearised Arrhenius expression for the dynamic viscosity used in this study corresponds to a Frank–Kamenetskii's approximation [46] whereby the argument of the exponential dependence on temperature is linearised, and the dynamic viscosity may be written as

$$\mu(T) = D\exp\left(H\ (T_0 - T)\right), \tag{2.19}$$

which increases exponentially with the temperature for $T < T_0$. The values of D and H can be easily deduced from Eq. (2.18).

Semi–crystalline Newtonian flows. Model of the molecular orientation–induced viscosity. The linear Newtonian friction law is expected to hold for small rates of strain. Some liquids important in the chemical industry, on the other hand, display non–Newtonian behaviour at moderates rates of strain. Polymer molecules that form liquid–crystalline phases in solution generally have rigid backbones and, consequently, have rod–like or disk–like shapes. In this work,

[†]The Navier–Stokes equation of motion was derived by Claude–Louis–Marie Navier in 1827 and, independently by Siméon–Denis Poisson in 1831. Latter, George Gabriel Stokes (in 1845) derived equation starting with the linear stress vs. rate–of–strain argument.

we model the solution of rod–like polymers as an ensemble of rigid dumbbells suspended in a Newtonian solvent [9]. In such a solution, the deviatoric stress tensor is assumed to be

$$\boldsymbol{\tau} = \boldsymbol{\tau}_N + \boldsymbol{\tau}_P, \tag{2.20}$$

where

$$\boldsymbol{\tau}_P = 3\, c\, k_B T \left[-\frac{\lambda}{\phi} F\left(\mathbf{S}\right) + 2\lambda \left(\left(\nabla \mathbf{v}\right)^T : \mathbf{S} \right) \left(\mathbf{S} + \frac{\mathbf{I}}{3} \right) \right], \tag{2.21}$$

c is the number of polymer molecules per unit volume, k_B is the Boltzmann constant,

$$F(\mathbf{S}) = -\frac{\phi}{\lambda} \left(\left(1 - \frac{N}{3} \right) \mathbf{S} - N\left(\mathbf{S}\cdot\mathbf{S}\right) + N\left(\mathbf{S}:\mathbf{S}\right) \left(\mathbf{S} + \frac{\mathbf{I}}{3} \right) \right), \tag{2.22}$$

is a function that characterizes the orientation dynamics independently of the flow, $\mathbf{I}$ is the identity tensor and the dimensionless scalar parameter N is a measure of the polymer number density (c) which is directly proportional to the excluded volume between two rigid rods, where each rod represents a polymer molecule. Here, ϕ is a dimensionless parameter related to the friction tensor; $0 \leq \phi \leq 1$, where $\phi = 1$ corresponds to an isotropic friction tensor, and smaller values of ϕ correspond to increasing the ratio of the resistance encountered perpendicularly to the dumbbell to that encountered parallel to the axis of the dumbbell. In addition, λ is a relaxation time associated with rotation of the dumbbell molecules which may depend on the temperature and the molecular orientation.

In this work, we also employ a linearised Arrhenius relation for relaxation time

$$\lambda(T) = \lambda_0 \exp\left(\omega\ \left(T_0 - T\right)\right), \tag{2.23}$$

where λ_0 is the relaxation time at temperature T_0, and ω (units of inverse of temperature) is a parameter which is determined from experiments.

Without loss of generality, we select the same temperature T_0 in Eqs. (2.19) and (2.23). Any other choice of experimental temperatures amounts to a simple translational rescaling.

Doi's equation [30] for the molecular orientation tensor corresponds to changing ϕ/λ for $6\, D_R$ in Eq. (2.22), where D_R is an averaged rotational diffusion coefficient, and $\mathbf{S} =< \mathbf{uu} - \mathbf{I}/3 >$, where $\mathbf{u}$ denotes the molecular orientation vector.

The deviatoric stress tensor depends on the molecular orientation tensor $\mathbf{S}$ which has been modelled by introducing a probability density function for the molecular orientation vector. By taking moments of the probability density function and modelling the fourth–order moments in terms of second–order ones, one can derive the following partial differential equation for the molecular orientation tensor which depends on the strain rate and the relaxation of the molecular chains [30]

$$\overset{\nabla}{\mathbf{S}} = F\left(\mathbf{S}\right) + G\left(\nabla \mathbf{v}, \mathbf{S}\right), \tag{2.24}$$

where $\overset{\nabla}{\mathbf{S}}$ represents the Upper Convective Maxwell (UCM) derivative of the tensor $\mathbf{S}$ given by

$$\overset{\nabla}{\mathbf{S}} \equiv \frac{\partial \mathbf{S}}{\partial t} + \mathbf{v}\cdot\nabla\mathbf{S} - \left[\left(\nabla\mathbf{v}\right)^T \cdot \mathbf{S} + \mathbf{S}\cdot\nabla\mathbf{v} \right], \tag{2.25}$$

and

$$G\left(\nabla\mathbf{v},\mathbf{S}\right)=\frac{1}{3}\left(\nabla\mathbf{v}+\left(\nabla\mathbf{v}\right)^{T}\right)-2\left(\left(\nabla\mathbf{v}\right)^{T}:\mathbf{S}\right)\left(\mathbf{S}+\frac{\mathbf{I}}{3}\right), \tag{2.26}$$

describes the flow–orientation interaction.

A scalar molecular orientation order parameter, $\mathcal{S}$, is defined in terms of the second invariant, Π_s, of the molecular orientation tensor $\mathbf{S}$ as

$$\mathcal{S}\equiv\sqrt{\frac{3}{2}\Pi_s}=\sqrt{\frac{3}{2}\left(\mathbf{S}:\mathbf{S}\right)}, \tag{2.27}$$

and is a measure of the spread of the molecular orientation vector with respect to a preferred direction. The scalar $\mathcal{S}$ is defined so that $\mathcal{S}=0$ corresponds to a purely random orientation, and $\mathcal{S}=1$ corresponds to the alignment of all the molecules along the principal axis of $\mathbf{S}$.

2.1.2 *Boundary conditions*

Equations (2.24) and (2.22) and (2.26) together with the conservation equations (2.4)–(2.6), govern the fluid dynamics of amorphous compound fibres such as it is shown in Figure 2.1 (*b*) and are subject to boundary conditions at the nozzle exit, $x=0$, downstream or take–up location, $x=L$, initial conditions, $t=0$, and symmetry boundary conditions at centreline $r=0$. In addition, at the to–be–determined core–cladding, $r=R_1(t,x)$, and cladding–surrounding, $r=R_2(t,x)$, interfaces which are assumed to be material surfaces, kinematic and dynamic boundary conditions that specify the continuity of axial and radial velocity components and tangential stresses, and the balance of the normal stress difference with surface tension, must be applied. Moreover, at $r=R_1$, there is continuity of temperatures and heat flux, while, at $r=R_2$, the heat flux from conduction in the cladding was assumed to be equal to the heat at flux the outer surface of the outer jet denoted here by q_e. Analogous thermal transfer process occurs at $r=R$ for hollow compound fibres and the heat from conduction in the core must be equal to the heat losses at the inner surface of the inner jet that will be denoted in this study by q_i.

The boundary conditions described above may be written mathematically as

- **Boundary conditions at the symmetry axis ($r=0$)**

  1. Velocity

$$v_1=0,\qquad\frac{\partial u_1}{\partial r}=0, \tag{2.28}$$

  2. Pressure

$$\frac{\partial p_1}{\partial r}=0, \tag{2.29}$$

3. Temperature

$$\frac{\partial T_1}{\partial r} = 0. \tag{2.30}$$

For hollow compound fibres (see Figure 2.1 (a)), the symmetry boundary conditions must be replaced by the following ones:

- **Boundary conditions at the surroundings–core interface ($r = R(x,t)$)**

1. Kinematic boundary conditions

$$\frac{D_1 S}{Dt} \equiv \frac{\partial S}{\partial t} + \mathbf{v}_1 \cdot \nabla S = 0$$

$$\frac{\partial R}{\partial t} + v_1 - u_1 \frac{\partial R}{\partial x} = 0, \tag{2.31}$$

2. Continuity of tangential stresses

$$\left(\mathbf{n}^T \cdot \boldsymbol{\tau}_1\right) \cdot \mathbf{t} = \left(\mathbf{n}^T \cdot \boldsymbol{\tau}_{\infty,1}\right) \cdot \mathbf{t}$$

$$\begin{aligned} &\left(\boldsymbol{\tau}_{1\ rr} - \boldsymbol{\tau}_{1\ xx}\right) \frac{\partial R}{\partial x} + \boldsymbol{\tau}_{1\ rx} \left(1 - \left(\frac{\partial R}{\partial x}\right)^2\right) \\ &= \left(\boldsymbol{\tau}_{\infty,1\ rr} - \boldsymbol{\tau}_{\infty,1\ xx}\right) \frac{\partial R}{\partial x} + \boldsymbol{\tau}_{\infty,1\ rx} \left(1 - \left(\frac{\partial R}{\partial x}\right)^2\right), \end{aligned} \tag{2.32}$$

3. Balance of the normal stress difference

$$\left(\mathbf{n}^T \cdot \boldsymbol{\tau}_{\infty,1}\right) \cdot \mathbf{n} - \left(\mathbf{n}^T \cdot \boldsymbol{\tau}_1\right) \cdot \mathbf{n} = \sigma\kappa - (p_1 - p_i)$$

$$\begin{aligned} &\boldsymbol{\tau}_{\infty,1\ xx} \left(\frac{\partial R}{\partial x}\right)^2 + \boldsymbol{\tau}_{\infty,1\ rr} - 2\boldsymbol{\tau}_{\infty,1\ rx} \frac{\partial R}{\partial x} \\ &-\boldsymbol{\tau}_{1\ xx} \left(\frac{\partial R}{\partial x}\right)^2 - \boldsymbol{\tau}_{1\ rr} + 2\boldsymbol{\tau}_{1\ rx} \frac{\partial R}{\partial x} \\ &= \sigma J - (p_1 - p_i) \left(1 + \left(\frac{\partial R}{\partial x}\right)^2\right), \end{aligned} \tag{2.33}$$

4. Balance of heat flux

$$\mathbf{q}_1 \cdot \mathbf{n} = q_i. \tag{2.34}$$

The boundary conditions at the other two interfacial surfaces of either compound or hollow compound fibres, may be written as

- **Boundary conditions at the core–cladding interface ($r = R_1(x,t)$)**

1. Kinematic boundary conditions

$$\frac{D_1 S_1}{Dt} \equiv \frac{\partial S_1}{\partial t} + \mathbf{v}_1 \cdot \nabla S_1 = 0,$$

$$\frac{\partial R_1}{\partial t} + v_1 - u_1 \frac{\partial R_1}{\partial x} = 0, \tag{2.35}$$

$$\frac{D_2 S_1}{Dt} \equiv \frac{\partial S_1}{\partial t} + \mathbf{v}_2 \cdot \nabla S_1 = 0$$

$$\frac{\partial R_1}{\partial t} + v_2 - u_2 \frac{\partial R_1}{\partial x} = 0, \tag{2.36}$$

2. Continuity of tangential stresses

$$\left(\mathbf{n}_1^T \cdot \boldsymbol{\tau}_2\right) \cdot \mathbf{t}_1 = \left(\mathbf{n}_1^T \cdot \boldsymbol{\tau}_1\right) \cdot \mathbf{t}_1$$

$$\begin{aligned} &\left(\boldsymbol{\tau}_{2\,rr} - \boldsymbol{\tau}_{2\,xx}\right) \frac{\partial R_1}{\partial x} + \boldsymbol{\tau}_{2\,rx} \left(1 - \left(\frac{\partial R_1}{\partial x}\right)^2\right) \\ &= \left(\boldsymbol{\tau}_{1\,rr} - \boldsymbol{\tau}_{1\,xx}\right) \frac{\partial R_1}{\partial x} + \boldsymbol{\tau}_{1\,rx} \left(1 - \left(\frac{\partial R_1}{\partial x}\right)^2\right), \end{aligned} \tag{2.37}$$

3. Balance of the normal stress difference

$$\left(\mathbf{n}_1^T \cdot \boldsymbol{\tau}_2\right) \cdot \mathbf{n}_1 - \left(\mathbf{n}_1^T \cdot \boldsymbol{\tau}_1\right) \cdot \mathbf{n}_1 = \sigma_1 \kappa_1 - (p_1 - p_2)$$

$$\begin{aligned}
&\boldsymbol{\tau}_{2\,xx}\left(\frac{\partial R_1}{\partial x}\right)^2+\boldsymbol{\tau}_{2\,rr}-2\boldsymbol{\tau}_{2\,rx}\frac{\partial R_1}{\partial x}\\
&-\boldsymbol{\tau}_{1\,xx}\left(\frac{\partial R_1}{\partial x}\right)^2-\boldsymbol{\tau}_{1\,rr}+2\boldsymbol{\tau}_{1\,rx}\frac{\partial R_1}{\partial x}\\
&=\sigma_1 J_1-(p_1-p_2)\left(1+\left(\frac{\partial R_1}{\partial x}\right)^2\right),
\end{aligned} \tag{2.38}$$

4. Continuity of temperature

$$T_1=T_2, \tag{2.39}$$

5. Continuity of heat flux

$$\mathbf{q}_1\cdot\mathbf{n}=\mathbf{q}_2\cdot\mathbf{n}. \tag{2.40}$$

- **Boundary conditions at the cladding–surroundings interface ($r=R_2(x,t)$)**

1. Kinematic boundary conditions

$$\frac{D_2S_2}{Dt}\equiv\frac{\partial S_2}{\partial t}+\mathbf{v}_2\cdot\nabla S_2=0$$

$$\frac{\partial R_2}{\partial t}+v_2-u_2\frac{\partial R_2}{\partial x}=0, \tag{2.41}$$

2. Continuity of tangential stresses

$$\left(\mathbf{n}_2^T\cdot\boldsymbol{\tau}_2\right)\cdot\mathbf{t}_2=\left(\mathbf{n}_2^T\cdot\boldsymbol{\tau}_{\infty,2}\right)\cdot\mathbf{t}_2$$

$$\begin{aligned}
&\left(\boldsymbol{\tau}_{2\,rr}-\boldsymbol{\tau}_{2\,xx}\right)\frac{\partial R_2}{\partial x}+\boldsymbol{\tau}_{2\,rx}\left(1-\left(\frac{\partial R_2}{\partial x}\right)^2\right)\\
&=\left(\boldsymbol{\tau}_{\infty,2\,rr}-\boldsymbol{\tau}_{\infty,2\,xx}\right)\frac{\partial R_2}{\partial x}+\boldsymbol{\tau}_{\infty,2\,rx}\left(1-\left(\frac{\partial R_2}{\partial x}\right)^2\right),
\end{aligned} \tag{2.42}$$

3. Balance of the normal stress difference

$$\left(\mathbf{n}_2^T\cdot\boldsymbol{\tau}_{\infty,2}\right)\cdot\mathbf{n}_2-\left(\mathbf{n}_2^T\cdot\boldsymbol{\tau}_2\right)\cdot\mathbf{n}_2=\sigma_2\kappa_2-(p_2-p_e)$$

$$\begin{aligned}
&\boldsymbol{\tau}_{\infty,2\ xx}\left(\frac{\partial R_2}{\partial x}\right)^2+\boldsymbol{\tau}_{\infty,2\ rr}-2\boldsymbol{\tau}_{\infty,2\ rx}\frac{\partial R_2}{\partial x}\\
&-\boldsymbol{\tau}_{2\ xx}\left(\frac{\partial R_2}{\partial x}\right)^2-\boldsymbol{\tau}_{2\ rr}+2\boldsymbol{\tau}_{2\ rx}\frac{\partial R_2}{\partial x}\\
&=\sigma_2 J_2-(p_2-p_e)\left(1+\left(\frac{\partial R_2}{\partial x}\right)^2\right),
\end{aligned} \tag{2.43}$$

4. Balance of heat flux

$$\mathbf{q}_2\cdot\mathbf{n}_2=q_e, \tag{2.44}$$

where σ, σ_1 and σ_2 denote the constant surface tension at the inner jet's inner surface, at the interface between the inner and outer jets, and at the outer jet's outer surface, respectively, and $\mathbf{n}$ and $\mathbf{n}_i$ denote the outward unit normal at R

$$\mathbf{n}=\frac{\nabla S}{|\nabla S|}=\frac{1}{\sqrt{1+\left(\frac{\partial R}{\partial x}\right)^2}}\left(\boldsymbol{e_r}-\frac{\partial R}{\partial x}\,\boldsymbol{e_x}\right), \tag{2.45}$$

and R_i,

$$\mathbf{n}_i=\frac{\nabla S_i}{|\nabla S_i|}=\frac{1}{\sqrt{1+\left(\frac{\partial R_i}{\partial x}\right)^2}}\left(\boldsymbol{e_r}-\frac{\partial R_i}{\partial x}\,\boldsymbol{e_x}\right), \tag{2.46}$$

respectively, where $|\cdot|$ is the euclidean norm.

Although in this work we have taken into account the viscous stress tensor of the gases surrounding the outer jet and enclosed by the inner jet, $\boldsymbol{\tau}_{\infty,i}$, these gases may be assumed to be dynamically passive, since, in general, they have smaller density and dynamic viscosity than those of liquids [121]. This implies that the gases surrounding the liquid may not introduce strong velocity variations along each cross section of the jet, although they may affect its dynamics. In addition, p_i and p_e are the pressures of the gases enclosed by and surrounding the hollow compound liquid jet, respectively which can be, in general, a function of the spatial coordinates and time.

The interface mean curvature, κ and κ_i, are given by the divergence of the unit vector normal to each free surface,

$$\kappa=\nabla\cdot\mathbf{n}=\frac{1}{\sqrt{1+\left(\frac{\partial R}{\partial x}\right)^2}}\left(\frac{1}{R}-\frac{\partial^2 R}{\partial x^2}\frac{1}{1+\left(\frac{\partial R}{\partial x}\right)^2}\right), \tag{2.47}$$

$$\kappa_i=\nabla\cdot\mathbf{n}_i=\frac{1}{\sqrt{1+\left(\frac{\partial R_i}{\partial x}\right)^2}}\left(\frac{1}{R_i}-\frac{\partial^2 R_i}{\partial x^2}\frac{1}{1+\left(\frac{\partial R_i}{\partial x}\right)^2}\right), \tag{2.48}$$

while J and J_i are related to the mean curvature using the following expressions

$$J = |\nabla S|^2 \cdot \kappa = \left(1 + \left(\frac{\partial R}{\partial x}\right)^2\right) \cdot \kappa = \frac{\sqrt{1 + \left(\frac{\partial R}{\partial x}\right)^2}}{R} - \frac{\frac{\partial^2 R}{\partial x^2}}{\sqrt{1 + (\frac{\partial R}{\partial x})^2}}, \tag{2.49}$$

$$J_i = |\nabla S_i|^2 \cdot \kappa_i = \left(1 + \left(\frac{\partial R_i}{\partial x}\right)^2\right) \cdot \kappa_i = \frac{\sqrt{1 + \left(\frac{\partial R_i}{\partial x}\right)^2}}{R_i} - \frac{\frac{\partial^2 R_i}{\partial x^2}}{\sqrt{1 + (\frac{\partial R_i}{\partial x})^2}}. \tag{2.50}$$

The heat flux q_e includes the effects of convection and radiation, i.e., $q_e = h_c \left(T(R_2, x, t) - T_{\infty,2}\right) + k_{SB}\epsilon^* \left(T(R_2, x, t)^4 - T_{\infty,2}^4\right)$, where h_c is the convective film heat transfer coefficient, $T_{\infty,2}$ is the temperature of the gases that surround the compound fibre, k_{SB} is the Stefan–Boltzmann constant and ϵ^* is the emissivity of the compound fibre's outer surface. The heat flux can also be written as $q_e = h_2 \left(T(R_2, x, t) - T_{\infty,2}\right)$, where $h_2 = h_c + k_{SB}\epsilon^* \left(T(R_2, x, t)^2 + T_{\infty,2}^2\right)\left(T(R_2, x, t) + T_{\infty,2}\right)$, which depends, amongst other parameters, on the fibre's temperature at R_2 and the velocity of the fibre. In addition, the film heat transfer coefficient h_c could depend on the local Reynolds and Prandtl numbers. For example, Kase and Matsuo [77] determined experimentally that, for single–component, round jets,

$$h_c = C \frac{k_\infty}{R(x)} \left(\frac{2\rho_\infty u(x) R(x)}{\mu_\infty}\right)^m \tag{2.51}$$

where k_∞, ρ_∞, and μ_∞ are the thermal conductivity, density and dynamic viscosity, respectively, of the ambient air at room temperature, $u(x)$ and $R(x)$ are the local axial velocity component and radius of the jet, respectively, and C and m are determined from experimental data [77]. A similar expression could be used for the heat flux q_i for hollow compound fibres.

Equations (2.35) and (2.36) imply that $(\mathbf{v}_2 - \mathbf{v}_1) \cdot \mathbf{n}_1 = 0$, i.e., the normal velocity at the outer–inner jet interface is continuous. Since the fluids are viscous, $(\mathbf{v}_2 - \mathbf{v}_1) \cdot \mathbf{t}_1 = 0$ at $r = R_1(t, x)$, where

$$\mathbf{t}_1 = \frac{1}{\sqrt{1 + \left(\frac{\partial R_1}{\partial x}\right)^2}} \left(\frac{\partial R_1}{\partial x} \boldsymbol{e_r} + \boldsymbol{e_x}\right), \tag{2.52}$$

is the unit vector tangent to the surface $S_1(r, x, t)$ and, therefore, the tangential velocity components at this interface are continuous, i.e.,

$$u_1 \left(R_1, x, t\right) = u_2 \left(R_1, x, t\right). \tag{2.53}$$

In addition to the above boundary conditions in the radial direction, conditions in the axial direction must also be provided. If the compound jet emerges from a nozzle or die, there is a stress singularity at the nozzle–jet's interface due to the relaxation of the velocity profile from no–slip conditions at the nozzle walls to the free–surface flow away from the nozzle. This relaxation may result in a jet contraction or swelling which implies that the radial velocity component is of importance near the nozzle. Moreover, the stress singularity at the nozzle exit and the jet contraction or swelling near the nozzle may result in a relatively important radial pressure

gradient near the nozzle; therefore, an accurate analysis of the flow near the nozzle requires a full solution of the Navier–Stokes equations within the nozzle and in the free surface flow, and requires the use of numerical methods and two–dimensional simulations.

2.2 NON–DIMENSIONALIZATION

For slender jets, i.e., $\epsilon = \frac{R_0}{L} << 1$, at low Reynolds numbers, it is convenient to non–dimensionalize r, x, t, u, v, p, ρ, C, μ and k with respect to R_0, L, $t_0 = (L/u_0)$, u_0, v_0, $p_0 = (\mu_0\, u_0/L)$, ρ_0, C_0, μ_0 and k_0, respectively, where R_0 and L denote a characteristic radius and a characteristic length in the axial direction, e.g., the die's exit radius and the distance from the die exit to the take–up point, respectively, u_0 is a characteristic (constant) axial velocity component, $v_0 = \epsilon u_0$, and ρ_0, C_0, μ_0 and k_0 are reference values for the density, specific heat, viscosity and thermal conductivity, respectively. The temperature may be non–dimensionalized as $(T - T_r)/\Delta T$ where $\Delta T = (T_0 - T_\infty)$, and $T_r = T_0$ and T_∞ denote a reference temperature at the die exit and the temperature of the surroundings, respectively. Alternatively, the temperature has been non–dimensionalized with respect to $\Delta T = T_0$ with $T_r = 0$ here. Since the density of the fluids has been assumed to be constant, ρ_0 can be taken equal to, for example, ρ_2, although we have preferred to introduce a reference density for non–dimensionalization purposes throughout the chapter; the same comment applies to the reference values employed for the non–dimensionalization of the specific heats, dynamic viscosities and thermal conductivities.

The dimensionless variables are:

$$\begin{aligned} &\hat{r} = \frac{r}{R_0}, \qquad \hat{x} = \frac{x}{L}, \qquad \hat{t} = \frac{t}{t_0}, \\ &\hat{u} = \frac{u}{u_0}, \qquad \hat{v} = \frac{v}{(u_0\,\epsilon)}, \qquad \hat{p} = \frac{p}{p_0}, \qquad \hat{T} = \frac{T}{T_0}, \\ &\hat{\rho} = \frac{\rho}{\rho_0}, \qquad \hat{C} = \frac{C}{C_0}, \qquad \hat{\mu} = \frac{\mu}{\mu_0}, \qquad \hat{k} = \frac{k}{k_0}, \qquad \hat{h} = \frac{h}{h_0}. \end{aligned} \tag{2.54}$$

Using this non–dimensionalization, Eqs. (2.10)–(2.13) become

- **Mass conservation equation**

$$\frac{1}{\hat{r}}\frac{\partial}{\partial \hat{r}}\left(\hat{r}\,\hat{v}_i\right) + \frac{\partial \hat{u}_i}{\partial \hat{x}} = 0, \qquad i = 1,\, 2, \tag{2.55}$$

- **Linear momentum equation – $\hat{r}$ axis**

$$(\epsilon\, Re)\,\hat{\rho}_i \hat{\mathcal{L}}(\hat{v}_i) = -\frac{\partial \hat{p}_i}{\partial \hat{r}} + \frac{1}{\hat{r}}\frac{\partial}{\partial \hat{r}}\left(\hat{r}\,\hat{\boldsymbol{\tau}}_{i\,rr}\right) + \frac{\partial}{\partial \hat{x}}\left(\epsilon\,\hat{\boldsymbol{\tau}}_{i\,rx}\right) - \frac{\hat{\boldsymbol{\tau}}_{i\,\theta\theta}}{\hat{r}}, \qquad i = 1,\, 2, \tag{2.56}$$

- **Linear momentum equation – $\hat{x}$ axis**

$$(\epsilon\, Re)\,\hat{\rho}_i \hat{\mathcal{L}}(\hat{u}_i) = -\epsilon^2 \frac{\partial \hat{p}_i}{\partial \hat{x}} + \frac{1}{\hat{r}}\frac{\partial}{\partial \hat{r}}\left(\hat{r}\,\epsilon\,\hat{\boldsymbol{\tau}}_{i\,rx}\right) + \epsilon^2 \frac{\partial}{\partial \hat{x}}\left(\hat{\boldsymbol{\tau}}_{i\,xx}\right) + \hat{\rho}_i \frac{Re}{Fr}, \qquad i = 1,\, 2, \tag{2.57}$$

- **Energy conservation equation**

$$(\epsilon\, Pe)\,\hat{\rho}_i\hat{C}_i\hat{\mathcal{L}}(\hat{T}_i) = \epsilon^2\hat{k}_i\frac{\partial^2\hat{T}_i}{\partial\hat{x}^2} + \frac{\hat{k}_i}{\hat{r}}\frac{\partial}{\partial\hat{r}}\left(\hat{r}\frac{\partial\hat{T}_i}{\partial\hat{r}}\right) + \left(\epsilon^2\, Br\right)\hat{\Phi}_i, \qquad i = 1,\, 2, \tag{2.58}$$

where the material derivative operator, $\hat{\mathcal{L}}$, is given now by

$$\hat{\mathcal{L}}(\mathrm{Y}_i) = t_0 \cdot \mathcal{L}(\mathrm{Y}_i) = \frac{\partial \mathrm{Y}_i}{\partial\hat{t}} + \hat{u}_i\frac{\partial \mathrm{Y}_i}{\partial\hat{x}} + \hat{v}_i\frac{\partial \mathrm{Y}_i}{\partial\hat{r}}, \qquad i = 1,\, 2, \tag{2.59}$$

the dimensionless heat dissipation rate, $\hat{\Phi}$, is given by

$$\begin{aligned}\hat{\Phi}_i &= \left(\frac{t_0}{p_0}\right)\cdot\Phi_i \\ &= \hat{\boldsymbol{\tau}}_{i\,rr}\frac{\partial\hat{v}_i}{\partial\hat{r}} + \hat{\boldsymbol{\tau}}_{i\,\theta\theta}\left(\frac{\hat{v}_i}{\hat{r}}\right) + \hat{\boldsymbol{\tau}}_{i\,xx}\frac{\partial\hat{u}_i}{\partial\hat{x}} + \hat{\boldsymbol{\tau}}_{i\,rx}\left(\frac{1}{\epsilon}\frac{\partial\hat{u}_i}{\partial\hat{r}} + \epsilon\frac{\partial\hat{v}_i}{\partial\hat{x}}\right), \qquad i = 1,\, 2,\end{aligned} \tag{2.60}$$

and

$$Re = \frac{\rho_0 u_0 R_0}{\mu_0}, \qquad Fr = \frac{u_0^2}{gR_0}, \qquad Ca = \frac{\mu_0 u_0}{\sigma_2} \qquad Pr = \frac{\mu_0 C_0}{k_0}, \tag{2.61}$$

$$Pe = Re\,Pr = \left(\frac{\rho_0 C_0}{k_0}\right)u_0 R_0, \qquad Br = \frac{\mu_0 u_0^2}{k_0 T_0}, \qquad Bi = \frac{h_0 R_0}{k_0}. \tag{2.62}$$

denote the Reynolds (i), Froude (ii), capillary (iii), Prandtl (iv), thermal Péclet (v), Brinkman (vi) and Biot (vii) numbers that (i) gives a measure of the ratio of inertial forces to viscous forces, (ii) parametrizes gravity relative to inertia, (iii) represents the relative effect of viscous forces versus surface tension acting across the external surface, (iv) is a measure of specific heat relative to thermal conductivity, (v) is the ratio of viscous diffusion to thermal diffusion rates, (vi) describes viscous heating relative to thermal conductivity and (vii) characterizes the heat loss relative to thermal conductivity, respectively. Note that the surface tensions and the reference convective heat transfer film coefficient, h_0, have been assumed to be constant, i.e., independent of the temperature.

The dimensionless stress tensor becomes

$$\begin{aligned}&\hat{\boldsymbol{\tau}} = \hat{\boldsymbol{\tau}}_N + \hat{\boldsymbol{\tau}}_P, \\ &\hat{\boldsymbol{\tau}}_N = \frac{\boldsymbol{\tau}_N}{p_0} = 2\hat{\mu}\,\hat{\boldsymbol{D}}, \\ &\hat{\boldsymbol{\tau}}_P = \frac{\boldsymbol{\tau}_P}{p_0} = \alpha\,\hat{T}\left[-\frac{\hat{\lambda}(\hat{T})}{\phi}\hat{F}(\mathbf{S}) + 2\hat{\lambda}(\hat{T})\left(\hat{\nabla}\mathbf{v}^T : \mathbf{S}\right)\left(\mathbf{S} + \frac{\boldsymbol{I}}{3}\right)\right],\end{aligned} \tag{2.63}$$

where $\alpha = \frac{3\,c\,k_B T_0}{p_0}$ parametrizes the molecular kinetic energy per unit volume relative to the reference pressure, the combination $\alpha\,\hat{\lambda}_0$ characterizes the relaxational stress due to molecular rotation relative to the reference pressure, $\hat{F}(\mathbf{S}) = t_0 \cdot F(\mathbf{S})$ and

$$\hat{\boldsymbol{D}} = t_0 \cdot \boldsymbol{D} = \begin{pmatrix} \frac{\partial \hat{v}}{\partial \hat{r}} & 0 & \frac{1}{2}\left(\epsilon \frac{\partial \hat{v}}{\partial \hat{x}} + \frac{1}{\epsilon}\frac{\partial \hat{u}}{\partial \hat{r}}\right) \\ 0 & \frac{\hat{v}}{\hat{r}} & 0 \\ \frac{1}{2}\left(\frac{1}{\epsilon}\frac{\partial \hat{u}}{\partial \hat{r}} + \epsilon \frac{\partial \hat{v}}{\partial \hat{x}}\right) & 0 & \frac{\partial \hat{u}}{\partial \hat{x}} \end{pmatrix}, \tag{2.64}$$

$$\hat{\nabla}\mathbf{v} = t_0 \cdot \nabla \mathbf{v} = \begin{pmatrix} \frac{\partial \hat{v}}{\partial \hat{r}} & 0 & \epsilon \frac{\partial \hat{v}}{\partial \hat{x}} \\ 0 & \frac{\hat{v}}{\hat{r}} & 0 \\ \frac{1}{\epsilon}\frac{\partial \hat{u}}{\partial \hat{r}} & 0 & \frac{\partial \hat{u}}{\partial \hat{x}} \end{pmatrix}. \tag{2.65}$$

The boundary ambient viscous stress may be expressed in dimensionless form as

$$\left(\hat{\mathbf{n}}^T \cdot \hat{\boldsymbol{\tau}}_{\infty,1}\right) = -\epsilon^2 \hat{\mathcal{T}}(\hat{x}, \hat{t})\,\hat{\mathbf{t}}, \tag{2.66}$$

$$\left(\hat{\mathbf{n}}_2^T \cdot \hat{\boldsymbol{\tau}}_{\infty,2}\right) = -\epsilon^2 \hat{\mathcal{T}}_2(\hat{x}, \hat{t})\,\hat{\mathbf{t}}_2, \tag{2.67}$$

which assume axisymmetric air drag and is a function of the process conditions. We use the following empirical formulae for the non–dimensional tangential component of air drag [143]

$$\hat{\mathcal{T}}(\hat{x}, \hat{t}) = C_{d1}\,\frac{\left(\hat{u}_1\,\hat{R}\right)^{\gamma}}{\hat{R}^2}, \tag{2.68}$$

$$\hat{\mathcal{T}}_2(\hat{x}, \hat{t}) = C_{d2}\,\frac{\left(\hat{u}_2\,\hat{R}_2\right)^{\gamma}}{\hat{R}_2^2}, \tag{2.69}$$

where C_{di} is the air drag coefficient and γ is fitted from experimental data, e.g., $\gamma = 1.39$ [94]. Kase and Matsuo [78] have included the effect of quench air flow normal to the fibre axis, and their proposed correlations are

$$\hat{\mathcal{T}} = C_{d1}\,\frac{\left(\hat{u}_1\hat{R}\right)^{\gamma}}{\hat{R}^2}\left[1 + 8\left(\frac{u_a}{u_1}\right)^2\right]^{1/6}, \tag{2.70}$$

$$\hat{\mathcal{T}}_2 = C_{d2}\,\frac{\left(\hat{u}_2\hat{R}_2\right)^{\gamma}}{\hat{R}_2^2}\left[1 + 8\left(\frac{u_a}{u_2}\right)^2\right]^{1/6}, \tag{2.71}$$

where u_a is the cross–flow velocity. In practice, u_a/u is less than 0.1 and the $1/6$–power of the term in the brackets renders the expression very close to 1. In this work we ignore cross–flow effects and only consider air drag given by (2.68)–(2.69) in order to formulate the equations of the model.

In this work, it is assumed that the molecular orientation tensor $\mathbf{S}$ is symmetric and, therefore, has only six components. Moreover, for slender fibres such as the ones considered here, it is an easy exercise using perturbation methods based on the slenderness ratio, ϵ, to show that S_{rx} must be $O(\epsilon)$ for proper scaling, and, therefore, this component does not appear in the leading–order

equations that result from an asymptotic analysis of slender fibres. Furthermore, by assuming that $S_{\theta x} = S_{r\theta} = 0$, the molecular orientation tensor becomes diagonal and, therefore, has only three components,

$$\mathbf{S} = \begin{pmatrix} S_{rr} & 0 & 0 \\ 0 & S_{\theta\theta} & 0 \\ 0 & 0 & S_{xx} \end{pmatrix}. \tag{2.72}$$

In this manner, the diagonal components of the deviatoric stress tensor may be written as

$$\hat{\boldsymbol{\tau}}_{rr} = 2\,\hat{\mu}\frac{\partial \hat{v}}{\partial \hat{r}} + \alpha\,\hat{T}\left\{2\hat{\lambda}\,\Pi^*\left(S_{rr}+\frac{1}{3}\right) + \left[S_{rr} - N\left(S_{rr}+\frac{1}{3}\right)\left(S_{rr}-\Pi_s\right)\right]\right\}, \tag{2.73}$$

$$\hat{\boldsymbol{\tau}}_{\theta\theta} = 2\,\hat{\mu}\frac{\hat{v}}{\hat{r}} + \alpha\,\hat{T}\left\{2\hat{\lambda}\,\Pi^*\left(S_{\theta\theta}+\frac{1}{3}\right) + \left[S_{\theta\theta} - N\left(S_{\theta\theta}+\frac{1}{3}\right)\left(S_{\theta\theta}-\Pi_s\right)\right]\right\}, \tag{2.74}$$

$$\hat{\boldsymbol{\tau}}_{xx} = 2\,\hat{\mu}\frac{\partial \hat{u}}{\partial \hat{x}} + \alpha\,\hat{T}\left\{2\hat{\lambda}\,\Pi^*\left(S_{xx}+\frac{1}{3}\right) + \left[S_{xx} - N\left(S_{xx}+\frac{1}{3}\right)\left(S_{xx}-\Pi_s\right)\right]\right\}, \tag{2.75}$$

where

$$\Pi_s = (\boldsymbol{S} : \boldsymbol{S}) = S_{rr}^2 + S_{\theta\theta}^2 + S_{xx}^2, \tag{2.76}$$

$$\Pi^* = \left(\hat{\nabla}\mathbf{v}^T : \boldsymbol{S}\right) = \left(S_{rr}\frac{\partial \hat{v}}{\partial \hat{r}} + S_{\theta\theta}\frac{\hat{v}}{\hat{r}} + S_{xx}\frac{\partial \hat{u}}{\partial \hat{x}}\right), \tag{2.77}$$

while the off–diagonal component, $\hat{\boldsymbol{\tau}}_{rx}$, can be written as

$$\hat{\boldsymbol{\tau}}_{rx} = \hat{\mu}\left(\frac{1}{\epsilon}\frac{\partial \hat{u}}{\partial \hat{r}} + \epsilon\frac{\partial \hat{v}}{\partial \hat{x}}\right). \tag{2.78}$$

The dimensionless viscosity law corresponding to Eq. (2.19) now reads

$$\hat{\mu}(\hat{T}) = \hat{D}\exp\left(\hat{H}(1-\hat{T})\right), \tag{2.79}$$

so that $\hat{\mu}$ increases exponentially as $\hat{T}$ decreases below the reference temperature. Moreover, it is very easy to show that $\hat{D} = D/\mu_0$ and $\hat{H} = T_0\,H$. Analogous expressions can also be derived for other viscosity laws, e.g., Eq. (2.18).

The dimensionless relaxation time corresponding to Eq. (2.23) can be written as

$$\hat{\lambda}(\hat{T}) = \hat{\lambda}_0\exp\left(\hat{\omega}(1-\hat{T})\right), \tag{2.80}$$

where $\hat{\lambda}_0 = \lambda_0/t_0$ is the dimensionless relaxation time at temperature T_0 and $\hat{\omega} = \omega\,T_0$.

Equation (2.24), that governs the evolution of the molecular orientation tensor $\mathbf{S}$, may be non–dimesionalized and rewritten as

$$\begin{aligned}
&\hat{\mathcal{L}}(\boldsymbol{S}) = \hat{F}(\boldsymbol{S}) + \hat{G}^*\left(\hat{\nabla}\mathbf{v}, \boldsymbol{S}\right), \\
&\hat{F}(\boldsymbol{S}) = -\frac{\phi}{\hat{\lambda}(\hat{T})}\left\{\left(1-\frac{N}{3}\right)\boldsymbol{S} - N\left(\boldsymbol{S}\cdot\boldsymbol{S}\right) + N\,\Pi_s\left(\boldsymbol{S}+\frac{\boldsymbol{I}}{3}\right)\right\}, \\
&\hat{G}^*(\hat{\nabla}\mathbf{v}, \boldsymbol{S}) = \frac{2}{3}\hat{\boldsymbol{D}} - 2\,\Pi^*\left(\boldsymbol{S}+\frac{\boldsymbol{I}}{3}\right) + \left(\hat{\nabla}\mathbf{v}^T\cdot\boldsymbol{S} + \boldsymbol{S}\cdot\hat{\nabla}\mathbf{v}\right),
\end{aligned} \tag{2.81}$$

where $\phi/\hat{\lambda}_0$ parametrizes the anisotropic drag on polymer molecular motion relative to the surrounding polymer molecules.

After some algebraic manipulations, one can obtains

$$\begin{aligned}
\hat{F}_{rr}(\boldsymbol{S}) &= -\frac{\phi}{\hat{\lambda}(\hat{T})}\left[S_{rr} - N\left(S_{rr}+\frac{1}{3}\right)\left(S_{rr}-\Pi_s\right)\right], \\
\hat{F}_{\theta\theta}(\boldsymbol{S}) &= -\frac{\phi}{\hat{\lambda}(\hat{T})}\left[S_{\theta\theta} - N\left(S_{\theta\theta}+\frac{1}{3}\right)\left(S_{\theta\theta}-\Pi_s\right)\right], \\
\hat{F}_{xx}(\boldsymbol{S}) &= -\frac{\phi}{\hat{\lambda}(\hat{T})}\left[S_{xx} - N\left(S_{xx}+\frac{1}{3}\right)\left(S_{xx}-\Pi_s\right)\right],
\end{aligned} \tag{2.82}$$

and

$$\begin{aligned}
\hat{G}^*_{rr}(\hat{\nabla}\mathbf{v}, \boldsymbol{S}) &= \left(S_{rr}+\frac{1}{3}\right)\left(2\frac{\partial\hat{v}}{\partial\hat{r}} - 2\Pi^*\right), \\
\hat{G}^*_{\theta\theta}(\hat{\nabla}\mathbf{v}, \boldsymbol{S}) &= \left(S_{\theta\theta}+\frac{1}{3}\right)\left(2\frac{\hat{v}}{\hat{r}} - 2\Pi^*\right), \\
\hat{G}^*_{xx}(\hat{\nabla}\mathbf{v}, \boldsymbol{S}) &= \left(S_{xx}+\frac{1}{3}\right)\left(2\frac{\partial\hat{u}}{\partial\hat{x}} - 2\Pi^*\right).
\end{aligned} \tag{2.83}$$

2.2.1 *Boundary conditions*

Upon non–dimensionalizing the boundary conditions corresponding to a compound fibre, one can write

- **Boundary conditions at the symmetry axis ($\hat{r} = 0$)**

  1. Velocity

$$\hat{v}_1 = 0, \qquad \frac{\partial\hat{u}_1}{\partial\hat{r}} = 0, \tag{2.84}$$

  2. Pressure

$$\frac{\partial\hat{p}_1}{\partial\hat{r}} = 0, \tag{2.85}$$

3. Temperature

$$\frac{\partial \hat{T}_1}{\partial \hat{r}} = 0, \tag{2.86}$$

- **Boundary conditions at the core–cladding interface ($\hat{r} = \hat{R}_1(\hat{x}, \hat{t})$)**

1. Kinematic boundary conditions

$$\hat{v}_1 = \frac{\partial \hat{R}_1}{\partial \hat{t}} + \hat{u}_1 \frac{\partial \hat{R}_1}{\partial \hat{x}}, \tag{2.87}$$

$$\hat{v}_2 = \frac{\partial \hat{R}_1}{\partial \hat{t}} + \hat{u}_2 \frac{\partial \hat{R}_1}{\partial \hat{x}}, \tag{2.88}$$

2. Continuity of tangential stresses

$$\begin{aligned} &\epsilon^2 \left(\hat{\boldsymbol{\tau}}_{2\,rr} - \hat{\boldsymbol{\tau}}_{2\,xx}\right) \frac{\partial \hat{R}_1}{\partial \hat{x}} + \left(\epsilon\, \hat{\boldsymbol{\tau}}_{2\,rx}\right) \left(1 - \epsilon^2 \left(\frac{\partial \hat{R}_1}{\partial \hat{x}}\right)^2\right) \\ =&\epsilon^2 \left(\hat{\boldsymbol{\tau}}_{1\,rr} - \hat{\boldsymbol{\tau}}_{1\,xx}\right) \frac{\partial \hat{R}_1}{\partial \hat{x}} + \left(\epsilon\, \hat{\boldsymbol{\tau}}_{1\,rx}\right) \left(1 - \epsilon^2 \left(\frac{\partial \hat{R}_1}{\partial \hat{x}}\right)^2\right), \end{aligned} \tag{2.89}$$

3. Balance of the normal stress difference

$$\begin{aligned} &\epsilon^2 \hat{\boldsymbol{\tau}}_{2\,xx} \left(\frac{\partial \hat{R}_1}{\partial \hat{x}}\right)^2 + \hat{\boldsymbol{\tau}}_{2\,rr} - 2\left(\epsilon\, \hat{\boldsymbol{\tau}}_{2\,rx}\right) \frac{\partial \hat{R}_1}{\partial \hat{x}} \\ -&\epsilon^2 \hat{\boldsymbol{\tau}}_{1\,xx} \left(\frac{\partial \hat{R}_1}{\partial \hat{x}}\right)^2 - \hat{\boldsymbol{\tau}}_{1\,rr} + 2\left(\epsilon\, \hat{\boldsymbol{\tau}}_{1\,rx}\right) \frac{\partial \hat{R}_1}{\partial \hat{x}} \\ =&\left(\frac{\sigma_1}{\sigma_2}\right) \frac{1}{(\epsilon\, Ca)} \hat{J}_1 - (\hat{p}_1 - \hat{p}_2) \left(1 + \epsilon^2 \left(\frac{\partial \hat{R}_1}{\partial \hat{x}}\right)^2\right), \end{aligned} \tag{2.90}$$

4. Continuity of temperature

$$\hat{T}_1 = \hat{T}_2, \tag{2.91}$$

5. Continuity of heat flux

$$\hat{k}_1 \left(\frac{\partial \hat{T}_1}{\partial \hat{r}} - \epsilon^2 \frac{\partial \hat{T}_1}{\partial \hat{x}} \frac{\partial \hat{R}_1}{\partial \hat{x}} \right) = \hat{k}_2 \left(\frac{\partial \hat{T}_2}{\partial \hat{r}} - \epsilon^2 \frac{\partial \hat{T}_2}{\partial \hat{x}} \frac{\partial \hat{R}_1}{\partial \hat{x}} \right), \tag{2.92}$$

- **Boundary conditions at the cladding–surroundings interface ($\hat{r} = \hat{R}_2(\hat{x}, \hat{t})$)**

1. Kinematic boundary conditions

$$\hat{v}_2 = \frac{\partial \hat{R}_2}{\partial \hat{t}} + \hat{u}_2 \frac{\partial \hat{R}_2}{\partial \hat{x}}, \tag{2.93}$$

2. Continuity of tangential stresses

$$\begin{aligned} &\epsilon^2 \left(\hat{\boldsymbol{\tau}}_{2\,rr} - \hat{\boldsymbol{\tau}}_{2\,xx} \right) \frac{\partial \hat{R}_2}{\partial \hat{x}} + \left(\epsilon\, \hat{\boldsymbol{\tau}}_{2\,rx} \right) \left(1 - \epsilon^2 \left(\frac{\partial \hat{R}_2}{\partial \hat{x}} \right)^2 \right) \\ &= -\epsilon^2 \hat{\mathcal{T}}_2(\hat{x}, \hat{t}), \end{aligned} \tag{2.94}$$

3. Balance of the normal stress difference

$$\begin{aligned} &\epsilon^2 \hat{\boldsymbol{\tau}}_{2\,xx} \left(\frac{\partial \hat{R}_2}{\partial \hat{x}} \right)^2 + \hat{\boldsymbol{\tau}}_{2\,rr} - 2 \left(\epsilon\, \hat{\boldsymbol{\tau}}_{2\,rx} \right) \frac{\partial \hat{R}_2}{\partial \hat{x}} \\ &= -\frac{1}{(\epsilon\, Ca)} \hat{J}_2 - (\hat{p}_e - \hat{p}_2) \left(1 + \epsilon^2 \left(\frac{\partial \hat{R}_2}{\partial \hat{x}} \right)^2 \right), \end{aligned} \tag{2.95}$$

4. Balance of heat flux

$$-\hat{k}_2 \left(\frac{\partial \hat{T}_2}{\partial \hat{r}} - \epsilon^2 \frac{\partial \hat{T}_2}{\partial \hat{x}} \frac{\partial \hat{R}_2}{\partial \hat{x}} \right) = Bi\, \hat{h}_2 \left(\hat{T}_2 - \hat{T}_\infty \right), \tag{2.96}$$

where

$$\hat{J}_i = \frac{\sqrt{1 + \epsilon^2 \left(\frac{\partial \hat{R}_i}{\partial \hat{x}} \right)^2}}{\hat{R}_i} - \epsilon^2 \frac{\frac{\partial^2 \hat{R}_i}{\partial \hat{x}^2}}{\sqrt{1 + \epsilon^2 \left(\frac{\partial \hat{R}_i}{\partial \hat{x}} \right)^2}}. \tag{2.97}$$

Equations (2.55)–(2.97) depend on ϵ, Re, Fr, Ca, $\hat{p}_e$, $\hat{\mathcal{T}}_2$, Pr, Br, Bi, $\hat{h}_2$, $\frac{\sigma_1}{\sigma_2}$, $\frac{\hat{C}_1}{\hat{C}_2}$, $\frac{\hat{k}_1}{\hat{k}_2}$, $\frac{\hat{\rho}_1}{\hat{\rho}_2}$, $\hat{D}_1$, $\hat{H}_1$, $\hat{D}_2$, $\hat{H}_2$, α_1, α_2, $\hat{\lambda}_{01}$, $\hat{\lambda}_{02}$, $\hat{\omega}_1$, $\hat{\omega}_2$, N_1 and N_2. In addition, the solution to these equations also depends on the boundary conditions at the die exit and take–up cross–sections. This large set of parameters does not allow us to obtain simpler equations except for slender geometries and small

values of the Reynolds, Biot and Brinkman numbers. We, therefore, consider typical operating conditions [143] in the manufacture of compound fibres which are usually characterized by small values of the Reynolds and very low values of the Biot and Brinkman numbers.

2.3 MOLECULAR ORIENTATION MODEL

As it was stated in § 2.2, the molecular orientation tensor, $\mathbf{S}$, is diagonal. However, since this tensor is also traceless, i.e., $S_{rr} + S_{\theta\theta} + S_{xx} = 0$, one of the components in its main diagonal can be related to the other two and this results in a molecular orientation tensor diagonal with only two independent components, i.e.,

$$\mathbf{S} = \frac{1}{3}\begin{pmatrix} -s_r & 0 & 0 \\ 0 & s_r - s_x & 0 \\ 0 & 0 & s_x \end{pmatrix}. \tag{2.98}$$

Using Eq. (2.98), the two components of the molecular orientation tensor given by the Doi–Edwards equation [30], i.e., Eq. (2.2) and Eqs. (2.82)–(2.83), are governed by the following equations

$$\frac{\partial s_{ir}}{\partial \hat{t}} + \hat{\mathbf{v}}_i \cdot \hat{\nabla} s_{ir} = (s_{ir} - 1)\left(2\frac{\partial \hat{v}_i}{\partial \hat{r}} - 2\Pi_i^*\right) - \frac{\phi_i}{\hat{\lambda}_i}\left\{s_{ir} - \frac{N_i}{3}\left[(1 - s_{ir})\left(s_{ir} + 3\,\Pi_{i,s}\right)\right]\right\}, \qquad i = 1, 2, \tag{2.99}$$

$$\frac{\partial s_{ix}}{\partial \hat{t}} + \hat{\mathbf{v}}_i \cdot \hat{\nabla} s_{ix} = (s_{ix} + 1)\left(2\frac{\partial \hat{u}_i}{\partial \hat{x}} - 2\Pi_i^*\right) - \frac{\phi_i}{\hat{\lambda}_i}\left\{s_{ix} - \frac{N_i}{3}\left[(s_{ix} + 1)\left(s_{ix} - 3\,\Pi_{i,s}\right)\right]\right\}, \qquad i = 1, 2, \tag{2.100}$$

where

$$\Pi_{i,s} = \frac{2}{9}\left(s_{ir}^2 + s_{ix}^2 - s_{ir}s_{ix}\right), \qquad i = 1, 2, \tag{2.101}$$

$$\Pi_i^* = \frac{1}{3}\left[s_{ir}\left(\frac{\hat{v}_i}{\hat{r}} - \frac{\partial \hat{v}_i}{\partial \hat{r}}\right) - s_{ix}\left(\frac{\hat{v}_i}{\hat{r}} - \frac{\partial \hat{u}_i}{\partial \hat{x}}\right)\right], \qquad i = 1, 2, \tag{2.102}$$

according with the traceless assumption of the molecular orientation tensor (cf. Eq. (2.98)).

From Eqs. (2.27) and (2.98), the molecular orientation order parameter becomes

$$\mathcal{S}_i = \sqrt{\frac{3}{2}\left(\mathbf{S}_i : \mathbf{S}_i\right)} = \sqrt{\frac{1}{3}\left(s_{ir}^2 + s_{ix}^2 - s_{ir}s_{ix}\right)}, \qquad i = 1, 2. \tag{2.103}$$

2.4 CRYSTALLIZATION MODEL

In order to account for the effects of both amorphous and crystalline phases in semi–crystalline compound fibres, we have assumed that the semi–crystalline materials that compose the core

and cladding behave as single–phase fluids whose degree of crystallization ($\mathcal{Y}$) is governed by Ziabicki's model [154], i.e.,

$$\frac{\partial \mathcal{Y}_i}{\partial \hat{t}} + \hat{\mathbf{v}}_i \cdot \hat{\nabla} \mathcal{Y}_i = k_{Ai}(\mathcal{S})(\mathcal{Y}_{\infty,i} - \mathcal{Y}_i) \qquad i = 1,\, 2, \tag{2.104}$$

where $k_{Ai}(\mathcal{S}) = k_{Ai}(0)\exp(a_{2i}\mathcal{S}_i^2)$ is the linearised crystal growth rate which increases exponentially with the molecular orientation order parameter and $k_{Ai}(0)$ is the amorphous growth rate.

In order to incorporate the effects of crystallization on the deviatoric stress tensor, the viscosity $\hat{\mu}_i$ that appears in Eq. (2.79) has been replaced by the following effective value

$$\hat{\mu}_{e,i}(\hat{T}_i, \mathcal{Y}_i) = \hat{\mu}_i(\hat{T}_i) \exp\left(\beta_i \left(\frac{\mathcal{Y}_i}{\mathcal{Y}_{\infty,i}}\right)^{n_i}\right) \qquad i = 1,\, 2, \tag{2.105}$$

where β_i and n_i are the crystallization viscosity rate and the crystallization viscosity index, respectively, which are material–dependent, e.g., $\beta_i = 4.605$ and $n_i = 12$ for nylon–66, and $\beta_i = 4$ and $n_i = 2$ for PET, and the effects of crystallization on the effective dynamic viscosity have been assumed to be multiplicative. Equation (2.105) indicates that, in addition to the contribution of the molecular orientation to the deviatoric stress tensor (cf. Eq. (2.20)), the degree of crystallization affects the effective viscosity and, therefore, the (modified) Newtonian stress tensor (cf. Eq. (2.20)). Equation (2.105) also indicates that the effective dynamic viscosity increases as the degree of crystallization tends to its ultimate value; for small degrees of crystallization, the effective dynamic viscosity is mainly a function of the temperature and increases as the temperature decreases.

3

ONE–DIMENSIONAL MODEL OF FIBRE FORMATION IN MELT SPINNING PROCESSES

Contents

3.1 ASYMPTOTIC 1–D MODEL FOR COMPOUND FIBRES

For small Reynolds numbers, $Re = \epsilon\bar{R}$ with $\bar{R} = O(1)$, and, depending on the magnitude of the Froude, capillary, Biot and Brinkmann numbers, several flow regimes can be identified. Here, we consider $Fr = \bar{F}/\epsilon$, $Ca = \bar{C}/\epsilon$, $Bi = \epsilon^2\bar{B}$ and $Br = \epsilon^2\bar{b}$ where $\bar{F} = O(1)$, $\bar{C} = O(1)$, $\bar{B} = O(1)$ and $\bar{b} = O(1)$ which correspond to small gravitational effects, small surface tension, small heat convection and radiation, and small heat generation due to viscous dissipation. These assumptions corresponds to moderately high draw speeds melting conditions. In addition, small values of the α parameter have been assumed in this work, i.e., $\alpha = \epsilon^2\bar{\alpha}$, where $\bar{\alpha} = O(1)$, which corresponds to low polymeric contributions to the stress tensor.

Substitution of these values and expansion of the dependent variables $\hat{R}_1$, $\hat{R}_2$, $\hat{u}_i$, $\hat{v}_i$, $\hat{p}_i$ and $\hat{T}_i$, where $i = 1, 2$, as

$$\Psi = \Psi_0 + \epsilon^2\Psi_2 + O\left(\epsilon^4\right), \tag{3.1}$$

where Ψ denotes a dependent variable, into the governing equations and boundary conditions for compound fibres, together with the expansion of the boundary conditions at $\hat{R}_1(\hat{t}, \hat{x})$ and $\hat{R}_2(\hat{t}, \hat{x})$ about $\hat{R}_{10}(\hat{t}, \hat{x}) \equiv \mathcal{R}_1$ and $\hat{R}_{20}(\hat{t}, \hat{x}) \equiv \mathcal{R}_2$, respectively, yield asymptotic expansions which at leading–order, i.e., at $O(\epsilon^0)$, correspond to

- **Mass conservation equation**

$$\frac{1}{\hat{r}}\frac{\partial}{\partial \hat{r}}\left(\hat{r}\hat{v}_{i,0}\right)+\frac{\partial \hat{u}_{i,0}}{\partial \hat{x}}=0, \qquad i=1,2, \tag{3.2}$$

- **Linear momentum equation – $\hat{r}$ axis**

$$-\frac{\partial \hat{p}_{i,0}}{\partial \hat{r}}+\frac{1}{\hat{r}}\frac{\partial}{\partial \hat{r}}\left(\hat{r}\,\hat{\boldsymbol{\tau}}_{i,0\;rr}\right)+\frac{\partial}{\partial \hat{x}}\left(\hat{\mu}_{i,0}\frac{\partial \hat{u}_{i,0}}{\partial \hat{r}}\right)-\frac{\hat{\boldsymbol{\tau}}_{i,0\;\theta\theta}}{\hat{r}}=0, \qquad i=1,2, \tag{3.3}$$

- **Linear momentum equation – $\hat{x}$ axis**

$$\frac{1}{\hat{r}}\frac{\partial}{\partial \hat{r}}\left(\hat{r}\,\hat{\mu}_{i,0}\frac{\partial \hat{u}_{i,0}}{\partial \hat{r}}\right)=0, \qquad i=1,2, \tag{3.4}$$

- **Energy conservation equation**

$$\frac{1}{\hat{r}}\frac{\partial}{\partial \hat{r}}\left(\hat{r}\frac{\partial \hat{T}_{i,0}}{\partial \hat{r}}\right)=0, \qquad i=1,2. \tag{3.5}$$

The boundary conditions for compound fibres at leading–order, $O(\epsilon^0)$, are

- **Boundary conditions at the symmetry axis ($\hat{r}=0$)**

  1. Velocity

$$\hat{v}_{1,0}=0, \qquad \frac{\partial \hat{u}_{1,0}}{\partial \hat{r}}=0, \tag{3.6}$$

  2. Pressure

$$\frac{\partial \hat{p}_{1,0}}{\partial \hat{r}}=0, \tag{3.7}$$

  3. Temperature

$$\frac{\partial \hat{T}_{1,0}}{\partial \hat{r}}=0. \tag{3.8}$$

- **Boundary conditions at the core–cladding interface $\left(\hat{r}=\hat{\boldsymbol{R}}_{\mathbf{1,0}}(\hat{x},\hat{t})\right)$**

1. Kinematic boundary conditions

$$\hat{v}_{1,0} = \frac{\partial \hat{R}_{1,0}}{\partial \hat{t}} + \hat{u}_{1,0}\frac{\partial \hat{R}_{1,0}}{\partial \hat{x}}, \tag{3.9}$$

$$\hat{v}_{2,0} = \frac{\partial \hat{R}_{1,0}}{\partial \hat{t}} + \hat{u}_{2,0}\frac{\partial \hat{R}_{1,0}}{\partial \hat{x}}, \tag{3.10}$$

2. Continuity of tangential stresses

$$\hat{\mu}_{2,0}\frac{\partial \hat{u}_{2,0}}{\partial \hat{r}} = \hat{\mu}_{1,0}\frac{\partial \hat{u}_{1,0}}{\partial \hat{r}}, \tag{3.11}$$

3. Balance of the normal stress difference

$$\hat{\boldsymbol{\tau}}_{2,0\ rr} - \hat{\boldsymbol{\tau}}_{1,0\ rr} - 2\left(\hat{\mu}_{2,0}\frac{\partial \hat{u}_{2,0}}{\partial \hat{r}} - \hat{\mu}_{1,0}\frac{\partial \hat{u}_{1,0}}{\partial \hat{r}}\right)\frac{\partial \hat{R}_{1,0}}{\partial \hat{x}} = \left(\frac{\sigma_1}{\sigma_2}\right)\frac{1}{\bar{C}\hat{R}_{1,0}} - (\hat{p}_{1,0} - \hat{p}_{2,0}), \tag{3.12}$$

4. Continuity of temperature

$$\hat{T}_{1,0} = \hat{T}_{2,0}, \tag{3.13}$$

5. Continuity of heat flux

$$\hat{k}_1\frac{\partial \hat{T}_{1,0}}{\partial \hat{r}} = \hat{k}_2\frac{\partial \hat{T}_{2,0}}{\partial \hat{r}}. \tag{3.14}$$

- **Boundary conditions at the cladding–surroundings interface** $\left(\hat{\boldsymbol{r}} = \hat{\boldsymbol{R}}_{\mathbf{2,0}}(\hat{\boldsymbol{x}}, \hat{\boldsymbol{t}})\right)$

1. Kinematic boundary condition

$$\hat{v}_{2,0} = \frac{\partial \hat{R}_{2,0}}{\partial \hat{t}} + \hat{u}_{2,0}\frac{\partial \hat{R}_{2,0}}{\partial \hat{x}}, \tag{3.15}$$

2. Continuity of tangential stresses

$$\hat{\mu}_{2,0}\frac{\partial \hat{u}_{2,0}}{\partial \hat{r}} = 0, \tag{3.16}$$

3. Balance of the normal stress difference

$$\hat{\boldsymbol{\tau}}_{2,0\,rr} - 2\,\hat{\mu}_{2,0}\frac{\partial \hat{u}_{2,0}}{\partial \hat{r}}\frac{\partial \hat{R}_{2,0}}{\partial \hat{x}} = -\frac{1}{\bar{C}\hat{R}_{2,0}} - (\hat{p}_e - \hat{p}_{2,0})\,, \tag{3.17}$$

4. Balance of heat flux

$$\hat{k}_2\frac{\partial \hat{T}_{2,0}}{\partial \hat{r}} = 0. \tag{3.18}$$

For the asymptotic analysis developed above, the equations of the diagonal components of the stress tensor at leading–order, $O(\epsilon^0)$, can be written as (cf. Eqs. (2.73)–(2.75))

$$\begin{aligned}
\hat{\boldsymbol{\tau}}_{i,0\,rr} &= 2\,\hat{\mu}_{i,0}\frac{\partial \hat{v}_{i,0}}{\partial \hat{r}},\\
\hat{\boldsymbol{\tau}}_{i,0\,\theta\theta} &= 2\,\hat{\mu}_{i,0}\frac{\hat{v}_{i,0}}{\hat{r}},\\
\hat{\boldsymbol{\tau}}_{i,0\,xx} &= 2\,\hat{\mu}_{i,0}\frac{\partial \hat{u}_{i,0}}{\partial \hat{x}}.
\end{aligned}$$

The solutions to these equations are

$$\hat{u}_{i,0} = B_i(\hat{t},\hat{x}), \qquad \hat{p}_{i,0} = \mathcal{D}_i(\hat{t},\hat{x}), \qquad \hat{T}_{i,0} = F_i(\hat{t},\hat{x}), \qquad i = 1,2, \tag{3.19}$$

$$\hat{v}_{i,0} = \frac{\mathcal{C}_i}{\hat{r}} - \frac{\partial B_i}{\partial \hat{x}}\frac{\hat{r}}{2}, \qquad i = 1,2, \tag{3.20}$$

which imply that, at leading–order, the axial velocity component $B_1 = B_2 \equiv \mathcal{B}$ (cf. Eq. (2.53)), the temperature $F_1 = F_2 \equiv \mathcal{F}$ (cf. Eqs. (3.13), (3.14) and (3.18)), and the pressure are only functions of the axial coordinate and time. $\mathcal{C}_1(t,x)$ and $\mathcal{C}_2(t,x)$ can be determined from the kinematic conditions provided by Eqs. (3.9), (3.10) and (3.15) and $\hat{v}_{1,0}(0,\hat{x},\hat{t}) = 0$ (cf. Eqs. (3.6), (3.7) and (3.8)) as

$$\mathcal{C}_1 = \mathcal{C}_2 = \frac{\partial}{\partial t}\left(\frac{R_{1,0}^2}{2}\right) + \frac{\partial}{\partial x}\left(\mathcal{B}\frac{R_{1,0}^2}{2}\right) = \frac{\partial}{\partial t}\left(\frac{R_{2,0}^2}{2}\right) + \frac{\partial}{\partial x}\left(\mathcal{B}\frac{R_{2,0}^2}{2}\right) = 0, \tag{3.21}$$

which, in turn, imply that

$$\frac{\partial \mathcal{A}_1}{\partial \hat{t}} + \frac{\partial}{\partial \hat{x}}(\mathcal{B}\mathcal{A}_1) = 0, \qquad \frac{\partial \mathcal{A}_2}{\partial \hat{t}} + \frac{\partial}{\partial \hat{x}}(\mathcal{B}\mathcal{A}_2) = 0, \tag{3.22}$$

where

$$\mathcal{A}_1 = \frac{\hat{R}_{1,0}^2}{2} = \frac{\mathcal{R}_1^2}{2}, \qquad \mathcal{A}_2 = \frac{\hat{R}_{2,0}^2 - \hat{R}_{1,0}^2}{2} = \frac{\mathcal{R}_2^2 - \mathcal{R}_1^2}{2}. \tag{3.23}$$

Equation (3.22) corresponds to mass conservation at leading–order.

Taking into account that axial velocity and acceleration in radial direction are independent of the radial coordinate (cf. Eqs. (3.19)– (3.20)) at leading–order, then

$$\Pi^{*}_{i,0} = \frac{1}{2}\frac{\partial \mathcal{B}}{\partial \hat{x}}\, s_{i\,x}. \tag{3.24}$$

It must be pointed out that, since the dynamic viscosity is a function of the temperature, i.e., $\hat{\mu}_i = \hat{\mu}\left(\hat{T}_{i,0} + \epsilon^2 \hat{T}_{i,2} + O(\epsilon^4)\right)$, a Taylor's series expansion about $\hat{T}_{i,0}$ shows that $\hat{\mu}(\hat{T}_i) = \hat{\mu}_{i,0} + \epsilon^2 \hat{\mu}_{i,2} + O(\epsilon^4)$, where $\hat{\mu}_{i,0} = \hat{\mu}_i(\hat{T}_{i,0})$ and $\hat{\mu}_{i,2} = \frac{d\hat{\mu}_i}{d\hat{T}_i}(\hat{T}_{i,0}) \cdot \hat{T}_{i,2}$.

From Eqs. (3.12), (3.17) and (3.20), one can easily obtain the following equations

$$\hat{p}_{1,0} = \mathcal{D}_1(\hat{x},\hat{t}) = \hat{p}_e + \frac{1}{\bar{C}}\left(\frac{1}{\mathcal{R}_2} + \left(\frac{\sigma_1}{\sigma_2}\right)\frac{1}{\mathcal{R}_1}\right) - \hat{\mu}_{1,0}\frac{\partial \mathcal{B}}{\partial \hat{x}}, \tag{3.25}$$

$$\hat{p}_{2,0} = \mathcal{D}_2(\hat{x},\hat{t}) = \hat{p}_e + \frac{1}{\bar{C}}\frac{1}{\mathcal{R}_2} - \hat{\mu}_{2,0}\frac{\partial \mathcal{B}}{\partial \hat{x}}. \tag{3.26}$$

Equations (3.19), (3.20), (3.22) and (3.25)–(3.26) contain four unknowns, i.e., $\mathcal{B}$, $\mathcal{R}_1$, $\mathcal{R}_2$, and $\mathcal{F}$; therefore, these equations are not a closed system. In order to close this system of equations, it is necessary to go to higher order in the asymptotic expansion.

At $O(\epsilon^2)$, the axial momentum equations yields

$$\hat{\mu}_{i,0}\left(\frac{\partial \hat{u}_{i,2}}{\partial \hat{r}} + \frac{\partial \hat{v}_{i,0}}{\partial \hat{x}}\right) = \mathcal{M}_i\,\frac{\hat{r}}{2} + \frac{\mathcal{P}_i}{\hat{r}}, \qquad i = 1,2, \tag{3.27}$$

where

$$\mathcal{M}_i = \bar{R}\hat{\rho}_i\frac{D\mathcal{B}}{D\hat{t}} - \frac{\bar{R}}{\bar{F}}\hat{\rho}_i + \frac{\partial \hat{p}_{i,0}}{\partial \hat{x}} - \frac{\partial}{\partial \hat{x}}\left(\hat{\boldsymbol{\tau}}_{i,0\;xx}\right), \tag{3.28}$$

where $\frac{D}{D\hat{t}}(\cdot) \equiv \frac{\partial}{\partial \hat{t}}(\cdot) + \mathcal{B}\frac{\partial}{\partial \hat{x}}(\cdot)$ and $\mathcal{P}_i$ is a function of integration that, in general, depends on $\hat{x}$ and $\hat{t}$.

The shear stress conditions at the interfaces (cf. Eqs. (2.89) and (2.94)), together with $v_{i,0}$ (cf. Eq. (3.20)) and the no–slip condition provided by Eq. (2.53) at second–order yield, after lengthy algebra,

$$\begin{aligned}\bar{R}\left(\hat{\rho}_1\mathcal{A}_1 + \hat{\rho}_2\mathcal{A}_2\right)\frac{D\mathcal{B}}{D\hat{t}} = \left(\hat{\rho}_1\mathcal{A}_1 + \hat{\rho}_2\mathcal{A}_2\right)\frac{\bar{R}}{\bar{F}} + \frac{1}{2\bar{C}}\left(\frac{\partial \mathcal{R}_2}{\partial \hat{x}} + \left(\frac{\sigma_1}{\sigma_2}\right)\frac{\partial \mathcal{R}_1}{\partial \hat{x}}\right)\\ + \frac{\partial}{\partial \hat{x}}\left\{3\left(\hat{\mu}_{1,0}\mathcal{A}_1 + \hat{\mu}_{2,0}\mathcal{A}_2\right)\frac{\partial \mathcal{B}}{\partial \hat{x}}\right\}\\ - \hat{\mathcal{T}}_2\,\mathcal{R}_2 - \frac{\partial \hat{p}_e}{\partial \hat{x}}\left(\mathcal{A}_1 + \mathcal{A}_2\right).\end{aligned} \tag{3.29}$$

The symmetry (cf. Eq. (3.6)) and continuity of tangential stresses at the interface $\mathcal{R}_1$ (cf. Eq. (3.11)) boundary conditions allow to obtain the functions $\mathcal{P}_i$ as

$$\mathcal{P}_1 = 0, \tag{3.30}$$

$$\mathcal{P}_2 = (\mathcal{M}_1 - \mathcal{M}_2)\ \mathcal{A}_1 + 3\,(\hat{\mu}_{2,0} - \hat{\mu}_{1,0})\ \frac{\partial \mathcal{B}}{\partial \hat{x}}\,\frac{\partial \mathcal{A}_1}{\partial \hat{x}}. \tag{3.31}$$

The energy Eq. (2.58) at second–order yields

$$\hat{T}_{i,2} = \left(\bar{P}\,\frac{\hat{\rho}_i \hat{C}_i}{\hat{k}_i}\frac{D\mathcal{F}}{D\hat{t}} - \frac{\partial^2 \mathcal{F}}{\partial \hat{x}^2}\right)\frac{\hat{r}^2}{4} + \mathcal{H}_i \ln \hat{r} + \mathcal{U}_i, \qquad i = 1, 2, \tag{3.32}$$

where $\bar{P} = \bar{R}Pr$, $Pr = O(1)$ and $\mathcal{H}_i$ and $\mathcal{U}_i$ are functions of $\hat{x}$ and $\hat{t}$. Equation (3.32) subject to the symmetry condition at $\hat{r} = 0$ for $i = 1$ and the thermal boundary conditions at the interfaces (at second–order) yields

$$\bar{P}\left(\hat{\rho}_1 \hat{C}_1 \mathcal{A}_1 + \hat{\rho}_2 \hat{C}_2 \mathcal{A}_2\right)\frac{D\mathcal{F}}{D\hat{t}} = \frac{\partial}{\partial \hat{x}}\left(\left(\mathcal{A}_1 \hat{k}_1 + \mathcal{A}_2 \hat{k}_2\right)\frac{\partial \mathcal{F}}{\partial \hat{x}}\right) - \bar{B}\,\hat{h}_2 \mathcal{R}_2\,(\mathcal{F} - \mathcal{F}_{\infty,2})\,, \tag{3.33}$$

which clearly shows that the compound jet behaves as a single–component jet with a thermal inertia and conductivity which are proportional to the cross–sectional areas and the thermal capacities and conductivities of the materials that compose the jet.

Equations (3.22), (3.29) and (3.33) reduce to those derived by Schultz and Davis [126, 127] and Gupta and Schultz [56] for steady, single–component jets under isothermal and non–isothermal conditions, respectively.

Equations (3.22), (3.29) and (3.33) constitute a system of four one–dimensional equations for $\mathcal{R}_1$, $\mathcal{R}_2$, $\mathcal{B}$ and $\mathcal{F}$. This system is asymptotically valid for small Reynolds, Biot and Brinkman numbers and large values of the Froude and capillary numbers, is much simpler than Eqs. (2.4)–(2.53), and includes the effects of the temperature through Eq. (3.29) and the dependence of the viscosity on temperature in the linear momentum equations (cf. Eq. (2.79)). However, this system of one–dimensional equations implies that the leading–order temperature and axial velocity components of the inner and outer jets are the same. It must be noted that no latent heat has been considered, and viscous dissipation has been disregarded.

3.2 ASYMPTOTIC 1–D MODEL FOR HOLLOW COMPOUND FIBRES

Since the derivation of the one–dimensional equations for the slender fibre's geometry and axial velocity component is analogous to that for isothermal slender hollow compound fibres [119, 122] and the derivation of the one–dimensional equation for the temperature is similar to that for non–isothermal slender compound fibres presented in § 2.2 and § 3.1, the details are omitted here.

The following leading–order equations for the hollow fibre's geometry and leading–order axial and radial velocity components, respectively, for hollow compound fibres have been obtained as

$$\begin{aligned}
\frac{\partial \mathcal{A}_1}{\partial \hat{t}} + \frac{\partial}{\partial \hat{x}}(\mathcal{B}\mathcal{A}_1) &= 0, \\
\frac{\partial \mathcal{A}_2}{\partial \hat{t}} + \frac{\partial}{\partial \hat{x}}(\mathcal{B}\mathcal{A}_2) &= 0, \\
\frac{\partial}{\partial \hat{t}}\left(\frac{\mathcal{R}_1^2}{2}\right) + \frac{\partial}{\partial \hat{x}}\left(\mathcal{B}\frac{\mathcal{R}_1^2}{2}\right) &= \mathcal{C}(\hat{x}),
\end{aligned} \tag{3.34}$$

where $\mathcal{A}_1 = \frac{\mathcal{R}_1^2 - \mathcal{R}_0^2}{2}$ and $\mathcal{A}_2 = \frac{\mathcal{R}_2^2 - \mathcal{R}_1^2}{2}$ denote the non–dimensional leading–order cross–sectional areas of the inner and outer hollow jets, respectively,

$$\begin{aligned}
\left(\hat{\rho}_1\mathcal{A}_1 + \hat{\rho}_2\mathcal{A}_2\right)\bar{R}\frac{D\mathcal{B}}{Dt} = \left(\hat{\rho}_1\mathcal{A}_1 + \hat{\rho}_2\mathcal{A}_2\right)\frac{\bar{R}}{\bar{F}} - \mathcal{A}_1\frac{\partial \mathcal{D}_1}{\partial \hat{x}} - \mathcal{A}_2\frac{\partial \mathcal{D}_2}{\partial \hat{x}} \\
+\frac{\partial}{\partial \hat{x}}\left(3\left(\hat{\mu}_{1,0}\mathcal{A}_1 + \hat{\mu}_{2,0}\mathcal{A}_2\right)\frac{\partial \mathcal{B}}{\partial \hat{x}}\right) \\
+2\,\mathcal{C}(\hat{x})\left(\hat{\mu}_{1,0}\frac{\partial \mathcal{A}_1}{\partial \hat{x}} + \hat{\mu}_{2,0}\frac{\partial \mathcal{A}_2}{\partial \hat{x}}\right) \\
-\hat{\mathcal{T}}_2\,\mathcal{R}_2 + \hat{\mathcal{T}}\,\mathcal{R}_0,
\end{aligned} \tag{3.35}$$

where

$$\mathcal{D}_1(\hat{x},\hat{t}) = \hat{p}_i - \frac{1}{\bar{C}}\left(\frac{\sigma}{\sigma_2}\right)\frac{1}{\mathcal{R}_0} - \hat{\mu}_{1,0}\frac{2\,\mathcal{C}(\hat{x})}{\mathcal{R}_0^2}, \tag{3.36}$$

$$\mathcal{D}_2(\hat{x},\hat{t}) = \hat{p}_e + \frac{1}{\bar{C}}\frac{1}{\mathcal{R}_2} - \hat{\mu}_{2,0}\frac{2\,\mathcal{C}(\hat{x})}{\mathcal{R}_2^2}, \tag{3.37}$$

$$\hat{v}_{i,0}(\hat{r},\hat{x}) = \frac{\mathcal{C}(\hat{x})}{\hat{r}} - \frac{\hat{r}}{2}\frac{\partial \mathcal{B}}{\partial \hat{x}}, \tag{3.38}$$

where $\mathcal{C}(\hat{x},\hat{t})$ is given by

$$\mathcal{C}(\hat{x},\hat{t}) = -\frac{1}{2}\frac{(\hat{p}_e - \hat{p}_i) + \frac{1}{\bar{C}}\left[\left(\frac{\sigma}{\sigma_2}\right)\frac{1}{\mathcal{R}_0} + \left(\frac{\sigma_1}{\sigma_2}\right)\frac{1}{\mathcal{R}_1} + \frac{1}{\mathcal{R}_2}\right]}{\hat{\mu}_{1,0}\left(\frac{1}{\mathcal{R}_0^2} - \frac{1}{\mathcal{R}_1^2}\right) + \hat{\mu}_{2,0}\left(\frac{1}{\mathcal{R}_1^2} - \frac{1}{\mathcal{R}_2^2}\right)}. \tag{3.39}$$

The first two equations of Eq. (3.34) can also be written making use of the third one as

$$\frac{\partial}{\partial \hat{t}}\left(\frac{\mathcal{R}_0^2}{2}\right) + \frac{\partial}{\partial \hat{x}}\left(\mathcal{B}\frac{\mathcal{R}_0^2}{2}\right) = \mathcal{C}(\hat{x}), \tag{3.40}$$

$$\frac{\partial}{\partial \hat{t}}\left(\frac{\mathcal{R}_2^2}{2}\right) + \frac{\partial}{\partial \hat{x}}\left(\mathcal{B}\frac{\mathcal{R}_2^2}{2}\right) = \mathcal{C}(\hat{x}). \tag{3.41}$$

Taking into account the expressions for the axial and radial velocity components at leading–order, the velocity gradient tensor for hollow compound fibres is written as

$$\hat{\nabla}\mathbf{v} = \frac{1}{2}\frac{\partial \mathcal{B}}{\partial \hat{x}}\begin{pmatrix} -1 & 0 & 0 \\ 0 & -1 & 0 \\ 0 & 0 & 2 \end{pmatrix} + \frac{\mathcal{C}}{\hat{r}^2}\begin{pmatrix} -1 & 0 & 0 \\ 0 & 1 & 0 \\ 0 & 0 & 0 \end{pmatrix}, \tag{3.42}$$

which, unlike in compound fibres, is a function of $\hat{r}$ and $\hat{x}$, and

$$\Pi^*_{i,0} = \frac{1}{2}\frac{\partial \mathcal{B}}{\partial \hat{x}}\, s_{i\,x} + \frac{1}{3}\frac{\mathcal{C}}{\hat{r}^2}\left(2 s_{i\,r} - s_{i\,x}\right), \qquad i = 1, 2. \tag{3.43}$$

Equation (3.32) subject to the thermal boundary conditions at the interfaces (at second–order) yields

$$\begin{aligned} \bar{P}\left(\hat{\rho}_1 \hat{C}_1 \mathcal{A}_1 + \hat{\rho}_2 \hat{C}_2 \mathcal{A}_2\right)\frac{D\mathcal{F}}{D\hat{t}} = \frac{\partial}{\partial \hat{x}}\left(\left(\mathcal{A}_1 \hat{k}_1 + \mathcal{A}_2 \hat{k}_2\right)\frac{\partial \mathcal{F}}{\partial \hat{x}}\right) \\ -\bar{B}\left[\hat{h}_2\, \mathcal{R}_2\left(\mathcal{F} - \mathcal{F}_{\infty,2}\right) + \hat{h}_1\, \mathcal{R}_0\left(\mathcal{F} - \mathcal{F}_{\infty,1}\right)\right], \end{aligned} \tag{3.44}$$

which clearly shows that the hollow compound jet behaves as a single–component jet with a thermal inertia and conductivity which are proportional to the cross–sectional areas and the thermal capacities and conductivities of the materials that compose the fibre.

The asymptotic analysis also indicates that, for slender fibres at low Reynolds and Biot numbers, the temperature is uniform across the hollow compound fibre at leading–order in the slenderness ratio. Although this assumption is valid for the small Biot numbers employed in the asymptotic analysis, it is not expected to be so near the hollow compound fibre's outer and inner interfaces. In particular, at $\mathcal{R}_2$ (and also at $\mathcal{R}_0$), where heat exchanges with the surroundings occur, a thermal boundary layers may form, especially at moderate and high Péclet numbers.

3.3 1–D MOLECULAR ORIENTATION AND DEGREE OF CRYSTALLIZATION MODELS

The molecular orientation model presented in § 2.3 requires the solution of two components of the assumed diagonal molecular orientation tensor and can be simplified by requiring that $s_x = 2\, s_r = 2\, s$ so that the resulting tensor

$$\mathbf{S} = \frac{s}{3}\begin{pmatrix} -1 & 0 & 0 \\ 0 & -1 & 0 \\ 0 & 0 & 2 \end{pmatrix}, \tag{3.45}$$

is proportional to the leading–order velocity gradient tensor for compound fibres which may be written as

$$\hat{\nabla}\mathbf{v} = \frac{\partial \mathcal{B}}{\partial \hat{x}}\begin{pmatrix} -1 & 0 & 0 \\ 0 & -1 & 0 \\ 0 & 0 & 2 \end{pmatrix}. \tag{3.46}$$

In this model, the molecular orientation tensor depends only on a single (order) parameter [45] and its contribution to the deviatoric stress tensor, $\boldsymbol{\tau}$, may be written through an effective dynamic viscosity $\hat{\mu}_{e,i}$ as

$$\boldsymbol{\tau}_i = \hat{\mu}_{e,i}\left(\nabla \mathbf{v}_i + (\nabla \mathbf{v}_i)^T\right), \qquad i = 1,\, 2, \tag{3.47}$$

where

$$\hat{\mu}_{e,i} = \hat{\mu}_i(\hat{T}_i)\exp\left(\beta_i\left(\frac{\mathcal{Y}_i}{\mathcal{Y}_{\infty,i}}\right)^{n_i}\right) + \frac{2}{3}\,\alpha_i\,\hat{\lambda}_i\,\hat{T}_i\,s_i^2, \qquad i = 1,\, 2. \tag{3.48}$$

Under these conditions, the Doi–Edwards equation, i.e., Eq.(2.24), can be written as

$$\frac{\partial \mathcal{S}_i}{\partial \hat{t}} + \mathcal{B}\frac{\partial \mathcal{S}_i}{\partial \hat{x}} = (1-\mathcal{S}_i)(2\mathcal{S}_i+1)\frac{\partial \mathcal{B}}{\partial \hat{x}} - \frac{\phi_i}{\hat{\lambda}_i}\,\mathcal{F}\,U(\mathcal{S}_i), \qquad i = 1,\, 2, \tag{3.49}$$

where

$$U\left(\mathcal{S}_i\right) = \mathcal{S}_i\left(1 - \frac{N_i}{3}(1-\mathcal{S}_i)(2\mathcal{S}_i+1)\right), \qquad i = 1,\, 2, \tag{3.50}$$

is a bulk free energy which is related to the intermolecular potential.

It must be noted that the molecular orientation parameter now reads as

$$\mathcal{S}_i = \sqrt{\frac{3}{2}\left(\mathbf{S}_i : \mathbf{S}_i\right)} = s_i, \qquad i = 1, 2. \tag{3.51}$$

The equation for degree of crystallization, $\mathcal{Y}$ is given by the well–known Ziabicki's model which for the one–dimensional model (see § 2.4) is written as

$$\frac{\partial \mathcal{Y}}{\partial \hat{t}} + \mathcal{B}\frac{\partial \mathcal{Y}_i}{\partial \hat{x}} = k_{Ai}(\mathcal{S})(\mathcal{Y}_{\infty,i} - \mathcal{Y}_i), \qquad i = 1,\, 2. \tag{3.52}$$

3.4 1–D STEADY–STATE MODEL FOR SEMI–CRYSTALLINE COMPOUND FIBRES

In this subsection, we employ a generalization of the model developed in § 3.1 and § 3.3 for fibres to analyse the effects of orientation and crystallization of the melt spinning of compound fibres. The contribution of air drag effects to the leading–order momentum equation has been neglected. Such a generalization requires the numerical solution of the following equations (cf. Eqs. (3.22), (3.29) and (3.33))

$$\frac{d}{d\hat{x}}(\mathcal{B}\mathcal{A}_1) = 0, \qquad \frac{d}{d\hat{x}}(\mathcal{B}\mathcal{A}_2) = 0, \tag{3.53}$$

$$\begin{aligned}\bar{R}\left(\hat{\rho}_1\mathcal{A}_1 + \hat{\rho}_2\mathcal{A}_2\right)\mathcal{B}\frac{d\mathcal{B}}{d\hat{x}} = {} & \left(\hat{\rho}_1\mathcal{A}_1 + \hat{\rho}_2\mathcal{A}_2\right)\frac{\bar{R}}{\bar{F}} + \frac{1}{2\bar{C}}\left(\frac{d\mathcal{R}_2}{d\hat{x}} + \left(\frac{\sigma_1}{\sigma_2}\right)\frac{d\mathcal{R}_1}{d\hat{x}}\right) \\ & + \frac{d}{d\hat{x}}\left\{3\left(\hat{\mu}_{e1,0}\mathcal{A}_1 + \hat{\mu}_{e2,0}\mathcal{A}_2\right)\frac{d\mathcal{B}}{d\hat{x}}\right\}\end{aligned} \tag{3.54}$$

$$\bar{P}\left(\hat{\rho}_1\hat{C}_1\mathcal{A}_1+\hat{\rho}_2\hat{C}_2\mathcal{A}_2\right)\mathcal{B}\frac{d\mathcal{F}}{d\hat{x}}=\frac{d}{d\hat{x}}\left(\left(\mathcal{A}_1\hat{k}_1+\mathcal{A}_2\hat{k}_2\right)\frac{d\mathcal{F}}{d\hat{x}}\right)-\bar{B}\,\hat{h}_2\,\mathcal{R}_2\left(\mathcal{F}-\mathcal{F}_{\infty,2}\right), \tag{3.55}$$

or

$$\bar{P}\left(\hat{\rho}_1\hat{C}_1\mathcal{A}_1+\hat{\rho}_2\hat{C}_2\mathcal{A}_2\right)\mathcal{B}\frac{d\mathcal{F}}{d\hat{x}}=-\bar{B}\,\hat{h}_2\,\mathcal{R}_2\left(\mathcal{F}-\mathcal{F}_{\infty,2}\right) \tag{3.56}$$

when axial conduction is neglected.

The steady–state equations for the molecular orientation order parameter and degree of crystallization can be written using § 3.3 as

$$\mathcal{B}\frac{d\mathcal{S}}{d\hat{x}}=\left(1-\mathcal{S}_i\right)\left(2\mathcal{S}_i+1\right)\frac{d\mathcal{B}}{d\hat{x}}-\frac{\phi_i}{\lambda_i}\,\mathcal{F}\,U(\mathcal{S}_i),\qquad i=1,2, \tag{3.57}$$

$$\mathcal{B}\frac{d\mathcal{Y}}{d\hat{x}}=k_{A\,i}\left(\mathcal{S}\right)\left(\mathcal{Y}_{\infty,i}-\mathcal{Y}_i\right),\qquad i=1,2, \tag{3.58}$$

where $k_{A\,i}(\mathcal{S})=k_{Ai}(0)\exp(a_{2\,i}\mathcal{S}_i^2)$,

The effective dynamic viscosity of the inner and outer jets is given by

$$\hat{\mu}_{e1,0}=\hat{D}_1\,\exp\left(\hat{H}_1\left(1-\mathcal{F}\right)\right)\exp\left(\beta_1\left(\frac{\mathcal{Y}_1}{\mathcal{Y}_{\infty,1}}\right)^{n_1}\right)+\frac{2}{3}\alpha_1\hat{\lambda}_1\mathcal{F}\mathcal{S}_1^2, \tag{3.59}$$

$$\hat{\mu}_{e2,0}=\hat{D}_2\,\exp\left(\hat{H}_2\left(1-\mathcal{F}\right)\right)\exp\left(\beta_2\left(\frac{\mathcal{Y}_2}{\mathcal{Y}_{\infty,2}}\right)^{n_2}\right)+\frac{2}{3}\alpha_2\hat{\lambda}_2\mathcal{F}\mathcal{S}_2^2. \tag{3.60}$$

In addition, the one–dimensional model of the melt spinning of semi–crystalline compound fibres is subject to the following boundary conditions:

- Geometry

$$\mathcal{R}_i(0)=\mathcal{R}_{i0},\qquad i=1,2, \tag{3.61}$$

- Axial velocity

$$\mathcal{B}(0)=\mathcal{B}_0,\qquad \mathcal{B}(1)=D_r\cdot\mathcal{B}_0, \tag{3.62}$$

- Temperature

  Equation (3.55) represents a two–point boundary value problem which is to be solved subject to a Dirichlet boundary condition at the die exit and a boundary condition at the take–up point. A plausible downstream boundary condition for the temperature is no heat flux at the downstream boundary,

$$\mathcal{F}(0)=\mathcal{F}_0,\qquad \frac{d\mathcal{F}}{d\hat{x}}(1)=0\quad\text{(when axial conduction is considered)}, \tag{3.63}$$

- Molecular orientation order parameter

$$\mathcal{S}_i(0) = \mathcal{S}_{i0}, \qquad i = 1, 2, \tag{3.64}$$

- Degree of crystallization

$$\mathcal{Y}_i(0) = \mathcal{Y}_{i0}, \qquad i = 1, 2, \tag{3.65}$$

where D_r is the draw ratio defined in § 1.1.1.

The molecular orientation (Eq. (3.57)) is affected by the axial velocity component, $\mathcal{B}$, and affects the degree of crystallization through Eq. (3.58); both the orientation and crystallization affect the axial velocity component (Eq. (3.54)) through the effective dynamic viscosities (Eqs. (3.59) and (3.60)), and, of course, the compound fibre's geometry (Eq. (3.53)) and temperature (Eq. (3.55) or Eq. (3.56)) are affected by the axial velocity component. This implies that the orientation and crystallization of the compound fibre are non–linearly coupled with the fibre's geometry, axial velocity component and temperature, and that Eqs. (3.53)–(3.58) must be solved numerically in an iterative fashion.

3.4.1 *1D Analytical solutions for steady, isothermal, amorphous compound fibres*

For steady, compound fibres, Eq. (3.53) has the following solutions

$$\mathcal{B}\mathcal{A}_1 = Q_1, \qquad \mathcal{B}\mathcal{A}_2 = Q_2, \tag{3.66}$$

where Q_1 and Q_2 denote the (constant) non–dimensional volumetric flow rates of the inner and outer jets, respectively whereas the total one is obtained from the sum of both terms $Q_1 + Q_2 = Q$.

If the effective dynamic viscosity is assumed to be constant (independent of the temperature, degree of crystallization and molecular orientation), one can obtain analytical solutions for simple flows [124].

Viscous regime. This regime is characterized by $\bar{R} = 0$ and finite values of $\bar{F}$, and no surface tension ($1/\bar{C} = 0$), i.e., Eq. (3.54) becomes

$$\frac{d}{d\hat{x}}\left\{3\left(\hat{\mu}_{1,0}\mathcal{A}_1 + \hat{\mu}_{2,0}\mathcal{A}_2\right)\frac{d\mathcal{B}}{d\hat{x}}\right\} = 0, \tag{3.67}$$

and has the following solution

$$\mathcal{B}(\hat{x}) = \exp\left(\delta + \frac{\chi}{2}\hat{x}\right), \tag{3.68}$$

where χ and δ are integration constants which can be easily determined from the conditions given by Eq. (3.62). Note that $\delta = \ln(\mathcal{B}_0)$ and $\chi = 2\,\ln(D_r)$. The values of $\mathcal{R}_1$ and $\mathcal{R}_2$ can be easily determined from Eq. (3.23) as

$$\mathcal{R}_1(\hat{x}) = \sqrt{2Q_1}\,\exp\left(-\tfrac{1}{2}\left(\delta + \tfrac{\chi}{2}\hat{x}\right)\right), \tag{3.69}$$

$$\mathcal{R}_2(\hat{x}) = \sqrt{2Q}\,\exp\left(-\tfrac{1}{2}\left(\delta + \tfrac{\chi}{2}\hat{x}\right)\right). \tag{3.70}$$

This simple solution has been used for validating the numerical method developed for solving more complex flow regimes.

Viscous–capillary regime. This regime is characterized by Eq.(3.66), and $\bar{R} = 0$ and $\frac{\bar{R}}{\bar{F}} = 0$, i.e., Eq. (3.54) becomes

$$\frac{1}{2\bar{C}}\left(\frac{d\mathcal{R}_2}{d\hat{x}} + \left(\frac{\sigma_1}{\sigma_2}\right)\frac{d\mathcal{R}_1}{\partial\hat{x}}\right) + \frac{d}{d\hat{x}}\left\{3\,\left(\hat{\mu}_{1,0}\mathcal{A}_1 + \hat{\mu}_{2,0}\mathcal{A}_2\right)\frac{d\mathcal{B}}{d\hat{x}}\right\} = 0, \tag{3.71}$$

and has the following solution

$$\mathcal{B}(\hat{x}) = \left(\exp\left(\delta + \frac{\chi}{2}\hat{x}\right) + \frac{Q^*}{\chi}\right)^2, \tag{3.72}$$

where χ and δ are integration constants that depend on the axial velocity at the take–up point, i.e., they depend on $\mathcal{B}(1)$ and

$$Q^* = \left(\frac{1}{\sqrt{18}\,\bar{C}}\right)\frac{\sqrt{Q} + \left(\frac{\sigma_1}{\sigma_2}\right)\sqrt{Q_1}}{\hat{\mu}_{1,0}Q_1 + \hat{\mu}_{2,0}Q_2}. \tag{3.73}$$

The values of $\mathcal{R}_1$ and $\mathcal{R}_2$ can be easily determined from Eq. (3.23), but they are not shown here.

Viscous–gravitationless regime. This regime corresponds to Eq. (3.66), and $\bar{F} = \infty$ and $\bar{R} \neq 0$, i.e., Eq. (3.54) becomes

$$\bar{R}\,\left(\hat{\rho}_1\mathcal{A}_1 + \hat{\rho}_2\mathcal{A}_2\right)\frac{d\mathcal{B}}{d\hat{x}} = \frac{d}{d\hat{x}}\left\{3\,\left(\hat{\mu}_{1,0}\mathcal{A}_1 + \hat{\mu}_{2,0}\mathcal{A}_2\right)\frac{d\mathcal{B}}{d\hat{x}}\right\}, \tag{3.74}$$

which has the following solution

$$\mathcal{B}(\hat{x}) = \left(\frac{\chi}{P}\right)\frac{\exp\left(\delta + \chi\hat{x}\right)}{1 - \exp\left(\delta + \chi\hat{x}\right)}, \tag{3.75}$$

where χ and δ are integration constants which can be easily determined from the conditions for the axial velocity at the die exit and take–up points, and

$$P = \left(\frac{\bar{R}}{3}\right)\frac{\hat{\rho}_1Q_1 + \hat{\rho}_2Q_2}{\hat{\mu}_{1,0}Q_1 + \hat{\mu}_{2,0}Q_2}, \tag{3.76}$$

Viscous–gravitationless–capillary regime. This regime corresponds to Eq. (3.66), and $\bar{R} \neq 0$ and $\frac{\bar{R}}{\bar{F}} = 0$, i.e., Eq. (3.54) becomes

$$\bar{R}\left(\hat{\rho}_1\mathcal{A}_1 + \hat{\rho}_2\mathcal{A}_2\right)\mathcal{B}\frac{d\mathcal{B}}{d\hat{x}} = \frac{1}{2\bar{C}}\left(\frac{d\mathcal{R}_2}{d\hat{x}} + \left(\frac{\sigma_1}{\sigma_2}\right)\frac{d\mathcal{R}_1}{\partial\hat{x}}\right) + \frac{d}{d\hat{x}}\left\{3\left(\hat{\mu}_{1,0}\mathcal{A}_1 + \hat{\mu}_{2,0}\mathcal{A}_2\right)\frac{d\mathcal{B}}{d\hat{x}}\right\}, \tag{3.77}$$

which can be easily integrated upon making the change $\mathcal{B} = z^2$

$$\frac{dz}{Pz^3 + \chi z - Q^*} = \frac{d\hat{x}}{2}, \tag{3.78}$$

and has different solutions depending on the roots of

$$Pz^3 + \chi z - Q^* = 0, \tag{3.79}$$

where P and Q^* have been defined previously.

Let us define $q = \frac{\chi}{3P}$ and $r = -\frac{Q^*}{2P}$. Then, the solution to Eq. (3.78) is

$$\prod_{i=1}^{3}(z - z_i)^{\prod_{j=1,j\neq i}^{3}(z_i - z_j)^{-1}} = \exp\left(\frac{P}{2}\hat{x}\right), \tag{3.80}$$

if $q^3 + r^2 < 0$ and z_i are the different (real) roots of Eq. (3.79)

$$-\frac{1}{2}\frac{1}{(z - z^*)^2} = \delta + \frac{P}{2}\hat{x}, \tag{3.81}$$

which corresponds to $q^3 + r^2 = 0$ and three identical (real) roots (z^*) of Eq. (3.79),

$$\left(\frac{z - z_1}{z - z_2}\right)^{\frac{1}{(z_2 - z_1)^2}} \exp\left(\frac{(z_2 - z_1)}{(z - z_1)}\right) = \delta \exp\left(\frac{P}{2}(z_2 - z_1)^2\hat{x}\right), \tag{3.82}$$

which corresponds to $q^3 + r^2 = 0$ and two identical (real) roots z_1 and another different (real) root z_2 of Eq. (3.79), and

$$-\frac{1}{(z_1 - z_r)^2 + z_i^2}\left(\frac{z_1 - z_r}{z_i}\arctan\frac{z - z_r}{z_i} + \ln\frac{\left((z - z_r)^2 + z_i^2\right)^{\frac{1}{2}}}{z - z_1}\right) = \delta + \frac{P}{2}\hat{x}, \tag{3.83}$$

which corresponds to $q^3 + r^2 > 0$, a real root (z_1) and two complex conjugate ones ($z_r \pm \mathrm{i}z_i$), $\mathrm{i}^2 = -1$, of Eq. (3.79), and χ and δ are integration constants which can be determined from $\mathcal{B}(0) = \mathcal{B}_0$ and depend on the value of the take–up velocity, i.e., $\mathcal{B}(1)$ or D_r.

For the temperature, the boundary condition at the downstream does not allow us to obtain closed–form analytical solutions to Eq. (3.55). However, if axial conduction is neglected and $\bar{St} \equiv \frac{\mathcal{B}}{\bar{P}} = O(1)$, where $\bar{St}$ is the STANTON number, Eq. (3.55) becomes a first–order ordinary differential equation (cf. Eq. (3.56)) whose solution may be written as

$$\mathcal{F}(\hat{x}) = \mathcal{F}_{\infty,2} + C\exp\left(-\frac{St}{\hat{\rho}_1\hat{C}_1Q_1 + \hat{\rho}_2\hat{C}_2Q_2}\int_0^{\hat{x}}\hat{h}_2\,\mathcal{R}_2(\zeta)d\zeta\right), \tag{3.84}$$

where the constant C can be easily determined from the condition at the die exit, i.e., $\mathcal{F}(0) = \mathcal{F}_0$, as $C = (\mathcal{F}_0 - \mathcal{F}_{\infty,2})$.

For the viscous flow regime considered above, the leading–order temperature of the compound fibre (assuming a constant value of $\hat{h}_2$) may be written as

$$\frac{\mathcal{F}(\hat{x}) - \mathcal{F}_{\infty,2}}{\mathcal{F}_0 - \mathcal{F}_{\infty,2}} = \exp\left\{-\frac{St\,\hat{h}_2}{\hat{\rho}_1\hat{C}_1Q_1 + \hat{\rho}_2\hat{C}_2Q_2}\sqrt{2Q}\left(\frac{4}{\chi}\right)\exp\left(-\frac{1}{2}\delta\right)\left[1 - \exp\left(-\frac{\chi}{4}\hat{x}\right)\right]\right\}. \quad (3.85)$$

For $\chi << 1$, a Taylor's series expansion of the inner exponential in Eq. (3.85) shows that the temperature decreases in an exponential fashion along the fibre axis and the rate of decrease increases as $\bar{B}$ is increased. Moreover, in the absence of swelling, the integral in Eq. (3.84) has the following upper and lower bounds $\mathcal{R}_2(0)\,L$ and $\mathcal{R}_2(1)\,L$, respectively, which also indicate that the temperature decreases in an exponential fashion along the fibre axis and its rate of decrease increases as $\bar{B}$ is increased.

Analytical solutions can also be obtained whenever axial conduction is neglected for the steady flow regimes considered previously in the present Subsection.

Moreover, if $\phi_i = 0$ in Eq. (3.57), then the resulting equation can be written as $\frac{d\mathcal{S}}{dy} = (1-\mathcal{S})(1+2\mathcal{S})$ where $y = \ln\mathcal{B}$ and the subscript i has been dropped, and has fixed points at $\mathcal{S} = 1$ and $\mathcal{S} = -\frac{1}{2}$ which are stable and unstable, respectively, and, since $\mathcal{S} \geq 0$, it can be easily shown that the solution to this equation evolves towards $\mathcal{S} = 1$. Moreover, this equation can be integrated analytically subject to, say, $\mathcal{S}(0) = \mathcal{S}_0$, to yield the molecular orientation as a function of the leading–order axial velocity component as

$$\mathcal{B}(\mathcal{S}) = \mathcal{B}_0\left(\frac{(1+2\mathcal{S}_0)^2}{1-\mathcal{S}_0}\right)^{-1/3}\left(\frac{(1+2\mathcal{S})^2}{1-\mathcal{S}}\right)^{1/3}, \quad (3.86)$$

from which one can easily obtain $\mathcal{S}(\hat{x}) = \mathcal{S}(\mathcal{B})$ as

$$\mathcal{S}(\mathcal{B}) = \frac{(\mathcal{B}^3 - \mathcal{B}_0^3) + \mathcal{S}_0\cdot(2\,\mathcal{B}^3 + \mathcal{B}_0^3)}{(\mathcal{B}^3 + 2\,\mathcal{B}_0^3) + 2\,\mathcal{S}_0\cdot(\mathcal{B}^3 - \mathcal{B}_0^3)}. \quad (3.87)$$

Furthermore, under the same assumptions as discussed above, Eq. (3.58) can be integrated analytically subject to $\mathcal{Y}(0) = \mathcal{Y}_0$ to yield

$$\frac{\mathcal{Y}(\hat{x}) - \mathcal{Y}_0}{\mathcal{Y}_\infty} = 1 - \exp\left(-\int_0^{\hat{x}}\frac{k_A(\mathcal{S})}{\mathcal{B}(\zeta)}\,d\zeta\right), \quad (3.88)$$

where $k_A(\mathcal{S})$ can be written as $k_A(\mathcal{B})$ upon using $\mathcal{S}(\mathcal{B})$ from Eq. (3.87). Both Eq. (3.87) and Eq. (3.88) indicate that, under the above assumptions, the molecular orientation and crystallization depend on $\mathcal{B}(\hat{x})$ which, in turn, depends in a non–linear fashion on the solutions to Eqs. (3.53)–(3.55).

3.4.2 *Numerical scheme*

In this subsection, a brief description of the numerical method used to solve the set of one–dimensional equations that governs the steady–state fluid–dynamics of melt spinning of semi–crystalline compound fibres is presented.

Firstly, the mass conservation equations (3.53) establish that

$$\frac{d}{d\hat{x}}\left(\mathcal{A}_i(\hat{x})\,\mathcal{B}(\hat{x})\right)=0, \qquad \Rightarrow \qquad A_i(\hat{x})\,\mathcal{B}(\hat{x})=Q_i \qquad i=1,2. \tag{3.89}$$

It must be noted that Q_i (constant) and

$$Q_i=\mathcal{A}_i(0)\,\mathcal{B}(0) \quad \Rightarrow \quad \begin{cases} Q_1=\frac{\mathcal{R}_{10}^2}{2}\,\mathcal{B}_0, \\ Q_2=\frac{\mathcal{R}_{20}^2-\mathcal{R}_{10}^2}{2}\,\mathcal{B}_0. \end{cases} \tag{3.90}$$

Taking into account Eq. (3.90), the axial momentum conservation equation (cf. Eq. (3.54)) can be written as,

$$\begin{aligned} \bar{R}\left(\hat{\rho}_1 Q_1+\hat{\rho}_2 Q_2\right)\frac{d\mathcal{B}}{d\hat{x}} &= \left(\hat{\rho}_1\mathcal{A}_1+\hat{\rho}_2\mathcal{A}_2\right)\frac{\bar{R}}{\bar{F}}+3\,\frac{d}{d\hat{x}}\left(\hat{\mu}_{e1,0}\mathcal{A}_1+\hat{\mu}_{e2,0}\mathcal{A}_2\right)\frac{d\mathcal{B}}{d\hat{x}} \\ &\quad +3\left(\hat{\mu}_{e1,0}\mathcal{A}_1+\hat{\mu}_{e2,0}\mathcal{A}_2\right)\frac{d^2\mathcal{B}}{d\hat{x}^2}+\frac{1}{2\bar{C}}\left(\frac{d\mathcal{R}_2}{d\hat{x}}+\left(\frac{\sigma_1}{\sigma_2}\right)\frac{d\mathcal{R}_1}{d\hat{x}}\right) \end{aligned} \tag{3.91}$$

which can be rewritten as

$$\begin{aligned} \frac{d^2\mathcal{B}}{d\hat{x}^2}+\left\{\frac{d}{d\hat{x}}\left(\ln\Pi_{\mu_e}\right)-\bar{R}\,W\,\frac{1}{3\,\Pi_{\mu_e}}\right\}\frac{d\mathcal{B}}{d\hat{x}} &= -\frac{\Pi_\rho}{3\,\Pi_{\mu_e}}\left(\frac{\bar{R}}{\bar{F}}\right) \\ &\quad -\frac{1}{2\bar{C}}\frac{1}{3\,\Pi_{\mu_e}}\left(\frac{d\mathcal{R}_2}{d\hat{x}}+\left(\frac{\sigma_1}{\sigma_2}\right)\frac{d\mathcal{R}_1}{d\hat{x}}\right) \end{aligned} \tag{3.92}$$

where $W=\hat{\rho}_1 Q_1+\hat{\rho}_2 Q_2$ represents a measurement of the dimensionless mass flow rate of the compound jet and $\Pi_\rho=\hat{\rho}_1\mathcal{A}_1+\hat{\rho}_2\mathcal{A}_2$ and $\Pi_{\mu_e}=\hat{\mu}_{e1,0}\mathcal{A}_1+\hat{\mu}_{e2,0}\mathcal{A}_2$ denote the mean values of the density and dynamic viscosity, respectively.

Equation (3.92) is a linear ordinary differential equation (supposing known $\mathcal{R}_1$ and $\mathcal{R}_2$, and so, $\mathcal{A}_1$ and $\mathcal{A}_2$, and $\mathcal{F}$, $\mathcal{S}$ and $\mathcal{Y}$) for $\mathcal{B}$ that must be solved subject to the Dirichlet boundary conditions given by Eq. (3.62).

Taking into account Eq. (3.90), the energy conservation equation (cf. Eq. (3.55)) may be written as

$$\begin{aligned} \bar{P}\left(\hat{\rho}_1\hat{C}_1 Q_1+\hat{\rho}_2\hat{C}_2 Q_2\right)\frac{d\mathcal{F}}{d\hat{x}} &= \frac{d}{d\hat{x}}\left(\mathcal{A}_1\hat{k}_1+\mathcal{A}_2\hat{k}_2\right)\frac{d\mathcal{F}}{d\hat{x}}+ \\ &\quad \left(\mathcal{A}_1\hat{k}_1+\mathcal{A}_2\hat{k}_2\right)\frac{d^2\mathcal{F}}{d\hat{x}^2}-\bar{B}\hat{h}_2\,\mathcal{R}_2\left(\mathcal{F}-\mathcal{F}_\infty\right), \end{aligned} \tag{3.93}$$

that is rewritten as

$$\frac{d^2\mathcal{F}}{d\hat{x}^2}+\left\{\frac{d}{d\hat{x}}\left(\ln\Pi_k\right)-\bar{P}\,W_C\,\frac{1}{\Pi_k}\right\}\frac{d\mathcal{F}}{d\hat{x}}-\bar{B}\hat{h}_2\,\frac{1}{\Pi_k}\,\mathcal{R}_2\,\mathcal{F}=-\bar{B}\,\frac{1}{\Pi_k}\,\mathcal{R}_2\,\mathcal{F}_{\infty,2}, \tag{3.94}$$

where $W_C = \hat{\rho}_1 \hat{C}_1 Q_1 + \hat{\rho}_2 \hat{C}_2 Q_2$ and $\Pi_k = \hat{k}_1 \mathcal{A}_1 + \hat{k}_2 \mathcal{A}_2$.

Equation (3.94) is a linear ordinary differential equation for $\mathcal{F}$ which must be solved under the boundary conditions given by Eq. (3.63).

The next instructions flow may be used for solving the coupled non–linear problem:

1. Use as seed for the axial velocity, $\mathcal{B}^{(0)}(\hat{x})$, the solution of the isothermal viscous regime (cf. Eq. (3.68)) characterized by $(\bar{R} = 0, \bar{C} \to \infty)$ and a finite (non–zero) value of $\bar{F}$. Likewise, the temperature, $\mathcal{F}^{(n)}(\hat{x})$, and molecular orientation order parameter, $\mathcal{S}_i^{(n)}(\hat{x})$, and degree of crystallization, $\mathcal{Y}_i^{(n)}(\hat{x})$, of the compound jet are guessed by using boundary conditions at the die–exit and imposing a flat axial profile for each variable (a linear one can be also imposed).
2. Calculate the compound fibre geometry $\mathcal{A}_1^{(n)}, \mathcal{A}_2^{(n)}, \mathcal{R}_1^{(n)}, \mathcal{R}_2^{(n)}$ using Eq. (3.89)–(3.90).
3. Determine the effective dynamic viscosity $\hat{\mu}_{ei,0}^{(n)} = f(\mathcal{F}^{(n)}, \mathcal{S}^{(n)}, \mathcal{Y}^{(n)})$ of the inner and outer jets.
4. Calculate the new axial velocity $\mathcal{B}^{(n+1)}(\hat{x})$ using Eq. (3.92).
5. Determine the new temperature profile, $\mathcal{F}^{(n+1)}(\hat{x})$, of the compound jet using Eq. (3.94).
6. Update the molecular orientation order parameter, $\mathcal{S}_i^{(n+1)}(\hat{x})$, using Eqs. (3.57) and degree of crystallization, $\mathcal{Y}_i^{(n+1)}(\hat{x})$, (cf. Eqs. (3.58)) of the core and cladding.
7. Iterate until specified convergence criteria are satisfied.

The steady–state solution is obtained numerically by means of an implicit finite difference method (scheme solved iteratively) that discretizes the advection–type terms by means of first–order accurate upwind difference expressions while second–order accurate differences are used to discretize the diffusion terms. In order to obtain grid independent results, the number of nodes in the non–dimensional axial direction $(\hat{x})$, N_x, must be at least 1001, which corresponds to an equispaced size grid of $\Delta\hat{x} = 1 \times 10^{-3}$.

Due to the non–linear coupling between fibre geometry, axial velocity, temperature, molecular orientation order parameter and degree of crystallization, an under–relaxation factor equal to $f_\psi = 0.5$,

$$\psi^{(n+1)} = f_\psi \, \psi^{(n)} + (1 - f_\psi) \, \psi^{(n+1)}, \qquad n = 0, 1, \ldots, N, \tag{3.95}$$

has been employed for each of these variables (N indicates the maximum number of iterations) in order to ensure convergence criteria which has been set to

$$L_2(\psi) = \sqrt{\frac{1}{N_x} \sum_{j=1}^{N_x} \left(\psi_j^{(n+1)} - \psi_j^{(n)} \right)^2} \leq \mathrm{TOL}, \tag{3.96}$$

where n is the n–th iteration, and ψ represents any of the unknowns of the problem, i .e., $\mathcal{B}$, $\mathcal{F}$, $\mathcal{S}_i$ and $\mathcal{Y}_i$. Typical values of N and TOL enough to reach convergence are 1000 and 10^{-8}, respectively.

3.5 1–D STEADY–STATE MODEL FOR SEMI–CRYSTALLINE HOLLOW COMPOUND FIBRE

In this subsection, we summarize the 1–D model of the melt spinning of hollow compound fibres that includes the effects of orientation and crystallization. The contribution of both the gases surrounding and enclosed by the hollow compound jet to the drag on the fibre to the leading–order momentum equation has been neglected. The one–dimensional model for hollow compound jet requires the numerical solution of the following equations (cf. Eqs. (3.34), (3.35) and (3.44))

$$\frac{d}{d\hat{x}}(\mathcal{B}\mathcal{A}_1) = 0, \qquad \frac{d}{d\hat{x}}(\mathcal{B}\mathcal{A}_2) = 0, \qquad \frac{d}{d\hat{x}}\left(\mathcal{B}\frac{\mathcal{R}_1^2}{2}\right) = \mathcal{C}(\hat{x}), \tag{3.97}$$

where $\mathcal{C}(\hat{x})$ was defined in Eq. (3.39),

$$\begin{aligned}\bar{R}\left(\hat{\rho}_1\mathcal{A}_1 + \hat{\rho}_2\mathcal{A}_2\right)\mathcal{B}\frac{d\mathcal{B}}{d\hat{x}} = \left(\hat{\rho}_1\mathcal{A}_1 + \hat{\rho}_2\mathcal{A}_2\right)\frac{\bar{R}}{\bar{F}} - \mathcal{A}_1\frac{d\mathcal{D}_1}{d\hat{x}} - \mathcal{A}_2\frac{d\mathcal{D}_2}{d\hat{x}} \\ + \frac{d}{d\hat{x}}\left\{3\left(\hat{\mu}_{e1,0}\mathcal{A}_1 + \hat{\mu}_{e2,0}\mathcal{A}_2\right)\frac{d\mathcal{B}}{d\hat{x}}\right\} \\ + 2\,\mathcal{C}(\hat{x})\left(\hat{\mu}_{e1,0}\frac{d\mathcal{A}_1}{d\hat{x}} + \hat{\mu}_{e2,0}\frac{d\mathcal{A}_2}{d\hat{x}}\right),\end{aligned} \tag{3.98}$$

where $\mathcal{D}_1$ and $\mathcal{D}_2$ are given by Eqs. (3.36) and (3.37), respectively,

$$\begin{aligned}\bar{P}\left(\hat{\rho}_1\hat{C}_1\mathcal{A}_1 + \hat{\rho}_2\hat{C}_2\mathcal{A}_2\right)\mathcal{B}\frac{d\mathcal{F}}{d\hat{x}} = \frac{d}{d\hat{x}}\left(\left(\mathcal{A}_1\hat{k}_1 + \mathcal{A}_2\hat{k}_2\right)\frac{d\mathcal{F}}{d\hat{x}}\right) \\ -\bar{B}\left[\hat{h}_2\,\mathcal{R}_2\left(\mathcal{F} - \mathcal{F}_{\infty,2}\right) + \hat{h}_1\,\mathcal{R}_0\left(\mathcal{F} - \mathcal{F}_{\infty,1}\right)\right],\end{aligned} \tag{3.99}$$

when axial conduction is accounted for, or

$$\bar{P}\left(\hat{\rho}_1\hat{C}_1\mathcal{A}_1 + \hat{\rho}_2\hat{C}_2\mathcal{A}_2\right)\mathcal{B}\frac{d\mathcal{F}}{d\hat{x}} = -\bar{B}\left[\hat{h}_2\,\mathcal{R}_2\left(\mathcal{F} - \mathcal{F}_{\infty,2}\right) + \hat{h}_1\,\mathcal{R}_0\left(\mathcal{F} - \mathcal{F}_{\infty,1}\right)\right], \tag{3.100}$$

when axial conduction is neglected.

For the molecular orientation order parameter and degree of crystallization, the model presented for compound semi–crystalline fibres in § 3.4 has been adopted. This model is given by Eqs. (3.57)–(3.58).

In addition, the one–dimensional model of the melt spinning of semi–crystalline hollow compound fibres is subject to the same boundary conditions as for compound fibres, and, therefore, a similar numerical method to that developed in § 3.4.2 was used to solve its governing equations.

4

TWO–DIMENSIONAL MODEL OF STEADY–STATE FIBRE FORMATION IN MELT SPINNING PROCESSES

Contents

4.1 2–D STEADY–STATE MODEL FOR SEMI–CRYSTALLINE COMPOUND FIBRES

The asymptotic analysis developed in § 3.1 shows that, for slender fibres at low Reynolds and Biot numbers, the temperature is uniform across the compound fibre at leading–order in the slenderness ratio, ϵ. This assumption is valid for the small Biot numbers employed in the asymptotic analysis, but it is not expected to be valid near the compound fibre's outer interface, i.e., at $\mathcal{R}_2$, where a thermal boundary layer may form.

It must be noted that, if one were to continue with the asymptotic analysis at higher orders in the slenderness ratio, one would obtain corrections to the velocity and temperature fields that depend on $\hat{r}$, $\hat{t}$ and $\hat{x}$. However, such a radial dependence is only observed at $O(\epsilon^2)$ in the asymptotic expansion and, therefore, it is expected to be small. Moreover, the algebra involved in deriving these second–order approximations is too cumbersome compared with the two–dimensional model developed in this work.

The hybrid steady–state model developed in this work, which we also called a $1+1/2$–D model, consists of solving the one–dimensional mass and linear momentum equations (Eqs. (3.53) and (3.54)) that govern the geometry and axial velocity of the compound jet at leading–order, respectively, and which were obtained with an asymptotic analysis using the fibre slenderness ratio, ϵ, as a perturbation parameter, together with the two–dimensional energy equation, i.e., Eq. (2.58), and two–dimensional equations for the degree of crystallization, e.g., [7, 33, 64], and the components of the diagonal molecular orientation tensor.

In this model, the first term in the right–hand side of Eq. (2.58) has been neglected

$$\bar{P}\left(\frac{\hat{\rho}_i\hat{C}_i}{\hat{k}_i}\right)\left(\hat{u}_{i,0}\frac{\partial\hat{T}_i}{\partial\hat{x}}+\hat{v}_{i,0}\frac{\partial\hat{T}_i}{\partial\hat{r}}\right)=\frac{1}{\hat{r}}\frac{\partial}{\partial\hat{r}}\left(\hat{r}\,\frac{\partial\hat{T}_i}{\partial\hat{r}}\right),\qquad i=1,2, \tag{4.1}$$

where $\bar{P}=\epsilon\,Pe=O(1)$ and $\hat{T}_i$ is a function depending of $\hat{r}$ and $\hat{x}$.

By approximating in Eq. (4.1), $\hat{u}_{i,0}$ and $\hat{v}_{i,0}$ by $\mathcal{B}$ and Eq. (3.20), respectively, one obtains a parabolic partial differential equation for the temperature field which uses the velocity profile from the leading–order asymptotic analysis of slender compound fibres. Note that the neglect of the first term in the right–hand side of Eq. (2.58) is a valid approximation for the slender fibres considered in this study.

Upon non–dimensionalization and using the results of the previous chapters, the two–dimensional steady–state equations for the components of the molecular orientation tensor and degree of crystallization can be written as

$$\begin{aligned}\left(\hat{u}_{i,0}\frac{\partial s_{ir}}{\partial\hat{x}}+\hat{v}_{i,0}\frac{\partial s_{ir}}{\partial\hat{r}}\right)&=(1-s_{ir})\,(1+s_{ix})\,\frac{d\mathcal{B}}{d\hat{x}}\\&\quad-\frac{\phi_i}{\hat{\lambda}_i}\left\{s_{ir}-\frac{N_i}{3}\left[(1-s_{ir})\,(s_{ir}+3\,\Pi_{i,s})\right]\right\},\qquad i=1,2,\end{aligned} \tag{4.2}$$

$$\begin{aligned}\left(\hat{u}_{i,0}\frac{\partial s_{ix}}{\partial\hat{x}}+\hat{v}_{i,0}\frac{\partial s_{ix}}{\partial\hat{r}}\right)&=(s_{ix}+1)\,(2-s_{ix})\,\frac{d\mathcal{B}}{d\hat{x}}\\&\quad-\frac{\phi_i}{\hat{\lambda}_i}\left\{s_{ix}-\frac{N_i}{3}\left[(s_{ix}+1)\,(s_{ix}-3\,\Pi_{i,s})\right]\right\},\qquad i=1,2,\end{aligned} \tag{4.3}$$

$$\left(\hat{u}_{i,0}\frac{\partial\mathcal{Y}_i}{\partial\hat{x}}+\hat{v}_{i,0}\frac{\partial\mathcal{Y}_i}{\partial\hat{r}}\right)=k_{Ai}(0)\exp\left(a_{2i}\mathcal{S}_i^2\right)(\mathcal{Y}_{\infty,i}-\mathcal{Y}_i),\qquad i=1,2, \tag{4.4}$$

where s_{ir} and s_{ix} and $\mathcal{Y}_i$ are functions that depend on $\hat{r}$ and $\hat{x}$.

It must be noted that because of the hyperbolic nature of the equations that govern both molecular orientation and degree of crystallization of semi–crystalline fibres, it is not possible to impose any boundary condition for these variables at the interface $\hat{r}=\hat{R}_1(\hat{x})$. This weakness suggests that this model may not be the most adequate since one expects that polymers may mix at this interface. However, we shall use this model in this work.

Equations (4.2) and (4.3) are first–order quasilinear partial differential equations while Eq. (4.4) is a linear one. These three equations can be written as

$$\left(\hat{u}_{i,0}\frac{\partial\Omega_i}{\partial\hat{x}}+\hat{v}_{i,0}\frac{\partial\Omega_i}{\partial\hat{r}}\right)=\mathcal{U}(\hat{r},\hat{x}),\qquad i=1,2, \tag{4.5}$$

and their solutions can be obtained (using the leading–order velocity) as

$$\frac{d\hat{x}}{\mathcal{B}}=\frac{d\hat{r}}{-\frac{\hat{r}}{2}\frac{d\mathcal{B}}{d\hat{x}}}=\frac{d\Omega}{\mathcal{U}}. \tag{4.6}$$

Integration of Eq. (4.6) yields

$$\frac{d\hat{r}}{d\hat{x}} = -\frac{\hat{r}}{2}\frac{1}{\mathcal{B}}\frac{d\mathcal{B}}{d\hat{x}} \qquad \Rightarrow \qquad \mathcal{B}\,\hat{r}^2 = \vartheta \tag{4.7}$$

$$\frac{d\Omega}{d\hat{x}} = \frac{\mathcal{U}}{\mathcal{B}} \tag{4.8}$$

where ϑ is a constant of integration. Therefore, these equations could be integrated by the method of characteristics. Because of their first–order and depending on the boundary conditions at $\hat{x} = 0$, the molecular orientation and crystallinity may not be continuous at the core–cladding interface.

The fact that $\mathcal{B}\,\hat{r}^2$ is constant will be used later when integrating these three equations as well as that for the temperature of the core and cladding.

Since the effective dynamic viscosity depends on the two–dimensional fields of $\hat{T}$, $\mathcal{Y}$ and $\mathcal{S}$, the dynamic viscosity that appears in Eq. (3.54) becomes

$$< \hat{\mu}_{e1} > (\hat{x}) = \frac{1}{\mathcal{A}_1}\int_0^{\mathcal{R}_1} \hat{\mu}_{e1,0}(\hat{r},\hat{x})\,\hat{r}\,d\hat{r}, \tag{4.9}$$

$$< \hat{\mu}_{e2} > (\hat{x}) = \frac{1}{\mathcal{A}_2}\int_{\mathcal{R}_1}^{\mathcal{R}_2} \hat{\mu}_{e2,0}(\hat{r},\hat{x})\,\hat{r}\,d\hat{r}. \tag{4.10}$$

Likewise, a global cross–sectionally averaged dynamic viscosity may be defined as

$$< \hat{\mu}_{e} > (\hat{x}) = \frac{1}{\mathcal{A}}\int_0^{\mathcal{R}_2} \hat{\mu}_{e}(\hat{r},\hat{x})\,\hat{r}\,d\hat{r}, \tag{4.11}$$

where $\mathcal{A} = \mathcal{A}_1 + \mathcal{A}_2$, which indicates that

$$\mathcal{A} < \hat{\mu}_e > (\hat{x}) = \mathcal{A}_1 < \hat{\mu}_{e1} > (\hat{x}) + \mathcal{A}_2 < \hat{\mu}_{e2} > (\hat{x}). \tag{4.12}$$

In this manner, Eq. (3.54) becomes

$$\bar{R}\,(\hat{\rho}_1\mathcal{A}_1 + \hat{\rho}_2\mathcal{A}_2)\,\mathcal{B}\frac{d\mathcal{B}}{d\hat{x}} = (\hat{\rho}_1\mathcal{A}_1 + \hat{\rho}_2\mathcal{A}_2)\,\frac{\bar{R}}{\bar{F}} + \frac{1}{2\bar{C}}\left(\frac{d\mathcal{R}_2}{d\hat{x}} + \left(\frac{\sigma_1}{\sigma_2}\right)\frac{d\mathcal{R}_1}{d\hat{x}}\right) + \frac{d}{d\hat{x}}\left\{3\,(< \hat{\mu}_{e1,0} > \mathcal{A}_1 + < \hat{\mu}_{e2,0} > \mathcal{A}_2)\,\frac{d\mathcal{B}}{d\hat{x}}\right\}. \tag{4.13}$$

Equations (4.2)–(4.3) and Eqs. (4.1), (4.4) and (3.66) and (4.13) represent the two–dimensional model for the fluid dynamics of semi–crystalline compound fibres developed in this study and are subject to specified conditions at the maximum swell cross–section, $\hat{x} = 0$,

- Axial velocity

$$\mathcal{B}(0) = \mathcal{B}_0, \tag{4.14}$$

- Temperature profile

$$\hat{T}_i(\hat{r},0) = \hat{T}_{i0}(\hat{r}), \tag{4.15}$$

- Molecular orientation order parameter profile

$$s_{i\,r}(\hat{r},0) = \mathcal{S}_{i0}(\hat{r}), \tag{4.16}$$
$$s_{i\,x}(\hat{r},0) = 2\,\mathcal{S}_{i0}(\hat{r}), \tag{4.17}$$

- Degree of crystallization profile

$$\mathcal{Y}_i(\hat{r},0) = \mathcal{Y}_{i0}(\hat{r}) \qquad i = 1,2, \tag{4.18}$$

downstream or take–up location, $\hat{x} = 1$,

$$\mathcal{B}(1) = D_r \cdot \mathcal{B}_0, \tag{4.19}$$

and symmetry boundary conditions at the centreline, $\hat{r} = 0$,

$$\frac{\partial \hat{T}_1}{\partial \hat{r}} = 0. \tag{4.20}$$

In addition, at the core–cladding interface, $\hat{r} = \mathcal{R}_1(\hat{x})$, there is continuity of temperature and heat flux, i.e.,

$$\hat{T}_1 = \hat{T}_2, \tag{4.21}$$

$$\hat{k}_1 \frac{\partial \hat{T}_1}{\partial \hat{r}} = \hat{k}_2 \frac{\partial \hat{T}_2}{\partial \hat{r}}, \tag{4.22}$$

while, at the cladding–surroundings interface, $\hat{r} = \mathcal{R}_2(\hat{x})$, the non–dimensional form of the thermal boundary condition is

$$-\frac{\partial \hat{T}_2}{\partial \hat{r}}\,(\mathcal{R}_2,\hat{x}) = Bi_2\left(\hat{T}_2(\mathcal{R}_2,\hat{x}) - \hat{T}_{\infty,2}\right), \tag{4.23}$$

where a term proportional to ϵ in the left hand–side has been neglected and $Bi_2 = \frac{\hat{h}_2}{\hat{k}_2}\,Bi$ depends on the film heat transfer coefficient $\hat{h}_2$ and the thermal conductivity of the cladding.

4.1.1 *Numerical method. Mapping*

In this work, we shall only be concerned with steady state conditions, and the numerical solution of the equations governing the two–dimensional free–surface model for semi–crystalline compound fibres presented above was obtained as follows. First, the following transformation $(\hat{r},\hat{x}) \to (\xi,\eta)$ for the inner and outer jets, where $\xi(\hat{r},\hat{x}) = \frac{\hat{r}}{\mathcal{R}_2(\hat{x})}$ and $\eta(\hat{r},\hat{x}) = \hat{x}$, was employed to map the curvilinear geometries of the inner and outer fibres into rectangles, i.e., $[0,\mathcal{R}_1(\hat{x})] \to [0,\sqrt{Q_1/Q}]$ and $[\mathcal{R}_1(\hat{x}),\mathcal{R}_2(\hat{x})] \to [\sqrt{Q_1/Q},1]$, respectively.

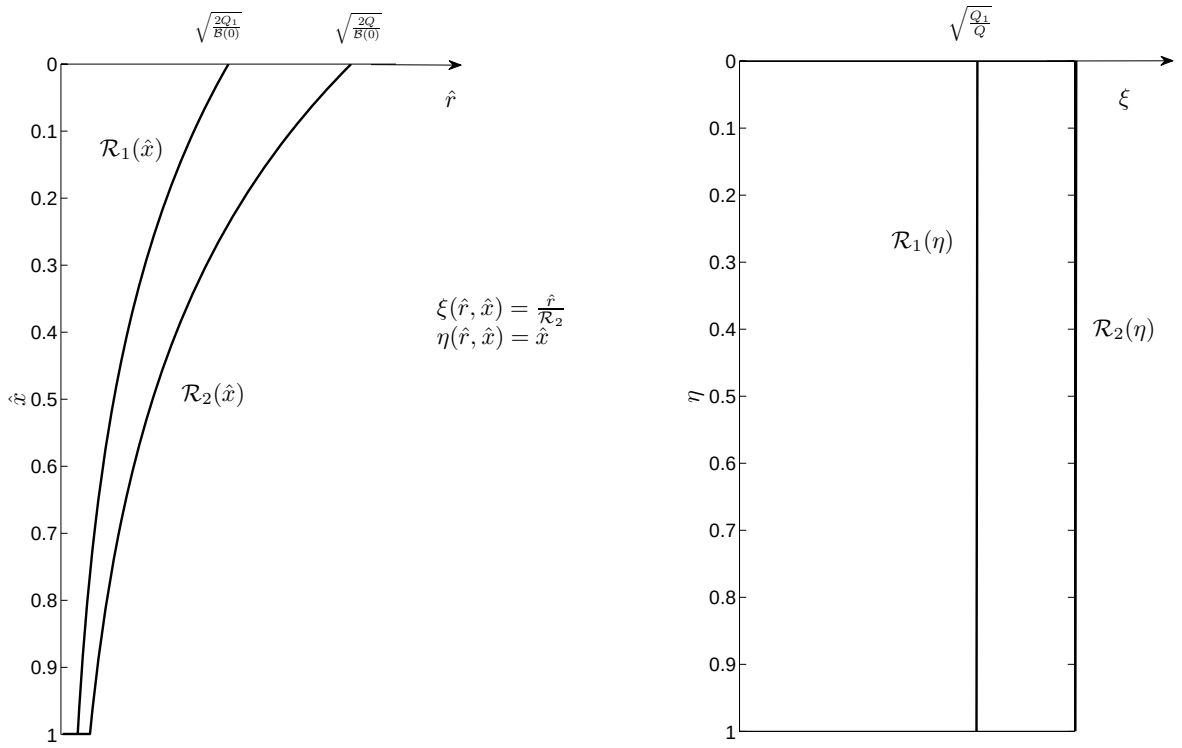

Figure 4.1: *Mapping between the physical domain* $(\hat{r}, \hat{x})$ *and the computational one* (ξ, η) *for compound fibres.*

Using this mapping, the differential operators can be written in the transformed domain taking into account the chain rule as

$$\frac{\partial}{\partial \hat{x}} = \frac{\partial \xi}{\partial \hat{x}}\frac{\partial}{\partial \xi} + \frac{\partial \eta}{\partial \hat{x}}\frac{\partial}{\partial \eta} = -\frac{\xi}{\mathcal{R}_2(\eta)}\frac{d\mathcal{R}_2(\eta)}{d\eta}\frac{\partial}{\partial \xi} + \frac{\partial}{\partial \eta}, \tag{4.24}$$

$$\frac{\partial}{\partial \hat{r}} = \frac{\partial \xi}{\partial \hat{r}}\frac{\partial}{\partial \xi} + \frac{\partial \eta}{\partial \hat{r}}\frac{\partial}{\partial \eta} = \frac{1}{\mathcal{R}_2(\eta)}\frac{\partial}{\partial \xi}. \tag{4.25}$$

The convective operator, $\mathfrak{L}$, that appears in Eqs. (4.1)–(4.4) may be written as

$$\mathfrak{L} = \hat{u}_{i,0}\frac{\partial}{\partial \hat{x}} + \hat{v}_{i,0}\frac{\partial}{\partial \hat{r}} = \mathcal{B}(\eta)\frac{\partial}{\partial \eta}, \tag{4.26}$$

where the continuity equation (cf. Eq. (3.23)), i.e.,

$$\frac{d}{d\eta}\left(\mathcal{B}(\eta)\frac{\mathcal{R}_2^2(\eta)}{2}\right) = \frac{d}{d\eta}\left(\mathcal{A}\,\mathcal{B}\right) = 0, \tag{4.27}$$

has been used.

Furthermore, the $\mathfrak{N}$ operator that appears in the energy equation (cf. (4.1)) can be written as

$$\mathfrak{N} \equiv \frac{1}{\hat{r}}\frac{\partial}{\partial \hat{r}}\left(\hat{r}\frac{\partial}{\partial \hat{r}}\right) = \frac{1}{\mathcal{R}_2\,\xi}\frac{1}{\mathcal{R}_2}\frac{\partial}{\partial \xi}\left(\mathcal{R}_2\,\xi\frac{1}{\mathcal{R}_2}\frac{\partial}{\partial \xi}\right) = \frac{1}{2\,\mathcal{A}}\frac{1}{\xi}\frac{\partial}{\partial \xi}\left(\xi\frac{\partial}{\partial \xi}\right). \tag{4.28}$$

In this manner, both the energy conservation equation and the equations that model the molecular orientation tensor components and degree of crystallization in the computational domain can be written as

$$\frac{\partial \hat{T}_i}{\partial \eta} = \frac{1}{2\,Q}\frac{1}{\bar{P}_i}\frac{1}{\xi}\frac{\partial}{\partial \xi}\left(\xi \frac{\partial \hat{T}_i}{\partial \xi}\right) \qquad i = 1, 2, \tag{4.29}$$

$$\begin{aligned}\mathcal{B}\,\frac{\partial s_{i\,r}}{\partial \eta} &= (1 - s_{i\,r})\,(1 + s_{i\,x})\,\frac{d\mathcal{B}}{d\eta} \\ &\quad - \frac{\phi_i}{\hat{\lambda}_i}\left\{s_{i\,r} - \frac{N_i}{3}\left[(1 - s_{i\,r})\,(s_{i\,r} + 3\,\Pi_{i,s})\right]\right\}, \qquad i = 1, 2,\end{aligned} \tag{4.30}$$

$$\begin{aligned}\mathcal{B}\,\frac{\partial s_{i\,x}}{\partial \eta} &= (s_{i\,x} + 1)\,(2 - s_{i\,x})\,\frac{d\mathcal{B}}{d\eta} \\ &\quad - \frac{\phi_i}{\hat{\lambda}_i}\left\{s_{i\,x} - \frac{N_i}{3}\left[(s_{i\,x} + 1)\,(s_{i\,x} - 3\,\Pi_{i,s})\right]\right\}, \qquad i = 1, 2,\end{aligned} \tag{4.31}$$

$$\mathcal{B}\,\frac{\partial \mathcal{Y}_i}{\partial \eta} = k_{Ai}(0)\exp\left(a_{2i}\mathcal{S}_i^2\right)(\mathcal{Y}_{\infty,i} - \mathcal{Y}_i), \qquad i = 1, 2, \tag{4.32}$$

where $\bar{P}_i = \bar{P}\left(\frac{\hat{\rho}_i \hat{C}_i}{\hat{k}_i}\right)$.

The boundary conditions in the transformed (computational) domain are

- Temperature of the jets

$$\hat{T}_i(\xi, 0) = \hat{T}_{i0}(\xi) \qquad i = 1, 2, \tag{4.33}$$

- Thermal boundary condition at the symmetry axis ($\xi = 0$)

$$\frac{\partial \hat{T}_1}{\partial \xi} = 0, \tag{4.34}$$

- Boundary conditions for the temperature at the core–cladding interface $\left(\xi = \sqrt{\frac{Q_1}{Q}}\right)$

$$\hat{T}_1 = \hat{T}_2, \tag{4.35}$$

$$\hat{k}_1\,\frac{\partial \hat{T}_1}{\partial \xi} = \hat{k}_2\,\frac{\partial \hat{T}_2}{\partial \xi}, \tag{4.36}$$

- Boundary condition for the temperature at the cladding–surrounding interface ($\xi = 1$)

$$\frac{\partial \hat{T}_2}{\partial \xi} + Bi_2\,\mathcal{R}_2\,\hat{T}_2 = Bi_2\,\mathcal{R}_2\,\hat{T}_{\infty,2}, \tag{4.37}$$

- Components of the molecular orientation tensor

$$s_{i\,r}(\xi,0) = \mathcal{S}_{i0}(\xi), \qquad i = 1,2, \tag{4.38}$$

$$s_{i\,x}(\xi,0) = 2\,\mathcal{S}_{i0}(\xi), \qquad i = 1,2, \tag{4.39}$$

- Degree of crystallization

$$\mathcal{Y}_i(\xi,0) = \mathcal{Y}_{i0}(\xi), \qquad i = 1,2. \tag{4.40}$$

The (two–dimensional) equations for the (two components of the) molecular orientation tensor (cf. Eqs. (4.30) and (4.31)) and the degree of crystallization (cf. Eqs. (4.32)) are hyperbolic and were discretized by means of first–order accurate upwind difference expressions in both the axial and the radial directions, whereas the (two–dimensional) energy equation is of the advection–diffusion type and its advection terms were discretized as those for the degree of crystallization, while second–order accurate finite differences were used to discretize the diffusion term in the radial direction. The set of finite difference equations for $\mathcal{B}$, $\hat{T}$, $\mathbf{S}$ and $\mathcal{Y}$ were solved iteratively in grids consisting of 1001 points in the axial direction and 301 points in the radial one (101 points in the core and 201 in the cladding), respectively, until a specified convergence criterion is achieved.

4.1.2 *Average temperature of the compound jet*

In order to compare the results of the hybrid model with those of the one–dimensional one, is mandatory to define the average temperature of the compound jet, $< \hat{T} >$. To do so, the cross–sectionally averaged of the energy conservation partial differential equations (Eqs. (4.29)) yields

$$2Q\bar{P}_1 \left(\frac{\hat{k}_1}{\hat{k}_2}\right) \frac{d}{d\eta}\left(< \hat{T}_1 > (\eta)\frac{Q_1}{2Q}\right) = \sqrt{\frac{Q_1}{Q}}\left(\frac{\hat{k}_1}{\hat{k}_2}\right)\frac{\partial \hat{T}_1}{\partial \xi}\left(\sqrt{\frac{Q_1}{Q}},\eta\right), \tag{4.41}$$

$$2Q\bar{P}_2 \frac{d}{d\eta}\left(< \hat{T}_2 > (\eta)\frac{Q_2}{2Q}\right) = \frac{\partial \hat{T}_2}{\partial \xi}(1,\eta) - \sqrt{\frac{Q_1}{Q}}\frac{\partial \hat{T}_2}{\partial \xi}\left(\sqrt{\frac{Q_1}{Q}},\eta\right), \tag{4.42}$$

where the average temperature, $< \hat{T}_i(\eta) >$, of each jet has been defined in the same way as the average dynamic viscosity, which, in the mapped domain, can be written as

$$< \hat{T}_1 > (\eta) = \frac{2\,Q}{Q_1}\int_0^{\sqrt{\frac{Q_1}{Q}}} \hat{T}_1(\xi,\eta)\,\xi\,d\xi, \tag{4.43}$$

$$< \hat{T}_2 > (\eta) = \frac{2\,Q}{Q_2}\int_{\sqrt{\frac{Q_1}{Q}}}^{1} \hat{T}_2(\xi,\eta)\,\xi\,d\xi. \tag{4.44}$$

The sum of Eqs. (4.41) and (4.42), taking into account the boundary conditions both at the interface, $\left(\xi = \sqrt{\frac{Q_1}{Q}}\right)$, and the convective one, $(\xi = 1)$, yields

$$\bar{P}_1 \left(\frac{\hat{k}_1}{\hat{k}_2}\right) \frac{d}{d\eta} \left(< \hat{T}_1 > (\eta) Q_1\right) + \bar{P}_2 \frac{d}{d\eta} \left(< \hat{T}_2 > (\eta) Q_2\right) = \frac{\partial \hat{T}_2}{\partial \xi}(1, \eta)$$

$$\left(\bar{P}_1 \left(\frac{\hat{k}_1}{\hat{k}_2}\right) Q_1 + \bar{P}_2 Q_2\right) \frac{d< \hat{T} > (\eta)}{d\eta} = -Bi_2 \, \mathcal{R}_2(\eta) \left(\hat{T}_2 \left(1, \eta\right) - \hat{T}_{\infty,2}\right). \tag{4.45}$$

In this manner, the average temperature of the jet, $< \hat{T}(\eta) >$, is a monotonically decreasing function depending on η due to the convection phenomena that the compound jet experiences as it is being drawn. It must be noted that

$$< \hat{T} > (\eta) = \frac{\bar{P}_1 \left(\frac{\hat{k}_1}{\hat{k}_2}\right) Q_1 \; < \hat{T}_1(\eta) > + \bar{P}_2 \, Q_2 \; < \hat{T}_2(\eta) >}{\bar{P}_1 \left(\frac{\hat{k}_1}{\hat{k}_2}\right) Q_1 + \bar{P}_2 \, Q_2} \tag{4.46}$$

and that the equation that governs its evolution in the transformed domain is

$$\frac{d< \hat{T} > (\eta)}{d\eta} = -\frac{St}{\hat{\rho}_1 \hat{C}_1 Q_1 + \hat{\rho}_2 \hat{C}_2 Q_2} \hat{h}_2 \, \mathcal{R}_2(\eta) \left(\hat{T}_2 \left(1, \eta\right) - \hat{T}_{\infty,2}\right), \tag{4.47}$$

where $St = Bi/\bar{P}$.

4.1.3 *Numerical scheme*

In this subsection, a brief description of the procedure for the solution of the two–dimensional model is presented.

The following instructions flow was followed in order to obtain the converged solution for the melt spinning of semi–crystalline compound fibres.

1. Use as an initial guess for the axial velocity, $\mathcal{B}^{(0)}(\eta)$, the solution of the isothermal viscous regime (cf. Eq. (3.68)) characterized by ($\bar{R}=0, \bar{C}\to\infty$) and a finite (non–zero) value of $\bar{F}$. Likewise, the temperature, $\hat{T}^{(n)}(\xi,\eta)$, and the components of the molecular orientation tensor, $\mathbf{S}^{(\mathbf{n})}(\mathbf{,},\mathbf{J})$, and degree of crystallization, $\mathcal{Y}_i^{(n)}(\xi,\eta)$, of the compound jet are guessed using the boundary conditions at $\eta=0$ and imposing a constant two–dimensional field for each variable (a linear one can also be imposed).

2. Calculate the compound fibre geometry $\mathcal{A}_1^{(n)}, \mathcal{A}_2^{(n)}, \mathcal{R}_1^{(n)}, \mathcal{R}_2^{(n)}$ using Eq. (3.89)–(3.90).

3. Determine the effective dynamic viscosity $\hat{\mu}_{ei}^{(n)}(\xi,\eta) = f\left(\hat{T}^{(n)}, \mathcal{Y}^{(n)}\right)$ of the inner and outer jets.

4. Obtain the averaged effective dynamic viscosity, $< \hat{\mu}_{ei} >^{(n)} (\eta)$, of the jets.

5. Calculate the new axial velocity $\mathcal{B}^{(n+1)}(\hat{x})$ using Eq. (4.13).

6. Calculate the temperature, $\hat{T}^{(n+1)}(\xi,\eta)$, of the compound jet using Eq. (4.29).

7. Calculate the molecular orientation order parameter, $\mathcal{S}_i^{(n+1)}(\xi,\eta)$, using Eqs. (4.30)–(4.31) and the degree of crystallization, $\mathcal{Y}_i^{(n+1)}(\xi,\eta)$, of the core and cladding.

8. Iterate until the convergence criteria are satisfied; this convergence criterion is

$$\sqrt{\frac{1}{N_x}\sum_{j=1}^{N_x}\left(\frac{1}{N_r}\sum_{k=1}^{N_r}\left(\Psi_{j,k}^{(n+1)}-\Psi_{j,k}^{(n)}\right)^2\right)} \leq \mathrm{TOL}, \tag{4.48}$$

where N_x and N_r are the number of nodes in the axial and radial directions, respectively, n is the n–th iteration, $\mathrm{TOL}=10^{-8}$ is the error tolerance and Ψ represents any of the two–dimensional unknown fields, $\hat{T}_i$, $\mathcal{S}_i$, and $\mathcal{Y}_i$.

4.2 2–D STEADY–STATE MODEL FOR SEMI–CRYSTALLINE HOLLOW COMPOUND FIBRES

The well–known conservation equations of mass, linear momentum and energy for axisymmetric flows of Newtonian fluids together with the equations for the molecular orientation tensor and the degree of crystallization presented in Chapter 1 are highly non–linearly coupled through the dependence of the dynamic viscosity on the temperature, molecular orientation order parameter and degree of crystallization which, in turn, are non–linearly coupled to the continuity, energy and linear momentum equations. In addition, the geometry of the hollow compound fibres must be determined as part of the solution. Therefore, an analysis of even Newtonian hollow compound fibres would require an intensive and expensive computational effort. In this section, this effort is substantially diminished by developing a simplified two–dimensional model which employs the one–dimensional equations for the (slender) fibre's radii and axial velocity component and two–

dimensional equations for the radial velocity component derived in the previous section and the two–dimensional equations of energy, molecular orientation tensor, and degree of crystallization.

Since the effective dynamic viscosity depends on the (two–dimensional) fields of $\hat{T}$ and $\mathcal{Y}$, the dynamic viscosity that appears in Eq. (3.35) is

$$< \hat{\mu}_{e1,0} > (\hat{x}) = \frac{1}{\mathcal{A}_1} \int_{\mathcal{R}_0}^{\mathcal{R}_1} \hat{\mu}_{e1,0}(\hat{r}, \hat{x})\, \hat{r}\, d\hat{r}, \tag{4.49}$$

$$< \hat{\mu}_{e2,0} > (\hat{x}) = \frac{1}{\mathcal{A}_2} \int_{\mathcal{R}_1}^{\mathcal{R}_2} \hat{\mu}_{e2,0}(\hat{r}, \hat{x})\, \hat{r}\, d\hat{r}, \tag{4.50}$$

and the integrals that appear in these averaged dynamic viscosities provide an integro–differential character to the melt spinning (or drawing) of hollow compound semi–crystalline fibres.

In order to consider the radial variations of temperature, we use Eqs. (3.34)–(3.38) for the fibre's geometry and (leading–order) axial and radial velocity components, while the temperature field will be determined by solving the two–dimensional energy equation which in non–dimensional form was written as Eq. (2.58). Note that the neglect of axial diffusion term in the right–hand side of Eq. (2.58) is a valid approximation for slender hollow compound fibres, i.e., for $\epsilon << 1$, considered in this study.

In the numerical simulations presented here, $\hat{u}$ and $\hat{v}$ have been replaced by $\mathcal{B}$ and Eq. (3.38), respectively, in Eq. (2.58). Therefore, in the two–dimensional model presented here, one employs a parabolic equation for the temperature field which uses the velocity profile from the leading–order asymptotic analysis of slender hollow compound fibres.

Under the conditions stated above, the two–dimensional steady–state equations for the components of the molecular orientation tensor and degree of crystallization are given by

$$\left(\hat{u}_{i,0}\frac{\partial s_{ir}}{\partial \hat{x}} + \hat{v}_{i,0}\frac{\partial s_{ir}}{\partial \hat{r}}\right) = (1 - s_{ir})\left[(1 + s_{ix})\,\frac{d\mathcal{B}}{d\hat{x}} + \frac{2}{3}\frac{\mathcal{C}(\hat{x})}{\hat{r}^2}\,(3 + 2\,s_{ir} - s_{ix})\right] - \frac{\phi_i}{\hat{\lambda}_i}\left\{s_{ir} - \frac{N_i}{3}\left[(1 - s_{ir})\,(s_{ir} + 3\,\Pi_{i,s})\right]\right\}, \tag{4.51}$$

$$\left(\hat{u}_{i,0}\frac{\partial s_{ix}}{\partial \hat{x}} + \hat{v}_{i,0}\frac{\partial s_{ix}}{\partial \hat{r}}\right) = (s_{ix} + 1)\left[(2 - s_{ix})\,\frac{d\mathcal{B}}{d\hat{x}} - \frac{2}{3}\frac{\mathcal{C}(\hat{x})}{\hat{r}^2}\,(2\,s_{ir} - s_{ix})\right] - \frac{\phi_i}{\hat{\lambda}_i}\left\{s_{ix} - \frac{N_i}{3}\left[(s_{ix} + 1)\,(s_{ix} - 3\,\Pi_{i,s})\right]\right\}. \tag{4.52}$$

and Eq. (4.4) where the molecular orientation order parameter, $\mathcal{S}_i$, which has the same expression as that derived for compound fibres, and $\mathcal{Y}_i$ are functions depending of $\hat{r}$ and $\hat{x}$.

As indicated in § 4.1, Eqs. (4.51)–(4.52) and (4.4) may be written as Eq. (4.5) which can be solved by the method of characteristics, i.e.,

$$\frac{d\hat{r}}{d\hat{x}} = \frac{1}{\mathcal{B}}\left(\frac{\mathcal{C}}{\hat{r}} - \frac{\hat{r}}{2}\frac{d\mathcal{B}}{d\hat{x}}\right) \tag{4.53}$$

$$\frac{d\Omega}{d\hat{x}} = \frac{\mathcal{U}}{\mathcal{B}} \tag{4.54}$$

but, in this case, the first equation does not have a simple solution as that for compound jets if $\mathcal{C} \neq 0$. However, if $\mathcal{C} = 0$ which corresponds to $\hat{p}_e = \hat{p}_i$ and $\frac{1}{\hat{C}} = 0$, the solution of the first

equation is $\mathcal{B}\,\hat{r}^2 = \vartheta$. In this case, however, Eqs. (4.51)–(4.52) and (4.4) may be solved by means of upwind difference techniques.

Equations (3.34)–(3.38), (2.58), (4.51)–(4.52), and (4.4), represent the two–dimensional model for the fluid dynamics of semi–crystalline hollow compound fibres and are subject to specified conditions at the location of maximum swell, $\hat{x} = 0$, identical to those of Eqs. (4.14)–(4.19).

The boundary conditions corresponding to the energy equation are

$$-\hat{k}_1 \frac{\partial \hat{T}_1}{\partial \hat{r}}(\mathcal{R}_0, \hat{x}) = Bi\,\hat{h}_1 \left(\hat{T}_{\infty,1} - \hat{T}_1(\mathcal{R}_0, \hat{x})\right), \tag{4.55}$$

$$\hat{T}_1(\mathcal{R}_1, \hat{x}) = \hat{T}_2(\mathcal{R}_1, \hat{x}), \tag{4.56}$$

$$\hat{k}_1 \frac{\partial \hat{T}_1}{\partial \hat{r}}(\mathcal{R}_1, \hat{x}) = \hat{k}_2 \frac{\partial \hat{T}_2}{\partial \hat{r}}(\mathcal{R}_1, \hat{x}), \tag{4.57}$$

$$-\hat{k}_2 \frac{\partial \hat{T}_2}{\partial \hat{r}}(\mathcal{R}_2, \hat{x}) = Bi\,\hat{h}_2 \left(\hat{T}_2(\mathcal{R}_2, \hat{x}) - \hat{T}_{\infty,2}\right), \tag{4.58}$$

where Bi depends on the (reference, constant) film heat transfer coefficient h_0 and the dimensionless heat transfer coefficients $\hat{h}_i = \frac{h_i}{h_0}$ may depend on the local Reynolds and Prandtl numbers.

The model for the melt spinning (or drawing) of hollow compound fibres presented in this chapter is a single–phase, bi–component formulation characterized by a Newtonian rheology and does not account for latent heat effects associated with solidification. The model does not account either for the presence of amorphous and crystalline phases in a separate manner either through conservation equations for these components or through a non–Newtonian rheology. Latent heat effects associated with phase changes may result in a locally small increase of temperature at the solidification point, but are usually small in melt spinning processes at moderate drawing speeds. By way of contrast, the fluid dynamics, rheology, heat transfer, molecular orientation and crystallization of hollow compound fibres are expected to be affected by the presence of amorphous and crystalline phases. It must be also noted that, in the model presented here, the axial velocity component, $\hat{u}$, only depends on $\hat{x}$, while $\hat{v}$, $\mathbf{S}$, $\mathcal{Y}$ and $\hat{T}$ depend on $\hat{r}$ and $\hat{x}$ for time–independent melt spinning processes.

4.2.1 *Numerical method. Mapping*

In this chapter, only steady hollow compound fibres are considered, and the numerical solution of the non–linear equations governing the two–dimensional multiple free–surface model presented above was obtained as follows. First, the following transformation $(\hat{r}, \hat{x}) \rightarrow (\xi, \eta)$ for the inner and outer jets, where $\xi(\hat{r}, \hat{x}) = \frac{\hat{r}^2 - \mathcal{R}_0^2(\hat{x})}{\mathcal{R}_2^2(\hat{x}) - \mathcal{R}_0^2(\hat{x})}$ and $\eta(\hat{r}, \hat{x}) = \hat{x}$, was employed to map the curvilinear geometries of the inner and outer jets/fibres into rectangles, i.e., $[\mathcal{R}_0(\hat{x}), \mathcal{R}_1(\hat{x})] \rightarrow [0, Q_1/Q]$ and $[\mathcal{R}_1(\hat{x}), \mathcal{R}_2(\hat{x})] \rightarrow [Q_1/Q, 1]$, respectively, where $Q = Q_1 + Q_2$ denotes the non–dimensional (total) volumetric flow rate of the hollow compound jet (cf. Figure 4.2).

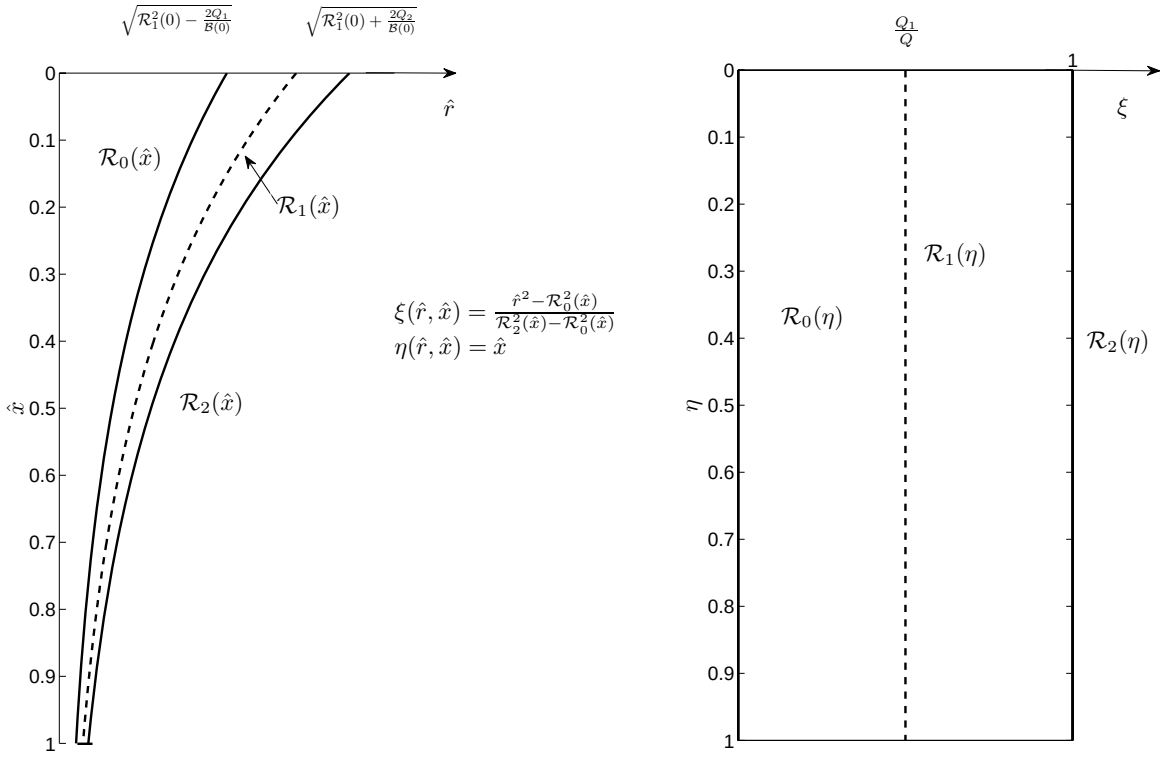

Figure 4.2: *Mapping between physical domain* $(\hat{r},\,\hat{x})$ *and the computational one* $(\xi,\,\eta)$ *in hollow compound fibres.*

Using the above mapping, the differential operators can be written in the transformed domain taking into account the chain rule as

$$\frac{\partial}{\partial \hat{x}} = \frac{-1}{\mathcal{A}(\eta)}\left(\frac{d\mathcal{A}_0(\eta)}{d\eta}+\xi\,\frac{d\mathcal{A}(\eta)}{d\eta}\right)\frac{\partial}{\partial \xi}+\frac{\partial}{\partial \eta}, \tag{4.59}$$

$$\frac{\partial}{\partial \hat{r}} = \frac{\hat{r}}{\mathcal{A}(\eta)}\,\frac{\partial}{\partial \xi}, \tag{4.60}$$

where $\mathcal{A}_0(\eta)=\frac{\mathcal{R}_0^2(\eta)}{2}$.

Using an analogous procedure than made for compound fibres on section 4.1.1 and taking into account Eqs. (3.34) and (3.38) the convective operator, $\mathfrak{L}$, that appears into Eqs. (4.1)–(4.4) may be written as

$$\mathfrak{L}=\hat{u}_{i,0}\,\frac{\partial}{\partial \hat{x}}+\hat{v}_{i,0}\,\frac{\partial}{\partial \hat{r}}=\left[\mathcal{B}(\eta)\,\frac{\partial \xi}{\partial \hat{x}}+\left(\frac{\mathcal{C}}{\hat{r}}-\frac{\hat{r}}{2}\frac{\partial \mathcal{B}}{\partial \hat{x}}\right)\frac{\partial \xi}{\partial \hat{r}}\right]\frac{\partial}{\partial \xi}+\mathcal{B}(\eta)\frac{\partial}{\partial \eta}=\mathcal{B}(\eta)\frac{\partial}{\partial \eta}. \tag{4.61}$$

Furthermore, the $\mathfrak{N}$ operator that appears in the energy equation may be written as

$$\mathfrak{N}=\frac{1}{\hat{r}}\,\frac{\partial}{\partial \hat{r}}\left(\hat{r}\frac{\partial}{\partial \hat{r}}\right)=\frac{2}{\mathcal{A}(\eta)}\,\frac{\partial}{\partial \xi}\left\{\left[\frac{\mathcal{A}_0(\eta)}{\mathcal{A}(\eta)}+\xi\right]\,\frac{\partial}{\partial \xi}\right\}. \tag{4.62}$$

Both energy conservation equation and the equations that model the molecular orientation tensor components and degree of crystallization in the computational domain can be written as

$$\frac{\partial \hat{T}_i}{\partial \eta} = \frac{1}{Q}\frac{2}{\bar{P}_i}\frac{\partial}{\partial \xi}\left[\left(\frac{\mathcal{A}_0}{\mathcal{A}} + \xi\right)\frac{\partial \hat{T}_i}{\partial \xi}\right], \qquad i = 1, 2, \tag{4.63}$$

$$\begin{aligned}\mathcal{B}\,\frac{\partial s_{ir}}{\partial \eta} &= (1 - s_{ir})\left[(1 + s_{ix})\,\frac{d\mathcal{B}}{d\eta} + \frac{1}{3}\frac{\mathcal{C}(\eta)}{\mathcal{A}(\eta)\xi + \mathcal{A}_0(\eta)}\,(3 + 2\,s_{ir} - s_{ix})\right] \\ &\quad - \frac{\phi_i}{\hat{\lambda}_i}\left\{s_{ir} - \frac{N_i}{3}\left[(1 - s_{ir})\,(s_{ir} + 3\,\Pi_{i,s})\right]\right\}, \qquad i = 1, 2,\end{aligned} \tag{4.64}$$

$$\begin{aligned}\mathcal{B}\,\frac{\partial s_{ix}}{\partial \eta} &= (s_{ix} + 1)\left[(2 - s_{ix})\,\frac{d\mathcal{B}}{d\eta} + \frac{1}{3}\frac{\mathcal{C}(\eta)}{\mathcal{A}(\eta)\xi + \mathcal{A}_0(\eta)}\,(2\,s_{ir} - s_{ix})\right] \\ &\quad - \frac{\phi_i}{\hat{\lambda}_i}\left\{s_{ix} - \frac{N_i}{3}\left[(s_{ix} + 1)\,(s_{ix} - 3\,\Pi_{i,s})\right]\right\}, \qquad i = 1, 2,\end{aligned} \tag{4.65}$$

$$\mathcal{B}\,\frac{\partial \mathcal{Y}_i}{\partial \eta} = k_{Ai}(0)\exp\left(a_{2i}\mathcal{S}_i^2\right)(\mathcal{Y}_{\infty,i} - \mathcal{Y}_i), \qquad i = 1, 2. \tag{4.66}$$

Boundary conditions in the computational domain now read as

- Temperature of the jets

$$\hat{T}_i(\xi, 0) = \hat{T}_{i0}(\xi) \qquad i = 1, 2, \tag{4.67}$$

- Thermal boundary condition at the surrounding–core interface $(\xi = 0)$

$$-\frac{\partial \hat{T}_1}{\partial \xi} + Bi_1\,\frac{\mathcal{A}}{\mathcal{R}_0}\,\hat{T}_1 = Bi_1\,\frac{\mathcal{A}}{\mathcal{R}_0}\,\hat{T}_{\infty,1}, \tag{4.68}$$

- Boundary conditions for the temperature at the core–cladding interface $\left(\xi = \frac{Q_1}{Q}\right)$

$$\hat{T}_1 = \hat{T}_2, \tag{4.69}$$

$$\hat{k}_1\,\frac{\partial \hat{T}_1}{\partial \xi} = \hat{k}_2\,\frac{\partial \hat{T}_2}{\partial \xi}, \tag{4.70}$$

- Boundary condition for the temperature at the cladding–surrounding interface $(\xi = 1)$

$$\frac{\partial \hat{T}_2}{\partial \xi} + Bi_2\,\frac{\mathcal{A}}{\mathcal{R}_2}\,\hat{T}_2 = Bi_2\,\frac{\mathcal{A}}{\mathcal{R}_2}\,\hat{T}_{\infty,2}, \tag{4.71}$$

and Eqs. (4.38)–(4.39) and (4.40) for the molecular orientation tensor and degree of crystallization, respectively, where $Bi_1 = \frac{\hat{h}_1}{\hat{k}_1}\,Bi$ depends on the film heat transfer coefficient $\hat{h}_1$ and the thermal conductivity of the core.

The governing equations were discretized by means of a finite difference method analogous to the one employed for compound fibres. The set of finite difference equations for $\mathcal{B}$, $\hat{T}$, $\mathbf{S}$ and $\mathcal{Y}$ were solved iteratively in grids consisting of 1001 points in the axial direction, and 101 points in the radial direction for both the inner and outer jets, until the L_2 norm of the differences between the solutions in two successive iterations given by Eq. (4.48) was less than or equal to 10^{-8}.

4.2.2 *Average temperature of the hollow compound jet*

In order to compare the results of the hybrid model for hollow compound fibres with those of the one–dimensional one, it is useful to define of the mean averaged temperature of the hollow compound jet, $< \hat{T} >$. To do that, the cross–sectionally averaged of the energy conservation partial differential equations (Eqs. (4.63)) yield

$$\bar{P}_1 \left(\frac{\hat{k}_1}{\hat{k}_2}\right) \frac{d}{d\eta} \left(< \hat{T}_1 > (\eta) Q_1 \right) = 2 \left(\frac{\hat{k}_1}{\hat{k}_2}\right) \left[\left(\frac{Q_1}{Q} + \frac{\mathcal{A}_0}{\mathcal{A}} \right) \frac{\partial \hat{T}_1}{\partial \xi} \left(\frac{Q_1}{Q}, \eta \right) - \frac{\mathcal{A}_0}{\mathcal{A}} \frac{\partial \hat{T}_1}{\partial \xi} (0, \eta) \right], \tag{4.72}$$

$$\bar{P}_2 \frac{d}{d\eta} \left(< \hat{T}_2 > (\eta) Q_2 \right) = 2 \left[\left(1 + \frac{\mathcal{A}_0}{\mathcal{A}} \right) \frac{\partial \hat{T}_2}{\partial \xi} (1, \eta) - \left(\frac{Q_1}{Q} + \frac{\mathcal{A}_0}{\mathcal{A}} \right) \frac{\partial \hat{T}_2}{\partial \xi} \left(\frac{Q_1}{Q}, \eta \right) \right], \tag{4.73}$$

where the average temperature, $< \hat{T}_i(\eta) >$, of each jet has been defined in the same way as the average dynamic viscosity which in the mapped domain can be written as

$$< \hat{T}_1 > (\eta) = \frac{Q}{Q_1} \int_0^{\frac{Q_1}{Q}} \hat{T}_1(\xi, \eta)\, d\xi, \tag{4.74}$$

$$< \hat{T}_2 > (\eta) = \frac{Q}{Q_2} \int_{\frac{Q_1}{Q}}^1 \hat{T}_2(\xi, \eta)\, d\xi. \tag{4.75}$$

The sum of Eqs. (4.72) and (4.73), taking into account the boundary conditions both at the interface, $\left(\xi = \frac{Q_1}{Q}\right)$, and the convective ones, and those at $\xi = 0$ and at $\xi = 1$, yields

$$\bar{P}_1 \left(\frac{\hat{k}_1}{\hat{k}_2}\right) \frac{d}{d\eta} \left(< \hat{T}_1 > (\eta) Q_1 \right) + \bar{P}_2 \frac{d}{d\eta} \left(< \hat{T}_2 > (\eta) Q_2 \right) = 2 \left[\left(1 + \frac{\mathcal{A}_0}{\mathcal{A}} \right) \frac{\partial \hat{T}_2}{\partial \xi} (1, \eta) - \left(\frac{\hat{k}_1}{\hat{k}_2}\right) \frac{\mathcal{A}_0}{\mathcal{A}} \frac{\partial \hat{T}_1}{\partial \xi} (0, \eta) \right], \tag{4.76}$$

$$\left(\bar{P}_1\left(\frac{\hat{k}_1}{\hat{k}_2}\right)Q_1+\bar{P}_2Q_2\right)\frac{d<\hat{T}>(\eta)}{d\eta}=$$
$$-\left[\mathcal{R}_2(\eta)\,Bi_2\,\left(\hat{T}_2\,(1,\eta)-\hat{T}_{\infty,2}\right)+\mathcal{R}_0(\eta)\,Bi_1\,\left(\frac{\hat{k}_1}{\hat{k}_2}\right)\left(\hat{T}_1\,(0,\eta)-\hat{T}_{\infty,1}\right)\right], \tag{4.77}$$

which indicates that the average temperature of the jet, $<\hat{T}(\eta)>$, is a monotonically decreasing function because due to the convection phenomena that the hollow compound jet experiences as it is drawn. One can also write

$$<\hat{T}>(\eta)=\frac{\bar{P}_1\left(\frac{\hat{k}_1}{\hat{k}_2}\right)\,Q_1\,<\hat{T}_1(\eta)>+\bar{P}_2\,Q_2\,<\hat{T}_2(\eta)>}{\bar{P}_1\left(\frac{\hat{k}_1}{\hat{k}_2}\right)\,Q_1+\bar{P}_2\,Q_2}, \tag{4.78}$$

being the equation that governs its evolution in the transformed axial location, η,

$$\frac{d}{d\eta}<\hat{T}>(\eta)=-\frac{St}{\hat{\rho}_1\hat{C}_1Q_1+\hat{\rho}_2\hat{C}_2Q_2}\cdot$$
$$\left[\mathcal{R}_2(\eta)\,\hat{h}_2\left(\hat{T}_2\,(1,\eta)-\hat{T}_{\infty,2}\right)+\mathcal{R}_0(\eta)\,\hat{h}_1\left(\hat{T}_1\,(0,\eta)-\hat{T}_{\infty,1}\right)\right]. \tag{4.79}$$

Part III

NUMERICAL RESULTS

5

NUMERICAL SIMULATIONS OF SEMI–CRYSTALLINE COMPOUND FIBRES

Contents

5.1 INTRODUCTION

Some sample two–dimensional results[†] obtained with the axisymmetric melt spinning model for semi–crystalline compound fibres described in Chapter 4 are presented here for, unless otherwise stated, the same thermal conductivities and pre–exponential factors and activation energies of the dynamic viscosity for the core and cladding, a constant film–heat transfer coefficient that corresponds to a constant Biot number, unity Reynolds, Prandtl, and Froude numbers, and a capillary number equal to ten. We have also used $\mathcal{R}_1(0) = 1$ and $Q_1 = 0.5$, i.e., the same non–dimensional volumetric flow rate for the core and the cladding have been selected, i.e., $Q_1 = Q_2$, and the non–dimensional axial velocity at the maximum swell cross–section is unity, i.e., $\mathcal{B}(0) = 1$.

In the cases considered here, the draw ratio, D_r, i.e., the relation between the axial velocity at the take–up cross–section and that at $\hat{x} = 0$ is 100. Since we are dealing with moderately high drawing speeds melting conditions, air drag was not included in our calculations ($\hat{\mathcal{T}}_2 = 0$). The relevant simulation parameters are summarized in Table 5.1 where $\bar{P}_i = \bar{P}\left(\frac{\hat{\rho}_i \hat{C}_i}{\hat{k}_i}\right)$ as it was defined in Chapter 4. It must be pointed out that Cases 4 and 5 correspond to $\hat{D}_1 = 10$ and 0.1, respectively; Cases 6 and 7 to $\hat{H}_1 = 40$ and 10, respectively; and, Cases 8 and 9 to $\hat{D}_2 = 10$ and 0.1, respectively. It must also be noted that Cases 8, 10 and 12 converged very slowly because these cases correspond to large values of the pre–exponential factor and activation energy, respectively, of the linearised Arrhenius expression for the dynamic viscosity law of the cladding and large Biot numbers; an increase in the first two corresponds to a substantial increase in the dynamic viscosity of the cladding, while an increase in the Biot number results in an increase in the heat transfer rate at the cladding–surroundings interface and lower temperatures for the cladding which, in turn, result in an increase of the dynamic viscosity.

[†]Most of text and figures presented in this chapter have been taken from an old version of [10].

Table 5.1: *Values of the parameters employed in the simulations of semi–crystalline compound fibres.*

Case	Bi	$\hat{H}_1$	$\hat{H}_2$	$\bar{P}_1$	$\bar{P}_2$	$\frac{\hat{k}_2}{\hat{k}_1}$	$\hat{D}_1$	$\hat{D}_2$
1	5	20	20	1	5	1	1	1
2	5	20	20	1	5	0.2	1	1
3	5	20	20	1	5	5	1	1
4	5	20	20	1	5	1	10	1
5	5	20	20	1	5	1	0.1	1
6	5	40	20	1	5	1	1	1
7	5	10	20	1	5	1	1	1
8	5	20	20	1	5	1	1	10
9	5	20	20	1	5	1	1	0.1
10	5	20	40	1	5	1	1	1
11	5	20	10	1	5	1	1	1
12	10	20	20	1	5	1	1	1
13	2.5	20	20	1	5	1	1	1

The other parameters employed in the simulations reported in this section are $N_i = 4$, $\alpha_i = 5$, $a_{21} = 10$, $a_{22} = 5$, $\hat{\lambda}_{i,0} = 1$, $\hat{\omega}_i = 0$, $\mathcal{Y}_{\infty,i} = 0.8$, $n_i = 12$, $\beta_i = 4$, $\frac{\sigma_1}{\sigma_2} = 1$, $\phi_i = 0.5$, $k_{A1}(0) = k_{A2}(0) = 0.005$, and $\hat{T}_{\infty,2} = 0$.

The following parabolic profile for the temperature of the compound fibre at the maximum swell cross–section, i.e., $\eta = 0$, was imposed

$$\hat{T}(\xi,0) = \begin{cases} 1 + \Delta T \left(1 - \left(\frac{\xi}{\xi_I}\right)^2\right), & 0 \le \xi \le \xi_I \\ 1 - \Delta T \left(\frac{\hat{k}_1}{\hat{k}_2}\right) \left(\left(\frac{\xi}{\xi_I}\right)^2 - 1\right), & \xi_I \le \xi \le 1 \end{cases} \tag{5.1}$$

where $\xi_I = \sqrt{\frac{Q_1}{Q}}$ corresponds to the interface between the inner and outer jets, and $\Delta T < \left(\frac{\hat{k}_2}{\hat{k}_1}\right)\left(\frac{Q_1}{Q_2}\right)$ in order to get positive temperature at the die exit ($\hat{T}(1,0) > 0$), and the molecular orientation parameter $\mathcal{S}$

$$\mathcal{S}(\xi,0) = \begin{cases} S_{10} - \Delta S_1 \left(1 - 2\left(\frac{\xi}{\xi_I}\right)^2\right), & 0 \le \xi \le \xi_I \\ S_{20} + \Delta S_2 \left(1 - \frac{2}{\left(\frac{1-\xi_I}{2}\right)^2}(\xi - 1)(\xi_I - \xi)\right), & \xi_I \le \xi \le 1 \end{cases} \tag{5.2}$$

where $\Delta S_i < \min(S_{i0}, 1 - S_{i0})$ for $i = 1, 2$. For the results presented in the next section, $\Delta T = 0.1$ and $(S_{10}, \Delta S_1) = (0.25, 0.10)$ and $(S_{20}, \Delta S_2) = (0.50, 0.20)$ have been employed.

5.2 RESULTS OF THE TWO–DIMENSIONAL MODEL FOR SEMI–CRYSTALLINE COMPOUND FIBRES

Figure 5.1 illustrates the temperature distribution in the compound fibre for Case 1. In this figure, the temperature distribution near $\hat{x} = 0$ is shown using a logarithmic scale, while that for $\hat{x} \in [0.1, 1]$ is shown in a linear scale. Figure 5.1 shows that a thermal boundary layer is formed at the outer interface of the cladding, while the inner jet exhibits a thermal core up to about $\hat{x} = 0.35$.

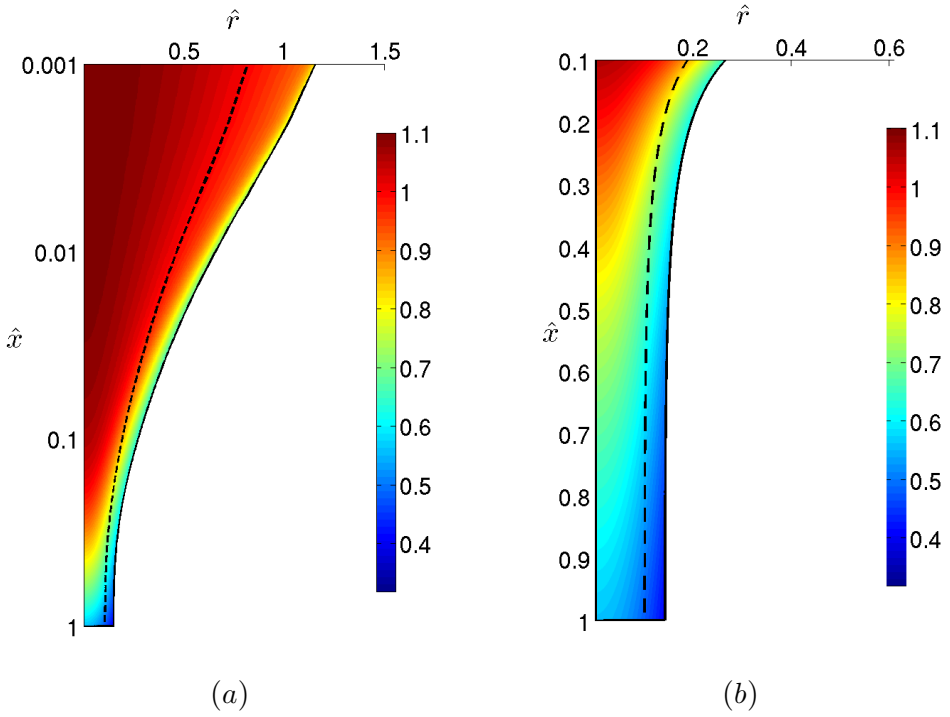

Figure 5.1: *Temperature distribution for Case 1. (The $\hat{x}$–axis of the left figure is in log scale.)*

The degree of crystallization and the molecular orientation order parameter corresponding to Case 1 are shown in Figure 5.2. For the values of the parameters of Case 1, very little crystallization is observed in the cladding, while that of the core increases rapidly and reaches a level close to its ultimate value at about $\hat{x} = 0.3$. By way of contrast, almost complete molecular orientation is observed at $\hat{x} = 0.01$ for both the core and the cladding, although there are substantial differences in the degree of orientation of the core and cladding near $\hat{x} = 0$ due to the initial conditions used in this study.

Although not shown here, the axial velocity component, $\mathcal{B}$, is uniform across the compound fibre, while the radial one, $\hat{v} = -\frac{\hat{r}}{2}\frac{\partial \mathcal{B}}{\partial \hat{x}}$ is directed towards the symmetry axis at a rate which first increases and then decreases along the fibre, before it reaches a nil value upon crystallization which corresponds to a large value of the effective dynamic viscosity.

The axial distributions of temperature, molecular orientation order parameter, degree of crystallization and (decimal logarithm of the) effective dynamic viscosity at the compound fibre's axis, core–cladding interface, and cladding–surroundings interface for Case 1 are illustrated in Figure 5.3. This figure indicates that the largest initial cooling occurs at the cladding–surroundings

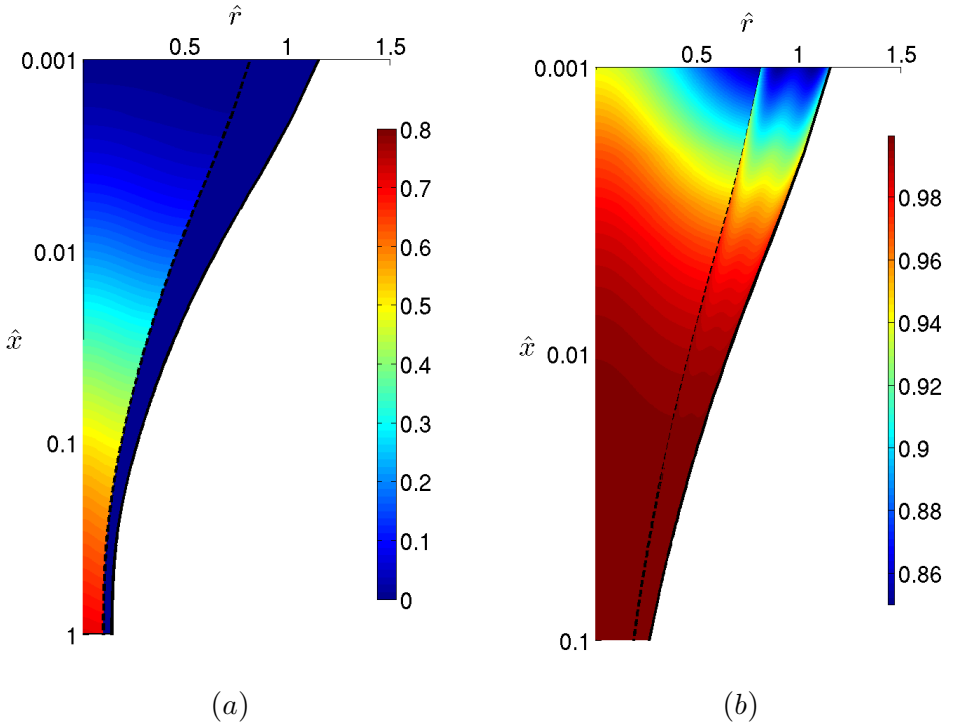

(a) (b)

Figure 5.2: *Distributions of the degree of crystallization* (a) *and order parameter for molecular orientation* (b) *for Case 1. (The* $\hat{x}$*–axis is in log scale in both figures.)*

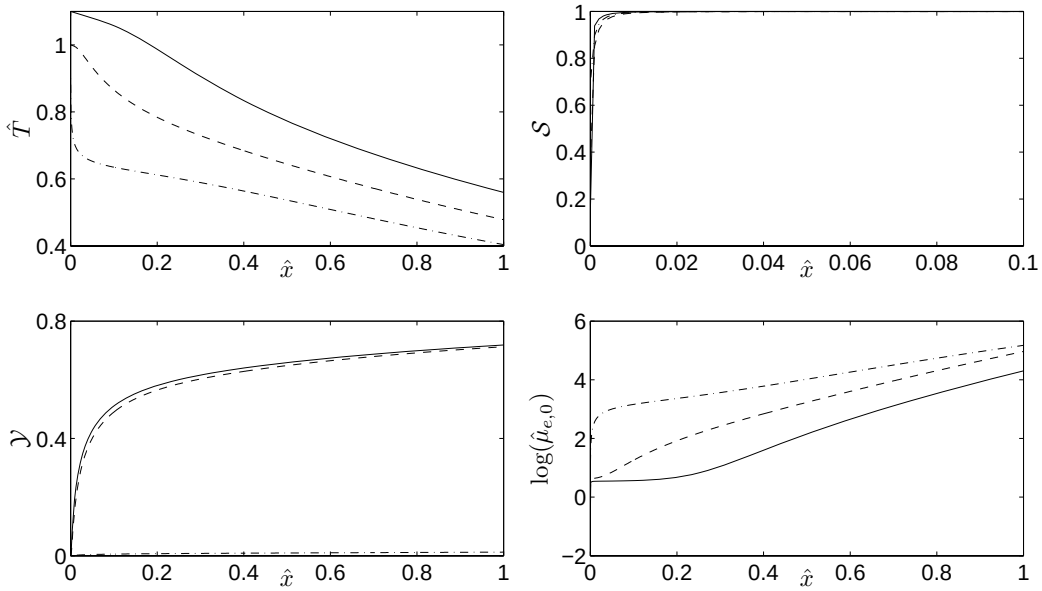

Figure 5.3: *(From left to right, from top to bottom) Temperature, molecular orientation order parameter, degree of crystallization and (decimal logarithm of) dynamic viscosity at the axis* ($\hat{r} = 0$) (—)*, core–cladding internal interface* ($\hat{r} = \mathcal{R}_1^-$) (– –) *and air–cladding interface* ($\hat{r} = \mathcal{R}_2$) (–·–) *for Case 1.*

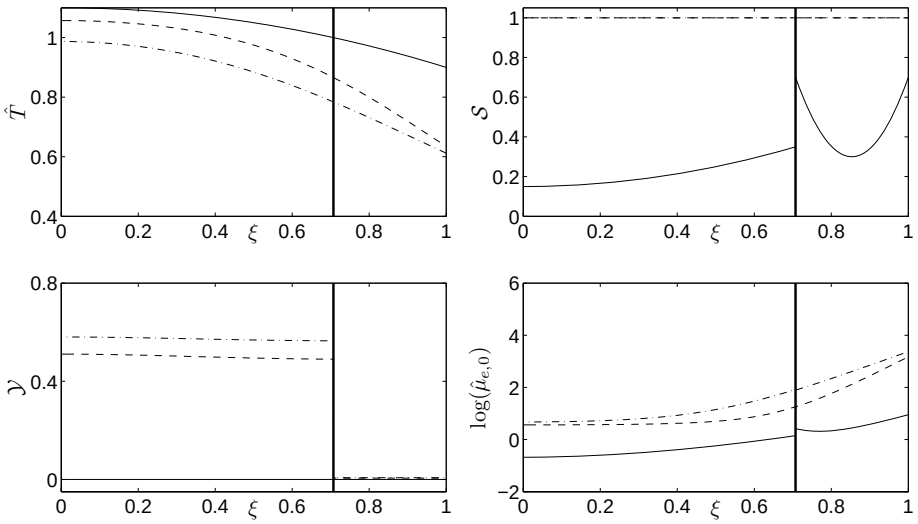

Figure 5.4: *(From left to right, from top to bottom) Temperature, molecular orientation order parameter, degree of crystallization and (decimal logarithm of) effective dynamic viscosity at $\hat{x} = 0$ (—), 0.1 (– –) and 0.2 (–·–) for Case 1.*

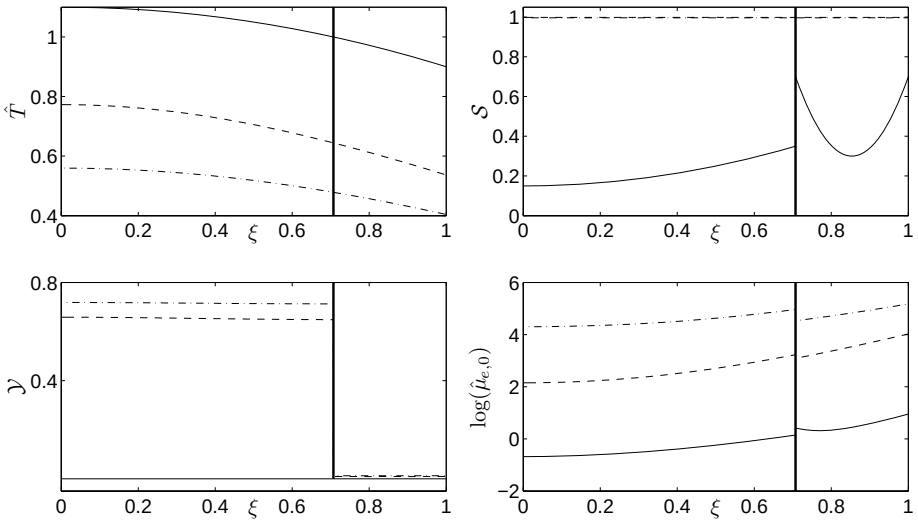

Figure 5.5: *(From left to right, from top to bottom) Temperature, molecular orientation order parameter, degree of crystallization and (decimal logarithm of) dynamic viscosity at $\hat{x} = 0$ (—), 0.5 (– –) and 1.0 (–·–) for Case* 1.

interface as observed in the temperature gradient, and this cooling results in an increase of the effective dynamic viscosity by about a factor of one hundred. However, the dynamic viscosity increase is not only due to the temperature drop; it is also caused by the increase in the molecular orientation order parameter and the degree of crystallization as a consequence of the formulation presented here (cf. Eq. (2.105)).

Figure 5.3 also shows that almost complete molecular orientation is reached near $\hat{x} = 0$ on account of the initial large contraction of the compound fibre there which results in an increase in the axial strain rate. Figure 5.3 also indicates that the degree of crystallization increases along the fibre but it is mainly a function of the temperature; therefore, for Case 1, it may be stated

that thermal effects are more important than flow–induced ones in determining the crystallization of the compound fibre.

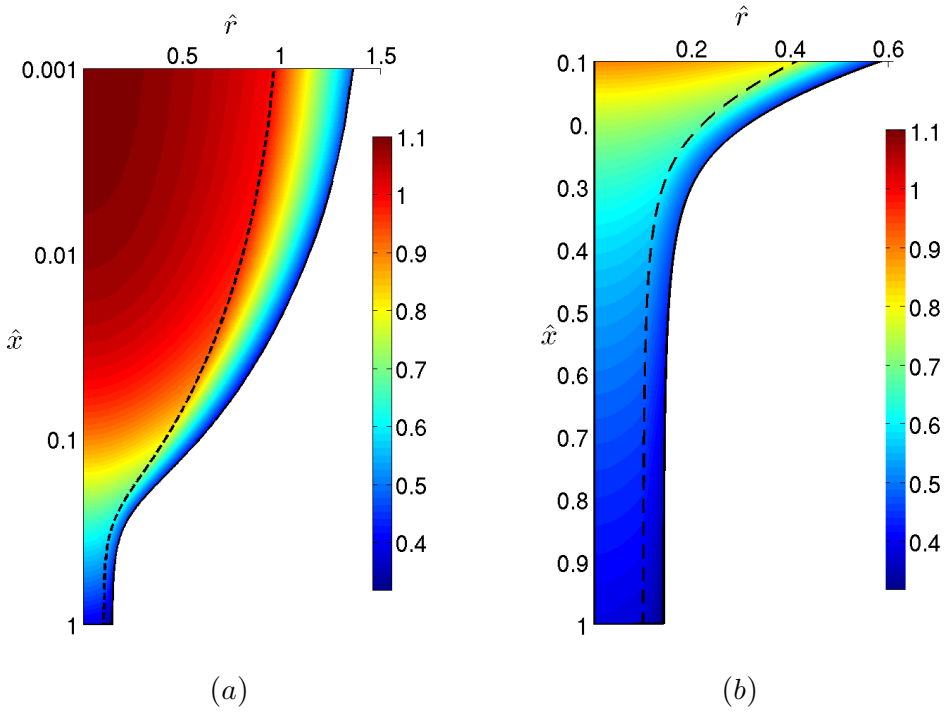

Figure 5.6: *Temperature distribution for Case 2. (The vertical axis of the left figure is in log scale.)*

Some radial distributions of temperature, molecular orientation and crystallization across the compound fibre are illustrated in Figures 5.4 and 5.5 for Case 1. These figures show that both the temperature and its radial derivative are continuous across the fibre, but the effective dynamic viscosity is not even continuous at the core–cladding interface because neither the molecular orientation order parameter nor the degree of crystallization are continuous there owing to the fact that these variables are governed by first–order advection–reaction equations and that their (identical) initial conditions were not uniform across the compound fibre at $\hat{x} = 0$. It must be noted that no discontinuities in the molecular orientation and crystallization are observed at the core–cladding interface when the initial conditions for these variables are uniform and identical at $\hat{x} = 0$ across the compound fibre.

For Case 2, the temperature distribution presented in Figure 5.6 clearly indicates that, as the thermal conductivity of the core is increased, the thermal boundary layer thickness formed at the cladding–surroundings interface increases and the core reaches an almost uniform temperature equal to about that of the cladding for $\hat{x} > 0.4$. As a consequence, the degree of crystallization of the core increases as the core's thermal conductivity is increased, as illustrated in Figure 5.7.

Although the molecular orientation order parameter presented in Figure 5.7 exhibits different patterns than those shown in Figure 5.2, almost complete orientation is achieved at about $\hat{x} = 0.1$. The differences between the molecular orientation presented in Figures 5.2 and 5.7 affect the degree of crystallization as discussed in Chapter 2, and the largest effect on the differences in the degree of crystallization observed in Figures 5.2 and 5.7 is associated with the cooling of the fibre, because almost complete molecular orientation is reached shortly after $\hat{x} = 0$. It must, however, be pointed out that, due to the dependence of the dynamic viscosity on temperature, a

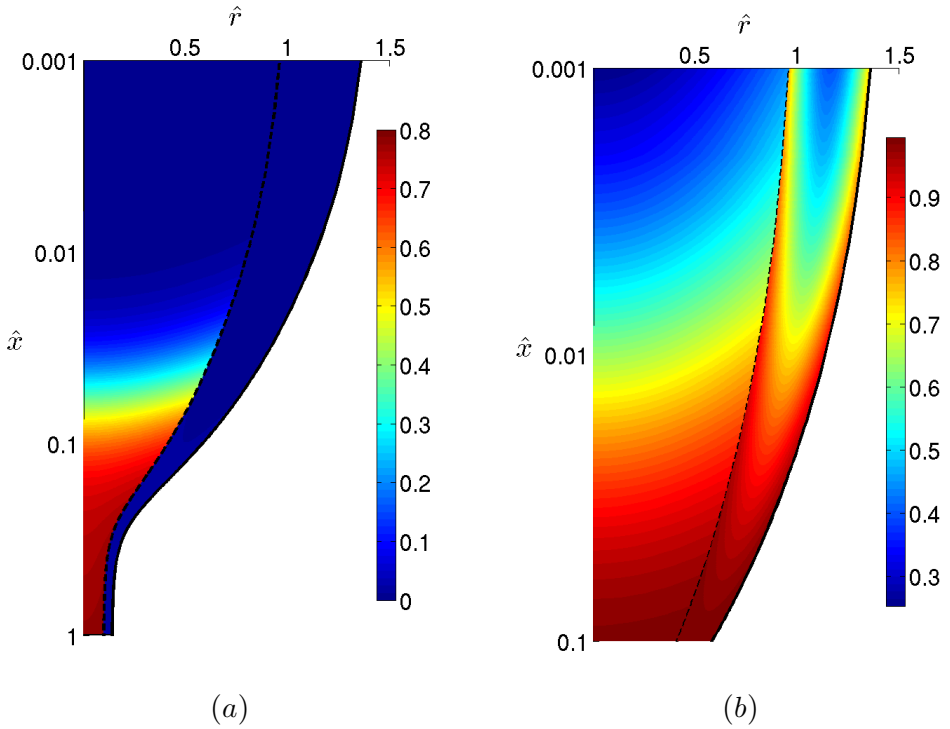

(a) (b)

Figure 5.7: *Distributions of the degree of crystallization* (a) *and molecular orientation order parameter for molecular orientation* (b) *for Case 2. (The* $\hat{x}$*–axis is in log scale in both figures.)*

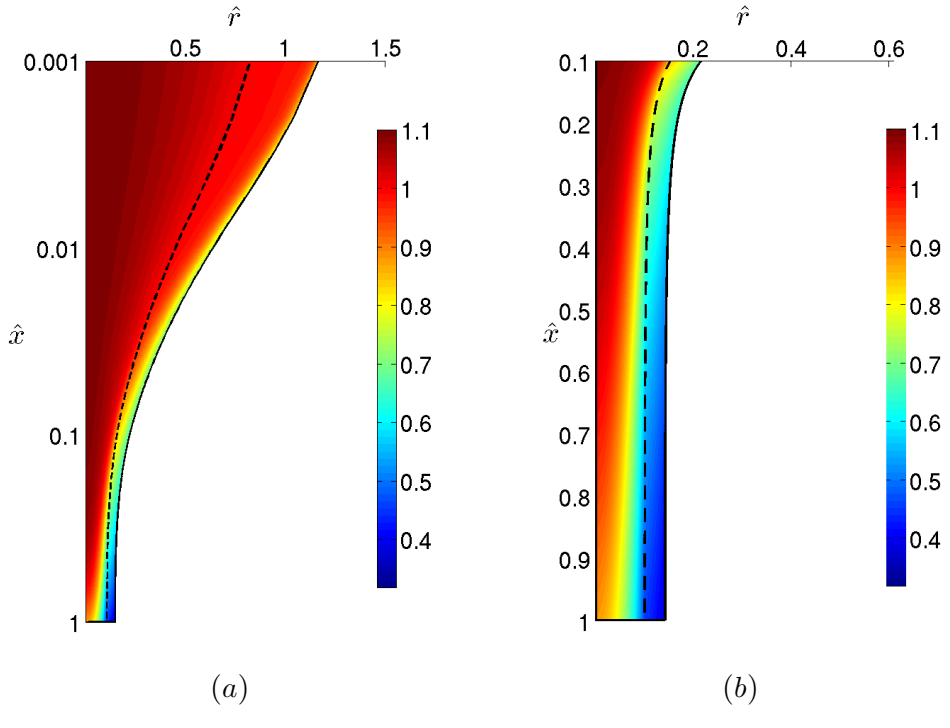

(a) (b)

Figure 5.8: *Temperature distribution for Case 3. (The vertical axis of the left figure is in log scale.)*

decrease in temperature results in an increase in viscosity, an increase in the solidification rate, and, by mass conservation, a correspondingly decrease in the compound fibre's cross–section. As a consequence, the axial strain rate increases, and, since the leading–order velocity field was used in the determination of the velocity field, the hoop and radial strain rates also increase.

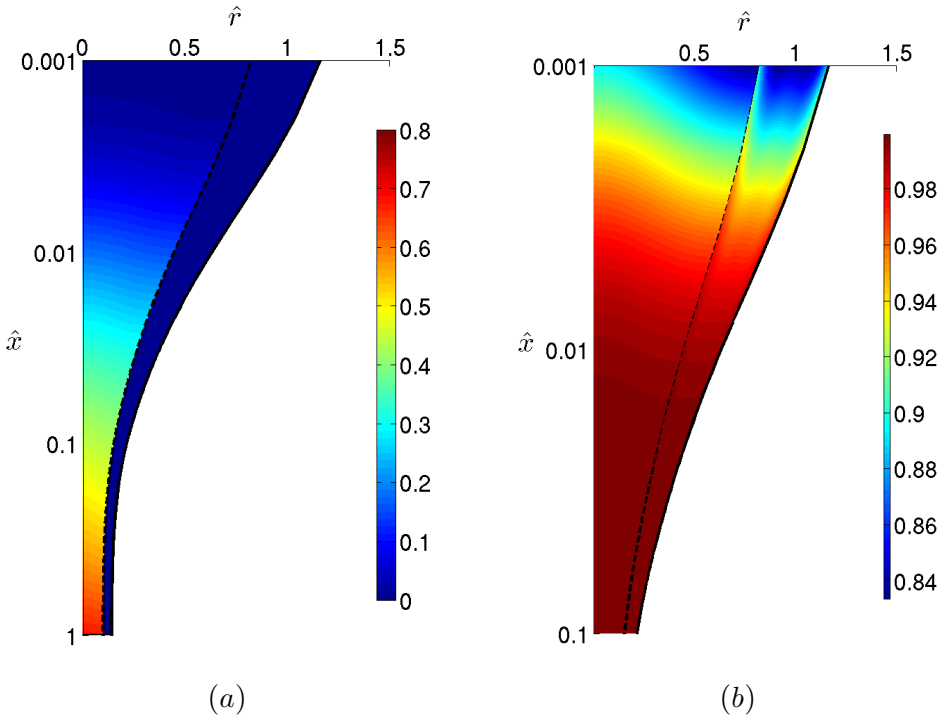

(a) (b)

Figure 5.9: *Distributions of the degree of crystallization* (a) *and molecular orientation order parameter for molecular orientation* (b) *for Case 3. (The* $\hat{x}$*–axis is in log scale in both figures.)*

As the thermal conductivity of the core is decreased, the boundary layer thickness formed at the cladding–surroundings interface decreases as illustrated in Figure 5.8. This figure also shows that the core presents a thermal core up to about $\hat{x} = 0.1$, there is a thermal boundary layer at the core–cladding interface, and the temperature at $\hat{x} = 1$ is still high at the compound fibre's centreline. As a consequence, the degree of crystallization of the core does not reach its ultimate value at the take–up point. However, a comparison between Figures 5.2 and 5.9 shows that the distributions of crystallinity and orientation for Cases 1 and 3 exhibit similar trends, thus indicating that the thermal conductivity of the core does not play a great qualitative role in these distributions when its value is varied from $\hat{k}_1 = 1$ to 5, while keeping $\hat{k}_2 = 1$. However, it plays a quantitative role as shown in Figure 5.10.

Figure 5.10 shows the cross–sectionally averaged values of the temperature, molecular orientation order parameter, degree of crystallization, and (logarithm of the) effective viscosity as well as the compound fibre's geometry and leading–order axial velocity component for Cases 1–3. Figure 5.10 shows that there is a strong contraction of the compound fibre near $\hat{x} = 0$ and the rate of this contraction increases as $\hat{k}_1$ is decreased; it also shows that the temperature is a decreasing function of the distance along the fibre, but the cross–sectionally averaged temperature is larger for small values of $\hat{k}_1$ than for large ones, and this result is in accord with those presented in Figures 5.1, 5.6 and 5.8.

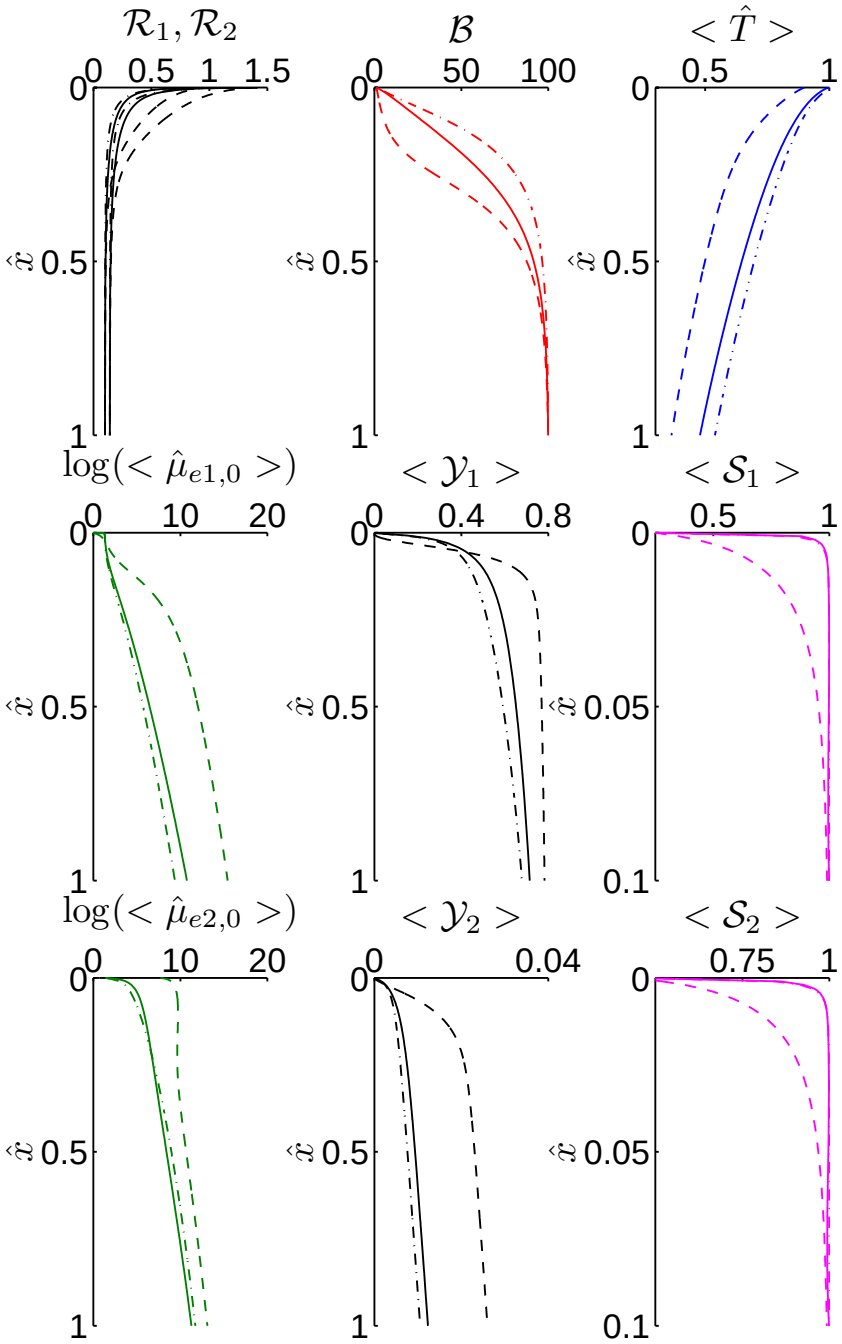

Figure 5.10: *(From left to right) Top row: fibre's radii, leading–order axial velocity, and cross-sectional averaged temperature. Middle row: Cross–sectionally averaged dynamic viscosity, degree of crystallization, and molecular orientation parameter for the core. Bottom row: Cross–sectionally averaged dynamic viscosity, degree of crystallization, and molecular orientation parameter for the cladding. (Case 1: —; case 2: – –; case 3: –·–).*

Figure 5.10 also shows that the axial velocity exhibits a one–sign curvature for Cases 1 and 3 and a two–sign one for Case 2, and this is due to the fact that the equation which governs the axial velocity component is one–dimensional and employs the cross–sectional average dynamic viscosity; this average depends on the temperature and the cross–section, and the latter is larger for the cladding than for the core.

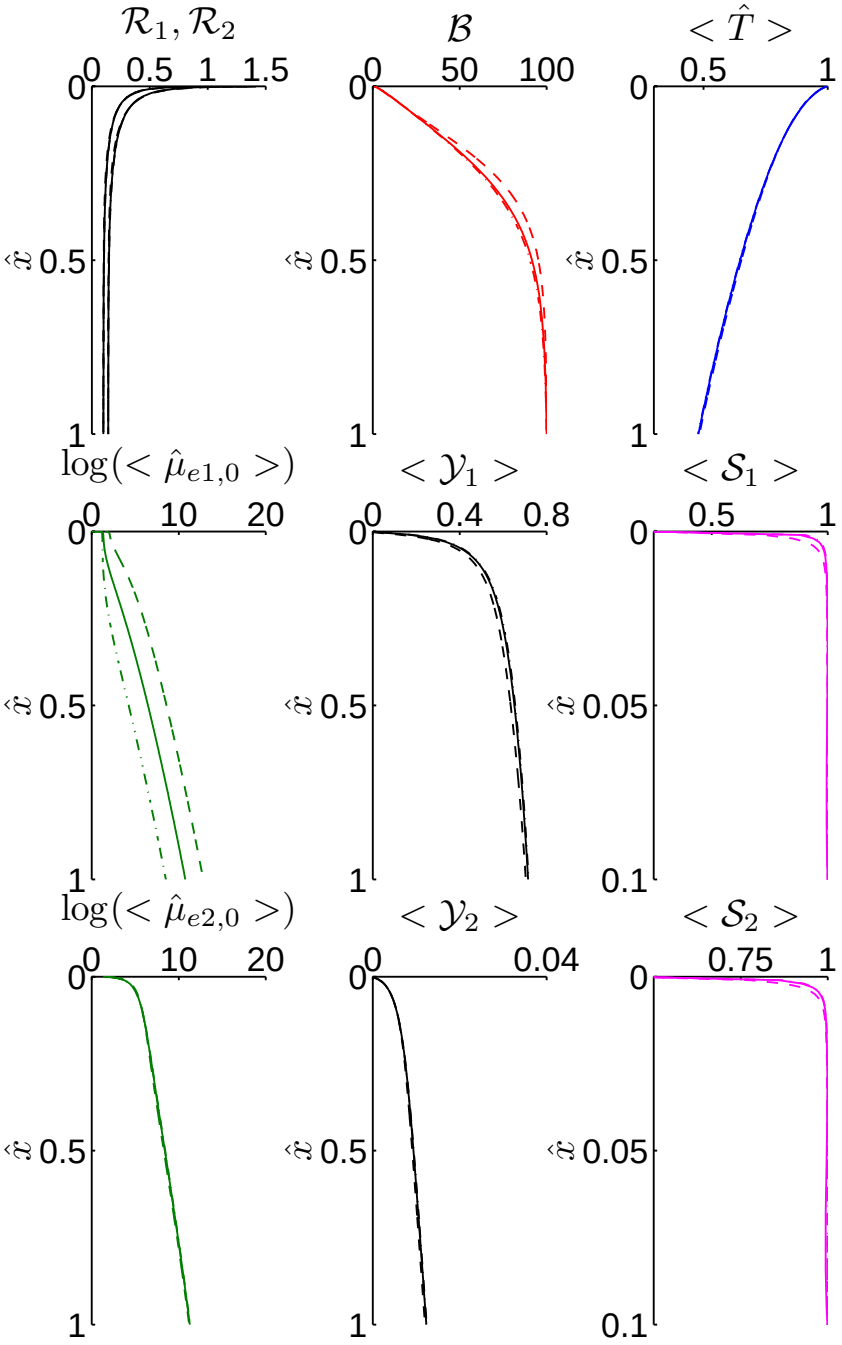

Figure 5.11: *(From left to right) Top row: fibre's radii, leading–order axial velocity, and cross-sectional averaged temperature. Middle row: Cross–sectionally averaged dynamic viscosity, degree of crystallization, and molecular orientation parameter for the core. Bottom row: Cross–sectionally averaged dynamic viscosity, degree of crystallization, and molecular orientation parameter for the cladding. (Case 1: —; case 4: – –; case 5: –·–).*

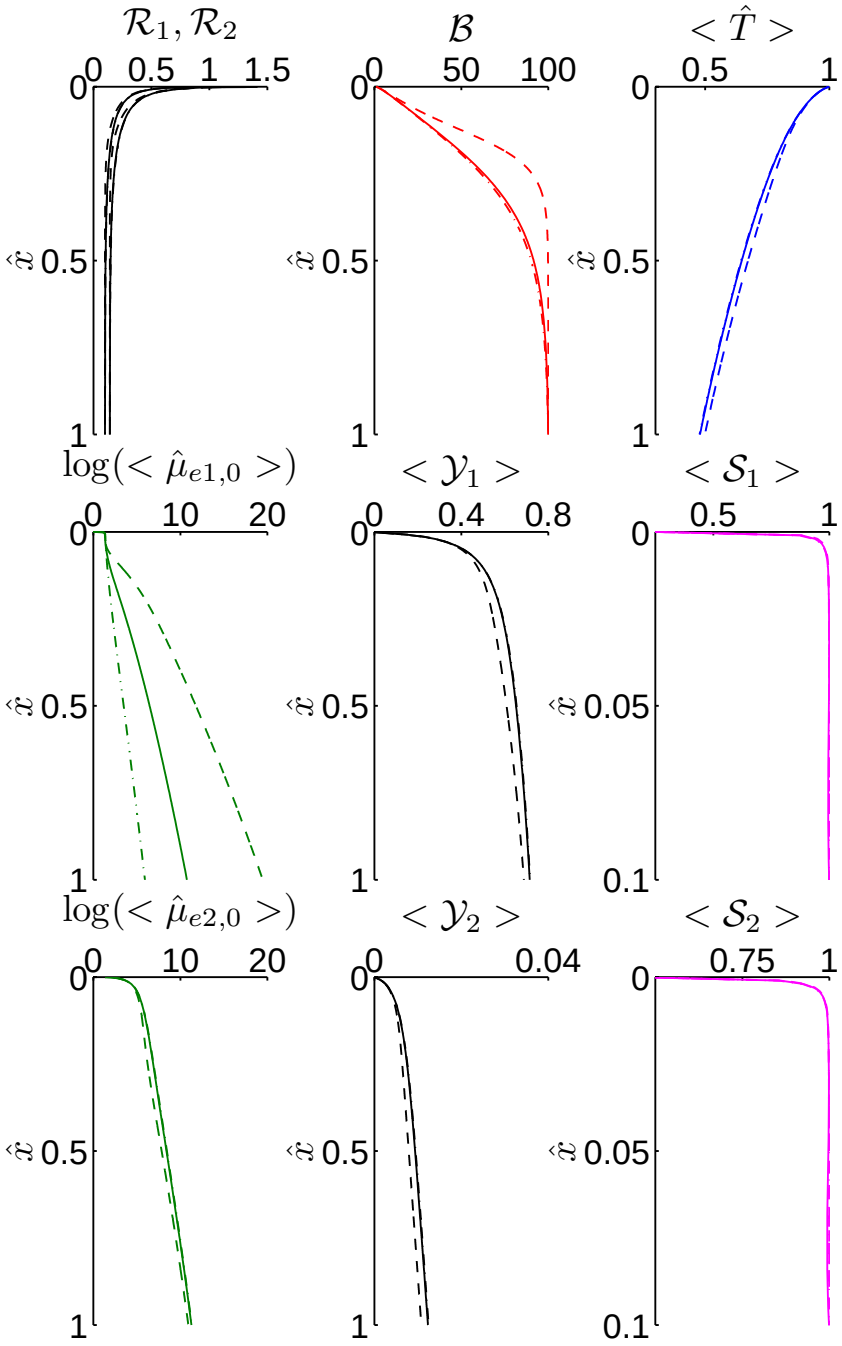

Figure 5.12: *(From left to right) Top row: fibre's radii, leading–order axial velocity, and cross-sectional averaged temperature. Middle row: Cross–sectionally averaged dynamic viscosity, degree of crystallization, and molecular orientation parameter for the core. Bottom row: Cross–sectionally averaged dynamic viscosity, degree of crystallization, and molecular orientation parameter for the cladding. (Case 1: —; case 6: – –; case 7: –·–).*

Since the initial contraction of the compound fibre for Case 2 is smaller than those for Cases 1 and 3, the initial axial strain rate is also smaller for Case 2 than for the other two cases, and these differences in strain rate are also observed in the molecular orientation order parameter shown in Figure 5.10; this parameter reaches a constant value of unity for Cases 1 and 3 at an axial location much smaller than that for Case 2. However, the ultimate degree of crystallization of Case 2 is reached before those for Cases 1 and 3 for both the core and cladding. This behaviour

is associated with the kinetics of the crystallization model employed in this study which indicates that the crystallization is mainly a function of the molecular orientation and the velocity field; therefore, an increase in the axial velocity component implies a shorter crystallization time as clearly observed in Figure 5.10 which, again, indicates that the axial velocity component is smaller for Case 2 than for Cases 1 and 3, except, of course, at the location of maximum swell and at the take–up point.

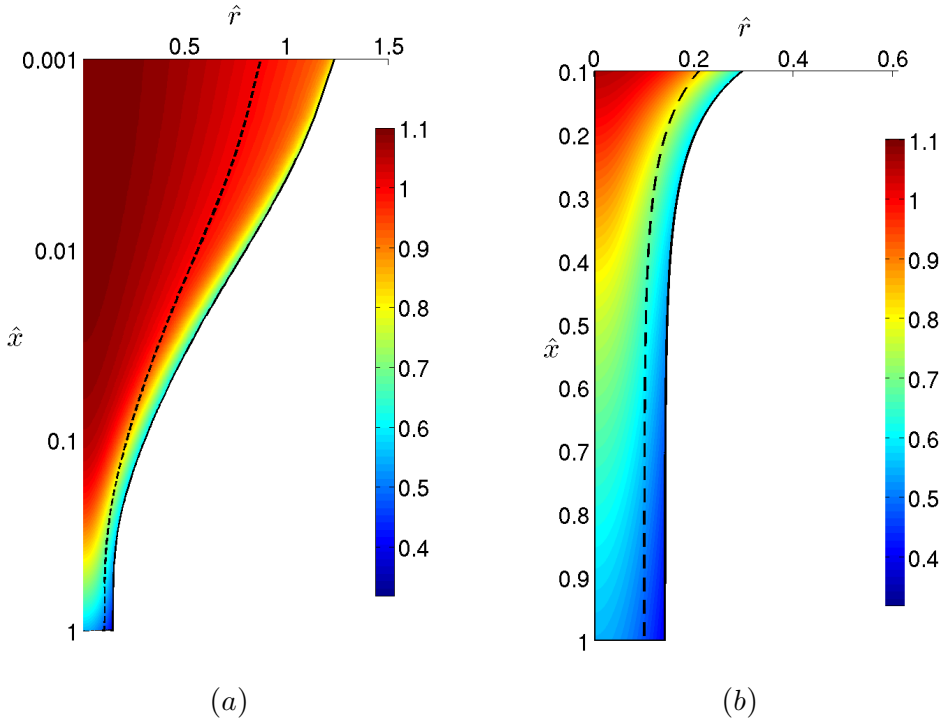

(a) (b)

Figure 5.13: *Temperature distribution for Case 9. (The vertical axis of the left figure is in log scale.)*

As shown in Figure 5.11, very few differences were observed among the cross–sectional averages of temperature, molecular orientation and crystallization between the results for Cases 4 and 5 and those for Case 1, except that Cases 4 and 5 result in slightly higher and smaller, respectively, axial velocities, slightly higher cross–sectionally averaged temperatures, and slightly smaller cross–sectionally averaged molecular orientation and crystallization than Case 1, and Case 4 resulted in a higher dynamic viscosity for the core than Cases 1 and 5. These results are to be expected, for they correspond to different pre–exponential factors of the Arrhenius dependence of the dynamic viscosity on the temperature of the core which, as shown in Figure 5.11,takes a longer distance to decrease its temperature and has a smaller cross–sectional area than the cladding.

On the other hand, Figure 5.12 indicates that there are very few differences in the cross–sectional averages of temperature, degree of crystallization and molecular orientation between Cases 1 and 7, whereas Case 6 predicts a smaller cross–sectionally averaged temperature, a larger initial contraction, axial velocity and dynamic viscosity for the core, smaller degrees of crystallization for both the core and the cladding, and an initially smaller viscosity for the cladding than Cases 1 and 7. Case 6 also requires a longer distance than Cases 1 and 7 to achieve complete molecular orientation.

Figures 5.13 and 5.14 correspond to Case 9 of Table 5.1. Figure 5.13 indicates a smaller initial contraction of the compound fibre than for Case 1, while Figure 5.14 shows a smaller crystallization and a longer region for achieving full molecular orientation than Case 1. The differences between Cases 1 and 9 are due to the larger pre–exponential factor of the dynamic viscosity of the cladding for Case 9.

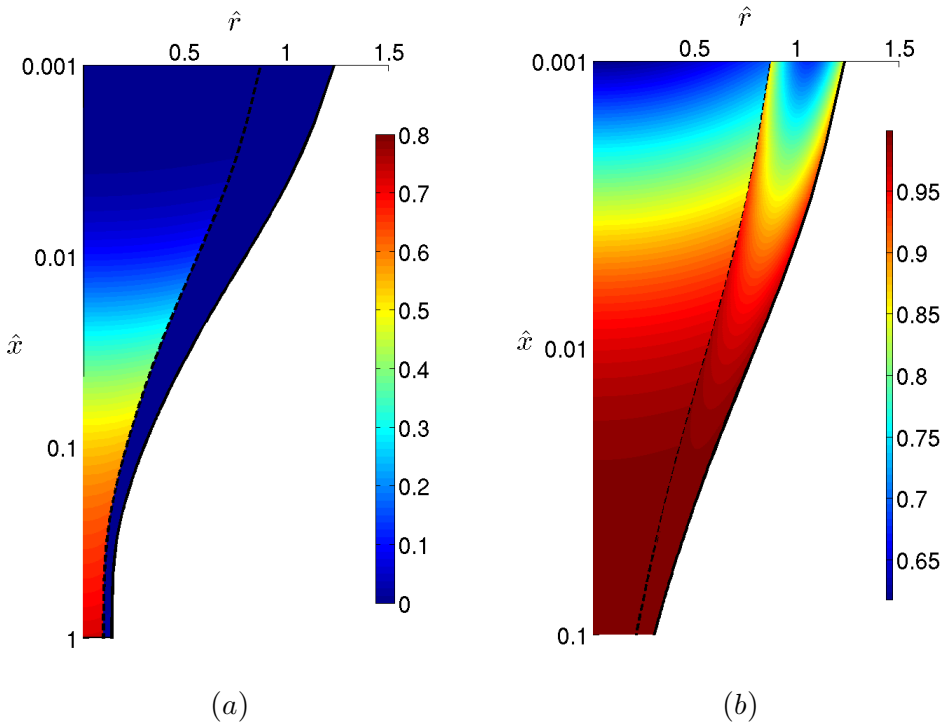

Figure 5.14: *Distributions of the degree of crystallization (a) and molecular orientation order parameter for molecular orientation (b) for Case 9. (The $\hat{x}$–axis is in log scale in both figures.)*

Although not shown here, the cross-sectional averaged temperature and the degrees of crystallization of the core and cladding are higher for Case 9 than for Case 1. On the other hand, the axial velocity is initially slightly smaller and then slightly larger for Case 9 than for Case 1, i.e., the two axial velocity profiles have an intersection point in the drawing region, and the degree of crystallization of the core and the molecular orientation for both the cladding and the core are slightly smaller for Case 9 than for Case 1.

The effects of the activation energy of the dynamic viscosity law of the core on the compound fibre can be appreciated by comparing the results presented in Figures 5.1 and 5.2 with those of Figures 5.15 and 5.16, respectively. Figure 5.15 shows a smaller initial contraction and a thicker boundary layer at the cladding–surroundings interface than Figure 5.1. On the other hand, the contraction of the compound fibre is higher at $\hat{x} = 0.1$ for Case 11 than for Case 1.

Figure 5.16 indicates that it takes longer distance to achieve full molecular orientation in Case 11 than in Case 1 for both the core and the cladding, but especially for the cladding. Figure 5.16 also shows that the degree of crystallization increases as the activation energy of the dynamic viscosity of the core is decreased.

Figures 5.17 and 5.18 illustrate the temperature, molecular orientation and crystallization fields for Case 13. Comparisons between Figures 5.1 and 5.2 and Figures 5.17 and 5.18 show that

the molecular orientation order parameter increases rapidly near $\hat{x} = 0$ towards a constant value of unity which corresponds to complete orientation but the rate at which this constant value is reached decreases as the Biot number is decreased; this result is consistent with the formulation presented here which indicates that the molecular orientation increases with the axial derivative of the leading–order axial velocity component. It should be pointed out that the solidification of the compound fibre is represented in this model by an increase of the effective dynamic viscosity which causes that the axial velocity component tend toward a constant value as illustrated in Figure 5.1 if the Biot number is sufficiently large.

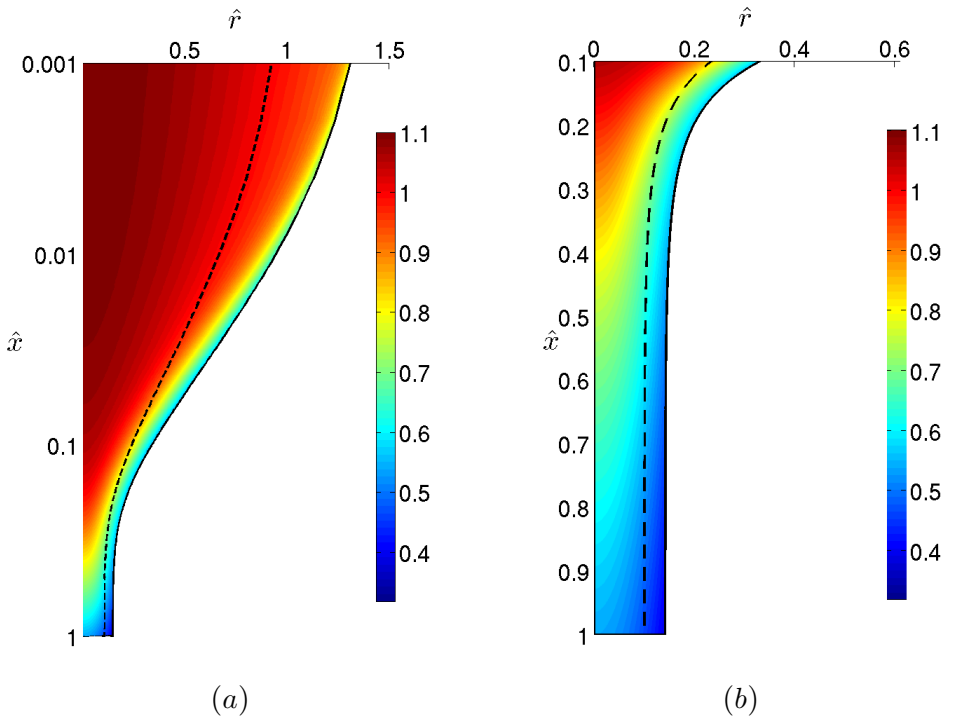

Figure 5.15: *Temperature distribution for Case 11. (The vertical axis of the left figure is in log scale.)*

Figures 5.1 and 5.17 also show that the contraction of the compound fibre increases as the Biot number is increased on account of the increase in heat losses, the corresponding drop in temperature and the increase in the dynamic viscosity due to the increase in the heat transfer as this number is increased and the no radial dependence of the axial velocity component employed in this study.

The degree of crystallization shown in Figure 5.18 increases with the axial distance along the compound fibre but decreases as the Biot number is increased. This result is consistent with the cross–sectionally averaged temperature discussed above and seems to indicate that the thermal crystallization dominates over the flow–induced one. This may be due to the single–phase, single–component approximation, the use of a Newtonian rheology, the neglect of latent heat effects associated with solidification, and the use of the Avrami–Kolmogorov kinetics which, in the Ziabicki's approximation employed here, plays a more important role than the flow–induced one.

Numerical simulations performed at different Biot numbers indicate that, depending on the parameters used, the leading–order axial velocity along the fibre may exhibit two different

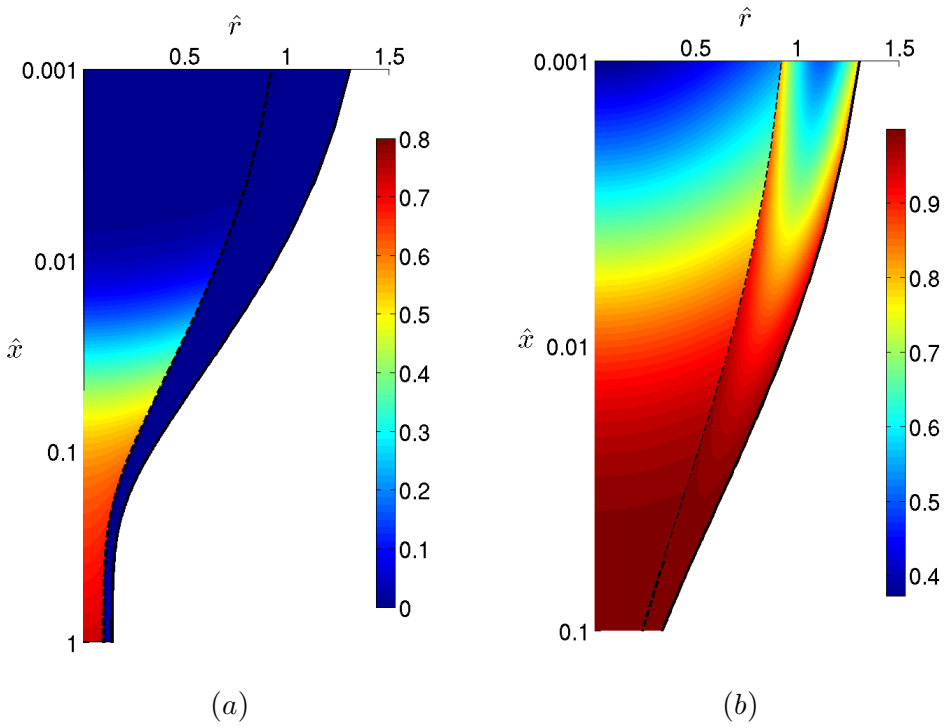

Figure 5.16: *Distributions of the degree of crystallization* (a) *and molecular orientation order parameter for molecular orientation* (b) *for Case 11. (The* $\hat{x}$*–axis is in log scale in both figures.)*

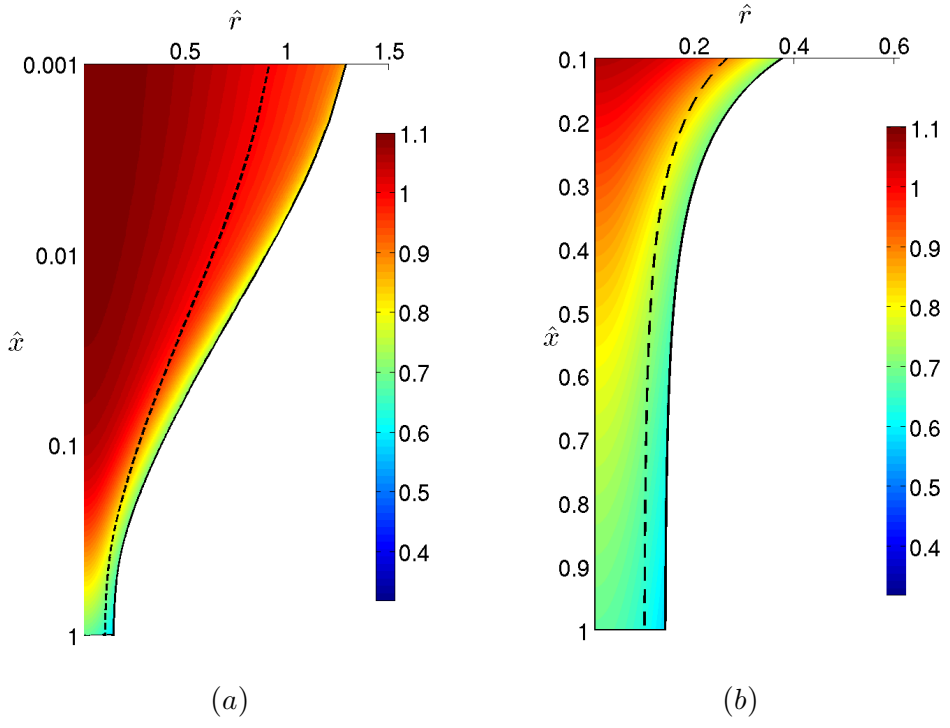

Figure 5.17: *Temperature distribution for Case 13. (The vertical axis of the left figure is in log scale.)*

curvatures at low Biot numbers, albeit only one for Biot numbers greater than unity. These simulations also indicate that, in some cases, the cross–sectionally averaged temperature and dynamic viscosity may increase as the Biot number is increased, despite the fact that the heat losses increase as this number is increased; this occurs because the cross–sectional area of the cladding is larger than that of the core.

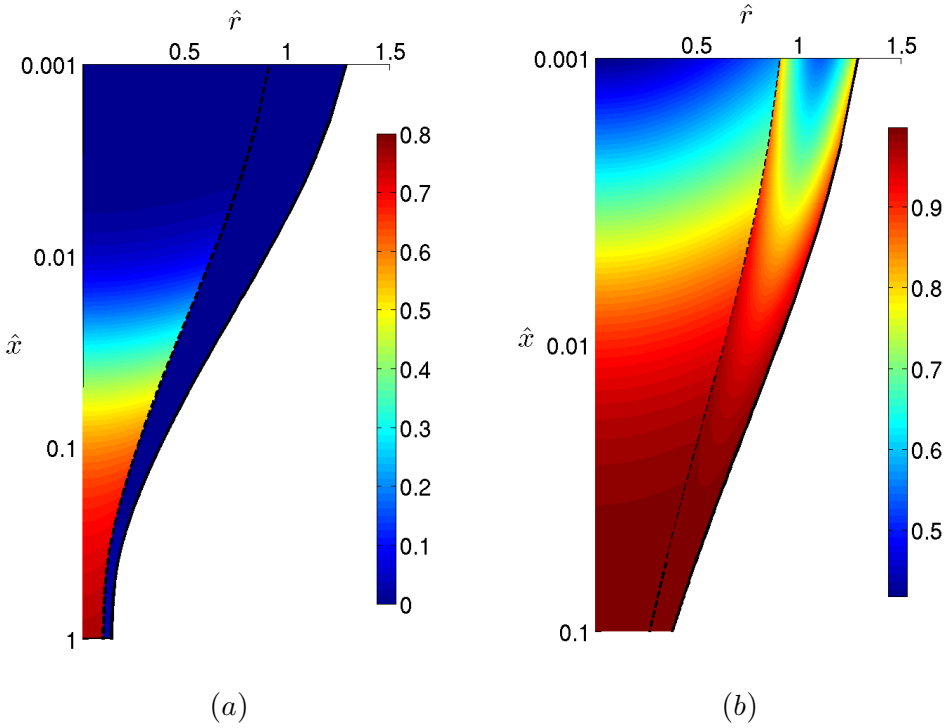

(a) (b)

Figure 5.18: *Distributions of the degree of crystallization* (a) *and molecular orientation order parameter for molecular orientation* (b) *for Case 13. (The* $\hat{x}$*–axis is in log scale in both figures.)*

Since, for example, for a Biot number equal to or greater than five, the axial velocity component reaches a constant value long before the take–up point, it has been found that, for the conditions considered here, the degree of crystallization is mainly a function of the temperature, i.e., it increases as the temperature decreases, in accord with the thermal formulation corresponding to the Avrami–Kolmogorov crystallization formalism employed in this study, and depends very little on the degree of molecular orientation, because almost complete orientation is achieved very near $\hat{x} = 0$. According to the model presented in this study, the molecular orientation is mainly a function of the axial strain rate and reaches its maximum close to the maximum swell location. Since the crystallization is mainly a function of the axial velocity field and this increases initially with the contraction of the compound fibre, and this contraction, in turn, increases with the cooling rate, one expects that the crystallization increases as the residence time is increased.

5.2.1 *Comparison between the two– and one–dimensional models*

In this subsection, we compare the results obtained with the two–dimensional model presented on Chapter 2 with those of the asymptotic one–dimensional model [121] that uses the slenderness ratio ($\epsilon = R_0/L$) as a perturbation parameter and results in a set of one–dimensional equations

for the compound fibre's radii, axial velocity component and temperature at low Reynolds and Biot numbers. It must be noted that there are two asymptotic one–dimensional models: one includes axial heat conduction and the other does not take into account axial conduction at all [121, 123]. These two models predict uniform temperature, crystallization and molecular orientation across the fibre; therefore, in order to compare their predictions with those of the two–dimensional model presented here, the values of these three quantities predicted by the two–dimensional model were cross–sectionally averaged.

As indicated above, the two–dimensional model uses one–dimensional equations for the compound fibre geometry and axial velocity component but solves a two–dimensional advection–diffusion equation for the temperature and two–dimensional hyperbolic equations for the components of the molecular orientation tensor and the degree of crystallization. This model shows that the temperature of the core is higher than that of the cladding because of heat losses.

Figure 5.19 shows comparisons between the two– and one–dimensional models when the latter accounts for axial heat conduction, and indicates that the two–dimensional model predicts a one–sign curvature axial velocity profile while the axial velocity predicted by the one–dimensional model exhibits a two–sign curvature sigmoid shape. Figure 5.19 also shows that the one–dimensional model which accounts for axial heat conduction predicts a higher temperature than the cross-sectional averaged one predicted by the two–dimensional model; it also predicts a larger contraction of the compound fibre, a smaller dynamic viscosity, and longer distances for achieving complete molecular orientation. The one-dimensional model which accounts for axial heat conduction also predicts slightly smaller and slightly larger degrees of crystallization for the cladding and core, respectively.

Although from Figure 5.19, it can be concluded that the two–dimensional model yields a cross–sectionally averaged temperature that exhibits the same qualitative features as that of the one–dimensional model which accounts for axial heat conduction, the latter is not able to predict accurately the temperature near the symmetry axis, at the core–cladding and, especially, at the cladding–surroundings interfaces. It must be noted that despite these differences between the one– and two–dimensional models, there are very few differences on the fibre's geometry, and averaged temperature, molecular orientation and crystallization at the take–up point, at least, for Case 1.

If axial conduction in the one–dimensional model is neglected, the following differences with respect to the two–dimensional model are observed. First, the one–dimensional model which does not account for axial heat conduction predicts a smaller temperature than the cross–sectionally averaged one of the two–dimensional model. Second, this one–dimensional model predicts a larger contraction of the fibre and an initially larger axial strain rate than the two–dimensional one. Third, the one–dimensional model which does not account for axial heat conduction requires longer distances to achieve complete molecular orientation and results in a smaller degree of crystallization than the two–dimensional one, as shown in Figure 5.20.

The results presented in Figures 5.19 and 5.20 indicate that, for the conditions presented here, axial conduction in one–dimensional models may be important, at least, for not too large thermal Péclet numbers.

For the conditions examined here and others not presented in this work, it has been observed that the molecular orientation parameter $\mathcal{S}$ reaches a value equal to unity very close to the section of maximum swell, i.e., $\hat{x} = 0$, and may decrease slightly thereafter if the source term in the equations for s_r and s_x which depend on the velocity gradient becomes smaller than the Maier–Saupe potential associated with the relaxation of the molecular chains. It must be noted

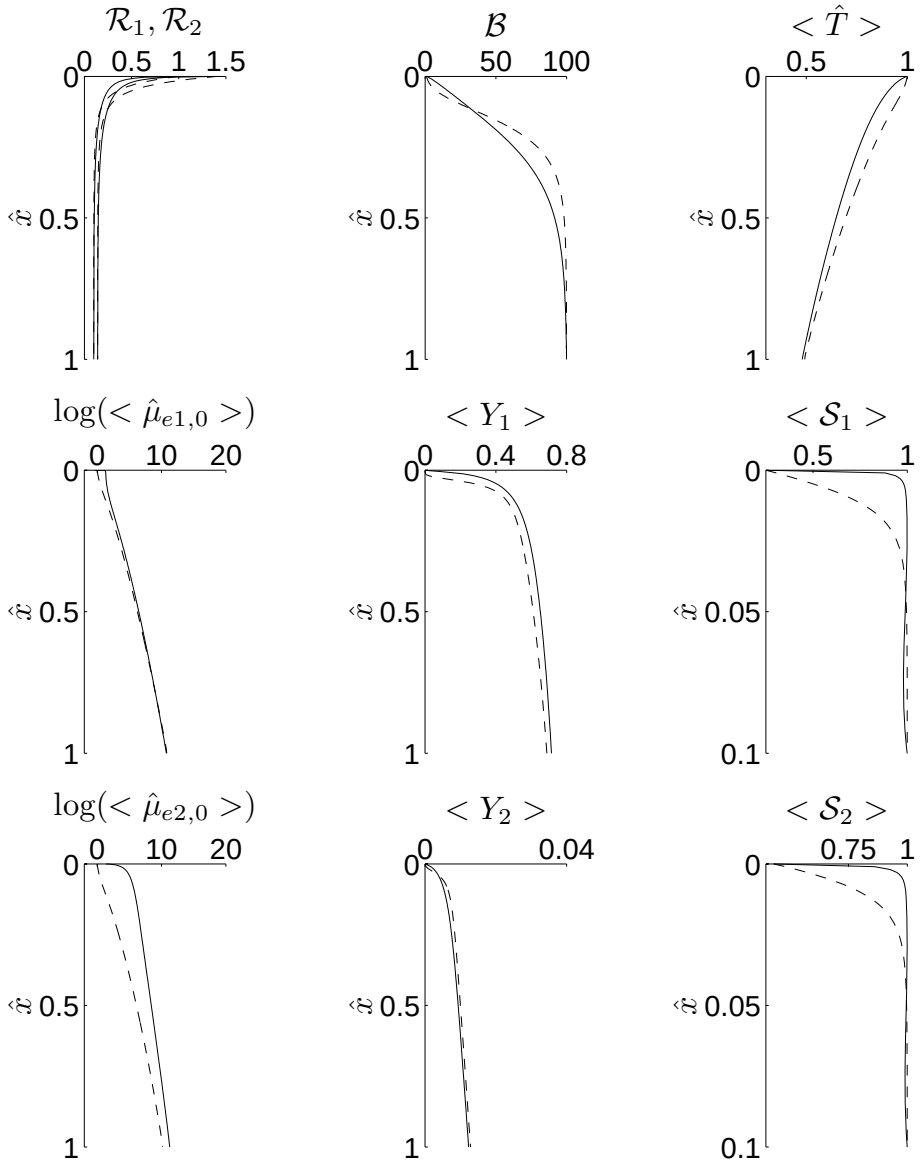

Figure 5.19: *(From left to right) Top row: fibre's radii, leading–order axial velocity, and cross-sectional averaged temperature. Middle row: Cross–sectionally averaged dynamic viscosity, degree of crystallization, and molecular orientation parameter for the core. Bottom row: Cross–sectionally averaged dynamic viscosity, degree of crystallization, and molecular orientation parameter for the cladding. Case 1. (Two–dimensional model: —; one–dimensional with axial conduction: – –).*

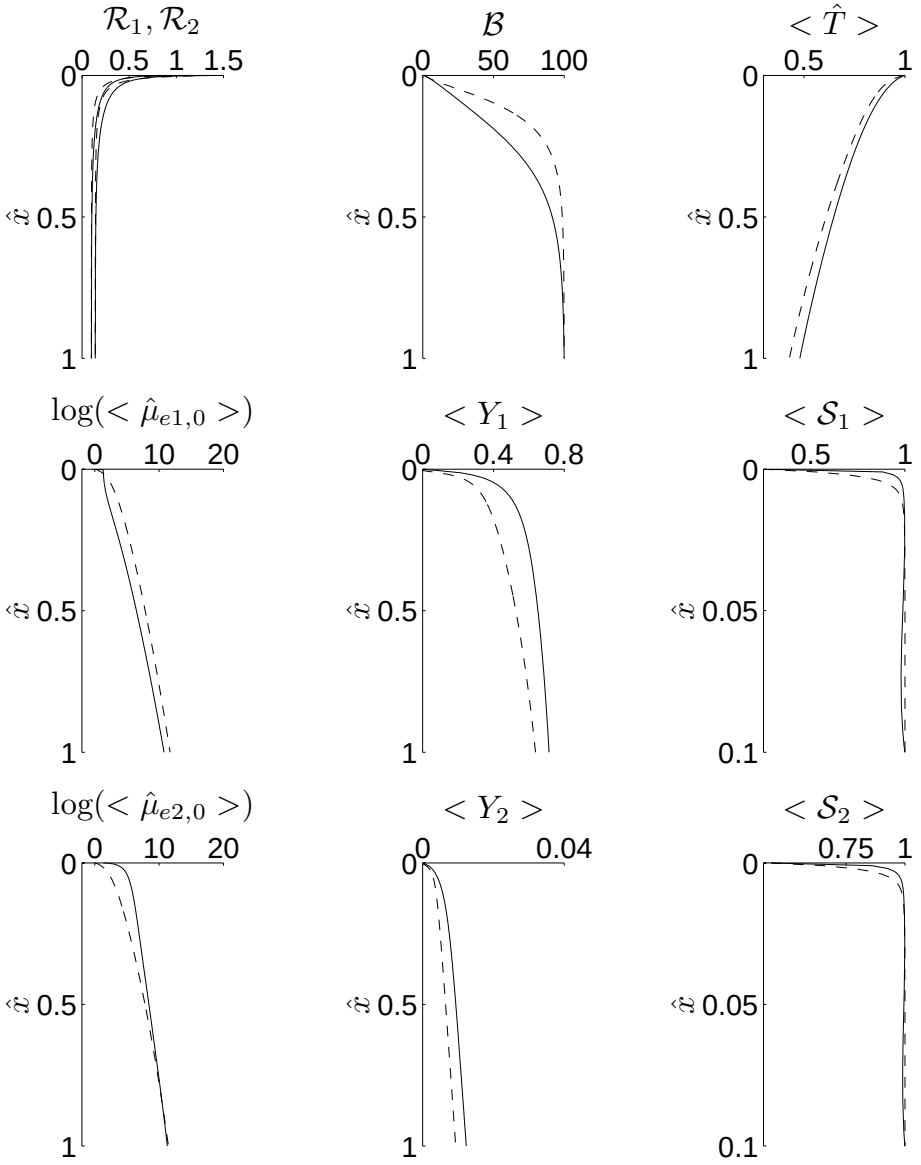

Figure 5.20: *(From left to right) Top row: fibre's radii, leading–order axial velocity, and cross-sectional averaged temperature. Middle row: Cross–sectionally averaged dynamic viscosity, degree of crystallization, and molecular orientation parameter for the core. Bottom row: Cross–sectionally averaged dynamic viscosity, degree of crystallization, and molecular orientation parameter for the cladding. Case 1. (Two–dimensional model: —; one–dimensional without axial conduction: – –).*

that, for $\Delta T = \Delta S_1 = \Delta S_2 = 0$, i.e., uniform distribution of the temperature and molecular orientation parameter at the maximum swell section, there are few differences between the degrees of crystallization predicted by the one– and two–dimensional models because the temperature at the maximum swelling section is assumed to be uniform across the fibre.

The two-dimensional model of the melt spinning or preform–drawing processes presented here has been built on the one–dimensional asymptotic models for slender compound fibres developed by Ramos [117, 121, 123] for isothermal and non–isothermal fibres. These one–dimensional models have been shown to predict correctly the onset of draw resonance under isothermal conditions, as well as the pulling/tension forces required to draw both single–component and compound amorphous fibres. For semi–crystalline fibres, these one–dimensional models predict the qualitative trends of the stresses reported by Shi et al. [132] who performed differential scanning calorimetry, wide–angle X–ray diffraction, birefringence and tensile tests on high-speed bi–component spinning of Poly(butylene terephthalate) (PBT) as sheath and Poly(butylene adipate–co–terephthalate) (PBAT) and found an improvement on the fibre's thermal and mechanical properties. Good qualitative agreement was also found between the predictions of the one–dimensional model and the experimental measured tensions obtained by Huang et al. [65] on bi–component fibres consisting of a sheath of PP and a core of Thermotropic Liquid–Crystalline Polymer (TLCP). Since the cross–sectionally averaged temperature, crystallization and molecular orientation fields predicted by the two–dimensional model presented in this paper show the same trends as the one–dimensional model, it may be stated that the tension predicted by the two–dimensional model presented in this paper is in good qualitative agreement with the tension measured experimentally on both amorphous and semi–crystalline compound fibres. However, such an agreement may not be a good indicator of either the accuracy or the predictive capabilities of one– and two–dimensional models because tension is a global value and the accuracy of one– and two–dimensional models should also include comparisons with experimentally measured local values of molecular orientation, crystallization, temperature, etc., which may be very difficult (or impossible) to measure accurately in a direct manner in melt spinning processes. In addition, as indicated above, the two–dimensional model presented here is a single–phase one that employs a Newtonian rheology, and may need to account for more realistic rheologies and two–phase effects associated with the liquid as well as the amorphous and crystalline phases as well as for the crimp contraction and thermal shrinkage [105], weight loss [152], interfacial instabilities at the core–cladding interface [21, 22], etc., observed in the processing of PET, PBT–PET, PE–PET, etc., bi–component fibres.

5.3 CONCLUSIONS

In this chapter, it has been found that the most important parameters that affect the thermo–fluid–dynamics characteristics of solidifying compound fibres are associated with the pre–exponential factor and activation energy of the dynamic viscosity for the cladding, the thermal conductivity of the cladding, and the Biot number. For Biot numbers larger than unity, it has been observed that the axial velocity profile is monotonously increasing until it reaches a constant value and has a one–sign curvature, whereas, at lower Biot numbers, it may have a two–sign curvature. It has also been shown that the Doi–Edwards formulation adopted here together with the Maier–Saupe potential predicts an almost complete molecular orientation near the maximum swell location where the largest contraction of the fibre occurs, while the degree of crystallization increases as the residence time is increased.

For the conditions analysed here, it was found that crystallization is mainly controlled by the thermal Avrami–Kolmogorov kinetics formulation and that flow–induced crystallization is small. This has been attributed to the fact that, in the single–phase model employed here, solidification is associated with a large increase in dynamic viscosity as the temperature decreases and the viscosity dependence on temperature exerts a greater influence than the effects of crystallization (and molecular orientation) on the dynamic viscosity.

Comparisons between the predictions of the two–dimensional model presented here and one–dimensional ones which either account or do not account for axial conduction indicate that, even though substantial differences between these models exist near the maximum contraction region, these models predict similar qualitative trends, at least, for the moderate Péclet numbers and conditions considered here.

The two–dimensional model shows that substantial temperature non–uniformities in the radial direction exist even at moderately low Biot numbers. These non–uniformities affect the degree of crystallization and may have great effects on the mechanical, electrical, optical, etc., properties of compound fibres. For very slender fibres and small Biot numbers, good agreement between predictions of one–dimensional models and the two–dimensional one have been observed.

6

NUMERICAL SIMULATIONS OF SEMI–CRYSTALLINE HOLLOW COMPOUND FIBRES

Contents

6.1 PRESENTATION OF NUMERICAL RESULTS

In this section, some sample results[†] obtained with the two–dimensional melt spinning model for semi–crystalline hollow compound fibres described in § 4.2 are presented. Unless otherwise stated, the results shown here correspond to the same thermal conductivities and pre–exponential factors and activation energies of the dynamic viscosity laws of the inner and outer hollow jets, a constant film heat transfer coefficient at the outer jet's outer interface that corresponds to a constant external Biot number, i.e., Bi_2, Reynolds, Prandtl and Froude numbers equal to one, and no surface tension ($1/\bar{C} = 0$). In addition, we have set $\mathcal{R}_1^2(0) = 1$, $\mathcal{R}^2(0) = 2$ and $\mathcal{R}_2^2(0) = 3$, so that $Q_1 = Q_2 = Q/2 = 0.5$, i.e., the non–dimensional volumetric flow rates of the inner and outer jets are identical, and the non–dimensional axial velocity at the maximum swell cross–section is unity, i.e., $\mathcal{B}(0) = 1$.

The values of other parameters employed in the simulations reported in this section are, unless stated otherwise, $\hat{\rho}_i = \hat{C}_1 = \hat{k}_1 = 1$, $\hat{h}_2 = 1$, $\sigma_i/\sigma = 1$, $D_1 = 1$, $\beta_i = 4$, $n_i = 12$, $\alpha_i = 5$; $\hat{\lambda}_{i,0} = 1$, $\omega_i = 0$, $\phi_i = 0.5$, $N_i = 4$, $k_{Ai}(0) = 0.005$, $a_{2i} = 10$; $T_{i,\infty} = 0$;and, $\mathcal{Y}_{i,\infty} = 0.8$ and $\mathcal{Y}_i(\hat{r}, 0) = 0$.

For the simulations carried out in the present chapter, a uniform temperature profile, $\hat{T}(\xi, 0) = 1$, has been considered for hollow compound fibres at the maximum swell cross–section. This may be obtained imposing $\Delta T = 0$ in Eq. (5.1).

The following initial conditions for the molecular orientation tensor have been used in this chapter

$$s_{i\,r}(0, \hat{r}) = \mathcal{S}_{i0}, \qquad s_{i\,x}(0, \hat{r}) = 2\,\mathcal{S}_{i0}, \qquad i = 1, 2, \tag{6.1}$$

where $\mathcal{S}_{i0} = \mathcal{S}_i(0, \hat{r})$, and parabolic profiles for the molecular orientation order parameter of the hollow compound fibre at the maximum swell cross–section, i.e., $\eta = 0$, were imposed following expressions given by Eq. (5.2) where $\xi_I = \frac{Q_1}{Q}$ corresponds to the interface between the inner and

[†]Most of text and figures presented in this chapter have been taken from the submitted version of the manuscript [11].

outer hollow jets and $\Delta S_i < \min(S_{i0}, 1 - S_{i0})$ for $i = 1, 2$. The results presented here correspond to, $(S_{10}, \Delta S_1) = (0.20, 0.10)$ and $(S_{20}, \Delta S_2) = (0.40, 0.20)$ and a draw ratio, D_r, is equal to 100 (moderate drawing speeds) which allow us to neglect the air drag of the gases surrounding $(\hat{\mathcal{T}}_2 = 0)$ and enclosed by $(\hat{\mathcal{T}} = 0)$ the hollow compound fibre. The values of other parameters employed in the numerical simulations reported in this section are summarized in Table 6.1.

Table 6.1: *Values of the parameters employed in the simulations for semi–crystalline hollow compound fibres.*

Case	Bi	$\hat{H}_1$	$\hat{H}_2$	$\bar{P}_2$	$\frac{\hat{k}_2}{\hat{k}_1}$	$\frac{\hat{D}_2}{\hat{D}_1}$	$\hat{h}_1$
1	4	20	20	1	1	1	0
2	2	20	20	1	1	1	0
3	4	10	20	1	1	1	0
4	4	20	10	1	1	1	0
5	4	20	20	10	1	1	0
6	4	20	20	1	10	1	0
7	4	20	20	1	1	10	0
8	4	20	20	1	1	0.1	0
9	4	20	20	1	1	1	0.5
10	2	20	20	1	1	1	0.5
11	4	10	20	1	1	1	0.5
12	4	20	10	1	1	1	0.5
13	4	20	20	10	1	1	0.5
14	4	20	20	1	10	1	0.5
15	4	20	20	1	1	10	0.5
16	4	20	20	1	1	0.1	0.5
17	4	20	20	1	1	1	1
18	2	20	20	1	1	1	1
19	4	10	20	1	1	1	1
20	4	20	10	1	1	1	1
21	4	20	20	10	1	1	1
22	4	20	20	1	10	1	1
23	4	20	20	1	1	10	1
24	4	20	20	1	1	0.1	1

Although all the cases considered in Table 6.1 have been studied, only the most relevant results (parameters whose changes cause greater effect on the results) will be explained in some detail in this section. The cross–sectionally averaged temperature, orientation order parameter and degree of crystallization at take–up cross–section are presented in Table 6.2.

Figure 6.1 corresponds to Case 1 of Table 6.1 and illustrates the temperature distribution across the hollow compound fibre at various axial locations, as well as the iso–contours of the molecular orientation order parameter, temperature and degree of crystallization. This figure clearly indicates that the orientation order parameter reaches its maximum value of unity close to the maximum swell region, while the degree of crystallization tends in a much smoother manner to (but does not reach) its ultimate value of 0.8. Figure 6.1 also illustrates the lack of

continuity of the degree of crystallization at the inner–outer hollow jets' interface which is due to the initial conditions employed in this study and the hyperbolic character of the equations for the molecular orientation tensor and the degree of crystallization. Although not shown here, it has been found that the magnitude of the discontinuities of both the order parameter and the degree of crystallization at the interface between the inner and outer hollow jets decreases along the hollow compound fibre.

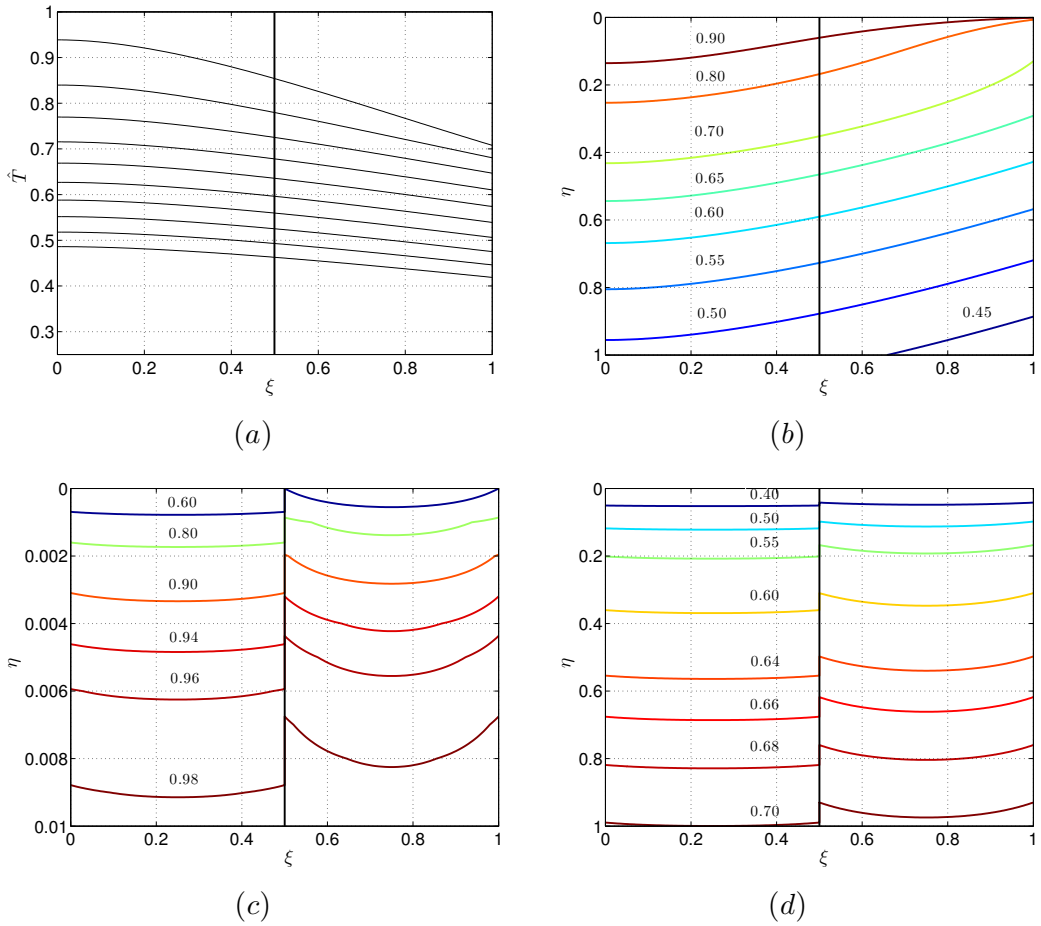

Figure 6.1: *Temperature distribution at* $\eta = 0, 0.1, \ldots, 1$ *(a), and iso–contours of temperature (b), molecular orientation order parameter (c) and degree of crystallization (d) for Case 1 of Table 6.1.*

Figure 6.1 also shows that the temperature is smooth, has a zero radial derivative at the the inner jet's inner interface and exhibits a boundary layer at the outer jet's outer interface. This figure also indicates that, initially, there is a large drop in temperature at the hollow fibre's outer interface.

Although not shown here, Case 2 of Table 6.1 requires a longer axial distance to achieve complete molecular orientation and reaches a higher degree of crystallization in the inner and outer hollow jets at the take–up cross–section than Case 1. This is due to the fact that the Biot number for Case 2 is half that for Case 1 and, as a consequence, Case 2 has lower heat transfer losses and takes a longer distance to solidify than Case 1 as illustrated in the temperature profiles exhibited in Figure 6.2. Since the heat transfer losses for Case 2 are lower than in Case 1, the hollow compound fibre's initial contraction for Case 2 is smaller than that for Case

1 and this results in smaller components of the strain rate tensor, a smaller flow–orientation interaction tensor, and smaller values of the components of the molecular orientation tensor. As a consequence, both the axial velocity component and the linearised crystal growth rate for Case 2 are smaller than that for Case 1. The net result of this is that Case 2 achieves a higher degree of crystallization than Case 1 at the take–up cross–section.

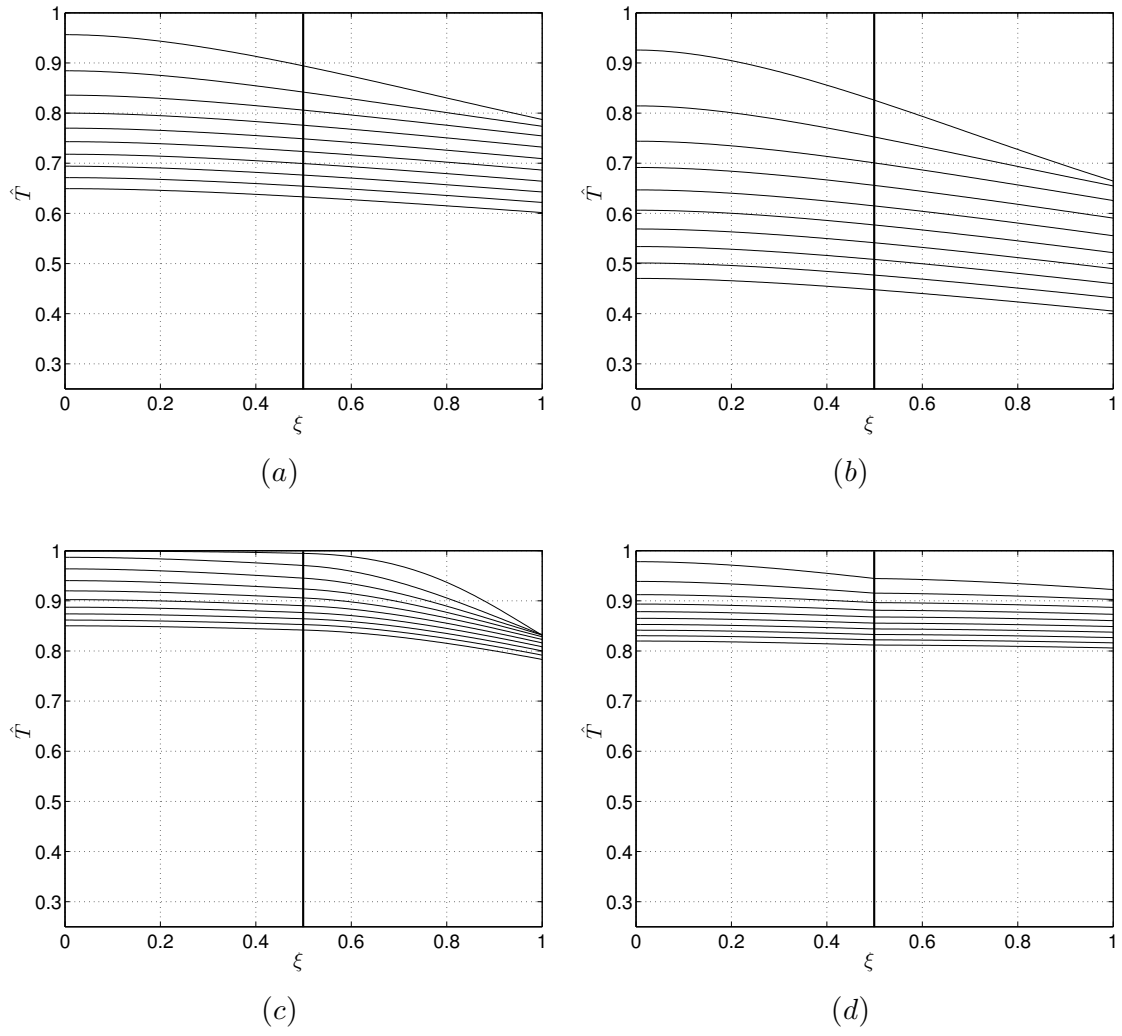

Figure 6.2: *Temperature distributions at* $\eta = 0, 0.1, \ldots, 1$ *for Case 2* (a)*, Case 4* (b)*, Case 5* (c) *and Case 6* (d) *of Table 6.1.*

Figure 6.3 shows the velocity field near the maximum swell region and clearly illustrates the hollow compound fibre contraction. Neither the immediate vicinity of the maximum swell region nor the region close to the take–up cross–section are presented in the figure for clarity reasons. Note that, for the conditions considered here, the axial velocity component at the take–up cross–section is one hundred times that at the maximum swell region; therefore, drawing velocity vectors beyond the cross–section at which solidification occurs would unnecessarily clutter the figure. On the other hand, as shown in Figure 6.3, the axial velocity component increases substantially near the maximum swell region and, therefore, the velocity vectors in the immediate vicinity of that region would not appear clearly if they were drawn.

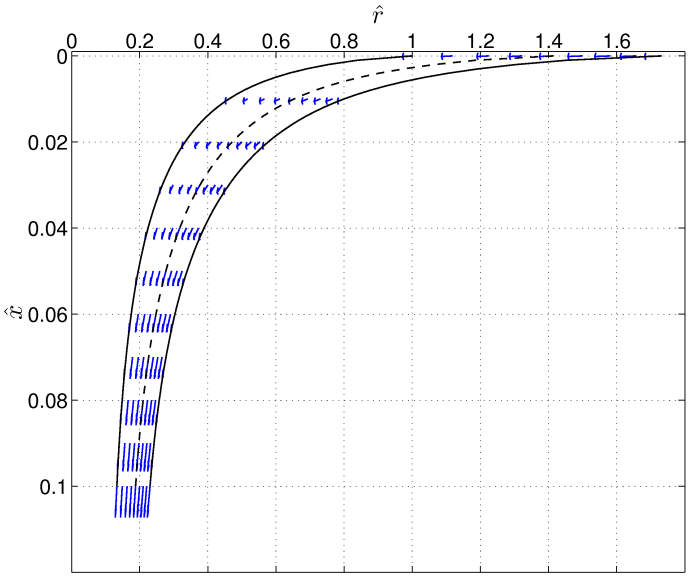

Figure 6.3: *Velocity field for Case 1.*

It has also been found that Case 3 exhibits similar molecular orientation, temperature and crystallization profiles to those of Case 1, except that the inner jet's effective dynamic viscosity is higher for Case 1 than for Case 3, and this is in accord with the values of the parameters shown in Table 6.1, for the activation energy of the effective dynamic viscosity of the inner jet for Case 2 is half that of Case 1, and the inner hollow jet is subject to adiabatic conditions at its inner interface.

Case 4 shows similar temperature profiles to those of Case 1 as illustrated in Figure 6.2 despite the fact that the activation energy of the Arrhenius dependence of the effective viscosity law of the hollow compound fibre's outer jet for Case 1 is twice that for Case 4 and, as a consequence, for the same heat transfer losses, the effective viscosity of the outer jet is lower for Case 4 than for Case 1. In addition, the initial jet contraction is larger for Case 1 than for Case 4 and, therefore, Case 4 requires a longer axial distance to achieve complete molecular orientation and, for the same reasons as discussed above for Case 2, Case 4 reaches a higher degree of crystallization at the take–up cross–section than Case 1. Although not shown here, the axial velocity profile for Case 4 is initially smaller than that for Case 1, but it exceeds it before they both reach the same constant value.

The temperature profiles for Case 5 shown in Figure 6.2 indicate that the fibre's temperature drop decreases as the thermal Péclet number is increased. Moreover, as this number is increased, the heat transfer losses and the initial contraction of the hollow fibre decrease, and, as a consequence, the magnitude of the components of the strain rate tensor and the molecular orientation order parameter decrease and, therefore, a larger axial distance is required to achieve complete molecular orientation for Case 5 than for Case 1. In addition, the effective dynamic viscosities of the inner and outer jets decrease as the Péclet number is increased and, for the same reasons as the ones discussed above for Case 2, the degree of crystallization at the take–up cross–section for both the inner and the outer jets is larger for Case 5 than for Case 1.

Case 6 yielded analogous results for the molecular orientation and the degree of crystallization to those of Case 5. However, substantial differences are observed in the temperature profiles

for these two cases, especially near the outer jet's outer interface and at the inner–outer jet interface where the temperature is continuous by its gradient is not, due to the different thermal conductivities for the inner and outer jets, as illustrated in Figure 6.2.

Figure 6.4 corresponds to Case 17 of Table 6.1 which includes heat transfer at the inner jet's inner interface. As a consequence, the temperature decreases at a faster rate for Case 17 than for Case 1. This decrease is accompanied by an initial larger contraction of the hollow compound fibre and an increase in the components of the strain rate tensor. As a consequence, Case 17 reaches complete molecular orientation earlier than Case 1, but the degree of crystallization at the take–up cross–section is larger for Case 1 than for Case 17. Also, since the heat transfer losses are larger for Case 17 than for Case 1, the effective dynamics viscosities of both the inner and the outer hollow jets are larger for Case 17 than for Case 1.

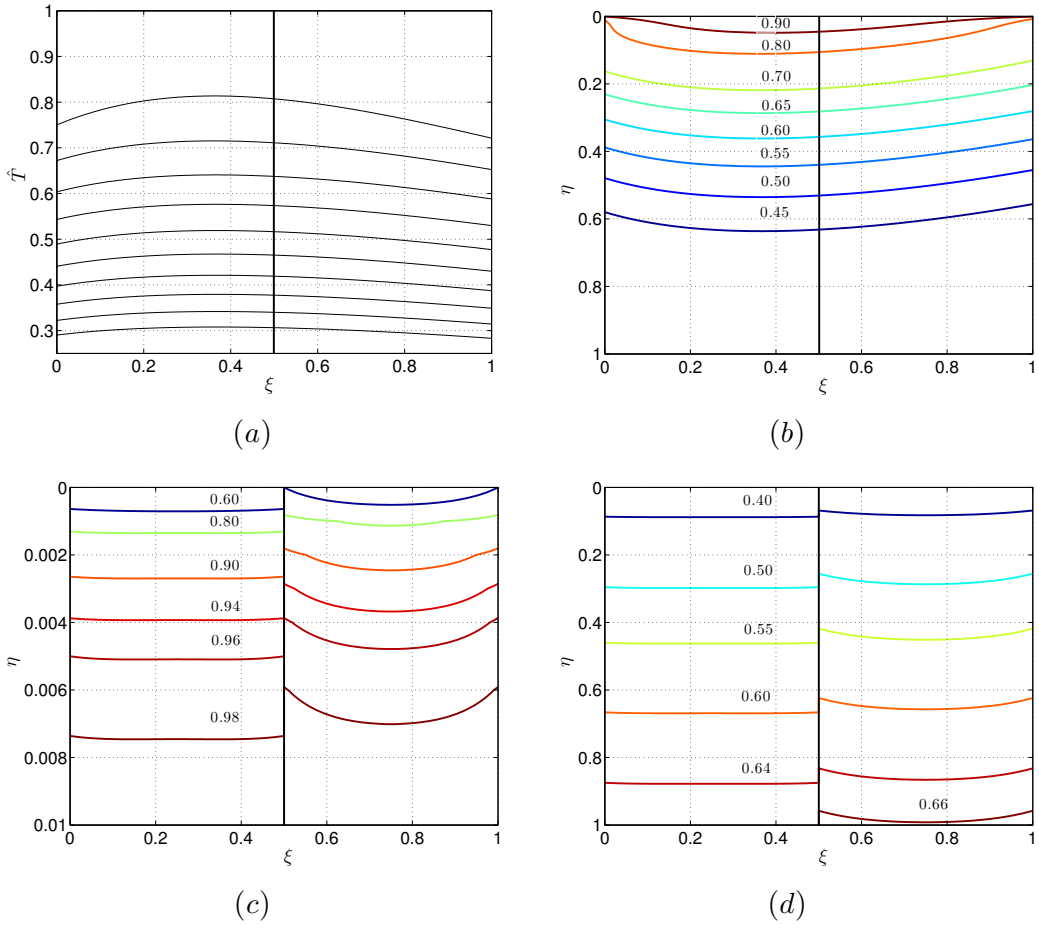

Figure 6.4: *Temperature distribution at* $\eta = 0, 0.1, \ldots, 1$ (a)*, and iso–contours of temperature* (b)*, molecular orientation order parameter* (c) *and degree of crystallization* (d) *for Case 17 of Table 6.1.*

Figure 6.4 also shows that the temperature gradient at the inner jet's inner interface is larger than that at the outer jet's outer interface and that the temperature at the take–up cross–section for Case 17 is lower than that for Case 1.

Figure 6.5 illustrates the temperature distributions for Cases 18, 20, 21 and 22. This figure clearly shows that the temperature gradient at the outer jet's outer interface decreases as the film heat transfer coefficient at that interface is decreased; a similar behaviour is observed at the

inner jet's inner interface. Figure 6.5 also indicates that there are very few qualitative differences between the temperature profiles corresponding to Cases 17 and 20, albeit the temperature at the take–up cross–section is lower for Case 20 than for Case 17.

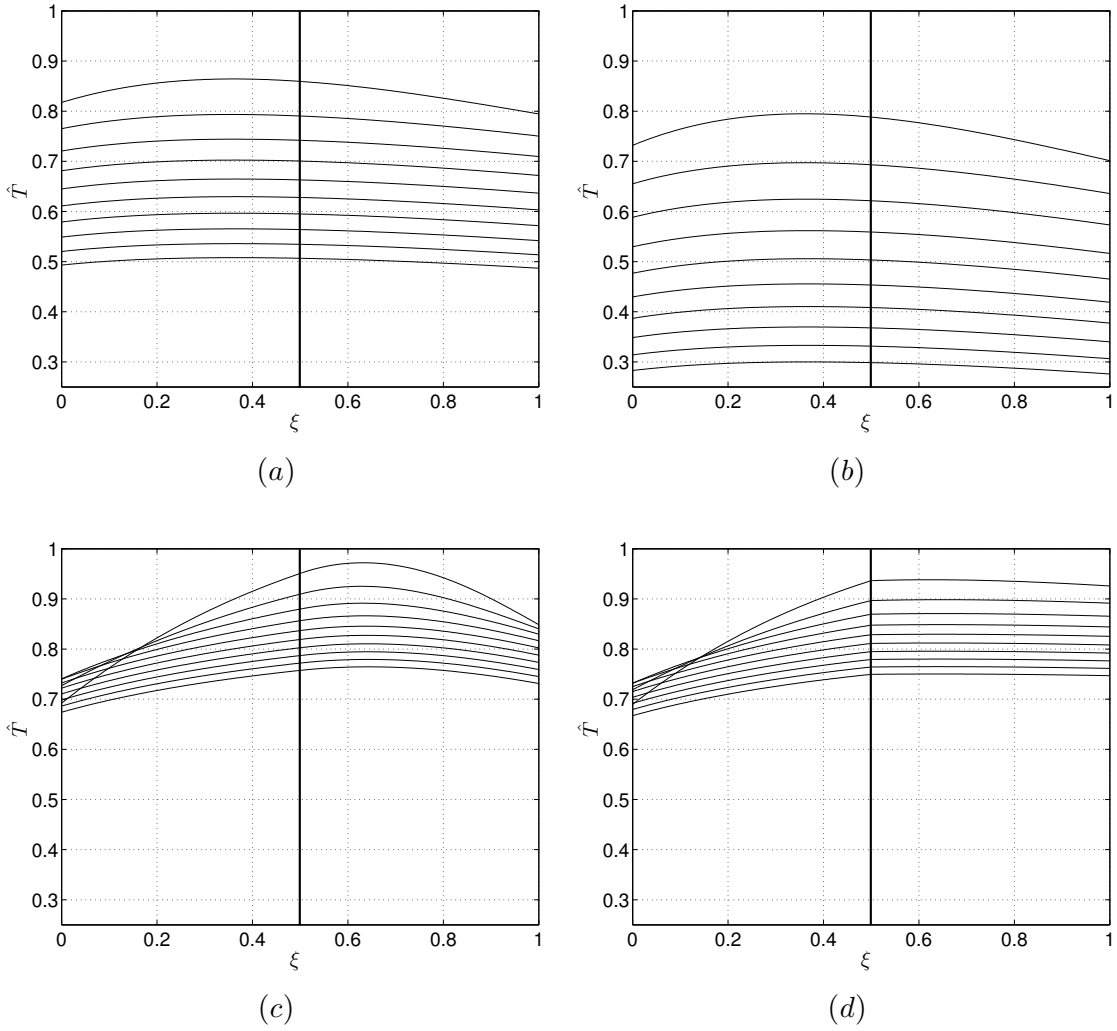

Figure 6.5: *Temperature distributions at* $\eta = 0, 0.1, \ldots, 1$ *for Case 18* (a)*, Case 20* (b)*, Case 21* (c) *and Case 22* (d) *of Table 6.1.*

The temperature profiles corresponding to Case 21 illustrated in Figure 6.5 clearly show the coupling between the thermal processes in the inner and outer hollow jets and, in particular, the larger heat transfer losses at the inner jet's inner interface ($\frac{\partial \hat{T}_1}{\partial \xi}(0, \eta)$) as the Péclet number of the outer jet is increased. For Case 22, the results presented in Figure 6.5 indicate that the temperature is continuous at the inner–outer hollow jets' interface and the discontinuity in the temperature gradient there is due to the different thermal conductivities of the inner and outer jets.

Figures 6.6– 6.8 illustrate the hollow compound fiber's geometry, axial velocity component and cross–sectionally averaged temperature, and the cross–sectional averages of the effective dynamic viscosity, molecular orientation order parameter and degree of crystallization for each annular jet, respectively, for Cases 1, 9 and 17 of Table 6.1.

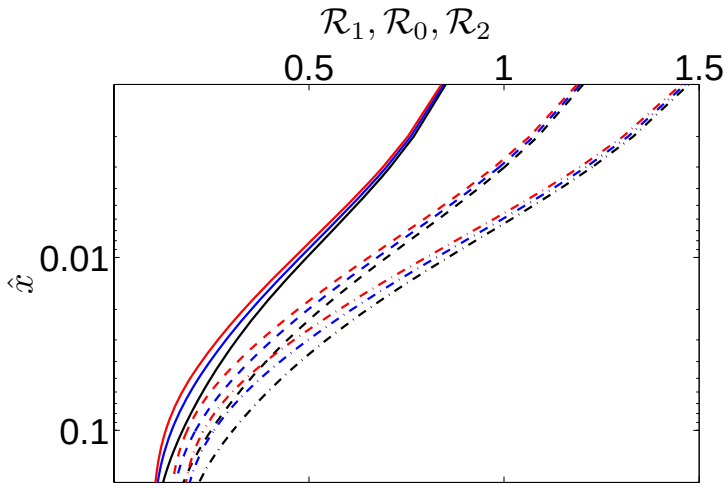

Figure 6.6: *Hollow compound fiber's geometry. ($\mathcal{R}_1$: —; $\mathcal{R}_0$: – –; $\mathcal{R}_2$: –·–). (Case 1, black curves; Case 9, blue curves; Case 17 red curves.)*

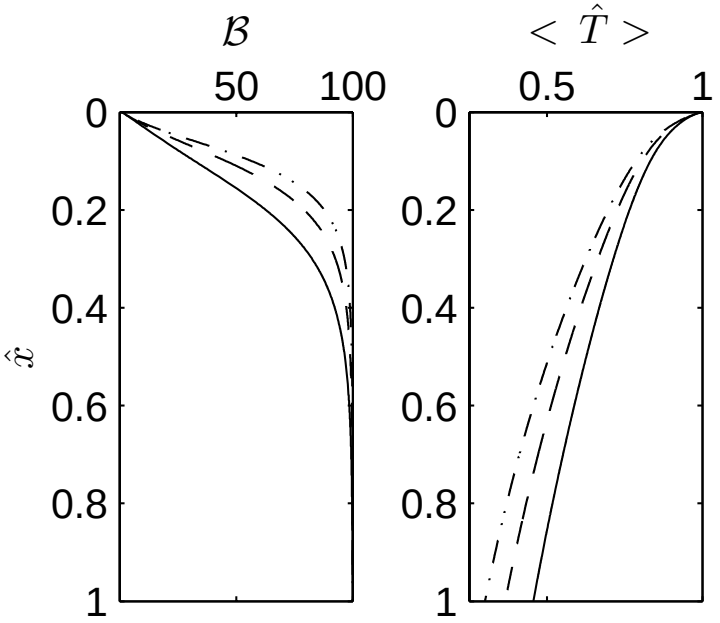

Figure 6.7: *Hollow compound fiber's axial velocity (left) and cross–sectional averaged temperature (right). (Case 1: —; Case 9: – –; Case 17: –·–)*

Figure 6.6 shows that the initial contraction of the hollow compound fiber increases as the film heat transfer coefficient at the core's (or inner jet's) inner interface is increased. Note that since the draw ratio for the three cases exhibited in Figure 6.6 is the same, the diameters of the fibers at the take–up cross–section are identical. Beyond $\hat{x} = 0.1$, the fiber's radii decrease in a much smaller manner than that for $\hat{x} < 0.1$, and, for this reason, the hollow compound fiber's geometry is only shown for $0 \leq \hat{x} \leq 0.1$ using a (decimal) logarithmic scale in the axial direction.

For the steady–state, hollow compound fibers considered in this study, Eq. (3.22) indicates that the volumetric flow rates of the inner and outer annular jets are constant, i.e., $\mathcal{BA}_1$ and $\mathcal{BA}_2$ are constant, and the non–dimensional axial velocity increases from unity at the maximum swell

cross–section to one hundred in a monotonic fashion as illustrated in Figure 6.7 which corresponds to Cases 1, 9 and 17. The axial velocity profile exhibits a two–signed curvature and an inflection point somewhere along the spin–line before reaching a constant value which corresponds to the fiber solidification, for Cases 9 and 17. It must be noted that the fiber solidification in the model presented here is entirely due to the large increase of the effective dynamic viscosity as the temperature decreases in accord with Eqs. (2.19) and (2.105) and the fact that, in Cases 9 and 17, there are heat transfer losses by convection at the hollow compound's fiber inner radius that result in lower temperatures than in Case 1 as illustrated in Figure 6.7.

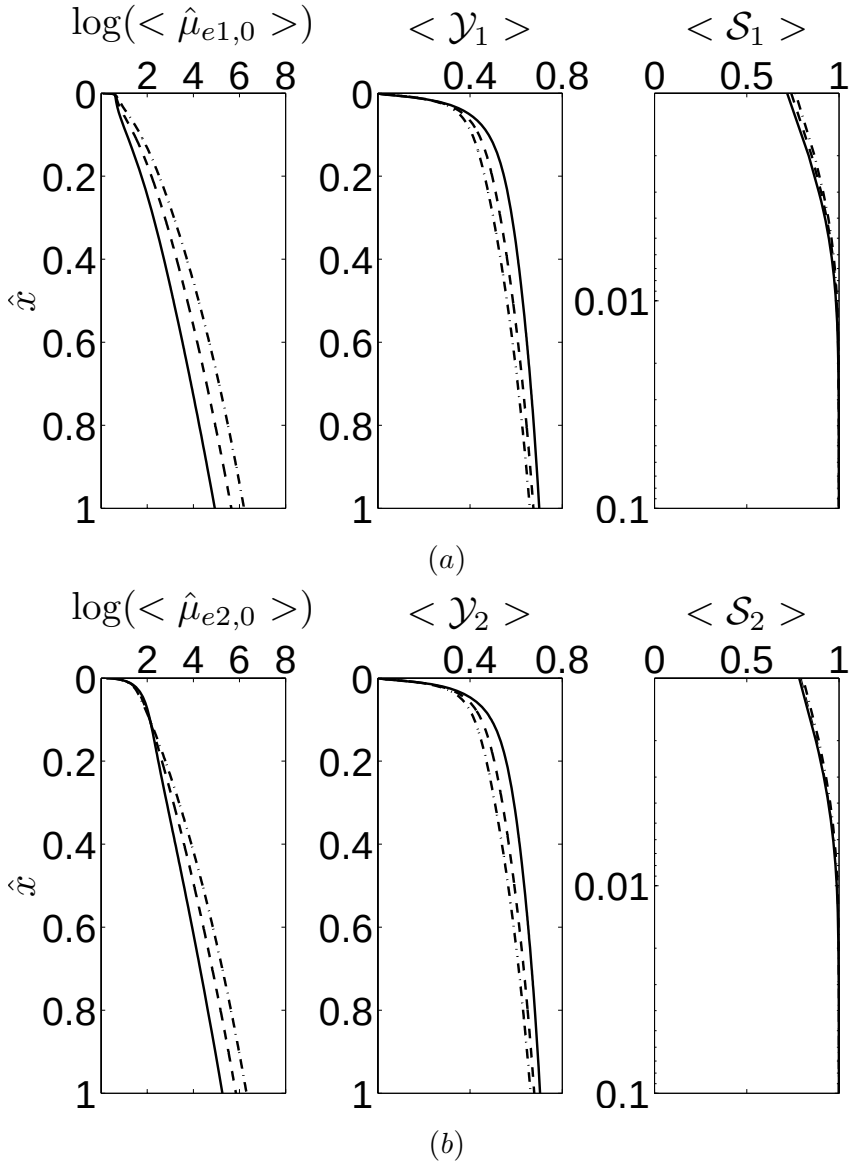

Figure 6.8: *Hollow compound fiber's cross–sectional averaged effective dynamic viscosity (left), degree of crystallization (middle) and molecular orientation order parameter (right) for the core (a) and cladding (b). (Case 1: —; Case 9: – –; Case 17: –·–)*

Figure 6.8 shows that the cross–sectional averaged values of the effective dynamic viscosity, the degree of crystallization and the molecular orientation order parameter of the core and cladding increase in a monotonic manner as the axial coordinate along the fiber is increased.

This figure also shows that the cross–sectional averaged molecular orientation order parameter reaches a constant value of unity very close to the maximum swell cross–section due to the large contraction of the hollow compound fiber and the magnitude of the components of the strain rate tensor there, while the degree of crystallization does not reach its ultimate (constant) value at the take–up cross–section and it increases along the fiber at a rate that increases as the heat film transfer coefficient at the inner jet's inner interface is increased. Note that a logarithmic scale has been used for both the effective dynamic viscosity and the molecular orientation order parameter because the former increases exponentially as the temperature decreases, while almost complete molecular orientation occurs near the maximum swell cross–section.

According to the model employed in this study, the effects of molecular orientation on crystallization are nil, once complete orientation is achieved; therefore, for non–dimensional axial distances larger than 0.1, the results presented in Figure 6.8 indicate that the crystallization of the hollow compound fibres considered in this study depends on the temperature and velocity fields.

Table 6.2: *Cross–sectionally averaged temperatures, degree of crystallization and orientation order parameter of the inner and outer materials at the take–up cross–section.*

Case	$< \hat{T}_1 >$	$< \hat{T}_2 >$	$< \mathcal{Y}_1 >$	$< \mathcal{Y}_2 >$	$< \mathcal{S}_1 >$	$< \mathcal{S}_2 >$
1	0.473	0.439	0.700	0.704	0.996	0.996
2	0.640	0.616	0.742	0.750	0.997	0.997
3	0.470	0.436	0.705	0.708	0.996	0.996
4	0.458	0.425	0.719	0.730	0.996	0.996
5	0.846	0.815	0.772	0.779	0.998	0.998
6	0.815	0.809	0.769	0.778	0.997	0.997
7	0.485	0.450	0.684	0.681	0.996	0.996
8	0.463	0.430	0.713	0.722	0.996	0.996
9	0.376	0.356	0.675	0.679	0.996	0.996
10	0.565	0.550	0.724	0.733	0.997	0.997
11	0.372	0.352	0.681	0.684	0.996	0.996
12	0.364	0.344	0.687	0.698	0.996	0.996
13	0.783	0.779	0.767	0.775	0.997	0.997
14	0.766	0.775	0.764	0.773	0.997	0.997
15	0.385	0.365	0.663	0.658	0.996	0.996
16	0.368	0.349	0.682	0.692	0.996	0.996
17	0.306	0.295	0.660	0.663	0.996	0.996
18	0.507	0.497	0.708	0.718	0.996	0.996
19	0.302	0.291	0.667	0.670	0.996	0.996
20	0.298	0.288	0.666	0.676	0.996	0.996
21	0.736	0.754	0.765	0.771	0.997	0.997
22	0.728	0.749	0.762	0.769	0.997	0.997
23	0.314	0.302	0.651	0.645	0.996	0.996
24	0.301	0.291	0.663	0.672	0.996	0.996

Table 6.2 shows the cross–sectionally averaged values of temperature, degree of crystallization, and molecular orientation order parameter for both the inner and the outer jets of the hollow

compound fibre at the take–up cross–section, and indicates that, for all the cases considered in this study, almost complete molecular orientation is achieved. However, the crystallization does not reach its ultimate value and there are some differences in the degree of crystallization between the inner and outer hollow jets; except for Cases 7, 15 and 23, the cross–sectional average degree of crystallization of the outer hollow jet at the take–up cross–section is larger than that for the inner jet.

Table 6.2 also shows that, except for Cases 14, 21 and 22, the cross–sectionally averaged temperature of the inner hollow jet at the take–up cross–section is higher than that of the outer jet. This table also shows that neither the temperature nor the crystallinity are uniform across the hollow compound fibre at the take–up cross–section for the conditions considered here. The non–uniformities in the degree of crystallization may have great effects on the mechanical, physical, chemical, optical, etc., properties of hollow compound fibres.

6.2 CONCLUSIONS

In this chapter, some numerical results for the melt spinning of semi–crystalline hollow compound fibres have been obtained using the simplified two–dimensional model developed in Chapter 4 that employs the leading–order one–dimensional equations for the hollow compound fibre's geometry and axial velocity component derived from an asymptotic analysis of slender fibres at low Reynolds and Biot numbers, and two–dimensional equations for the temperature, molecular orientation tensor and degree of crystallization

For the conditions considered here, it has been found that full molecular orientation is reached near the maximum swell region due to the large contraction of the hollow compound fibre and the magnitude of the components of the strain rate tensor there. The degree of crystallization was found to increase along the fibre and was mainly a function of the velocity and temperature fields.

In none of the cases considered in this study, the ultimate degree of crystallization was reached at the take–up cross–section, but its value there was found to i) increase as the film heat transfer coefficient at the outer jet's outer interface was decreased, ii) increase slightly as the activation energy of the Arrhenius expression for the dynamic viscosity law of the inner jet was increased, and iii) increase as the activation energy of the Arrhenius expression for the dynamic viscosity law of the outer jet, thermal Péclet number of the outer jet and the ratio of the thermal conductivity of the outer jet to that of the inner one are increased. However, the degree of crystallization at the take–up cross–section was found to decrease as the film heat transfer coefficient at the inner jet's inner interface was increased. This behaviour is associated with the kinetics of crystallization model employed in this work which indicates that the crystallization is mainly a function of the molecular orientation and the velocity field; therefore, an increase in the axial velocity component due to an increase in the heat transfer implies a shorter crystallization time as clearly observed in Table 6.2.

It has been found that the temperature variations in the radial direction decrease as the film heat transfer coefficient at the inner jet's inner interface is increased but they increase as the thermal Péclet number of the outer jet and the ratio of the thermal conductivity of the outer jet to that of the inner one are increased.

Part IV

CLOSURE

7

CONCLUSIONS AND RECOMMENDATIONS

Contents

7.1 CONCLUSIONS

A single–phase, two–dimensional model of the spinning of semi–crystalline compound and hollow compound fibres that employs a Newtonian rheology modified by the degrees of crystallization and molecular orientation and temperature through an effective dynamic viscosity, was developed. The model accounts for the molecular orientation of the liquid crystalline polymer through a diagonal orientation tensor that depends on the velocity gradient and a Maier–Saupe potential that enhance and hinder, respectively, the orientation. This molecular orientation tensor has been derived from the Doi–Edwards theory applied to slender fibres. The two–dimensional model employs the one–dimensional equations for the compound fibre's geometry and axial velocity component corresponding to the leading–order equations from an asymptotic analysis of slender fibres at low Reynolds and Biot numbers, and two–dimensional equations for the temperature, molecular orientation tensor and degree of crystallization; the latter has been modelled by means of the thermal Avrami–Kolmogorov kinetics formulation. The model is applicable from the maximum swell location to the take–up point.

The most important conclusions of this work can be summarized as follows.

- The two–dimensional model presented here is really a hybrid model, for it employs one–dimensional equations for the compound fibre's geometry, whereas two–dimensional equations are employed for the temperature, orientation and crystallization fields. As a consequence, the model is not computationally as expensive as a fully two–dimensional one that determines the fibre's geometry in the solution process, while it is expected to be more accurate than the second approximation of asymptotic ones, for slender fibres.
- Due to the non–linear coupling between the dependent variables, the exponential dependence of the dynamic viscosity on temperature, the degree of crystallization and the molecular orientation and the use of a leading–order equations for the axial momentum equation and the compound fibre's geometry, the model is of integro–differential type and its results are highly dependent on the pre–exponential factor and activation energy of the Arrhenius law used for the dynamic viscosity of the inner and outer jets.

- The results of the two–dimensional model proposed here indicate that substantial temperature non–uniformities in the radial direction exist even for small Biot numbers. These non–uniformities affect the degree of crystallization and may have great effects on the mechanical, electrical, etc. properties of compound fibres.
- For very slender fibres and small Biot numbers, good agreement between the leading–order one–dimensional model and the two–dimensional one presented here has been observed, although some differences have been observed in the initial curvature of the axial velocity profile when axial heat conduction is neglected in the one–dimensional model.
- For the conditions considered here, it was found that the crystallization of the compound fibre was mostly affected by thermal effects rather than by flow–induced ones, while almost complete orientation was observed near the maximum swell location where the strain rate is largest.
- It must be pointed out that the solidification of the compound fibres considered here is mainly due to the increase in dynamic viscosity as the fibre is cooled along the spinning line.

This work is part of a larger project that has been carried out by the research group which the author belongs to and draws heavily upon the results previously obtained by it. The contributions of this thesis to this larger project can be summarized as follows:

A. The one–dimensional model developed by the research group was extended by means of a perturbation method for slender fibres at low Reynolds and Biot numbers to semi–crystalline (hollow) compound fibres by considering a molecular orientation order parameter. This extension is based on the introduction of a molecular orientation tensor that, for axisymmetric slender fibres with initial and axisymmetric boundary conditions, is diagonal and traceless, and includes a model that accounts for the molecular order parameter when the orientation tensor is proportional to the velocity gradient that results from the leading–order approximation to slender fibres at low Reynolds and Biot numbers.

B. The model described in the previous item was implemented in a code developed on `MATLAB`® and its results have been shown to agree with the analytical and computational solutions which had been previously obtained by the research group with a code written on `FORTRAN`.

C. A hybrid two–dimensional model based on the one–dimensional equations for the geometry and axial velocity which result from a leading–order approximation in the analysis of the slender polymeric fibre at low Reynolds and Biot numbers and the two–dimensional equations for the energy, molecular orientation tensor and degree of crystallization has been developed. The equations for the energy and the molecular orientation and degree of crystallization are parabolic and hyperbolic, respectively.

D. An iterative finite difference method based on a mapping transformation of the physical geometry onto a computational one consisting of two rectangles (one per jet) was developed and implemented on `MATLAB`®.

E. An extensive parametric study has been carried out in order to determine the most influential parameters on the fluid dynamics, temperature, molecular orientation and degree of crystallization processes that occur in the melt spinning of slender polymeric compound and hollow compound fibres.

f. An extensive comparison between the results of the one–dimensional model which may or not may include axial conduction and cross–sectional averaged ones predicted by the two–dimensional one where the axial conduction is disregarded has been carried out. From these comparisons, the following conclusions have been obtained:

   a) both models exhibit the same qualitative trends,

   b) while the two–dimensional method can predict a one–sign curvature velocity profile, the one–dimensional one may predict two–sign profile under certain conditions,

   c) large differences may exist between one– and two–dimensional methods near the maximum swell section where the deformation rate is largest, and

   d) the two–dimensional model predicts non–uniformities temperature profile in the radial direction at the take–up point, and these non–uniformities may affect the mechanical, electrical, optical, etc., properties of the (hollow) compound fibres.

7.2 SUGGESTIONS FOR FUTURE WORK

Most of the subjects on future work suggested here are aimed at the development of a two–dimensional model of the melt spinning process that includes the study of the flow in the spinneret, although some of them should perhaps be undertaken in order to improve the two–dimensional model presented in this thesis. These suggestions are as follows:

- Development of a fully two–dimensional model of the melt spinning of non–isothermal single–component single–phase semi–crystalline jets that takes into account the flow in the spinneret. The author has spent some efforts in this direction using the open source computational fluid dynamics toolbox `OpenFOAM` (**Open** Source **F**ield **O**peration **A**nd **M**anipulation).
- Development of a fully two–dimensional model of the melt spinning of non–isothermal bi–component and hollow compound single–phase semi–crystalline jets that takes into account the flow in the spinneret.
- The two–dimensional model presented here can be improved by accounting for the effect of air drag and latent heat of crystallization. However, for moderate draw ratios, the author estimates that the results provided by this improved model would be very similar to those presented here. At high draw ratios, the model should account in a more explicit manner for the amorphous and crystalline phases, relaxation times, non–Newtonian rheology, etc., so that it can predict neck–in phenomena.
- Study and modelling of the dependence of the relaxation time on the molecular orientation tensor.
- Development and validation of a symmetric but non–diagonal molecular orientation tensor.
- The one–dimensional models for liquid–crystalline polymers previously developed by the research group which the author belongs to and the two–dimensional one presented in this thesis use transport equations for the molecular orientation tensor and the degree of crystallization that are hyperbolic; as a consequence, these two variables may be discontinuous at the core–cladding interface. One should, however, expect that at this interface there is entanglement of the polymer molecules from the core and the cladding which the models

presented here do not account for. Therefore, a model for polymer entanglement at the interface between two polymers and a model for the molecular orientation tensor that takes into account this entanglement may have to be developed. Such an entanglement may also affect the crystallization at the interface and, therefore, must be taken into account in the crystallization model.

Part V

APPENDIXES

A

RESUMEN EXTENDIDO

Contenidos

A.1 INTRODUCCIÓN

En los diez últimos años ha habido un gran interés en el desarrollo de fibras ópticas tanto microestructuradas (MOF), es decir, fibras que contienen agujeros u otro tipo de estructura repetitiva a lo largo de toda su longitud como no microestructuradas. En estas fibras, la luz puede ser guiada a lo largo de su núcleo (*core*) por dos mecanismos, la *reflexión total interna*, como en las fibras convencionales, y la *reflexión especular de Bragg*. En las primeras, el índice de refracción del núcleo es mayor que el índice de refracción "efectivo" del revestimiento (*cladding*) gracias a la presencia de la microestructura, por lo que se requiere que el núcleo sea sólido (*solid core*). En las segundas, las ondas son guiadas en modos que se encuentran en la banda prohibida (*band–gap*) generada por la microestructura del revestimiento, por lo que el núcleo puede ser hueco y el revestimiento puede estar formado por capas cilíndricas concéntricas. Las fibras microestructuradas suelen fabricarse en torres de estirado por diferentes procedimientos. El más usado, cuando se precisan agujeros grandes en el revestimiento, es el estirado de una preforma formada juntando varios capilares alrededor de un sólido. Hasta muy recientemente se

han fabricado MOF's de sílice pero, hoy en día, también se fabrican de plástico o polímero (POF), e incluso se han llegado a fabricar fibras que combinan materiales conductores, semiconductores y dieléctricos.

La transparencia y ancho de banda de estas POF's junto con su alta capacidad de transmisión, facilidad de manejo, flexibilidad y economía permiten que estas fibras puedan sustituir a los cables de cobre y a fibras ópticas de vidrio en enlaces de comunicaciones así como en otros dispositivos opto–electrónicos. La sección transversal de una POF puede ser microestructurada (MOF) o circular (fibras de Bragg). En este último caso, la fibra generalmente consta de tres capas: la capa interna es el núcleo, la parte intermedia constituye el revestimiento y la parte externa es la cubierta de protección. En la manufactura de POF's circulares, un cilindro sólido llamado preforma de varios centímetros de diámetro y aproximadamente medio metro de longitud, cuya estructura determina los perfiles de los índices de refracción tanto en el núcleo como en el revestimiento, se extrusiona en un proceso de *melt spinning* análogo al que se utiliza en la fabricación de fibras textiles y fibras de vidrio. El perfil del índice de refracción en el núcleo en la dirección radial puede obtenerse diseñando la preforma con dicho perfil; cuando se necesitan perfiles más complejos tales como perfiles graduales (*graded indices*), se utiliza un proceso de estirado en el que un extremo de la preforma se calienta hasta alcanzar la temperatura de fusión o *melting*. Actualmente, la producción de POF's con índice de refacción gradual se basa en procesos de *polimerización de gel* y *difusión*. La polimerización de gel requiere la fabricación de un cilindro hueco de polímero tal como PMMA que da lugar al revestimiento y que se rellena con monómeros, un iniciador, y un dopante que cuando se calientan dan lugar a la formación de un polímero que constituye el núcleo de la fibra. Una vez obtenida la preforma, uno de sus extremos se calienta en un horno hasta alcanzar la viscosidad necesaria para ser extruida a la velocidad adecuada para obtener el diámetro deseado de la fibra. Finalmente, se aplica una protección (*coating*) a la misma con objeto de mejorar su resistencia y facilitar su manejo.

A.2 CARACTERÍSTICAS DEL PROCESO DE MELT SPINNING

El proceso de *melt spinning* involucra la extrusión y el estirado de un cilindro de líquido. Un diagrama típico del proceso se muestra en la Figura 1.1 (*a*). Copos de polímero son fundidos en

el dispositivo de extrusión, proceso tras el cual se bombea el líquido a través de la boquilla de salida para formar las fibras líquidas. Este filamento es estirado y enfriado hasta que solidifica en la zona de estirado. La velocidad final de la fibra es fijada por el tambor de recogida de la misma el cuál consiste en una o más ruedas que giran a velocidad constante. La fibra ya sólida se mueve a la misma velocidad lineal que las ruedas debido a las fuerzas de fricción en la zona de contacto. Como las bobinas de hilo, la fibra es finalmente enroscada en un carrete para su posterior almacenaje. El estirado de fibras compuestas se distingue del estirado de una fibra sólida en que en el primero de ellos dos fluidos han de ser extruidos y estirados al mismo tiempo. El chorro interno o núcleo, a menudo, consiste en un gas inerte pero puede ser otro fluido.

Estos procesos son, generalmente, divididos en cuatro regiones para su análisis: (1) la **región de flujo cortante** que se da en el interior de la boquilla de salida; (2) la **región de flujo reorganizado** en la que el flujo cortante se convierte en elongacional; (3) la **zona de estirado** del fluido fundido donde la fibra es estirada hasta el diámetro deseado en contacto con un fluido refrigerante (aire) para facilitar la transferencia de calor; (4) la **región de solidificación** donde el fluido ya frío se transforma en sólido. Cada una de esas regiones están identificadas en la Figura 1.1 (*b*).

Las variables de operación que se especifican de forma más habitual son el diámetro de la boquilla de salida y la temperatura de los chorros en esa posición, la temperatura del aire circundante y su velocidad, los flujos másicos extruidos y la velocidad de rotación del tambor de recogida. La relación entre la velocidad media del fluido a la salida de la boquilla y la velocidad lineal de recogida se denomina relación de estirado (*draw ratio*), D_r, y, a menudo, es especificada en lugar de la tasa de extrusión. Las especificaciones correctas de las variables de operación permiten la producción de fibras para un tamaño y tasa de fabricación dadas.

Un análisis riguroso del proceso requiere resolver las ecuaciones de conservación de masa, cantidad de movimiento y energía en un dominio complejo tridimensional. Para evitar cálculos numéricos costosos, se han introducido un número de aproximaciones simplificadas en la literatura, algunas de las cuales han sido asumidas en este trabajo y, que han dado como resultado las bases para el análisis del filamento esbelto (TFA). Los mecanismos de esta simplificación han tomado varias formas en la literatura. De entre ellos, los métodos asintóticos de aproximación son los más rigurosos proporcionando correcciones a los resultados de la teoría de fibra esbelta que no

están disponibles en los otros métodos. Algunos trabajos demostraron que la única consideración del primer orden del análisis asintótico era un aproximación muy buena para un amplio rango de condiciones para una fibra sólida de una única fase.

En el presente estudio se evita el tratamiento explícito de las **regiones 1 y 2** asumiendo que el flujo cortante del interior de la boquilla se modifica hacia el flujo elongacional en una distancia mucho más pequeña que la longitud total de la zona de estirado. Cálculos mediante elementos finitos verifican esta hipótesis e indican que esta transición ocurre en una distancia igual a dos o tres veces el diámetro de la boquilla. Aunque el origen exacto de la zona de estirado no está definido, esta ambigüedad es mucho más pequeña que la longitud de la zona de estirado. El diámetro de la fibra inicial suele seleccionarse igual al diámetro de la boquilla de salida o al máximo radio de la zona de hinchado (*maximum die swell radius*) si éste es significante. No obstante, para la zona de hinchado se requieren medidas experimentales o correlaciones apropiadas.

El análisis de la **región 4** se obvia aquí asumiendo la hipótesis de una transición instantánea e isoentálpica hacia un sólido rígido a una temperatura de transición apropiada (temperatura de fusión o de transición vítrea). El significado de esta hipótesis no está bien definido en la literatura existente. Para materiales cristalinos, especialmente a altas velocidades (velocidades mayores de $1000\,m/min$), la validez es cuestionable porque la transición vítrea puede ser una función muy dependiente de la cristalinidad y la orientación molecular. Para materiales vítreos a bajas velocidades de estirado, el uso de una temperatura de transición vítrea acarrea resultados razonables. Pequeñas variaciones en la temperatura de transición vítrea no provocan cambios significativos en los niveles de esfuerzos finales en el fluido ni en la geometría final de la fibra.

Las hipótesis realizadas reducen el problema únicamente al análisis de la **región 3** que constituye la zona de estudio objeto de la presente tesis. El hecho de que el diámetro de la fibra sea típicamente mucho más pequeño que la longitud de la zona de estirado permite simplificar el análisis de una forma extraordinaria.

A.3 FUNDAMENTOS Y RESULTADOS DEL MODELO PROPUESTO

En este trabajo se presenta un modelo bidimensional del proceso de *melt spinning* bajo condiciones no isotermas para fibras semicristalinas compuestas tanto macizas como anulares que considera la orientación molecular y la cristalización. Este modelo está basado en las ecuaciones asintóticas de orden más bajo para la geometría y la componente axial de la velocidad para fibras esbeltas a bajo número de Reynolds y Biot, y las ecuaciones bidimensionales para la temperatura, orientación molecular y cristalización. A su vez, el modelo emplea una reología Newtoniana, incluye los efectos tanto de temperatura como de cristalización inducida por el flujo y considera los efectos de orientación molecular en el tensor de tensiones así como en la cristalización a través de la formulación de Doi–Edwards y la cinética de cristalización de Avrami–Kolmogorov, respectivamente. La orientación molecular es modelada por medio de un tensor cuya evolución depende principalmente del tensor de tasa de deformación, mientras que la cristalización depende de la orientación molecular y del campo de temperaturas; las ecuaciones para la cristalización y la orientación molecular están fuertemente acopladas con las de conservación de masa, cantidad de movimiento y energía.

El modelo presentado en este trabajo ha sido usado para estudiar numéricamente el estado estacionario del fenómeno de *melt spinning* para fibras compuestas tanto macizas como anulares por medio de ecuaciones en diferencias finitas en el dominio computacional resultado de transformar la geometría curvilínea de las fibra compuestas en dos rectángulos. Experimentos numéricos han sido realizados para relaciones de estiramientos moderadas en el dominio físico que, en la dirección axial, viene delimitado por la sección de máximo hinchado y el punto de recogida de la fibra.

Los resultados numéricos obtenidos para fibras compuestas semicristalinas indican que, incluso a bajo número de Biot, la temperatura puede no ser uniforme a través de la sección transversal de la fibra como consecuencia de las pérdidas de calor. Para los casos reportados aquí, las no uniformidades térmicas son principalmente función del número de Biot, la conductividad térmica y el factor pre–exponencial y energía de activación de la ley de viscosidad dinámica que modela el revestimiento. Los resultados también muestran que la temperatura promediada a través de la sección transversal predicha por el modelo bidimensional exhibe la misma tendencia cualitativa

que las de los modelos asintóticos unidimensionales que consideran la conducción axial y que sólo son válidos para números de Reynolds y Biot bajos.

Para fibras compuestas huecas semicristalinas, se observa que casi se alcanza la orientación molecular completa cerca de la región de máximo hinchado de la fibra debido a la enorme contracción de ésta en esa zona, mientras que, para las condiciones consideradas aquí, en la zona de recogida de la fibra no se obtiene el grado de cristalización máximo. También se observa que en el punto de recogida existen no uniformidades en los perfiles de temperatura y cristalización; estas no uniformidades pueden influir enormemente en las propiedades de la fibra.

A.4 CONCLUSIONES

Las conclusiones más importantes extraídas del presente trabajo se pueden resumir como siguen.

- El modelo bidimensional que se presenta aquí es en realidad un modelo híbrido; emplea ecuaciones unidimensionales para la geometría y velocidad axial de la fibra compuesta, mientras que usa ecuaciones bidimensionales para los campos de temperatura, orientación y grado de cristalización. Como consecuencia, la resolución del mismo no supone un coste computacional tan elevado como el de un modelo completamente bidimensional que determina la geometría de la fibra en el propio proceso de resolución. Asimismo, es un modelo más preciso que el de modelos asintóticos para fibras esbeltas que incluyen hasta la segunda aproximación.
- Debido al acoplamiento no lineal entre las variables dependientes del problema, la dependencia exponencial de la viscosidad dinámica con la temperatura, el grado de cristalización y la orientación molecular y el uso de ecuaciones para el orden más bajo en las ecuaciones de cantidad de movimiento y geometría de la fibra compuesta, el modelo es integro–diferencial y sus resultados son altamente dependientes del factor pre–exponencial y la energía de activación de la ley de Arrhenius usada para la viscosidad dinámica de los chorros interno y externo.
- Los resultados del modelo bidimensional propuesto aquí indican que existen importantes no–uniformidades en la temperatura en la dirección radial incluso para pequeños valores

del número de Biot. Estas no–uniformidades afectan al grado de cristalización y pueden tener grandes efectos en las propiedades mecánicas, eléctricas, etc. de las fibras compuestas.

- Para fibras muy esbeltas y pequeños números de Biot, se aprecia buena concordancia entre el modelo unidimensional asintótico y el bidimensional presentado aquí, aunque se observan algunas diferencias en la curvatura inicial de los perfiles de velocidad axial cuando la conducción de calor axial es despreciada en el modelo unidimensional.
- Para las condiciones consideradas aquí, se ha encontrado que la cristalización de la fibra compuesta viene afectada principalmente por los efectos térmicos más que por los de flujo inducido, mientras que se ha observado también que la orientación molecular casi completa se produce cerca de la sección de máximo hinchado donde la tasa de deformación es máxima.
- Se debe reseñar que la solidificación de la fibra compuesta considerada aquí es principalmente debido al incremento de la viscosidad dinámica conforme ésta se va enfriando a lo largo de la línea de estirado.

Las contribuciones de este trabajo al proyecto del que forma parte pueden ser resumidas en los siguientes puntos:

A. El modelo unidimensional desarrollado por el grupo de investigación ha sido extendido por medio de un método de perturbaciones para fibras esbeltas para bajos números de Reynolds y Biot a fibras compuestas (o anulares compuestas) semicristalinas considerando un parámetro de orden para la orientación molecular. Esta extensión está basada en la introducción de un tensor de orientación molecular que, para fibras esbeltas axilsimétricas con condiciones iniciales y de contorno axilsimétricas, es diagonal y con traza nula, e incluye un modelo que tiene en cuenta el paramétro de orden cuando el tensor de orientación es proporcional al tensor gradiente de velocidad que se obtiene a partir de una aproximación asintótica para el orden más bajo para fibras esbeltas a bajo número de Reynolds y Biot.

B. El modelo descrito en el item previo fue implementado mediante un código numérico desarrollado en `MATLAB`® y sus resultados han mostrado concordancia con las soluciones analíticas y computacionales que fueron previamente obtenidas por el grupo de investigación mediante un código escrito en `FORTRAN`.

C. Se ha desarrollado un modelo híbrido bidimensional basado en las ecuaciones unidimensionales para la geometría y la velocidad axial las cuáles provienen de una aproximación asintótica para el orden más bajo en el análisis de fibras poliméricas esbeltas a bajo número de Reynolds y Biot y las ecuaciones bidimensionales de la energía, tensor de orientación molecular y grado de cristalización. Las ecuaciones para la energía son parabólicas mientras que las de la orientación molecular y el grado de cristalización son de carácter hiperbólico.

D. Un método iterativo en diferencias finitas basado en una transformación de coordenadas que mapea el dominio físico en uno computacional consistente en dos rectángulos (uno por cada uno de los chorros) ha sido desarrollado e implementado usando MATLAB®.

E. Se ha llevado a cabo un vasto estudio paramétrico con objeto de determinar los parámetros más influyentes en los procesos fluido–dinámicos, de temperatura, orientación molecular y grado de cristalización que ocurren en el proceso de *melt spinning* de fibras poliméricas esbeltas tanto compuestas como anulares compuestas.

F. En este estudio también se han llevado a cabo comparaciones entre los resultados del modelo unidimensional que puede o no tener en cuenta la conducción axial y los resultados promediados transversalmente previstos por el modelo bidimensional en el que la conducción axial es despreciada. A partir de estas comparaciones las siguientes conclusiones pueden ser obtenidas:

   a) ambos modelos exhiben los mismos comportamientos cualitativos,

   b) mientras que el modelo bidimensional predice perfiles de velocidad axial con una única curvatura, el bidimensional exhibe perfiles con doble curvatura bajo ciertas condiciones,

   c) existen diferencias importantes entre los modelos uni– y bidimensional cerca de la sección de máximo hinchado donde la tasa de deformación es máxima, y

   d) el modelo bidimensional predice perfiles de temperatura no uniformes en la dirección radial en el punto de recogida de la fibra, y estas no uniformidades pueden afectar a las propiedades mecánicas, eléctricas, ópticas, etc., de las fibras compuestas tanto macizas como anulares.

A.5 SUGERENCIAS PARA TRABAJOS FUTUROS

La mayoría de las sugerencias que proponemos para desarrollar futuros trabajos relacionadas con el tema de esta tesis están enfocadas hacía el desarrollo de un modelo completamente bidimensional del proceso de *melt spinning* que incluya el estudio del flujo en la boquilla de salida, aunque algunos de ellos deberían quizás ser emprendidos con objeto de mejorar los resultados del modelo bidimensional presentado en esta tesis.

Estas sugerencias son las que a continuación se exponen:

- Desarrollo de un modelo completamente bidimensional del fenómeno no isotermo de *melt spinning* para chorros monofásicos semicristalinos de un único componente que tenga en cuenta el flujo en el interior de la boquilla. El autor de esta tesis ha hecho grandes esfuerzos en esta dirección haciendo uso del paquete libre de computación fluido-dinámica `OpenFOAM` (**Open** Source **F**ield **O**peration **A**nd **M**anipulation).
- Desarrollo de un modelo completamente bidimensional del fenómeno no isotermo de *melt spinning* para chorros monofásicos semicristalinos de dos componentes, tanto macizos como anulares o huecos, que tenga en cuenta el flujo en el interior de la boquilla.
- El modelo bidimensional que se presenta en este trabajo puede ser mejorado sustancialmente teniendo en cuenta en las simulaciones numéricas los efectos de arrastre del aire y el calor latente de cristalización. Sin embargo, para relaciones de estiramiento moderadas, el autor estima que los resultados que proporcionaría este modelo mejorado serán muy similares a los presentados en este trabajo. Para relaciones de estiramiento altas, el modelo debe tener en cuenta de una manera más explícita la presencia de las fases amorfa y cristalina, los tiempos de relajación, la reología no Newtoniana, etc., para poder predecir los fenómenos de *neck–in*.
- Estudio y modelado de la dependencia del tiempo de relajación con el tensor de orientación molecular.
- Desarrollo y validación del tensor de orientación molecular simétrico pero no diagonal.
- Los modelos unidimensionales para polímeros líquidos cristalinos desarrollados previamente por el grupo de investigación del que el autor forma parte y el bidimensional propuesto

en esta tesis usan ecuaciones de transporte para el tensor de orientación molecular y el grado de cristalización lo que origina ecuaciones en derivadas parciales de carácter hiperbólico; como consecuencia, estas dos variables pueden ser discontinuas en la interfase núcleo–revestimiento. Sin embargo, debe esperarse que en dicha interfase se produzcan enredos entre las cadenas poliméricas del núcleo y del revestimiento que no son tenidas en cuenta por los modelos que se presentan en este trabajo. Por tanto, se deben desarrollar sendos modelos para las uniones entre las cadenas de ambos polímeros en la interfase así como para el tensor de orientación molecular que considere esta interacción. Dichos enredos entre cadenas de polímeros pueden también afectar la cristalización en la interfase y, por tanto, ser tenidas en cuenta en el modelo de cristalización.

NOMENCLATURE

Symbol	Description	Units
$\mathcal{A}$	Non–dimensional cross–sectional area	$[\cdot]$
a_2	Constant of the linearised crystal growth rate	$[\cdot]$
c	Number of polymeric units per unit volume	$[m^{-3}]$
$\mathbf{c}$	Conformational tensor	$[\cdot]$
$\mathcal{B}$	Non–dimensional leading–order axial velocity	$[\cdot]$
C	Specific heat	$[J\,kg^{-1}\,K^{-1}]$
$\mathcal{D}$	Non–dimensional leading–order pressure	$[N\,m^{-2}]$
D	Pre–exponential factor	$[N\,m^{-2}\,s]$
D_r	Draw ratio	$[\cdot]$
E	Activation energy	$[J\,mol^{-1}]$
$\boldsymbol{e}$	Unit vector	$[\cdot]$
$\mathcal{F}$	Non–dimensional leading–order temperature	$[K]$
$\mathbf{f}^m$	Body force per unit mass	$[N\,kg^{-1}]$
g	Gravitational acceleration	$[9.81\ m\,s^{-2}]$
h	Film heat transfer coefficient	$[W\,m^{-2}\,K^{-1}]$
H	Inverse of activation temperature	$[K^{-1}]$
$\mathbf{I}$	Identity or unit tensor	$[\cdot]$
k	Thermal conductivity	$[W\,m^{-1}\,K^{-1}]$
k_A	Linearised crystal growth rate	$[\cdot]$
$k_A(0)$	Amorphous growth rate	$[\cdot]$
k_B	Boltzmann constant	$[1.3806503 \times 10^{-23}\ \ m^2\,kg\,s^{-2}\,K^{-1}]$
k_{SB}	Stephan–Boltzmann constant	$[5.670373 \times 10^{-8}\ \ W \cdot m^{-2} \cdot K^{-4}]$
L	Characteristic length in the axial direction	$[m]$
n	Crystallization viscosity index	$[\cdot]$
N	Dimensionless measure of c	$[\cdot]$
p	Pressure	$[N\,m^{-2}]$
q	Heat flux	$[W\,m^{-2}]$
Q	Non–dimensional volumetric flow rate	$[\cdot]$
r	Radial coordinate	$[m]$
R	Fibre/jet's radius	$[m]$
R_g	Ideal gas constant	$[8.314\ J\,K^{-1}\,mol^{-1}]$
$\mathcal{R}$	Non–dimensional jet's radius	$[\cdot]$
S	Surface	$[m]$
$\mathcal{S}$	Molecular orientation parameter	$[\cdot]$

$\mathbf{S}$	Molecular orientation tensor	$[\cdot]$
t	Time	$[s]$
T	Temperature	$[K]$
T_∞	Temperature of the gases	$[K]$
u	Axial velocity component	$[m\,s^{-1}]$
$\mathbf{u}$	Molecular orientation vector	$[\cdot]$
v	Radial velocity component	$[m \cdot s^{-1}]$
$\mathbf{v}$	Velocity vector	$[m \cdot s^{-1}]$
x	Axial coordinate	$[m]$
$\mathcal{Y}$	Degree of crystallization	$[\cdot]$
$\mathcal{Y}_\infty$	Ultimate degree of crystallization	$[\cdot]$
z	Degree of transformation	$[\cdot]$

Greek symbols

α	Relation between kinetic energy and internal energy	$[\cdot]$
β	Crystallization viscosity rate parameter	$[\cdot]$
ϵ	Slenderness ratio	$[\cdot]$
η	Mapping of the non–dimensional axial coordinate	$[\cdot]$
θ	Azimuthal coordinate	$[\cdot]$
λ	Relaxation time	$[s]$
λ_0	Relaxation time at reference temperature	$[s]$
μ	Dynamic viscosity	$[N\,m^{-2}\,s]$
ξ	Mapping of the non–dimensional radial coordinate	$[\cdot]$
ρ	Density	$[kg\,m^{-3}]$
σ	Surface tension	$[N\,m^{-1}]$
$\boldsymbol{\tau}$	Stress tensor	$[N\,m^{-2}]$
$\boldsymbol{\tau}_N$	Newtonian contribution to the stress tensor	$[N\,m^{-2}]$
$\boldsymbol{\tau}_P$	Polymer contribution to the stress tensor	$[N\,m^{-2}]$
ϕ	Dimensionless parameter related to the friction tensor	$[\cdot]$
$\mathbf{\Phi}$	Viscous rate of heat dissipation	$[N\,m^{-2}\,s^{-1}]$
ω	Inverse of activation temperature for the relaxation time	$[K^{-1}]$

Dimensionless numbers

Bi	Biot number
Br	Brinkmann number
Ca	Capillary number
Fr	Froude number
Pe	Péclet number
Pr	Prandtl number
Re	Reynolds number
St	Stanton number

Subscripts

$_0$	Reference values
$_1$	Inner jet
$_2$	Outer jet
$_e$	Effective
$_m$	Melting conditions
$_p$	Polymer
$_r$	Radial direction
$_x$	Axial direction
$_\theta$	Azimuthal angle

Superscripts

^{T}	Transpose
$^\nabla$	Upper Convective Maxwell derivative
$\hat{}$	Non–dimensional variables

BIBLIOGRAPHY

[1] Allain, C., Cloitre, M., and Perrot, P. Experimental investigation and scaling law analysis of die swell in semi-dilute polymer solutions. *Journal of Non-Newtonian Fluid Mechanics 73* (1997), 51–66.

[2] Ashman, B. Stability of hollow fiber spinning. Master's thesis, University of Toledo, Toledo, OH, USA, 1998.

[3] Avrami, M. Kinetics of phase change. I. General theory. *Journal of Chemical Physics 7* (1939), 1103–1112.

[4] Avrami, M. Kinetics of phase change. II. Transformation-time relations for random distribution of nuclei. *Journal of Chemical Physics 8* (1940), 212–224.

[5] Avrami, M. Kinetics of phase change. III. Granulation, phase change, and microstructure. *Journal of Chemical Physics 9* (1941), 177–184.

[6] Batarseh, M. T. Formation of anisotropic hollow fiber membranes via tipsb. Master's thesis, University of Texas, Austin, TX, USA, 1999.

[7] Bell, P. W., and Eddie, D. D. Calculated internal stress distributions in melt spun fibers. *Journal of Applied Polymer Science 33* (1987), 1073–1088.

[8] Bertola, V., Meulenbroek, B., Wagner, C., Strom, C., Morozov, A., van Saarloos, V., and Bonn, D. Experimental evidence for an intrinsic route to polymer melt fracture phenomena: A nonlinear instability of viscoelastic poiseuille flow. *Physical Review Letters 90* (2003), 114502.

[9] Bird, R. B., Curtis, C. F., Armstrong, R. C., and Hassager, O. *Dynamics of Polymeric Liquids: Kinetic Theory*, vol. 2. John Wiley & Sons, New York, USA, 1987.

[10] Blanco-Rodríguez, F. J., and Ramos, J. I. Melt spinning of semi–crystalline compound fibers. *Polymer 52*, 24 (November 2011), 5573–5586.

[11] Blanco-Rodríguez, F. J., and Ramos, J. I. A simplified two–dimensional model of the melt spinning of semi–crystalline hollow compound fibers. Under review in *International Journal of Thermal Sciences*, 2011.

[12] Broek, A. P., Teunis, H. A., Bargeman, D., Sprengers, E. D., and Smolders, C. A. Characterization of hollow fiber hemodialysis membranes: Pore size distribution and performance. *Journal of Membrane Science 73* (1992), 143–152.

[13] Burger, M., Capasso, V., and Eder, G. Modelling of polymer crystallization in temperature fields. *ZAMM, Zeitschrift for Angewandte Mathematik und Mechanik 82* (2002), 51–63.

[14] Cain, J. J., and Morton, M. M. Multiplicities and instabilities in film blowing. *Polymer Engineering Science 28* (1988), 1527–1541.

[15] Cao, J. Numerical simulation of draw resonance in melt spinning of polymer fluids. *Journal of Applied Polymer Science 43* (1993), 1759–1768.

[16] Cao, J. Obtaining precise critical draw ratio of draw resonance in melt spinning by numerical simulation of difference equations. *Chinese Journal of Polymer Science 23* (2005), 311–318.

[17] Capasso, V. *Mathematical Modelling for Polymer Processing.* Springer-Verlag, New York, USA, 2003.

[18] Caswell, B., and Viriyayuthakorn, M. Finite element simulation of die swell for a Maxwell fluid. *Journal of Non-Newtonian Fluid Mechanics 12* (1983), 13–29.

[19] Chang, J. C., and Denn, M. M. An experimental study of isothermal spinning of a newtonian and a viscoelastic liquid. *Journal of Non-Newtonian Fluid Mechanics 5* (1979), 369–385.

[20] Chang, J. C., Denn, M. M., and Geyling, F. T. Effects of inertia, surface tension, and gravity on the stability of isothermal drawing of newtonian fluids. *Industrial and Engineering Chemistry Fundamentals 20* (1981), 147–149.

[21] Cho, H. H., Kim, K., Kang, Y. A., Ito, H., and Kikutani, T. Fine structure and physical properties of polyethylene/poly(ethylene terephthalate) bicomponent fibers in high-speed spinning. I. Polyethylene sheath/poly(ethylene terephthalate) core fibers. *Journal of Applied Polymer Science 77*, 10 (2000), 2254–2266.

[22] Cho, H. H., Kim, K., Kang, Y. A., Ito, H., and Kikutani, T. Fine structure and physical properties of polyethylene/poly(ethylene terephthalate) bicomponent fibers in high-speed spinning. II. Poly(ethylene terephthalate) sheath/ polyethylene core fibers. *Journal of Applied Polymer Science 77*, 10 (2000), 2267–2277.

[23] Christensen, R. E. Extrusion coating of polypropylene. *Society of Petroleum Engineers Journal 18* (1962), 751–755.

[24] Crochet, M. J., and Keunings, R. Die swell of a maxwell fluid: Numerical prediction. *Journal of Non-Newtonian Fluid Mechanics 7* (1980), 199–212.

[25] D'Andrea, R. G., and Weinberger, C. B. Effects of surface tension and gravity forces in determining the stability of isothermal fiber spinning. *AIChE Journal 22* (1976), 923–925.

[26] Dealy, J. M., and Kim, S. *Polymer processing instabilities: Control and understanding.* Marcel Dekker, New York, USA, 2005, ch. Gross melt fracture in extrusion.

[27] Demay, Y., and Agassant, J.-F. Experimental study of the draw resonance in fiber spinning. *Journal of Non-Newtonian Fluid Mechanics 18* (1985), 187–198.

[28] Denn, M. M. Continuous drawing of liquids to form fibers. *Annual Review of Fluid Mechanics 12* (1980), 365–387.

[29] Denn, M. M. *Computational Analysis of Polymer Processing.* Applied Science Publisher, London, UK, 1983, ch. Fibre Spinning, pp. 179–216.

[30] Doi, M., and Edwards, S. F. *The Theory of Polymer Dynamics*, second ed. Clarendon Press: Oxford University Press, Oxford, UK, 1988.

[31] Donnelly, G. J., and Weinberger, C. B. Stability of isothermal fiber spinning of a newtonian fluid. *Industrial and Engineering Chemistry Fundamentals 14* (1975), 334–337.

[32] Doufas, A. K., and McHugh, A. J. Simulation of melt spinning including flow-induced crystallization. Part III. Quantitative comparisons with PET spinline data. *Journal of Rheology 45* (2001), 403–420.

[33] Doufas, A. K., and McHugh, A. J. Two-dimensional simulation of melt spinning with a microstructural model for flow-induced crystallization. *Journal of Rheology 45* (2001), 855–879.

[34] Doufas, A. K., McHugh, A. J., and Miller, C. Simulation of melt spinning including flow-induced crystallization. Part I: Model development and predictions. *Journal of Non-Newtonian Fluid Mechanics 92* (2000), 27–66.

[35] Doufas, A. K., McHugh, A. J., Miller, C., and Immaneni, A. Simulation of melt spinning including flow-induced crystallization. Part II: Quantitative comparisons with industrial spinline data. *Journal of Non-Newtonian Fluid Mechanics 92* (2000), 81–103.

[36] Eder, G. *Macromolecular design of polymeric materials.* Marcel Dekker, Inc., New York, USA, 1997.

[37] Eder, G., Janeschitz-Kriegl, H., and Liedaues, S. Crystallization processes in quiescent and moving polymer melts under heat transfer conditions. *Progress in Polymer Science 15* (1990), 629–714.

[38] Fisher, R. J., and Denn, M. M. Finite-amplitude stability and draw resonance in isothermal melt spinning. *Chemical Engineering Science 30* (1975), 1129–1134.

[39] Fisher, R. J., and Denn, M. M. A theory of isothermal melt spinning and draw resonance. *AIChE Journal 22* (1976), 236–246.

[40] Fitt, A. D., Furusawa, K., Monro, T. M., Please, C. P., and Richardson, D. J. The mathematical modelling of capillary drawing for holey fiber manufacture. *Journal of Engineering Mathematics 43* (2002), 201–227.

[41] Flory, P. J. Thermodynamics of crystallization in high polymers I. Crystallization induced by stretching. *Journal of Chemistry and Physics 15* (1947), 397–408.

[42] Forest, M. G., and Ueda, T. An isothermal model for high-speed spinning of liquid crystalline polymers: coupling of flow, orientation and crystallization. *Journal of Non-Newtonian Fluid Mechanics 84* (1999), 109–121.

[43] Forest, M. G., Wang, Q., and Bechtel, S. E. 1-D isothermal spinning models for liquid crystalline polymer fibers. *Journal of Rheology 41* (1997), 821–850.

[44] Forest, M. G., Wang, Q., and Bechtel, S. E. 1-D models for thin filaments of liquid crystalline polymers: Coupling of orientation and flow in the stability of simple solutions. *Physics D 99* (1997), 527–554.

[45] Forest, M. G., Zhou, H., and Wang, Q. Thermotropic liquid crystalline polymer fibers. *SIAM Journal of Applied Mathematics 60* (2000), 1177–1204.

[46] Frank-Kamenetskii, D. A. *Diffusion and Heat Transfer in Chemical Kinetics.* Plenum Press, New York, USA, 1969.

[47] Freeman, H. I., and Coplan, M. J. Fiber melt extrusion: deviations from steady-state behavior in the spin line. *Journal of Applied Polymer Science 8* (1964), 2389–2398.

[48] Gelder, D. The stability of fiber drawing processes. *Industrial and Engineering Chemistry Fundamentals 10* (1971), 534–535.

[49] George, H. H. Model of steady-state melt spinning at intermediate take-up speeds. *Polymer Engineering and Science 22* (1982), 292–299.

[50] George, H. H., Holt, A., and Buckley, A. A study of structural development in the high speed spinning of poly(ethylene terephthalate). *Polymer Engineering and Science 23* (1983), 95–99.

[51] Georgiu, K. *Polymer processing instabilities: Control and understanding.* Marcel Dekker, New York, USA, 2005, ch. Stick-slip instability.

[52] Geyling, F. T. Basic fluid-dynamic considerations in the drawing of optical fibers. *The Bell System Technical Journal 55* (1976), 1011–1056.

[53] Ghaneh-Fard, A., Carreau, P. J., and Lafleur, P. G. Study of instabilities in film blowing. *AIChE Journal 42* (1996), 1388–1396.

[54] Gospodinov, P., and Yarin, A. L. Draw resonance of optical microcapillaries in non-isothermal drawing. *International Journal of Multiphase Flow 23* (1997), 967–976.

[55] Greenberg, J. M. Melt fracture revisited. *European Journal of Applied Mathematics 12* (2001), 465–477.

[56] Gupta, G., and Schultz, W. W. Non-isothermal flows of newtonian slender glass fibers. *International Journal of Non-Linear Mechanics 33* (1998), 151–163.

[57] Gupta, G. K., Schultz, W. W., Arruda, E. M., and Lu, X. Nonisothermal model of glass fiber drawing stability. *Rheologica Acta 35* (1996), 584–596.

[58] Han, C. D., and Lamonte, R. R. A study of polymer melt flow instabilities in extrusion. *Polymer Engineering Science 11* (1971), 385–394.

[59] Han, C. D., and Lamonte, R. R. Studies on melt spinning. III. Flow instabilities in melt spinning: Melt fracture and draw resonance. *Journal of Applied Polymer Science 16* (1972), 3307–3323.

[60] Han, C. D., and Shetty, R. Flow instability in tubular film blowing. 1. Experimental study. *Industrial and Engineering Chemistry Fundamentals 16* (1977), 49–56.

[61] Hatzikiriakos, S. G., and Dealy, J. M. Role of slip and fracture in the oscillating flow of hdpe in a capillary. *Journal of Rheology 36* (1992), 845–884.

[62] Hatzikiriakos, S. G., and Migler, K. B. The onset of wall slip and sharkskin melt fracture in capillary flow. *Polymer Engineering Science 34* (1994), 1441–1449.

[63] Hatzikiriakos, S. G., and Migler, K. B., Eds. *Polymer processing instabilities: Control and understanding*. Marcel Dekker, New York, USA, 2005.

[64] Henson, G., Cao, D., Bechtel, S. E., and Forest, M. G. A thin-filament melt spinning model with radial resolution of temperature and stress. *Journal of Rheology 42* (1998), 329–360.

[65] Huang, J., Baird, D. G., Loos, A. C., Rangarajan, P., and Powell, A. Filament winding of bicomponent fibers consisting of polypropelene and a liquid crystalline polymer. *Composites: Part A 32* (2001), 1013–1020.

[66] Huynh, B. P. Some finite elements studies of extrusion. *Journal of Non-Newtonian Fluid Mechanics 13* (1983), 1–20.

[67] Hyun, J. C. Theory of draw resonance. Part I. Newtonian fluids. *AIChE Journal 24* (1978), 418–422.

[68] Hyun, J. C. Theory of draw resonance. Part II. Power-law and maxwell fluids. *AIChE Journal 24* (1978), 423–426.

[69] Ishihara, H., and Kase, S. Studies of melt spinning. V. Daw resonance as a limit cycle. *Journal of Polymer Science A 19* (1975), 557–565.

[70] Ishihara, H., and Kase, S. Studies of melt spinning. VI. Simulation of draw resonance using newtonian and power law viscosities. *Journal of Polymer Science A 20* (1976), 169–191.

[71] Ji, C.-C., and Yang, J.-C. Mechanics of steady flow in coextrusion fiber spinning. *Polymer Engineering and Science 36* (1996), 1399–1409.

[72] Ji, C.-C., Yang, J.-C., and Lee, W.-S. Stability of newtonian coextrusion fiber spinning. *Polymer Engineering and Science 36* (1996), 2685–2693.

[73] Joo, Y. L., Sun, J., Smith, M. D., Armstrong, R. C., Brown, R. A., and Ross, R. A. Two-dimensional numerical analysis of non-isothermal melt spinning with and without phase transition. *Journal of Non-Newtonian Fluid Mechanics 102* (2002), 37–70.

[74] Jung, H. W., Song, H.-S., and Hyun, J. C. Draw resonance and kinematic waves in viscoelastic isothermal spinning. *AIChE Journal 46* (2000), 2106–2111.

[75] Kalika, D. S., and Denn, M. M. Wall slip and extrudate distortion in linear low-density polyethylene. *Journal of Rheology 31* (1987), 815–834.

[76] Kase, S. Studies of melt spinning. IV. On the stability of melt spinning. *Journal of Polymer Science A 18*, 11 (1974), 3279–3304.

[77] Kase, S., and Matsuo, T. Studies of melt spinning. I. Fundamental equations on the dynamics of melt spinning. *Journal of Polymer Science A 3* (1965), 2541–2554.

[78] Kase, S., and Matsuo, T. Studies of melt spinning. II. Steady-state and transient solutions of fundamental equations compared with experimental results. *Journal of Applied Polymer Science 11*, 2 (1967), 251–287.

[79] Keunings, R., Crochet, M. J., and Denn, M. M. Profile development in continuous drawing of viscoelastic liquids. *Polymers for Advanced Technologies 22* (1983), 347–355.

[80] Kim, B. M., Hyun, J. C., Oh, J. S., and Lee, S. J. Kinematic waves in the isothermal melt spinning of newtonian fluids. *AIChE Journal 42* (1996), 3164–3169.

[81] Kim, S., and Dealy, J. M. Gross melt fracture of polyethylene. I: A criterion based on tensile stress. *Polymer Engineering Science 42* (2002), 482–494.

[82] Kim, S., Fang, Y., Lafleaur, P. G., and Carreau, P. J. Dynamics and criteria for bubble instabilities in a single layer film blowing extrusion. *Polymer Engineering Science 44* (2004), 283–302.

[83] Kolmogorov, A. N. On the statistical theory of the crystallization of metals. *Bulletion of the Academy of Sciences of the USSR, Mathematical Series 1* (1937), 355–359.

[84] Laffargue, J., Parent, L., Lafleur, P. G., Carreau, P. J., Demay, Y., and Agassant, J. F. Investigation of bubble instabilities in film blowing process. *International Polymer Processing 17* (2002), 347–353.

[85] Landau, L. D., and Lifshitz, E. M. *(Course of Theoretical Physics) Statistical Physics: Part 1*, vol. 5. Pergamon Press, New York, USA, 1980.

[86] Landau, L. D., and Lifshitz, E. M. *(Course of Theoretical Physics) Statistical Physics: Part 2*, vol. 9. Pergamon Press, New York, USA, 1980.

[87] Lee, J. S., Jung, H. W., and Hyun, J. C. Melt spinning dynamics of phan-thien-tanner fluids. *Korea-Australia Rheology Journal 12* (2000), 119–124.

[88] Lee, J. S., Jung, H. W., Hyun, J. C., and Scriven, L. E. Simple indicator of draw resonance instability in melt spinning processes. *AIChE Journal 51* (2005), 2869–2874.

[89] Lee, J. S., Jung, H. W., Kim, S. H., and Hyun, J. C. Effect of viscoelasticity on the draw resonance dynamics of melt spinning. *Journal of Non-Newtonian Fluid Mechanics 99* (2001), 159–166.

[90] Lee, W.-S., and Park, C.-W. Stability of a bicomponent fiber spinning flow. *ASME Journal of Applied Mechanics 62* (1995), 511–516.

[91] Lipscomb, G. G. The melt hollow fiber spinning: Steady-state behavior, sensitivity and stability. *Polymers for Advanced Technologies 5* (1994), 745–758.

[92] Lyngaae-Jorgensen, J., and Marcher, B. "Spurt" fracture in capillary flow. *Chemical Engineering Communications 32* (1985), 117–151.

[93] Maier, W., and Saupe, A. Eine einfache molekulare theorie des nematischen kristallinflussigen zustandes. *Z. Naturforsch. A 13* (1958), 564.

[94] Matsui, M. Air drag on a continuous filament in melt spinning. *Transaction of the Society of Rheology 20*, 4 (1976), 465–473.

[95] McHugh, A. J., and Doufas, A. K. Modeling flow-induced crystallization in fiber spinning. *Composites: Part A 32* (2001), 1059–1066.

[96] Micic, P., Bhattacharya, S. N., and Field, G. Transient elongational viscosity of lldpe/ldpe blends and its relevance to bubble stability in the film blowing process. *Polymer Engineering Science 38* (1998), 1685–1693.

[97] Middleman, S. *Fundamental of Polymer Processing.* McGraw-Hill, New York, USA, 1977.

[98] Migler, K. B. *Polymer processing instabilities: Control and understanding.* Marcel Dekker, New York, USA, 2005, ch. Sharkskin instability in extrusion.

[99] Miller, J. C. Swelling behavior in extrusion. *Society of Petroleum Engineers Transactions 3* (1963), 134–137.

[100] Muke, S., Connell, H., Sbarski, I., and Bhattacharya, S. N. Numerical modeling and experimental verification of blown film processing. *Journal of Non-Newtonian Fluid Mechanics 116* (2003), 113–138.

[101] Naboulsi, S. K., and Bechtel, S. E. Bicomponent newtonian fibers. *Physics of Fluids 11* (1999), 807–820.

[102] Nakamura, K., Katayama, K., and Amano, T. Some aspects of nonisothermal crystallization of polymers. II. Consideration of the isokinetic condition. *Journal of Applied Polymer Science 17* (1973), 1031–1041.

[103] Nam, S., and Bogue, D. C. Dynamics of steady and unsteady melt spinning. *Industrial and Engineering Chemistry Fundamentals 23* (1984), 1–8.

[104] Nickell, R. E., Tanner, R. I., and Caswell, B. The solution of viscous incompressible jet and free-surface flows using finite-element-methods. *Journal of Fluid Mechanics 65* (1974), 189–206.

[105] Oh, T. H. Melt spinning and drawing processes of pet side-by-side bicomponent fibers. *Journal of Applied Polymer Science 101* (2006), 1362–1367.

[106] Otter, J. L. D. Mechanisms of melt fracture. *Plastics and Polymers 38* (1970), 155–168.

[107] Otter, J. L. D. Some investigations of melt fracture. *Rheologica Acta 10* (1971), 200–207.

[108] Oyanagi, Y. Melt fracture and shark skin. *Progress in Rubber and Plastics Technology 4* (1997), 231–247.

[109] Park, C.-W. Extensional flow of a two-phase fiber. *AIChE Journal 36* (1990), 197–206.

[110] Pearson, J. R. A., and Matovich, M. A. Spinning a molten threadline: Stability. *Industrial and Engineering Chemistry Fundamentals 8* (1969), 605–609.

[111] Pearson, J. R. A., and Matovich, M. A. Spinning a molten threadline: Steady state isothermal viscous flows. *Industrial and Engineering Chemistry Fundamentals 8* (1969), 512–520.

[112] Pearson, R. J. A. *Mechanics of Polymer Processing.* Elsevier Applied Sciense Publications, Ltd., New York, USA, 1985.

[113] Petrie, C. J. S., and Denn, M. M. Instabilities in polymer processing. *AIChE Journal 22* (1976), 209–236.

[114] Pone, E., Dubois, C., Guo, N., Lacroix, S., and Skorogatiy, M. Newtonian and non-Newtonian models of the hollow all-polymer Bragg fiber drawing. *Journal of Lightwave Technology 24* (2006), 4991–4999.

[115] Ramakrishna, S., Mu, Z., and Matsuura, T. *Polymer Membranes in Biotechnology.* World Scientific Publishing Co., Singapore, 2011.

[116] Ramalingam, S., and Armstrong, R. C. Analysis of isothermal spinning of liquid-crystalline polymers. *Journal of Rheology 37* (1993), 1141–1169.

[117] Ramos, J. I. Asymptotic analysis of compound liquid jets at low Reynolds numbers. *Applied Mathematics and Computation 100* (1999), 223–240.

[118] Ramos, J. I. Drawing of annular liquid jets at low Reynolds numbers. *Computational and Theoretical Polymer Science 11* (2001), 429–443.

[119] Ramos, J. I. Nonlinear dynamics of hollow, compound jets at low Reynolds numbers. *International Journal of Engineering Science 39* (2001), 1289–1314.

[120] Ramos, J. I. Stability and nonlinear dynamics of planar film casting processes. *International Journal of Engineering Science 39* (2001), 1949–1961.

[121] Ramos, J. I. Compound liquid jets at low Reynolds numbers. *Polymer 43* (2002), 2889–2896.

[122] Ramos, J. I. Convection and radiation effects in hollow, compound optical fibers. *International Journal of Thermal Sciences 44* (2005), 832–850.

[123] Ramos, J. I. Modelling of liquid crystalline compound fibres. *Polymer 46* (2005), 12612–12625.

[124] Ramos, J. I. *Polymer Research Developments.* Nova Science Publishers, Inc., New York, USA, 2006, ch. Chapter 7. Mathematical models of compound, polymer optical fibers, pp. 127–185.

[125] Rao, I. J., and Rajagopal, R. K. A thermodynamic framework for the study of crystallization in polymers. *ZAMP, Zeitschrift for Angewandte Mathematik und Physik 53* (2002), 365–406.

[126] Schultz, W. W., and Davis, S. H. One-dimensional liquid fibers. *Journal of Rheology 26* (1982), 331–345.

[127] Schultz, W. W., and Davis, S. H. Effects of boundary conditions on the stability of slender viscous fibers. *ASME Journal of Applied Mechanics 51* (1984), 1–5.

[128] Schultz, W. W., Zebib, A., Davis, S. H., and Lee, Y. Nonlinear stability of newtonian fibres. *Journal of Fluid Mechanics 149* (1984), 455–475.

[129] Shah, Y. T., and Pearson, J. R. A. On the stability of nonisothermal fiber spinning. *Industrial and Engineering Chemistry Fundamentals 11* (1972), 145–149.

[130] Shah, Y. T., and Pearson, J. R. A. On the stability of nonisothermal fiber spinning - General case. *Industrial and Engineering Chemistry Fundamentals 11* (1972), 150–153.

[131] Shah, Y. T., and Pearson, J. R. A. Stability of fiber spinning of power-law fluids. *Polymer Engineering Science 12* (1972), 219–223.

[132] Shi, X. Q., Ito, H., and Kikutani, T. Structure development and properties of high-speed melt spun poly(butylene terephthalate)/poly(butylene adipate-co-terephthalate) bicomponent fibers. *Polymer 47*, 2 (2006), 611–616.

[133] Shore, J. D., Ronis, D., Piché, L., and Grant, M. Theory of melt fracture instabilities in the capillary flow of polymer melts. *Physics Review E 55* (1997), 2976–2992.

[134] Sombatsompop, N., and Wood, A. K. An examination of melt fracture in molten polymers. *Polymer-Plastics Technology and Engineering 37* (1998), 317–331.

[135] Song, L., Li, B., Zarkadas, D., Christian, S., and Sirkar, K. K. Polymeric hollow-fiber heat exchangers for thermal desalination processes. *Industrial Engineering and Chemistry Research 49* (2010), 11961–11977.

[136] Sun, J., Subbiah, S., and Marchal, J. A. Numerical analysis of nonisothermal viscoelastic melt spinning with ongoing crystallization. *Journal of Non-Newtonian Fluid Mechanics 93* (2000), 133–151.

[137] Tanner, R. I. A theory of die-swell. *Journal of Polymer Science 8* (1970), 2067–2078.

[138] Tanner, R. I. A new inelastic theory of extrudate swell. *Journal of Non-Newtonian Fluid Mechanics 6* (1980), 289–302.

[139] Tanner, R. I. *Engineering Rheology*. Clarendon Press, Oxford, UK, 1985.

[140] Timbercon, I. Plastic optical fiber, September 2011. http://www.timbercon.com/plastic-optical-fiber.

[141] Tordella, J. P. Capillary flow of molten polyethylene - a photo graphic study of melt fracture. *Transactions of the Society of Rheology 1* (1957), 203–212.

[142] Voyce, C. J., Fitt, A. D., and Monro, T. M. Mathematical model of the spinning of microstructured fibres. *Optics Express 12* (2004), 5810–5820.

[143] Wang, Q., Forest, M. G., and Zhou, H. A model study of the spinning of thermotropic liquid crystalline polymers: Fiber performance predictions and bounds on throughput. *Advances in Polymer Technologies 18*, 4 (1999), 314–335.

[144] Weinberger, C. B., Cruz-Saenz, G. F., and Donnelly, G. J. Onset of draw resonance during isothermal melt spinning: A comparison between measurements and predictions. *AIChE Journal 22* (1976), 441–448.

[145] White, J. L. Dynamics, heat transfer and rheologiucal aspects of melt spinning: a critical review. *Polymer Engineering Review 1* (1981), 297–362.

[146] Xue, S. C., Tanner, R. I., Barton, G. W., Lwin, R., Large, M. C. J., and Poladian, L. Fabrication of microstructured optical fibers-Part I: Problem formulation and numerical modeling of transient draw process. *Journal of Lightwave Technology 23* (2005), 2245–2254.

[147] Xue, S. C., Tanner, R. I., Barton, G. W., Lwin, R., Large, M. C. J., and Poladian, L. Fabrication of microstructured optical fibers-Part II: Numerical modeling of steady–state draw process. *Journal of Lightwave Technology 23* (2005), 2255–2266.

[148] Yarin, A. L. *Free Liquid Jets and Films: Hidrodynamics and Rheology*. Longman, New York, USA, 1993.

[149] Yarin, A. L., Gospodinov, P., Gottlieb, O., and Graham, M. D. Newtonian glass fiber drawing: Chaotic variation of the cross-sectional radius. *Physics of Fluids 11* (1999), 3201–3208.

[150] Yarin, A. L., Gospodinov, P., and Roussinov, V. I. Stability loss and sensitivity in hollow-fiber drawing. *Physics of Fluids 6* (1994), 1454–1463.

[151] Yeow, Y. L. Stability of tubular film flow: A model of the film-blowing process. *The Journal of Fluid Mechanics 75* (1976), 577–591.

[152] Zeronian, S. H., Inglesby, M. K., Pan, N., Lin, D., Sun, G., Soni, B., Alger, K. W., and Gibbon, J. D. The fine structure of bicomponent polyester fibers. *Journal of Applied Polymer Science 71*, 7 (1999), 1163–1173.

[153] Ziabicki, A. *Fundamentals of Fibre Formation.* John Wiley & Sons, New York, USA, 1976.

[154] Ziabicki, A., Jarecki, A., and Wasiak, A. Dynamic modelling of melt spinning. *Computational and Theoretical Polymer Science 8* (1998), 143–157.

[155] Zubia, J., and Arrue, J. Plastic Optical Fibers: An introduction to their technological processes and applications. *Journal of Optical Fiber Technology 7* (2001), 101–140.

Francisco José Blanco Rodríguez

Universidad de Málaga
Departamento de Lenguajes y Ciencias de la Computación
Escuela de Ingenierías
C/ Doctor Ortíz Ramos, s/n, Málaga 29071

Phone: (+34) 951952522
Fax: (+34) 951952542
Email: fjblanco@lcc.uma.es

PERSONAL

- Nacido el 30 de agosto de 1979 en Aguadulce, Sevilla (España).
- Nacionalidad española.

FORMACIÓN ACADÉMICA

2009–2011 **Universidad de Málaga** *(Málaga)*
Doctor Ingeniero Industrial

2007–2009 **Universidad de Málaga** *(Málaga)*
Diploma de Estudios Avanzados (DEA) en Ingenieria Mecatrónica
Calificación: Sobresaliente (3.0/4.0)

1998–2006 **Universidad de Málaga** *(Málaga)*
Ingeniero Industrial
Calificación: 1.61/4.0

1997–1998 **I.E.S. Rio Verde** *(Marbella, Málaga)*
Curso de Orientación Universitaria (C.O.U)
Calificación: 7.04/10.0

1994–1996 **I.E.S. Rio Verde** *(Marbella, Málaga)*
Título de Bachiller

BECAS Y AYUDAS

2007–2011 **Beca de Formación de Profesorado Universitario (FPU)**
Ministerio de Educación y Ciencia, España
Referencia: AP2006-02242

ESTANCIAS DOCTORALES

2011 **Technische Universiteit Eindhoven** (Eindhoven, Holanda)
Department of Mechanical Enginering, Polymer Technology
3 meses en colaboración con Dr.ir. Martien Hulsen
(m.a.hulsen@tue.nl)

2009 **University of Manchester** (Manchester, Reino Unido)
School of Mathematics
3 meses en colaboración con Prof. Matthias Heil
(M.Heil@maths.man.ac.uk)

PUBLICACIONES

Revistas Internacionales

- Francisco J. Blanco–Rodríguez and J. I. Ramos, **Melt spinning of semi–crystalline compound fibers**, *Polymer* 52, 2011, pp. 5573–5586.
- Francisco R. Villatoro, Francisco J. Blanco–Rodríguez and J. I. Ramos, **Numerical analysis of the effect of small geometrical imperfections on photonic crystal wires**, *Applied Mathematics and Computation* 218, 2012, pp. 5989–5993.

Artículos en preparación

- Francisco J. Blanco–Rodríguez and J. I. Ramos, **A simplified two–dimensional method of the melt spinning of semi–crystalline hollow compound fibers**, *International Journal of Thermal Sciences*. Under review

Conferencias Internacionales

- Francisco J. Blanco–Rodríguez and J. I. Ramos, **Shell formation due to heat and mass transfer**, *Advances in Computational Heat Transfer CHT-12*. Under review
- J. I. Ramos and Francisco J. Blanco–Rodríguez, **Two–dimensional analysis of the crystallization of hollow compound plastic fibers**, *Seventh International Conference on Computational Heat and Mass Transfer*, Istanbul, Turkey. July 18–22, 2011.
- Francisco J. Blanco–Rodríguez and J. I. Ramos, **Modelling of molecular orientation and crystallization in the manufacture of semi–crystalline compound fibres**, *ASME-ATI-UIT Conference on Thermal and Environmental Issues in Energy Systems*, Sorrento, Italy. May 16–19, 2010, pp. 1177–1183. ISBN: 978-884672659-9
- Francisco J. Blanco–Rodríguez and J. I. Ramos, **Crystallization of compound plastic optical fibers**, *Fifth International Conference on Thermal Engineering: Theory and Applications* Marrakech, Morocco. May 10–14, 2010, pp. 284–289. ISBN: 1-894503-937

Otros

- Francisco J. Blanco–Rodríguez, **Crystallization of compound plastic optical fibers**, *MAGIC 2009 Postgraduate Conference*, Leeds, United Kingdom. December 14–16, 2009.

IDIOMAS

Español, lengua materna.

Inglés, nivel alto escrito y leído; nivel medio hablado.

Last updated: March 12, 2012
http://www.lcc.uma.es/~fjblanco

DECLARATION

I hereby certify that this material, which I now submit for assessment on the programme of study leading to the award of Ph. D. is entirely my own work, that I have exercised reasonable care to ensure that the work is original, and does not to the best of my knowledge breach any law of copyright, and has not been taken from the work of others save and to the extent that such work has been cited and acknowledged within the text of my work.

Málaga, March 2012

Francisco José Blanco Rodríguez